BISRU

BLAST IMPACT & SURVIVABILITY RESEARCH UNIT

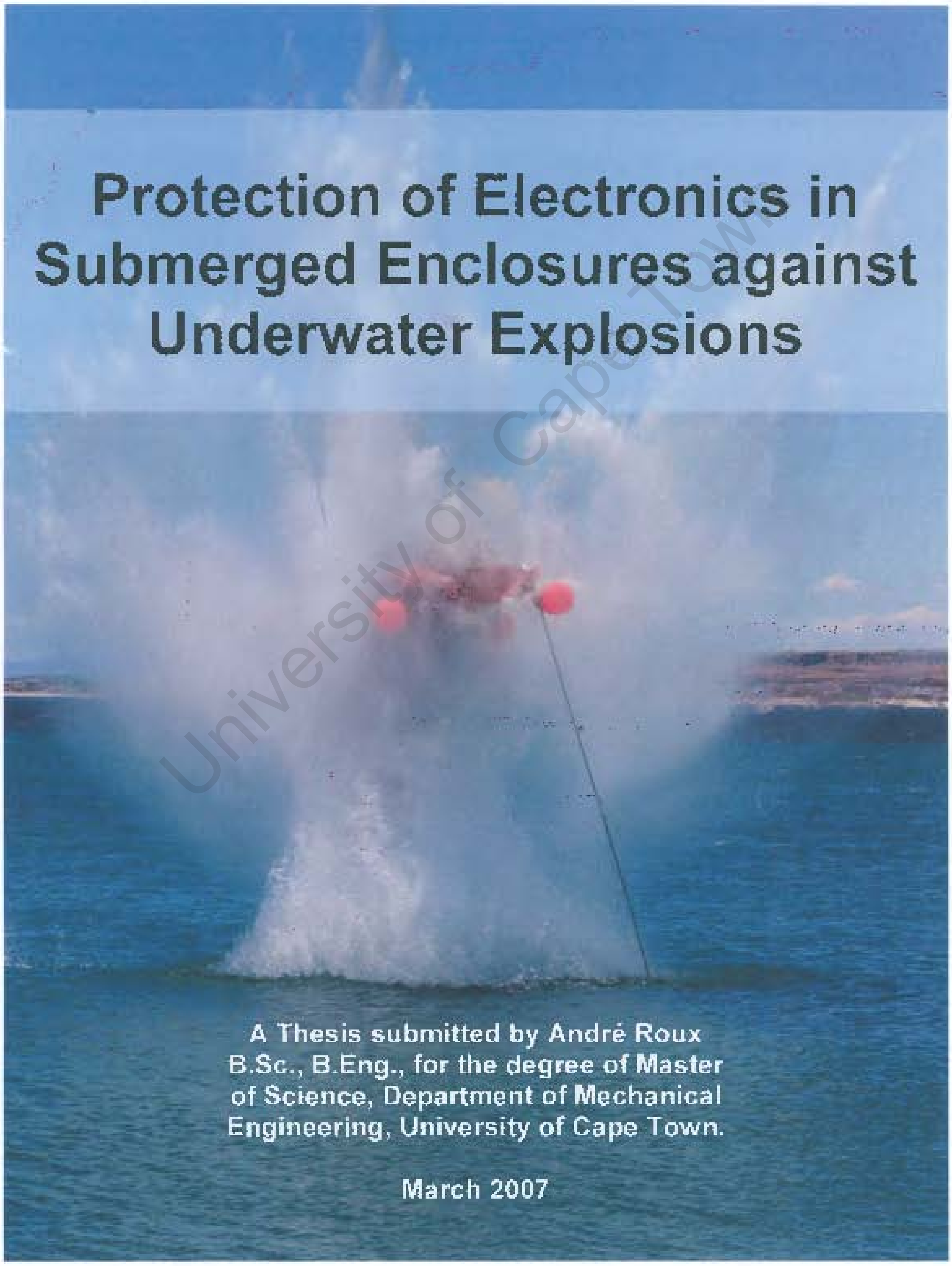

Protection of Electronics in Submerged Enclosures against Underwater Explosions

A Thesis submitted by André Roux
B.Sc., B.Eng., for the degree of Master
of Science, Department of Mechanical
Engineering, University of Cape Town.

March 2007

ACKNOWLEDGEMENTS

Soli Deo Gloria

My sincere gratitude is also extended to:

Professor G.N. Nurick:	for his esteemed advice, wisdom, willing guidance and support in his professional overall supervisory capacity, and also as respected friend for many years.
Mr. S. Ginsberg:	for his valued technical input and advice in his supervisory capacity for this study as electronic measurement specialist.
Mr. J. Treurnicht:	for his support and input with respect to the control systems theory.
BISRU personnel:	for their general support and scientific assistance whenever it was required.
Colleagues:	D.F. Malan for his support, assistance and organisational skills during field tests, A. Coetzee for the drawing and manufacture of the Aluminium Enclosure, and T. Maskowitz for his assistance with the measurement setup before and during field trials.
SA Defence Force:	for their untiring and motivated assistance at the underwater demolition range.

STATEMENT

This thesis contains no material which has been presented for the award of any other degree or diploma in any university. I understand the meaning of plagiarism and declare that, to the best of my knowledge and belief, contains no material previously written or published by another person, except where due reference and acknowledgement is made in the text.

Signed by candidate

André Roux

SYNOPSIS

Background

In the past, the subject of damage to contained electronics due to underwater blasting has generally been prone to speculation, as scientific publications on this topic have only become available in recent times. The problem of controlling damage to enclosed electronics and hardening[1] of electronics against the blast environment have now come to require urgent attention as an input to the design and manufacture of military equipment. This study provided direction with respect to discovering the root cause(s) of the problem and to solve the problem.

Rationale

In the milieu of military sea mine design, it is often necessary to design mines that are to be placed at small distances from each other. A possible tactical purpose may require that each mine be set to explode at controlled instances in time without disturbing the operation of the other mines in the field, or causing sympathetically detonated reactions. Thus two problems (on face value) are prevalent when reliable operation of two mines in close proximity is to be considered:

The first problem is sympathetic detonation. This is the term used when one explosion causes another explosion to occur, due to the shock-effect of the blast of the original explosion. The cause of this sympathetic phenomenon is generally ascribed to the effect of the shock caused by the blast of the first explosion on the primary[2] explosives of the neighbouring mine detonation chain (or train), which can initiate the explosion of this neighbouring explosive chain. (Chung and Kinsey [1] have executed compelling experiments in this field). Modern tendencies are to use only insensitive explosives, to avoid the sympathetic detonation effect. However, insensitive munitions are not generally used in South Africa, and therefore the problem of sympathetic detonation should still be addressed.

The second problem is reliability failure. Although the description in the previous paragraph may suggest that the shock effects on the primary explosives are the only causes of sympathetic detonation, it must be said that this phenomenon is only valid under certain circumstances. In practice, the first link in the explosive chain is a detonator, which contains primary explosives. This detonator forms part of a "safety arming and firing unit" (SAFU), which is constructed by mechanical parts as well as electronic assemblies. The detonator is initiated by electrical means. If a failure of the SAFU is experienced, the operation of the mine is compromised. The experience during military operations has been that failures do occur due to blast effects, when sympathetic detonations do not occur.

In general, it was observed by military investigations that sympathetic detonations occur when the standoff distance between the two explosive bodies (mines) are extremely small, relative to the size of the explosive mass. When the standoff distance is increased to the extent that

---

[1] The word "hardening" refers to a design process to protect the electronics against the blast effects of this environment.

[2] The term "primary explosives" is in fact etomology of the concept of explosives that are not as stable as the "secondary explosives" (also an etomology) or insensitive explosives in the final stage of an explosive chain. Primary explosives thus effectively are the "sensitive explosives" in the explosive chain and form part of the sections of the chain that initiate the explosion. The speaking term of "primary explosives" is derived from its implementation origin.

sympathetic detonation does not occur, the shock effect was still powerful enough to damage the SAFU of the neighbouring mine. A dangerous disadvantage of damage to the SAFU (by whatever means), is that the damage occurs in an uncontrolled manner, and therefore could also cause initiation (or delayed initiation) of the explosive chain, causing a face-value (possibly incorrect) conclusion that the second explosion was caused by sympathetic detonation.

The second problem, as discussed above, forms the basis of this study, which is intended to find a viable solution to eliminate damage to the SAFU at standoff distances as small as possible beyond the sympathetic detonation distance.

Results and Conclusions

The shock wave of an underwater explosion was found to be the main contributor towards the damage results, and therefore the well published shock wave characteristics were revisited, with respect to the specific problem as addressed by this dissertation.

On the evidence found in the literature, it was hypothesised that the shock wave induced an acceleration into an Electronics Enclosure of an adjacently positioned mine (in the mine field). This induced acceleration was then passed onto the printed circuit board which was mounted inside the Enclosure, and hence to the electronic components, each having a different mass (therefore a different inertia). Each component then acquired a different momentum and brakeage occurred.

Field tests were performed to obtain results of acceleration of the Enclosure as well as acceleration of the electronics hardware under different conditions. Internal (to the Enclosure) damping devices were also tested to measure the acceleration attenuation.

The results obtained indicated that a very uncomplicated, but feasible damping-solution had been found, and that the mathematical description had been established for simulation purposes and repeatability reasons. Application of the newly prescribed method would successfully protect the electronics of a neighbouring mine in the presence of an explosion of one of the mines in the minefield.

LAYOUT OF THIS DISSERTATION

Chapter 1:	This chapter describes the aim of the study. For better understanding of the course of the study, it was necessary to describe (or to summarise) the work that had been done on this subject before this study was undertaken. These data sets which are summarised in Chapter 1 have not been published widely before. The reasons for doing the study are noted and it was thought to be appropriate to include the research design to emphasise the structural approach to the execution of this research project.
Chapter 2:	This chapter presents the main literature review, which discusses the main contributions to this specific topic, as well as some of the supporting literature for the sake of characterising an underwater explosion. The rationale was that it is necessary to understand the scientific characteristics of the phenomenon which causes damage to electronics before an acceptable and repeatable solution could be found to counteract the phenomenon. The literature research therefore concentrated on the characterisation of an underwater explosion, and its effects on objects in close proximity. The single most significant contribution was found in the form of an unpublished short report by Ström and Janzon [10], and a set of raw data of digital measurements using 20 measurement series. It was thus necessary to elaborate on this data in order to form the basis of the analysis to steer the study in the appropriate direction, and to characterise an underwater shock wave.
Chapter 3:	This chapter discusses the factors leading to the cause of damage to electronics, taking cognizance of the characteristics established in Chapter 2. If the cause were known, the solution could be found. This chapter therefore produces the hypothesis of the most probable cause of damage to electronics during and after an underwater explosion. Leading from the hypothesis, two postulations were formulated, which were expected to lead to the mitigation of the effects of the underwater blast on nearby electronic equipment. Chapter 3 furthermore considers a possible solution, which this study accepts as the main subject of measurement and analysis to prove the hypothesis.
Chapter 4:	The hypothesis in Chapter 3 required that certain measurements should be taken to be able to conclude, by analysis, whether the hypothesis was true. The characteristics established in Chapter 2 were taken into consideration to select the appropriate sensors and measurement apparatus. The characteristics of the sensors and the characteristics of the detonators, as well as the estimated time delays and the synchronisation requirements are discussed in this chapter, together with the limitations of the fast digital measurement equipment that was envisaged to be used for the data collection. A discussion on the asymmetrical waveform that was to be measured, and the measurement limitations of sampled-data systems, led to the detailed analysis and empirical verification of a possible bandwidth problem.

Chapter 5: This chapter describes the practical field work that was done to obtain and analyse the digital data that eventually led to the solution of the stated problem. The first experiment was aimed at gaining hands-on experience with respect to finding a convenient size of scaled explosive mass in relation to the wall thickness of the Enclosure at convenient scaled standoff distances. No sensors were used, due to the uncertain variables. In the second and third experiments sensors were used, and a grommet-suspension was evaluated. The fourth experiment replaced the grommets with a softer (sponge rubber) suspension method, which was ultimately accepted as the ideal suspension method. In the experiments that included sensors, it was found that the synchronisation method was not ideal. A fifth experiment was executed to evaluate the use of a light sensor for improved synchronisation, and was successful. A sixth and final experiment used the best features of the previous experiments, and using an optical sensor synchronisation was successful. This experiment also used sponge rubber as a suspension method to verify that this was the best suspension method.

Chapter 6: This chapter concludes the findings of Chapter 5, and verifies that a solution had been found. This chapter also emphasises the contributions made towards the shock wave theory, and the mitigating factors to counteract the shock wave effects.

LAYOUT OF THIS DISSERTATION

Chapter 1: This chapter describes the aim of the study. For better understanding of the course of the study, it was necessary to describe (or to summarise) the work that had been done on this subject before this study was undertaken. These data sets which are summarised in Chapter 1 have not been published widely before. The reasons for doing the study are noted and it was thought to be appropriate to include the research design to emphasise the structural approach to the execution of this research project.

Chapter 2: This chapter presents the main literature review, which discusses the main contributions to this specific topic, as well as some of the supporting literature for the sake of characterising an underwater explosion. The rationale was that it is necessary to understand the scientific characteristics of the phenomenon which causes damage to electronics before an acceptable and repeatable solution could be found to counteract the phenomenon. The literature research therefore concentrated on the characterisation of an underwater explosion, and its effects on objects in close proximity. The single most significant contribution was found in the form of an unpublished short report by Ström and Janzon [10], and a set of raw data of digital measurements using 20 measurement series. It was thus necessary to elaborate on this data in order to form the basis of the analysis to steer the study in the appropriate direction, and to characterise an underwater shock wave in the far field.

Chapter 3: This chapter discusses the factors leading to the cause of damage to electronics, taking cognizance of the characteristics established in Chapter 2. If the cause were known, the solution could be found. This chapter therefore produces the hypothesis of the most probable cause of damage to electronics during and after an underwater explosion. Leading from the hypothesis, two postulations were formulated, which were expected to lead to the mitigation of the effects of the underwater blast on nearby electronic equipment. Chapter 3 furthermore considers a possible solution, which this study accepts as the main subject of measurement and analysis to prove the hypothesis.

Chapter 4: The hypothesis in Chapter 3 required that certain measurements should be taken to be able to conclude, by analysis, whether the hypothesis was true. The shock wave characteristics established in Chapter 2 were taken into consideration to select the appropriate sensors and measurement apparatus. The characteristics of the sensors and the characteristics of the detonators, as well as the estimated time delays and the synchronisation requirements are discussed in this chapter, together with the limitations of the fast digital measurement equipment that was envisaged to be used for the data collection. A discussion on the asymmetrical waveform that was to be measured, and the measurement limitations of sampled-data systems, led to the detailed analysis and empirical verification of a possible bandwidth problem.

Chapter 5: This chapter describes the practical field work that was undertaken to obtain and analyse the digital data that eventually led to the solution of the stated problem. The first experiment was aimed at gaining hands-on experience with respect to finding a convenient size of scaled explosive mass in relation to the wall thickness of the Enclosure at convenient scaled standoff distances. No sensors were used, due to the uncertain variables. In the second and third experiments sensors were used, and a grommet-suspension was evaluated. The fourth experiment replaced the grommets with a softer (sponge rubber) suspension method, which was ultimately accepted as the ideal suspension method. In the experiments that included sensors, it was found that the synchronisation method was not ideal. A fifth experiment was executed to evaluate the use of a light sensor for improved synchronisation, and was successful. A sixth and final experiment used the best features of the previous experiments as well as using optical sensor synchronisation, which was successful. This experiment also used sponge rubber as a suspension method to verify that this was the best suspension method.

Chapter 6: This chapter concludes the findings of Chapter 5, and verifies that a solution had been found. This chapter also emphasises the contributions made towards the shock wave theory, and the mitigating factors to counteract the shock wave effects.

TABLE OF CONTENTS

TABLE OF FIGURES

Chapter 1

Chapter 2

Chapter 3

Chapter 4

Chapter 5

Experiment 1

Experiment 2

Experiment 3

Experiment 4

Experiment 5

Experiment 6

Appendices

LEGEND OF ABBREVIATIONS AND ACRONYMS

a	Acceleration in an equation
a_0	Charge radius in an equation
A/D	Analogue to Digital conversion
ASCII	American Standard Code for Information Interchange
BISRU	Blast Impact and Survivability Research Unit
C	Denotes a capacitor in an electronic circuit
CCA	Circuit Card Assembly
C_{CE}	Capacitance measured between the Collector and the Emitter
CD	Compact Disc
CSIR	Council for Scientific and Industrial Research
DAQ	Data Acquisition
DSTO	Defence Science and Technology Organisation
ESAD	Electronic Safety Arming Device
E_b	Bubble energy
E_s	Shock energy, also written as e_{shock}
F	Force in an equation
FET	Field-effect Transistor
g	Unit of acceleration : 1 g = 9.81 m/s^2
gm	Unit of mass (gram)
Hz	Unit of frequency = Hertz
IC	Integrated Circuit
ICP	A Supplier of piezo-electric sensors
J	Unit of energy = Joule
kg	Unit of mass = kilogram
LED	Light Emitting Diode
m	Mass in an equation
m	Unit of length = meters
mm	Unit of length = millimetres
m/s	Unit of velocity = meters per second
ms	Unit of time = milliseconds
mA	Measure of electrical current (milli-Amps)
mV	Unit of electronic potential = millivolt
MPa	Unit of pressure = Mega-pascal
MJ	Unit of energy = Mega-joule
MS/s	Mega-samples per second
nF	Unit of capacitance = nano-farad
Pa	Unit of pressure = pascal
PCB	Printed Circuit Board

PE4	Plastic Explosives type 4
psi	Unit of pressure = pounds per square inch
PXI	Personal Computer Expanded Interface
SAFU	Safety Arming and Firing Unit
s	Unit of time = seconds
SOD	Standoff Distance
P	Pressure in an equation
Q	Mass of explosives in an equation
R	Standoff distance in an equation
R	Denotes a resistor in an electronic circuit
R_{CE}	Resistance measured between the Collector and the Emitter
RSA	Republic of South Africa
SM	Surface Mounted (components)
TNT	Tri-Nitro-Toluene
TTL	Transistor-Transistor Logic
USA	United States of America
V	Volt
VOD	Velocity of Detonation
V_{p-p}	Volt (peak-to-peak)
ω_c	Denotes the carrier frequency in an equation
Ω	Unit of electrical resistance/impedance
θ	Decay constant in an equation of shock pressure
υ	Particle velocity in an equation
ρ	Density in an equation
μF	Unit of capacitance = micro-farad
μs	Unit of time = micro-seconds
Ω	Measure of resistance (Ohm)

Chapter 1

1.1. TITLE

Protection of Electronics contained in Submerged Enclosures against Underwater Explosions

1.2. AIM

An empirical study was done to investigate the parameters that are involved leading to the design of electronic equipment which would be subjected to blast loading during its operational life, and which should be able to withstand several such blast-loading events.

1.3. INTRODUCTION

Typical blast loading in practise would be generated by explosive charges of 40 kg and more, at typical distances of 5 m. Charges of 40 kg and more were, for practical purposes, too large with which to execute experiments. According to established scaling parameters (Cole [5] and Equation 3 on page 29), these target specifications could be scaled to typical standoff distances of 250 mm to 350 mm from an explosive charge of 30 gm Pentolite.

It was proposed that an in-depth study be done on the characteristics of an underwater blast, in close proximity to the blast, and to determine the physical effects on electronics enclosures that are situated in close proximity to the blast. The study shows how these effects translate to ultimate damage of electronics contained within the enclosures, and that solutions needed to be found to eliminate damage to the electronics.

This study was undertaken after literature recording of the information that follows had been perused.

The problem of damage to electronics contained in Aluminium enclosures was investigated by the CSIR some years ago. A number of identical pieces of equipment (contained electronics) were placed at various distances from an explosive charge. After the explosives had been detonated, the electronic equipment was retrieved and examined for damage caused by the explosion.

First-line tests were conducted at the scene of the explosion, and more extensive tests were executed in the laboratories at a later stage. A CSIR internal report by Malan [12] explained that a certain[3] piece of equipment was placed at various distances from an underwater explosion, to find a correlation between stand-off distance and damage for a certain explosive charge weight.

---

[3] This "certain" piece of equipment was a custom-designed unit that was specifically designed to have mechanical as well as electronic "soft spots".

The Test setup is depicted graphically in Figure 1. The test results were evaluated by Roos [18], but the tests were found to be inconclusive due to the fact that some damage was sustained at long distances, while less or no damage of the same kind was sustained at closer stand-off distances. The stand-off distances which produced no damage were also declared unacceptable. This test was the catalyst that induced further research to find a solution to the problem of operating equipment much closer to an underwater explosion without the risk of damage.

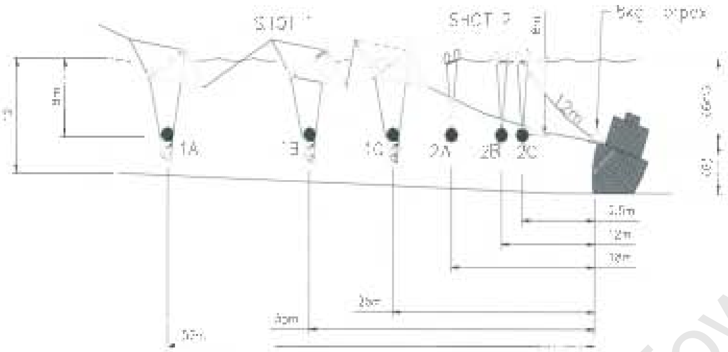

Figure 1: Test Setup for the damage tests

Further research was conducted by Hattingh [8] whose approach was to add a shock-absorbing protective layer to the outside of the equipment to reduce the intensity of the shock before the residual shock wave made contact with the equipment. According to Hattingh [8], pumice-stone is used in the USA for this shock-absorbing purpose, but he also states that this material is not readily available in the RSA. Four different materials were used in the research conducted by Hattingh [8], and a general-purpose electro-mechanical time clock was used as test object. The test objects were fully enclosed in the shock absorbent materials, and placed at a stand-off distance of 2 m from a 253-gram charge, at a depth of 3 m. This charge would generate a shock wave with peak amplitude of 14.86 MPa at a stand-off distance of 2 m, according to the Cole [5] Equation. Hattingh [8] concluded that two of the four types of materials used were not suitable due to excessive heat release during the casting and curing phases. The other materials protected the electronics adequately for that specific test setup, but it was estimated that only one shock of this magnitude would be withstood, due to cracking of the material after the first blast.

Hattingh's [3] results showed that this type of external shock absorber casing has the distinct disadvantage that it covers the equipment completely, and does not allow for testing or settings after the casing is moulded into position. The requirement for accuracy of external dimensions, plus characteristics such as testability, setting ability, and waterproof ability can not be met when using the prescribed material for the application as addressed by this study. See Figure 2 for damage to the shock-absorbing material. Unfortunately, not enough tests were conducted to formulate any trends, and therefore no statistical conclusions could be drawn.

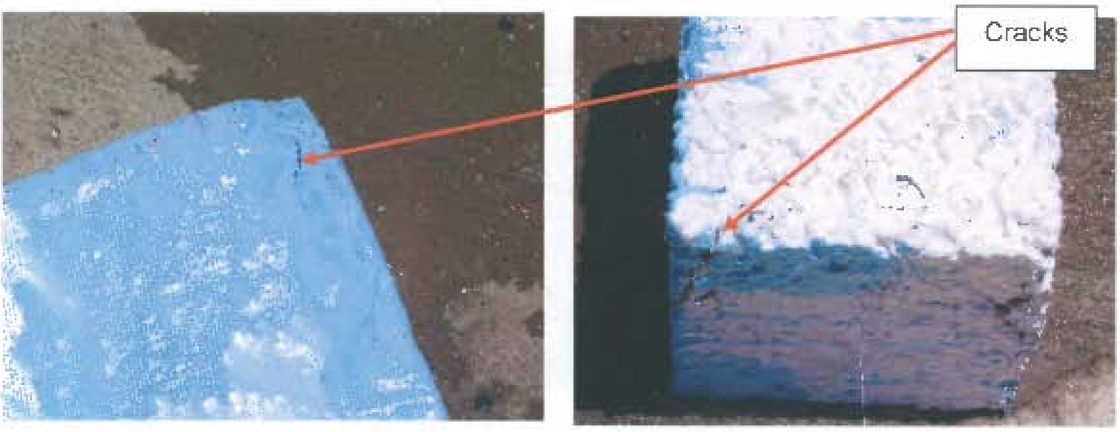

Figure 2: **Cracks on the test sample of shock-absorbent protective material**

The inconclusive findings derived from Hattingh's [3] work, led to a decision to do more trials with a typical aluminium enclosure containing typical electronics to find solutions with improved results.

Further trials were conducted with three of the units as described by Malan [12], but the electronics were replaced by a single CCA containing typical electronics for this discipline, such as a battery, ICs, capacitors, LEDs and micro-switches (see Figure 3). The design was kept simple, for easy testing before and after the blast occurred.

Figure 3: **Custom electronics used by Malan [13]**

The results were recorded by Malan [13], who used three mechanical housings (containers) containing the special custom electronics. The units were placed at three stand-off distances from a 1.17 kg PE4 explosive charge, by suspending the test units below the charge as in Figure 4.

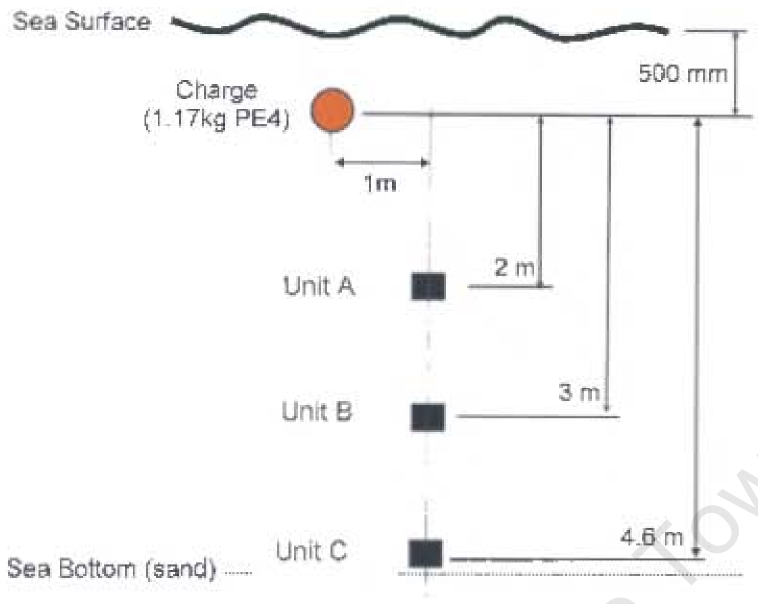

Figure 4: **The test set-up by Malan [13]**

The units were retrieved only minutes after the detonation and it was immediately apparent that all units sustained severe damage. It was also apparent that the unit closest to the charge sustained the most damage, and the unit furthest away from the blast sustained the least amount of damage, as would be expected. Both mechanical assemblies and electronic assemblies sustained damage. The electronics damage is shown in Figure 5.

Figure 5: **Electronics damage as recorded by Malan [13]**

The damage was sufficiently examined at the laboratory. Particular attention was given to details to enable a conclusion that the electronics damage was mainly caused by collateral effects. Mechanical parts were sheared off from their mountings and struck the electronics due to the momentum of the parts that were dislodged. There is some degree of evidence that the electronic components sustained damage without interference from the moving mechanical parts. A recommendation was made by Malan [13] to perform further trials, but with the use of a custom-designed enclosure, which would ensure that (if the electronics sustained damage) the damage would not result from collateral effects.

1.4. Research Design

1.4.1. General

The conclusion drawn from the preliminary literature study summarised above, is that recent tests done at sea found that typical ESAD electronics in watertight containers in close proximity to a blast sustain damage due to the effects of underwater blasts.

The extent of such damage has been enough to render the electronics unserviceable. This posed a general question about the physical design parameters of the present equipment for use under these circumstances, and about whether it is able to withstand the effects of an underwater blast. There are no user specifications as yet to specify the size of the explosive mass and the stand-off distance to be achieved without damage to the electronics, but preliminary target figures are defined as: 40 kg PE4 explosive charge, at a stand-off distance of 4 m.

The electronic unit of choice that was to be used in the experiments as input to this dissertation was a generic ESAD, containing most of the popular electronic components generally used for an ESAD, as well as specific "soft"[4] components, which were expected to sustain damage more readily. The soft components, as shown in Figure 6, were:

Commercial plastic enclosed switches Figure 6(A)

Crystals Figure 6(B)

Socket-mounted integrated circuits Figure 6(C)

Through-hole soldered transistors Figure 6(D)

Commercial Batteries Figure 7(E)

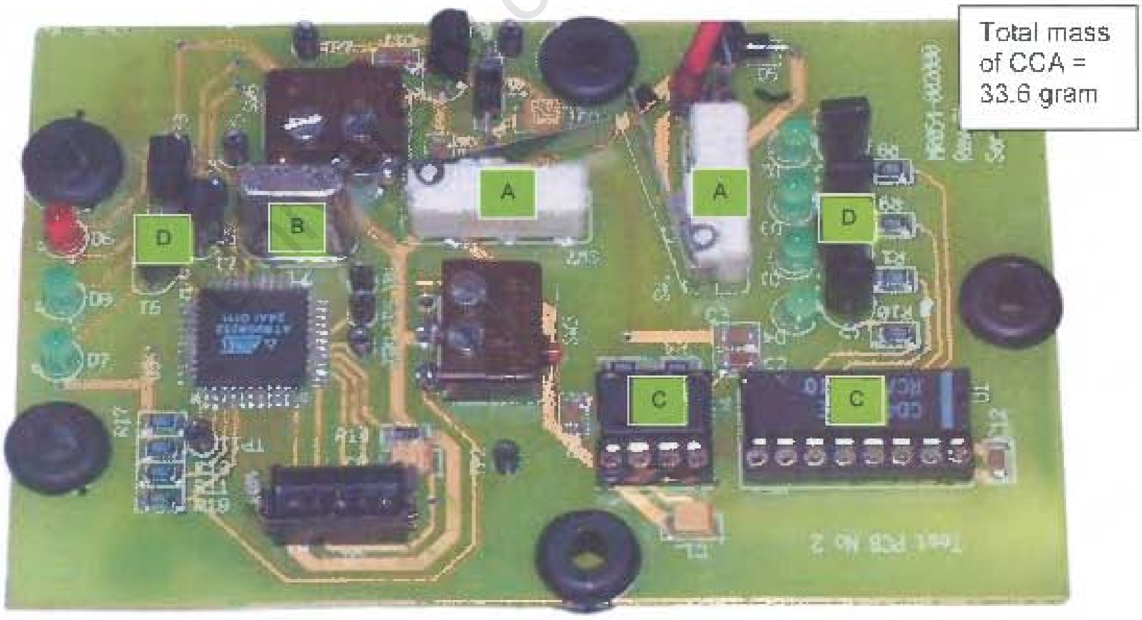

Total mass of CCA = 33.6 gram

Figure 6: **The electronics Circuit Card Assembly (CCA) used in experiments for this dissertation**

---

[4] By incorporating 'soft' components, the ruggedness of a mixed-component design could be assessed for design reference purposes. If it were in fact true that these components did not withstand the rigours of the experiments, clear design specifications could be drawn up concerning components (or component types) that have to be omitted from ESAD designs.

The CCA that was designed for the experiments of this thesis were contained in an Aluminium enclosure, of which the wall thickness and general layout was a good representation of a typical ESAD mechanical design (see Figure 7). The mechanics were designed in such a manner that four CCAs could be fitted into one enclosure, to gain a larger statistical value for the experiments.

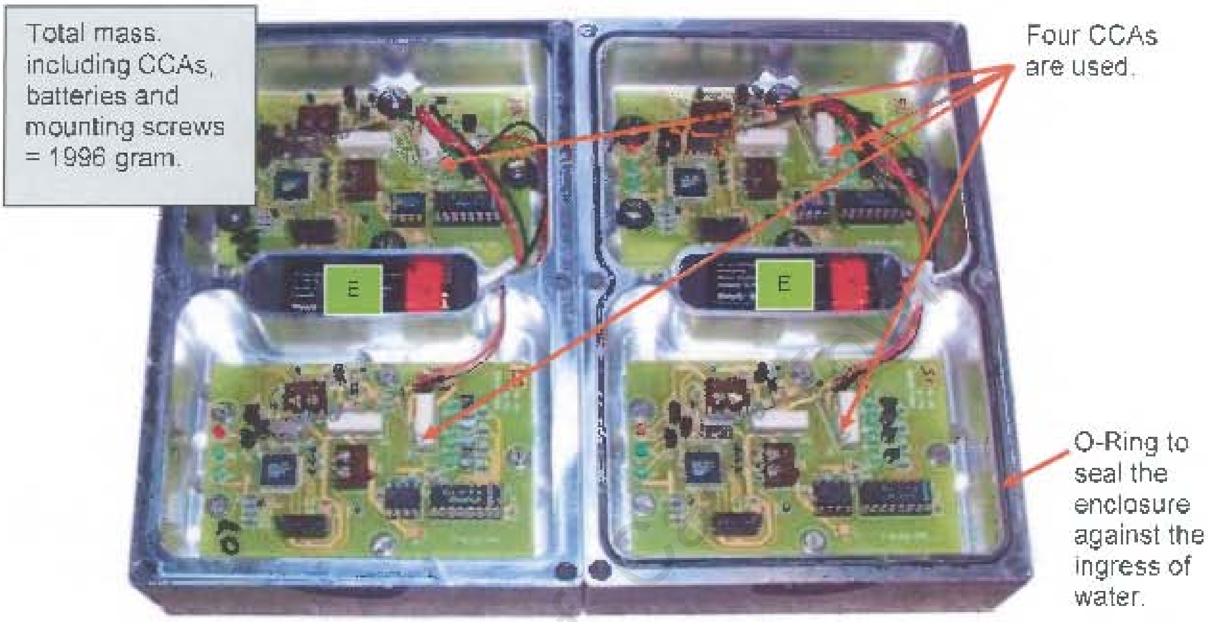

Figure 7: The Electronics Enclosure containing four CCAs

The preliminary literature study gave the background to this study, which seeks to determine the causes of electronics damage or failure in environments where they are exposed to severe shock. No clear conclusion could be drawn up to this point in the investigation as to the root cause of the damage, and therefore no process could be implemented to harden the electronics against the shock effects of blasts.

It is important to distinguish between the different characteristics of an underwater blast and its effects on an object in close proximity to the blast, to make it possible to formulate a postulation that will lead to a solution to the research problem. The research design thus includes an in-depth study of the characteristics of an underwater blast. From the knowledge of these characteristics, a clear understanding of the cause of the electronic damage was to be derived.

The research problem is based on practical experience gained through placing sensor equipment (for measuring and recording data) close to underwater explosions, as well as subsequent experimentation as part of the investigations to solve the problem. The results obtained during these investigations have not led to a solution yet. This present study is therefore designed to include an overview of investigations into this specific problem that were executed in South Africa, and to conclude whether the principles that were followed/suggested by the investigations, constitute possible true and effective solutions, or whether different approaches should be followed.

A literature study involving current literature on the subject was required to determine what has been published on an international level, to direct the postulation for the solution of this research problem. The research problem is a military problem by nature, and therefore it was expected that a strict secrecy classification would be placed on information at the level of international publication. However, a vast amount of research has been done and published in the specialized area of underwater blast, and the relevant publications were to be filtered to select topics that might contribute to the body of knowledge concerning the specific problem of protecting electronic assemblies of a military nature typical of the units used in this study.

Fieldwork was to be conducted to extend hands-on knowledge and experience. It was expected that such fieldwork would also reveal certain practical aspects of the research problem, which would contribute to the solution. The data gathered from the fieldwork were to be analysed, a solution suggested, and simulations planned to constitute design models and design parameters.

1.4.2. Methodology

In broad terms, an underwater blast causes different kinds of pressure in the water. It is known that these pressures can be divided into two sequential operations, i.e. the shock wave (creating shock wave energy E_s) and the bubble formation (creating bubble energy E_b). It is therefore necessary to establish which of these phenomena causes the specific damage as described, and then to establish the characteristics of the phenomena to be able to determine measures for mitigation. Chung and Kinsey [1] have highlighted the probability that the shock wave effect causes the damage and that this is more probable than that damage will be sustained as a result of the bubble effect at distances greater than the near field of the explosion.

There is no freely available data to establish design parameters for these environmental conditions at present, and also no test recommendations or standards to prescribe laboratory qualification tests for this specific application. The intention with this study is therefore to obtain or generate information that will lead to the successful hardening of electronics intended to operate under these extreme conditions.

The foregoing statements are taken as a starting point for this study. The probability of the shock wave effects being the root cause of electronic damage is demonstrated in this study. Therefore the shock wave characteristics of a blast were to be analyzed by studying the literature, and confirmed by experimentation. These characteristics were expected to be related in terms of possible cause of damage to instrumentation. In more detail, what was planned was:

1. To undertake a literature study concerning the characteristics of shock waves created by explosions in sea water with regard to the aspects listed below, and conclude the findings of the literature study in terms of a transfer function, and/or other physical characteristics:
   a. The velocity function of the shock waves,
   b. The mathematical function: pressure amplitude vs. distance from the charge,
   c. The shock wave pressure decay function,
   d. The rise time of the pressure wave,
   e. The impulse energy.

2. To determine the following characteristics of the shock waves created by explosions, as measured by Ström and Janzon [10] in Sweden:
   a. The mathematical velocity function at which the shock waves of explosions are propagated through seawater.
   b. The predicted mathematical function of the shock wave in seawater, pressure amplitude vs. distance from the charge.
   c. The shock wave pressure decay function,
   d. The rise time of the pressure shock wave.
   e. The impulse energy.

3. Then, by mathematical modelling, to predict by interpolation or extrapolation what the pressure amplitude will be at variable distances (relatively close to the charge) when a variable mass of explosive charge is detonated.

4. To determine from the above, the requirements of a measurement setup to measure the same characteristics as calculated in 1.a, 1.b, and 1.c.

5. To acquire the test equipment.

6. To measure explosions in the sea, and correlate the findings with the theoretical model of the measurements as supplied by Ström and Janzon [10].

7. To repeat the measurements until a clear conclusion can be drawn on the characteristic behaviour of a certain compound of explosive, when detonated at a certain depth.

8. To incorporate a standard electronic unit in the above experiments, and determine damage for various standoff distances.

9. To define, from the results of this study, physical design and test rules for electronic equipment that would service under these conditions, to test this solution by experimentation, and conclude the findings.

Chapter 2

2.1. Literature Review

Two sections of the literature review are presented:

a.) The section in Chapter 2 which had a direct impact specifically on the characteristics of a shock wave, and which were extracted according to specific characteristic, and

b.) The section in Appendix 5 which was applicable by author. A detailed analysis of the data sets given by Ström and Janzon [10] is also contained in this section, because it had not yet been published.

The intention behind this study was to find a solution to the problem of damage to electronics due to underwater blast effects. To be able to contribute significantly to a solution, the root cause of the problem has to be well defined. The root cause of the damage, by definition, of course is the underwater blast itself. If the characteristics of the blast could be understood, a target postulation of the root cause of the damage may readily be concluded, from which a solution could be found.

This chapter presents the review and analysis of the literature and data that was found to be relevant to the definition of the root cause of the problem, and in some cases relevant to the imminent solution.

It was essential to study the physical and the mathematical descriptions of the blast, and to list the characteristics that play a role in causing the damage to enclosed electronics. These characteristics were extracted from the sources, and are discussed/listed in this chapter. The main parameters that contributed to damage were filtered into a group of parameters that seemed to reveal the probable cause of damage.

This group of parameters was reduced to:

1. *Shock Wave propagation velocity at the position of the target;*
2. *Peak pressure of the Shock Wave versus the stand-off distance; and*
3. *Shock Impulse Density versus stand-off distance.*

2.2. Shock Wave Characteristics from the Literature

The author of this dissertation was privileged to have obtained raw data from underwater blast measurements in Sweden. These measurements were taken in fjords with a depth of 40 m, at a measurement depth of 20 m, and at stand-off distances ranging from 3.5 m to 20 m.

The measurements taken by Ström and Janzon [10] were analysed and this is presented in Appendix 5 on Page 195. These measurements were taken in the far field of the underwater explosions.

2.2.1. Characteristic 1: Shock Wave Propagation Velocity:

A consolidation of the calculations of the propagation velocity is shown in Figure 8. A curve representing all the velocity data was fitted over the velocity measurement results. The "best fit" for a linear graph that represents the data set, is y = 1469.6x – 0.0367. This result means that the average propagation velocity is 1469.6 m/s (the offset of -0.0233 should be ignored), and the fact that this fit is linear to a probability of 99.95% (R^2 = 0.9995) means that the velocity is constant over the data range of the data set. The stand-off distance ranged between 3.5 m and 20 m, and the charge size ranged between 9.41 kg and 27.33 kg. The largest charge radius (27.33 kg for Plastic X Blast 3) is calculated to be 160 mm if a relative density of 1.6 is assumed. The charges closest to the blasts were at stand-off distances near to 3.5 m. This is more than 20x the Charge radii. As discussed in the paragraph labelled Conclusions drawn from the Literature Review on page 40, the charge diameter (or radius) in relation to the stand-off distance is generally used to determine whether the stand-off distance is in the near field or the far field of the explosion.

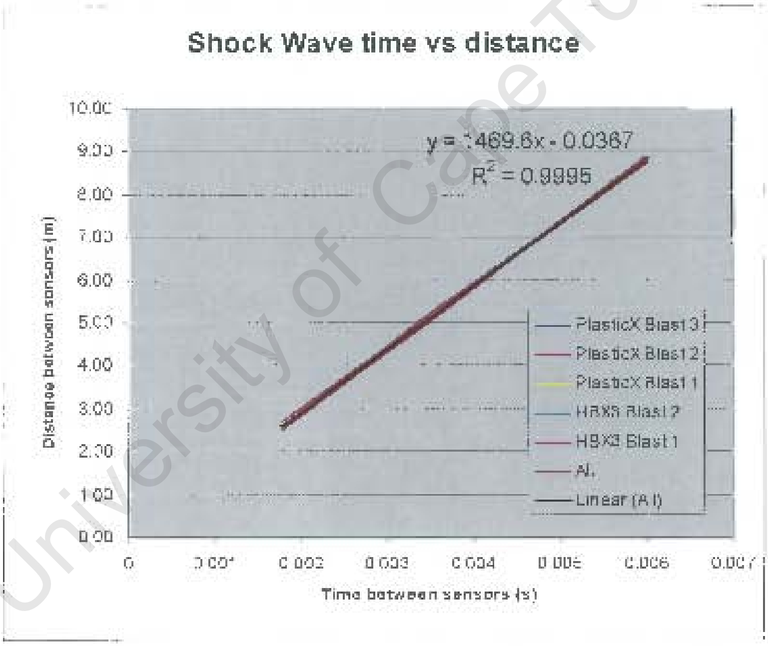

Figure 8: **Graph of the shock wave distance propagated, vs. time.**

If the individual velocities are taken (from Table 44 to Table 48) as data input, the average propagation velocity is calculated to be 1460 m/s. This is a good correlation with the graph-average of 1469.6 m/s shown in Figure 8. This Shock Wave Propagation Velocity for this set of data is constant, and is in the range of the speed of sound in water.

2.2.2. Characteristic 2: Peak-Pressure Function

Ström and Janzon [10] defined the peak pressure to reduce at a rate of:

$$P_{max} = 51.175\left(R \middle/ Q^{\frac{1}{3}} \right)^{-1.1255} \quad \text{MPa} \quad \text{-------------} \quad 1$$

Where
R is the standoff distance in m.
Q is the charge weight in kg.

Traditionally, the equation for P_{max} is written such that the charge weight (mass) is divided by the distance. Rewriting the Ström and Janzon [10] Equation in the traditional format, we get:

$$P_{max} = 51{,}175\left(W^{\frac{1}{3}} \middle/ R \right)^{1{,}1255} \quad \text{MPa} \quad \text{-------------} \quad 2$$

2.2.2.1. The shock pressure function

Far Field Pressure:

Giving due consideration to the above discussion and combining the equations for the shock-history-functions as given in the literature, the complete definition of the shock pressure wave, is:

The peak pressure at a distance R from the blast (given by Cole [5: p241] and Cooper [6: p413] for Pentolite):

$$P_{max} = 2.25\times10^{4}\left(\frac{W^{\frac{1}{3}}}{R}\right)^{1.13} \quad lb/in^2$$

Where:
P_{max} is in lb/in^2
W is in lb
R is the standoff distance from the blast in ft.

Or in the metric system:

$$P_{max} = 54.57\left(\frac{W^{\frac{1}{3}}}{R}\right)^{1.13} \quad MPa$$

Where:
P_{max} is in **MPa**
W is in kg
R is the standoff distance from the blast in m.

This equation is true in the far field of the explosion. The Shock wave front end or slope function has not yet been determined.

The shock wave decay function (as defined by Cole [5]):

$$P(t) = P_0 e^{-t/\theta} MPa$$

Where:

$$\theta = 92.5W^{1/3}\left(\frac{W^{1/3}}{R}\right)^{-0.22} \quad \mu s$$

$P(t)$ is in MPa
For t = 0 to typically Θ, when the most important energy containing portion of the shock front is considered.
Where:
P_0 = Peak pressure at time t=R/c in MPa
R = stand-off distance from the blast in m
c = speed of sound in water in m/s
t = time in μs
Θ = decay constant in μs
W is in kg

Equation 3: Composite Equation for the shock pressure history in the far field

Near Field Pressure:

The shock pressure function as given in Equation 3 above was quoted from Cole [5]. This empirical approach by Cole [5], however, does not present any accuracy in the near field. Kira *et al* [10] gave a different approach, using more modern methods as well as numerical methods to obtain the pressure function, especially in the near field. In fact, their measurements were taken from the edge of the explosive charge (standoff distance R = 0). Although they did not measure the actual pressure at R = 0, they calculated the pressure as follows:

Kira *et al* [10] first measured the shock wave by streak photography, and then plotted the Distance vs. Time graph as it was captured by this photography method (see Figure 9A). By using nonlinear curve fitting methods, they extracted an equation for R:

$$R = A_1\left(1-e^{-B_1 t}\right)+A_2\left(1-e^{-B_2 t}\right)+A_3\left(1-e^{-B_3 t}\right)+C_0 t \qquad \text{-------------} \quad 4$$

Where R = Standoff Distance
C_0 = Sound Velocity in the medium
A_n and B_n = coefficients obtained by using nonlinear curve fitting methods.

Differentiating Equation 4 with t, the propagation velocity of the underwater shock wave was obtained:

$$U_s = dR/dt \qquad \text{-----------------------------------} \quad 5$$

$$\therefore U_s = A_1 B_1 e^{-B_1 t} + A_2 B_2 e^{-B_2 t} + A_3 B_3 e^{-B_3 t} - C_0 \qquad \text{----------} \quad 6$$

Kira *et al* [22] as well as Cooper [6: p186] described the relationship between propagation velocity and particle velocity as follows:

$$U_s = C_0 + s u_p \qquad \text{-----------------------------------} \quad 7$$

Where U_s = Shock velocity
C_0 = Sound Velocity in the medium
u_p = Particle velocity
s = constant

According to Kira *et al* [10], the constant s = 1.79, while Klaseboer *et al* [11] named this constant the "shock density ratio parameter" and quoted it to be 1.815. Cooper [6: p187] explained that the relationship between the shock velocity and the particle velocity was linear, and that s = slope of the relationship for that material. So it would be expected that s would differ between materials, but that one should recognise that s in water should not differ.

U_s was known from Equation 5, and substituted into Equation 7 to obtain u_p.

Comparing Equations 6 and 7, the following equation could be derived:

$$\therefore su_p = A_1B_1e^{-B_1t} + A_2B_2e^{-B_2t} + A_3B_2e^{-B_3t} \qquad \text{-----------} \qquad 8$$

$$\therefore u_p = A_1B_1 / e^{-B_1t} / s + A_2B_2e^{-B_2t} / s + A_1B_3e^{-B_3t} / s \qquad \text{-----} \qquad 9$$

Cole [5: p35] and Cooper [22: p182] reported that:

$$P - P_0 = \rho_0 U_s u_p \qquad \text{-----------------------------------} \qquad 10$$

Where P = Shock pressure
P_o = Atmospheric pressure
ρ_0 = Density of sea water
U_s = Shock velocity
u_0 = Particle velocity

With U_s and u_0 derived from Equations 7 and 9 and substituted into Equation 10, the shock pressure P could be calculated as shown in Equation 11.

$$P - P_0 = \rho_0\left(A_1B_1e^{-B_1t} + A_2B_2e^{-B_2t} + A_3B_2e^{-B_3t} + C_0\right)\left(\left(A_1B_1e^{-B_1t}\right)/s + \left(A_2B_2e^{-B_2t}\right)/s + \left(A_2B_3e^{-B_3t}\right)/s\right)$$

$$\text{-----------} \qquad 11$$

Conclusion: If the shock velocity is known, then the shock pressure could be calculated.

Kira *et al* [10] calculated the pressure (presumably) in this way, and the result is shown in Figure 9B. Note that the curves for all three explosive masses were very nearly the same when the experimental results were compared to the calculated results. Note also that the value of the pressure at the border condition of the explosive mass after full detonation had been reached, (R+r)/r = 1), was approximately 100 000 atmospheres for all three explosive masses. This was also confirmed by Cooper [6], who stated that the peak pressure generated by an explosion was dependent only upon the explosive mass material, not the size of the explosive mass (as may intuitively be expected).

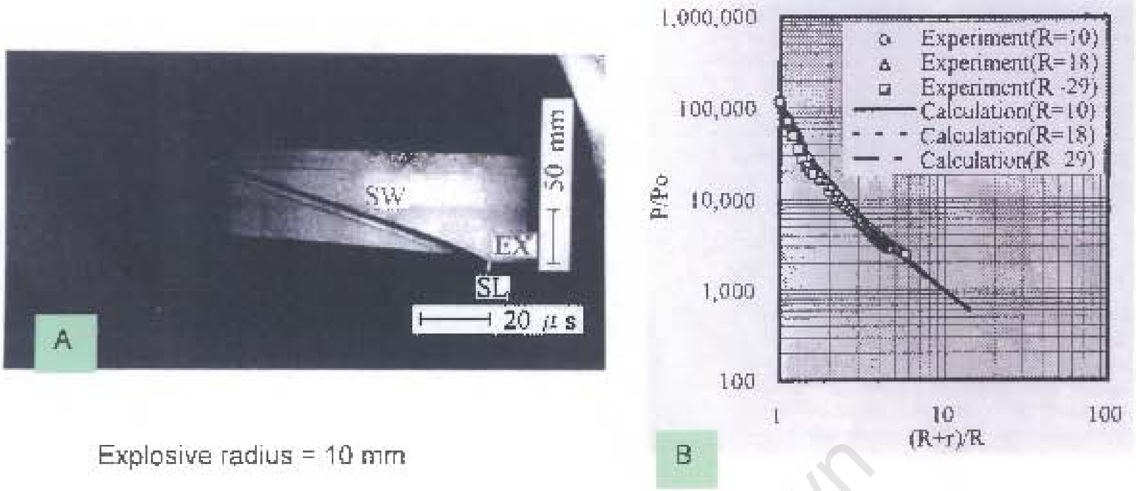

Explosive radius = 10 mm

Figure 9: **The calculated pressure result, photographs and results courtesy from the paper of Kira *et al* [10]**

From the data obtained, Kira *et al* [10] an empirical equation had been obtained for the peak pressure of SEP explosives (Asahi Chemical Industry) with a VOD of 6970 m/s as a function of explosive radius at standoff distances in the near field. See Equation 12:

$$\frac{P}{P_0} = \alpha\{(R+r)/R\}^{-\beta} \quad \text{------------------------------} \quad 12$$

Where P = Shock pressure
P_o = Atmospheric pressure
r = Explosive radius
R = Standoff Distance
α = $1.1\text{x}10^5$
β = 1.8

Note: α and β are coefficients that depend upon the explosive formulation.

The peak pressure, according to Equation 12, will therefore always be the same for the same explosive formulation, regardless of the mass of the explosive. Equation 12 is shown graphically in Figure 10, for three sizes of explosive mass. The figure is only shown in the near field, because not enough information is at hand to compare Equation 12 (for SEP) with Equation 2 by Ström and Janzon [10] which was for an RDX formulation with a VOD of approximately 8700 m/s, and valid for the far field. The coefficients α and β in Equation 12 would be different for a different explosive formulation.

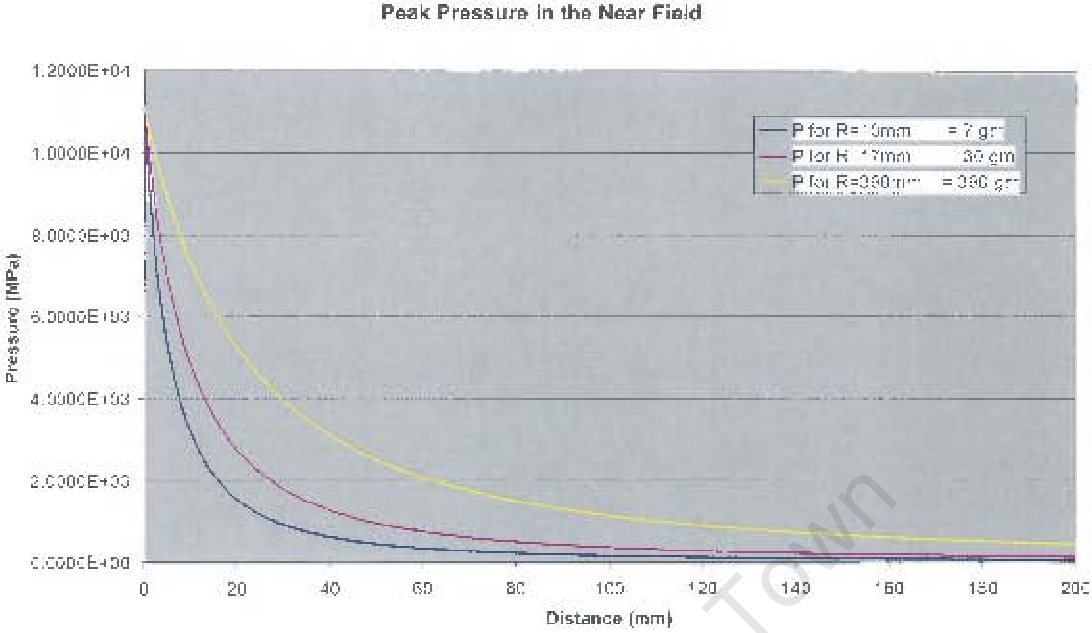

Figure 10: **Comparative Peak Pressure graphs for 3 sizes of SEP explosives**

Possible Error Conditions:

In the paper of Kira *et al* [10], the shock velocity was measured and calculated by first measuring the physical distance on a streak photograph (see Figure 9A), and then by plotting the data. In this figure, Kira *et al* [10] used the inverse notation for standoff distance and charge radius: R= Charge Radius, and r= standoff distance (in this dissertation the notation for standoff distance, the letter R was used, and for the Charge Radius the letter r was used). The vertical line in Figure 9A corresponded to the real distance of 50 mm. The horizontal line corresponded to the real time of 20 μs. The horizontal straight line EX indicated the explosive charge. The white line SL corresponded to the light due to the detonation. The edge of the curve SW indicated the propagation of the underwater shock wave. A result of approximately 10 GPa (100 000 atmospheres) was obtained (see Figure 9B). An error in the measurement at the blast origin may have been possible, due to the fact that the P_c for the explosive is given by Cooper [6] at approximately 24 GPa or more. That would give a much higher initial pressure, and consequently a higher initial shock velocity than the published results.

A possible method of error insertion was discovered by the author of this dissertation by synthesizing the data from the results published by Takahashi *et al* [22], who also used this streak photography method to obtain shock velocity (see Figure 11A). It was found that, if a small error in physical digitisation of the optical data was made, then a large error for the shock velocity could be made. The data from the printed paper by Takahashi *et al* [22] was extracted as accurately as possible, and the end result corresponded quit well by visual inspection, see Figure 11B. The curve-fitted data was integrated, and a graph for the velocity was obtained (see Figure 11B).

However, when a slight change was made to the information around the shock origin, changing the slope to a larger initial value, a large change in shock velocity was obtained. A visual inspection and comparison between the black graphs in Figure 11B and Figure 11C revealed no (or extremely small) visible change, and the graphs compared very well with the original streak photograph, yet the velocity comparison between the two sets of data differed quite drastically at the origin of the shock wave, as shown in Figure 11C.

Conclusion:

The conclusion may be drawn that the streak photography method may not be the best method to obtain velocity measurements at the origin of the blast, but is a good method to obtain the shock characteristics from a position very close (to within 1 radius) of the blast.

If the pressure is required for a certain explosive formulation, the shock speed for that formulation and explosive weight must be measured. The pressure may then be calculated from Equation 11, after first determining by non-linear curve fitting methods, the constants A_1 to A_3, and B_1 to B_3

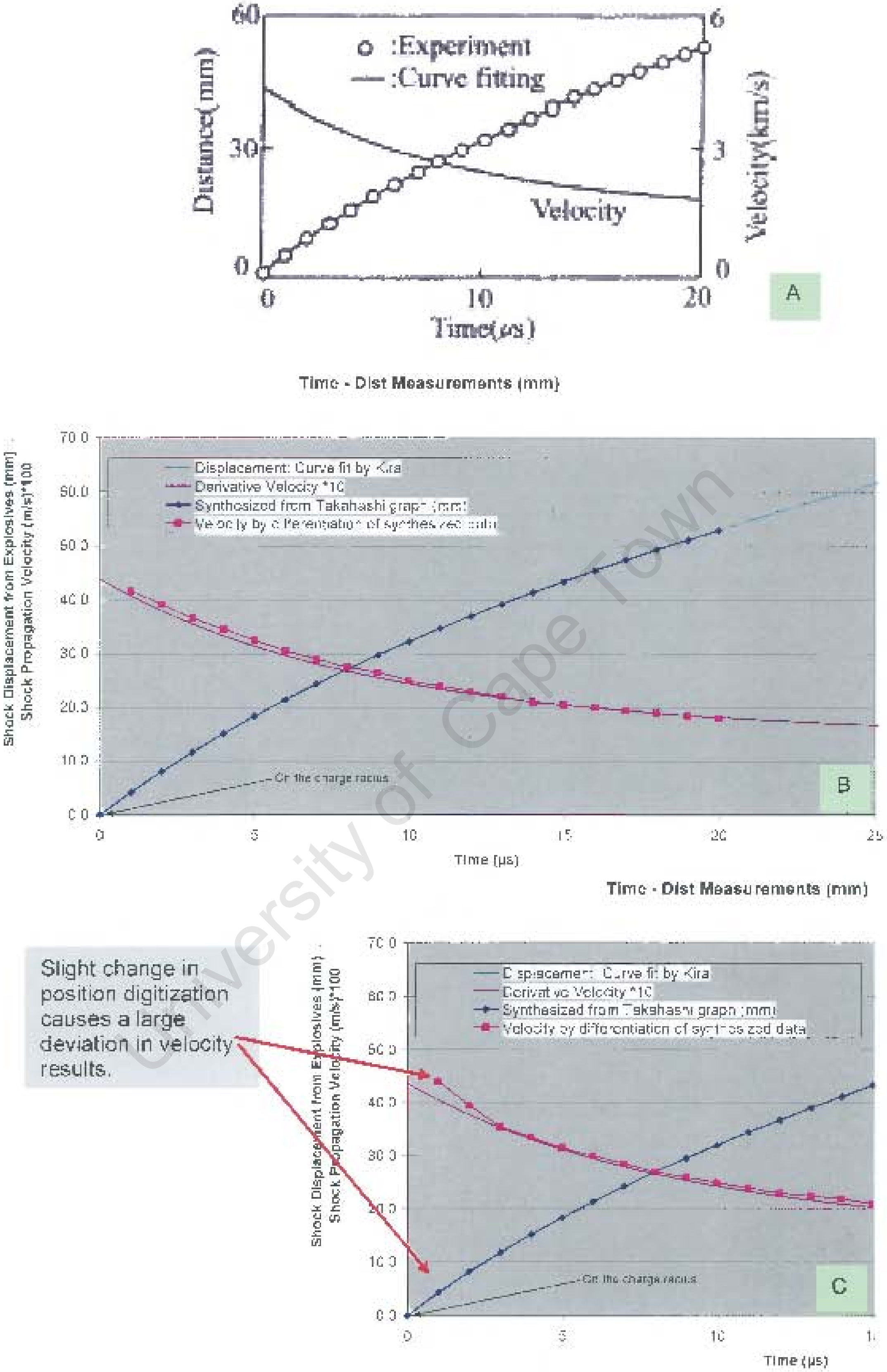

Slight change in position digitization causes a large deviation in velocity results.

Figure 11: Synthesized data from the printed data as supplied in the paper by Takahashi *et al* [22], and illustrating error conditions.

2.2.3. Characteristic 3: Shock Impulse Density

The shock impulse density is in fact the shock wave pressure which is time-integrated over a certain period. In broad terms, this means that the longer the high pressure persists, the higher the shock impulse density.

A mathematical representation of this characteristic was given by Cole [5] (see page 213). However, this study was interested in enclosures in the near field of an underwater explosion. This meant that Cole's [4] approximations were not valid for this study. Cooper [6] reported the phenomenon of pressure much closer to the edge of the explosive mass. The pressure-characteristics within an explosive mass during the explosion are known. From this data, one could extrapolate the effect that the water exerted on the pressure after the explosive mass was converted to a gas bubble.

The pressure at the boundary condition at the time when the explosive mass has completed the conversion to a gas bubble, and before the gas bubble starts with the expansion process, is given by Cooper [6] as Pcj (first defined by Chapman-Jouguet, see Figure 12). The Von Neumann Spike disappears quickly (in the transfer of pressure to the sea water) in relation to the rest of the rarefaction wave, and therefore its effect is negated for this study. This pressure differs with regard to the type of explosive material, but not with explosive mass. An increase of the explosive mass would increase the time that the high pressure is maintained, increasing the shock impulse density.

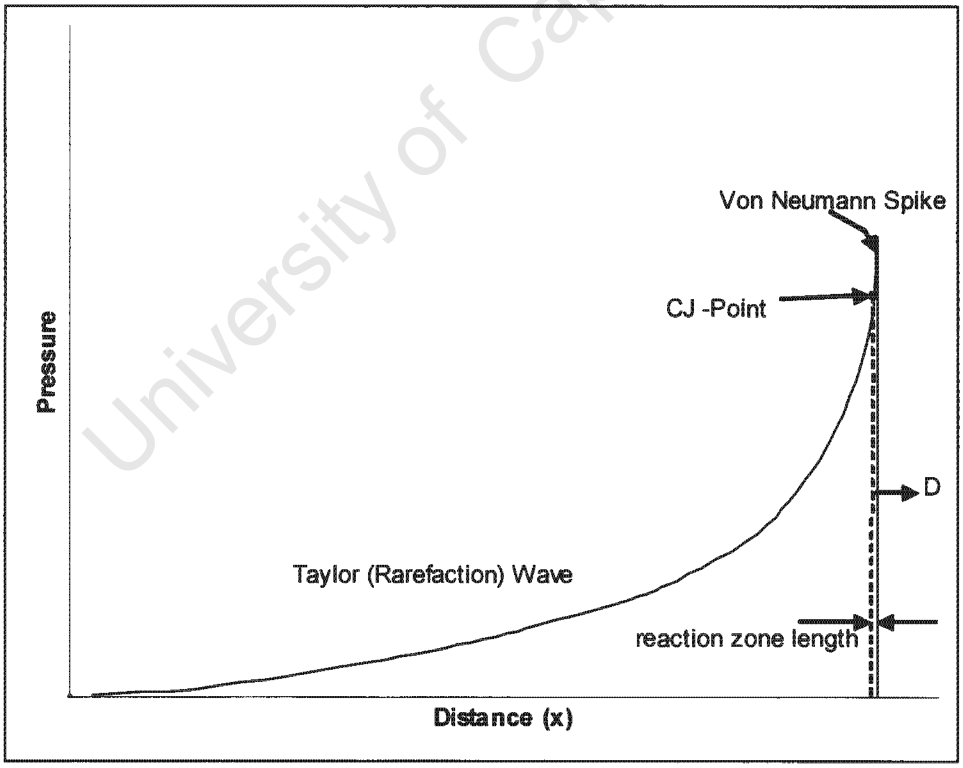

Figure 12: The pressure within an explosive mass during the explosion process. (Picture by courtesy of Cooper [6: p256]) and redrawn by F. Mostert.

Kira *et al* [10] contributed significantly to the understanding and calculation of the shock impulse density, due to the fact that mechanisms were put in place with which the impulse density could be calculated.

From Equation 3, the following pressure-time history function is repeated:

$$P(t) = P_0 e^{-t/\theta} \quad \text{------------------------------} \quad \mathbf{13}$$

When the pressure is normalised, Equation 13 can be rewritten as:

$$P(t)_1 = e^{-t/\theta} \quad \text{------------------------------} \quad \mathbf{14}$$

θ is a time constant which indicates the inclination of the pressure-time history after arrival at a certain standoff position. To be able to show Equation 14 graphically, θ would have to be known. Kira *et al* [10] gives the following linear equation for θ:

$$\theta = kR + h \quad \text{------------------------------} \quad \mathbf{15}$$

Where k and h are coefficients and R is the standoff distance. Both the coefficients are dependent upon the explosive charge radius, r, by:

$$k = 0.0041r + 0.058 \quad \text{----------------------} \quad \mathbf{16}$$

$$h = 0.093r + 2.9 \quad \text{----------------------} \quad \mathbf{17}$$

The coefficients that are multiplied by the charge radius r are for the charge radius being expressed in mm.

Therefore, the time constant is dependent upon charge radius, as well as the standoff distance. This relationship is depicted in Figure 13. The relationships are linear relative to the charge radii.

Figure 13: **The relationship between THETA and the standoff distance, for several charge radii.**

The mass of the explosive charge is dependent upon the density of the explosive material, and the charge radius in a non-linear equation. due to the volume being non-linear to the charge radius.

The time constant θ can now be calculated using Equation 15, and the result inserted into Equation 14. The result is shown in Figure 14.

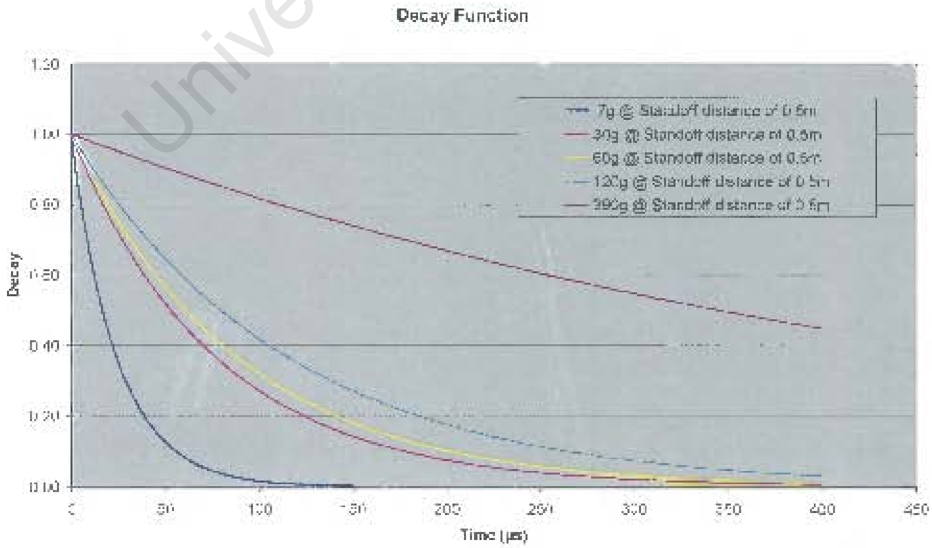

Figure 14: **The normalised pressure decay function (Equation 14) for several charge masses, at one standoff distance of 0.5 m.**

The impulse density function is the integral with time of the curves shown in Figure 14, multiplied by the peak pressure at that specific standoff position. It is obvious that the impulse density is more for larger explosive masses.

Note also that, for one specific charge mass, the time constant becomes longer the further the standoff distance. This observation is shown in Figure 15, and agrees with Equation 3.

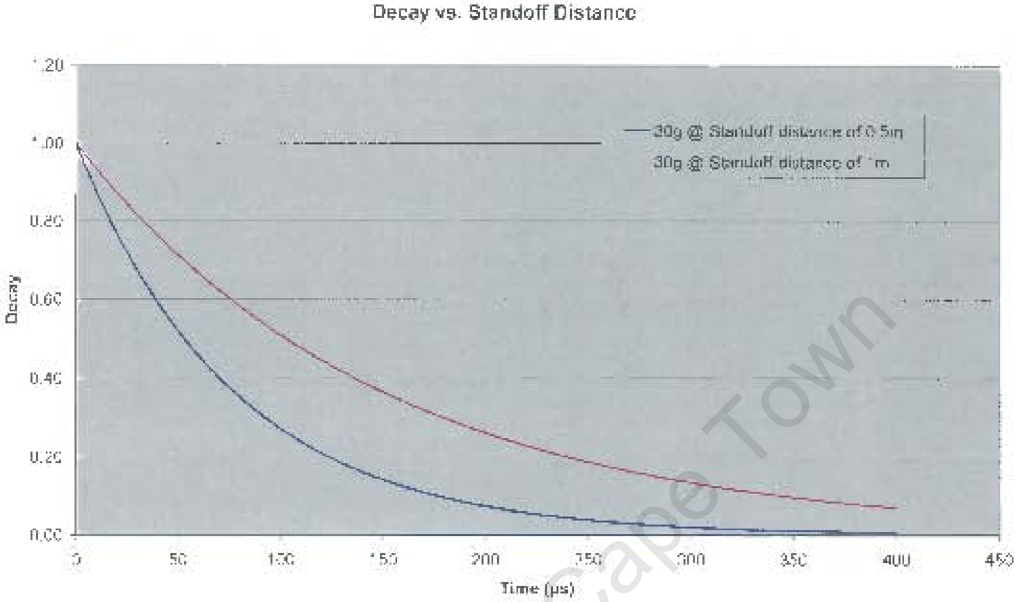

Figure 15: The decay time constant relative to the standoff distance, using standoff distances of 0.5 m and 1 m.

Using the preceding data, the Shock Impulse Density could be calculated.

Cole [5: p241] gives an empirically formulated impulse for Pentolite as follows:

$$I\left(t / W^{1/3}\right) = lW^{1/3}\left(\frac{W^{1/3}}{R}\right)^{\beta} \quad \text{----------------} \quad \mathbf{18}$$

Where W = Explosive weight in lb.
R = Standoff Distance in ft.
l = Constant = 2.18 for Pentolite
β = 1.05 for Pentolite

There seems to be some disagreement in the literature on the value of β: (Held [9] assumes that β=0.89 whilst Cole [5] reports it to be 1.05 for Pentolite). These differences could be attributed to the fact that each researcher studies a different explosive formulation, and then uses β freely according to the researched formulation.

2.3.2. Conclusions: Near Field vs. Far Field characteristic

In many studies reference is made of the near field and the far field of the shock wave, because some results are different depending whether the standoff position is in the near or far fields.

In this study, reference to the extent of the damage to contained electronics can be referenced to whether the contained electronics is positioned within the range which is defined as the near field, or the far field.

The near field and far field definition has been discussed by many authors, but comparing the results and opinions has made the author of this dissertation aware of the distinct probability that the difference between the near and far fields is generally defined to suit the specific needs (effects and after-effects) of the specific application of the specific researcher, and an absolute scientific definition is (in the author's opinion) still lacking.

Examples are listed below:

1. Hammond [7: p12] discussed the near and far fields, and mentioned the propagation velocity differences: *"The velocity of the shock wave in the near field to the underwater explosion is typically several percent greater than the acoustic wave velocity in the far field region."* This was however not offered as a definition, but rather stated as a fact. In the same chapter, Hammond also noted: *"Near-field interactions involve relatively smaller standoff distances to an extent that the expanding gas-bubble is close enough to the target structure so as to interact with it."*
2. Cole [5: p5] discussed the properties of the shock wave as follows: *"The velocity of propagation near the charge is several times the limiting value of about 5000 ft/s, this value being approached quite rapidly as the wave advances outward and the pressure falls to 'acoustic' values."*

It seems as if these different definitions do not tie up to a firm definition to suit applications universally. The author of this dissertation leans towards offering a definition of the near and far fields of a shock wave that is scientifically uncompromised in nature as follows:

Definition Offered:

> *In the far field, the shock wave has reached a constant velocity, equal to the speed of sound in that medium. Before this constant velocity characteristic is reached, the shock wave velocity is higher than the speed of sound, with a maximum value at the border condition (0 charge radii), and tapers down non-linearly towards the speed of sound as the standoff distance increases. This is the near field. This near field is usually defined by a number of charge radii.*

2.3. Conclusions drawn from the Literature Review

2.3.1. General Conclusions

1. Two distinct phases of pressure history are associated with an underwater blast, the shock wave pressure history, and the bubble pressure history. The shock wave and bubble are closely associated in time at the origin of the explosion, after which the shock wave pressure is propagated at a greater rate than the bubble pressure.
2. There is evidence to suggest that the blast shock wave would induce more damage than the blast bubble.
3. All reviewed writers on the subject as cited in this study agree that the shock wave characteristics can be accepted from the empirical findings recorded in the literature where the scaled distance (principle of similitude) $W^{1/3}/R$ of the charge weight (W) and the stand-off distance (R) are used to describe the nature of the shock wave. This scaled distance parameter forms the basis of the scalability conquest as always prevalent in the calculation of underwater blast effects. This study will make extensive use of this parameter.
4. It is clear that all reviewed writers agree that the characteristics of the shock wave differ in two distinctive phases, i.e. the near field, and the far field. However, these phases are not well defined and therefore the area of cross-over between the near field and the far field is undefined at this stage and ranges from 10 charge radii to 25 charge radii. In the near field, the propagation velocity of the shock wave is higher than the speed of sound, and the peak pressure parameter decays at a faster rate than the normal sound pressure parameter 1/R. In the far field, the shock pressure assumes the same characteristics as sound pressure.
5. There seems to be some disagreement between Cole [5] and Swisdak [21] as to the number of decay time-constants used to calculate the impulse of a shock wave. Cole [5] uses 6.7θ, while Swisdak [21] uses 5θ.
6. The mounting methods of the electronic components on a PCB are important, because not all of the shock acceleration is absorbed by the PCB soft-mounts. Designers also have to cater for smaller-amplitude vibration testing, as well as for shocks produced when the equipment is dropped.
7. The velocity of both the bubble and the shock wave has been measured by Chung and Kinsey [1] at distances where $R=a_0$. It was concluded that the velocity in the explosive boundary conditions, is approximately 4 times the normal speed of sound in water.
8. According to the form characteristic of the velocity curves, the "near field" could quite comfortably be defined as the region where the velocity is greater than the speed of sound. Chung and Kinsey measured this distance to be 2.3 charge radii.
9. There seems to be some disagreement with respect to the rise time of the leading edge of a shock pressure pulse. The author assumes at this stage (to be verified) that the slope of the leading edge is important to determine the impact history on a freestanding object (electronic enclosure) in the water in close proximity to the blast. This leading edge and the velocity of impact have the greatest influence on the acceleration of the enclosure. It is therefore very important to analyse the slope of the leading edge in more detail. See paragraph on Conclusions: Near Field vs. Far Field characteristic on page 41.

2.3.3. Conclusions: Pressure Pulse Leading Edge Analysis

Refer to Figure 176 presented here for ease of discussion as Figure 16 below.

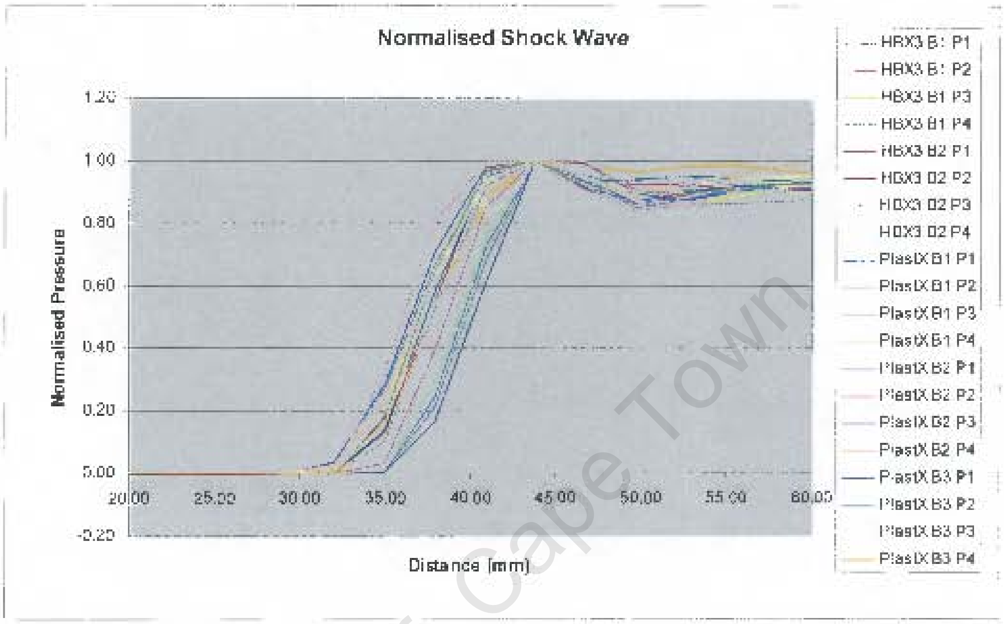

Figure 16: Incremental distance vs. normalised (relative to their individual maximum values = 1) shock at all four sensor positions

It is clear that in the far field of the shock pressure pulse, the rise-time of the leading edge is measured to be approximately 6 - 8 µs in all cases in this data set.

In the quest to determine the rise function of the leading edge of the shock wave, these measurements are of some importance. Taking the limitations of the test equipment (and in this case more importantly the sensors) into consideration, it cannot be stated that the shock wave leading edge is in fact 6 - 8 µs, although it has been measured as such. In consulting with the authors of these measurements (Paul Ström and Bo Janzon of FOI in Sweden), their comment was that the width of the sensors (approximately 10 mm) and the constant propagation velocity in the far field (1469.6 m/s as shown in Figure 8) causes the pressure to rise at the sensor elements (contained within the sensor housing) to maximum value in:

$$10mm / 1469.6m/s = 6.8\mu s \quad \text{---------------} \quad 19$$

This value of 6.8 µs rise time (see Equation 19) means that the measured value of 6 - 8 µs is too inaccurate to determine the actual rise time. Measuring of the actual rise time may have to be done by other means, not the Tourmaline gauges used by Ström and Janzon [10], which were also chosen for the measurements for this dissertation.

Chapter 3

3.1. DAMAGE TO ELECTRONICS: HYPOTHESIS

3.1.1. General

The purpose of this study, briefly, is to find a solution to the problem that electronics contained in aluminium enclosures are damaged as a result of underwater blast when these containers are placed in close proximity to the blast.

The first course of action, and method that was followed in this study, was to postulate the causes of damage, after due consideration of the facts that were gathered up to this stage of the study. A possible solution was deducted, and a model tested in field experiments. Refinement of the model was necessary, and the refinement was also tested in further field experiments, with positive results. This chapter is concentrated on the facts leading to a postulation, as well as the postulation.

Note: It would be desirable to build a mathematical model that would determine the stand-off distance from a specific charge at which enclosed electronic equipment might be placed, before imminent damage might occur.

The underlying method of research is to characterise an explosive charge, and to measure the effect of blast loading on nearby electronics. Additionally, in this process, also to determine the primary cause of electronic damage, then to prescribe corrective actions.

It 's clear that the underwater blast causes rapid movement of the equipment (enclosed electronics). The rapid movement of the enclosure is transmitted to the contained electronics, causing the electronic components to gain relatively unequal momentum. These components then tear loose from their mounted positions. For example, a switch (such as may sometimes be used on a PCB) is constructed by the assembly of various smaller parts. In this case, each part of the switch is accelerated to gain the total switch momentum, but each part differs in construction and mass and therefore attempts to accelerate at a different rate. This causes the switch construction to collapse, and the switch breaks apart.

Consider the movement of a shock wave generated by an explosion, as depicted from actual measurements supplied by Ström and Janzon [10], in Figure 17:

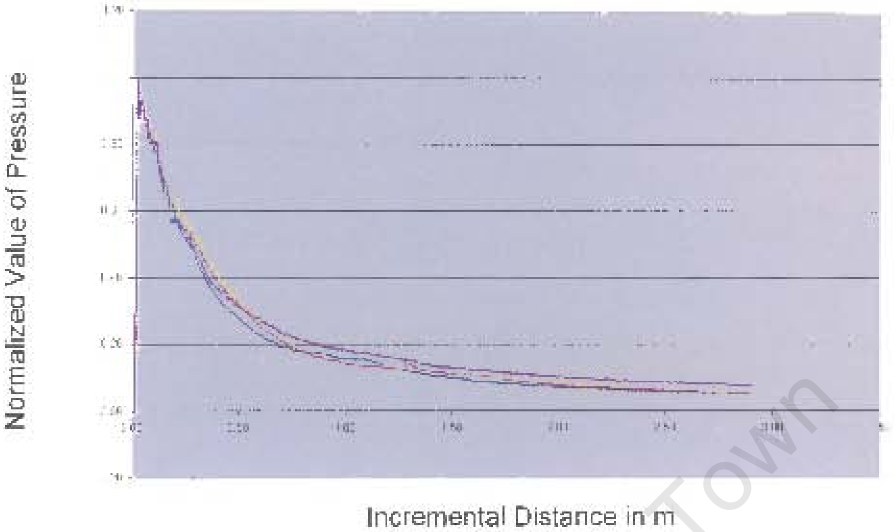

Figure 17: **Normalised shock wave of five blasts, using different charge sizes, at sensor 1 position**

The analysis of the raw data provided by Ström & Janzon [20] showed that the shock front moves through the water at the speed of sound in water, i.e. 1469.6 m/s (see Figure 8). The speed of sound is generally rounded to 1500 m/s for ease of comprehension of the problem, and for quick calculation.

For ease of reading, the graph in Figure 167 is presented in this section as Figure 18 to show the selected data series. To be able to visualise the physical size of the electronics container of this study, it was necessary to transpose the time axis of Figure 167 to a distance axis (see Figure 18) with the use of the far-field characteristic (constant propagation velocity (see Figure 8)). In Figure 19, the Plastic X Blast 1 Sensor 1 graph is expanded horizontally, keeping the horizontal axis in the distance unit. Note: In the near field, the velocity is not constant. The shock pressure propagation velocity starts at a high value and then drops to the velocity of sound within a few charge diameters, depending on the pressure resulting from the composition of the explosive material and the sustained period during which the pressure is above the elastic pressure threshold (Cooper [6]) caused by the mass of the explosive material. The effect of the shock wave in the near field is discussed later in this study.

To be able to formulate a hypothesis on the cause of damage to the electronics, the shock wave in the far field is considered.

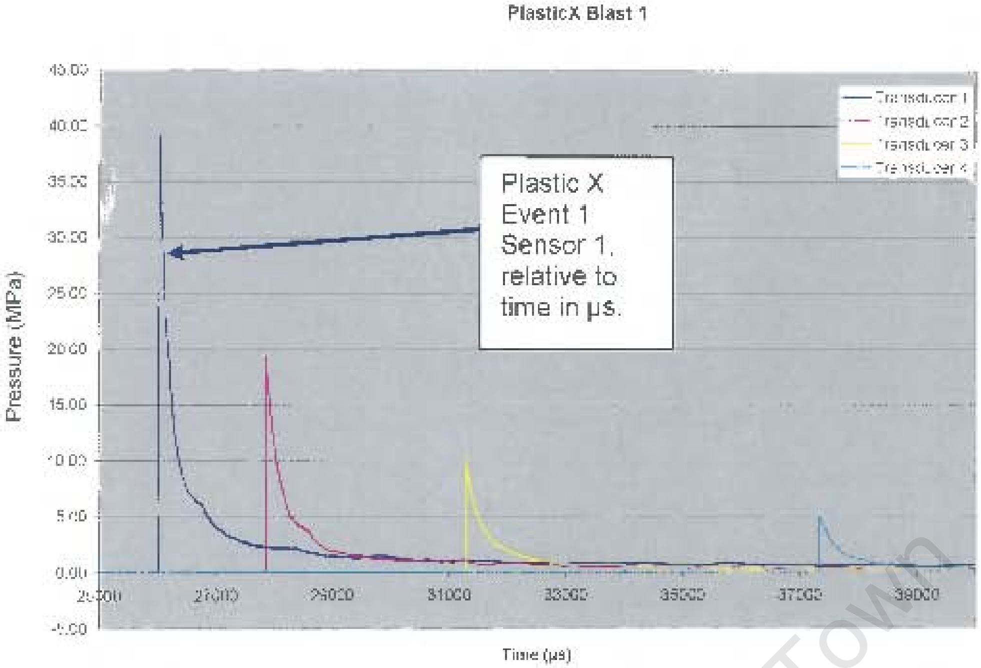

Figure 18: **Pressure results from Plastic X Blast 1, Ström & Janzon [20]**

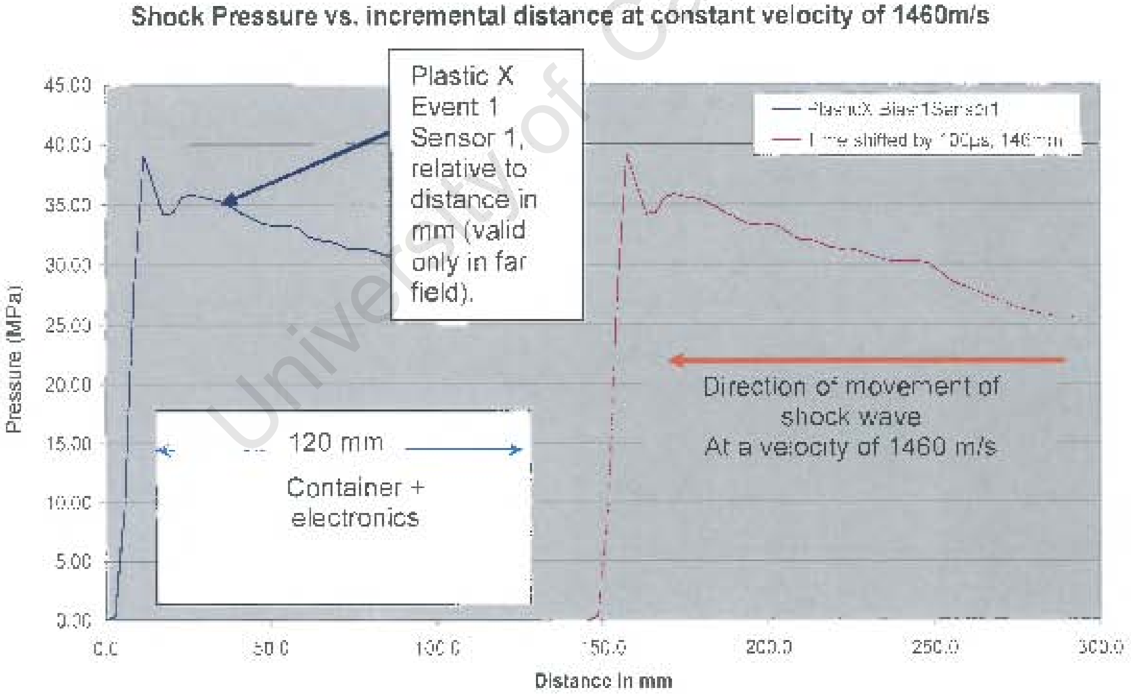

Figure 19: **The movement of a shock front approaching and passing an object**

The author considered the fact that a shock wave is a high-pressure front moving through the water at the speed of sound (in the far field). This causes impact on any stationary equipment in the water. If the impact of the extremely high pressure front on the electronics container is considered, Newton's second law should be considered:

$$F = m * a \quad \text{------------------------------} \quad 20$$

or

$$ma = \sum F \quad \text{------------------------------} \quad 21$$

It is implied that a force F is exerted on an object (container with electronics) with mass m by the moving shock front, and this causes the object to accelerate. In this equation, two variable characteristics are to be observed: the force, and the acceleration. If any one of these characteristics is minimised, the damage to the contained electronics will be minimised.

If the force on an object is to be minimised, the object could be made physically more streamlined, which implies that the object must be modified. This is not an option, because the object is a given enclosure, containing specific electronics, and the manufacturer will only consider modifications to the internal structure. Therefore, the only remaining characteristic to be minimised is the acceleration of the object.

The shock wave of an underwater explosion is a high pressure front of relatively short duration and moving through the water at the speed of sound (in the far field). The force exerted by the shock front on the electronics container causes the container to accelerate. The short duration of the force means that the displacement could be relatively small.

Before any solution to this acceleration problem is considered, it is necessary to consider the amount of movement (displacement). This is possible if the amount of acceleration and time of acceleration is known.

When movement of an object (e.g. electronics enclosure) is to be considered, and displacement is to be calculated, then Equation 22 should be considered. In the case of Equation 22 the acceleration is a constant value, and should only be used when a constant acceleration is experienced by the object. However, when an *average* acceleration is known, the average value may be used in Equation 22 to obtain an approximate value for the displacement.

$$s = ut + {}^1/_2\, at^2 \quad \text{-----------} \quad 22$$

Where:
s = distance (displacement) in m
u = initial speed in m/s
t = time in seconds
a = acceleration (m/s^2)

3.1.2. Acceleration and Displacement Prediction

To be able to formulate the hypothesis of the cause of damage to electronics, it was necessary to consider the amplitude of the acceleration, as well as the displacement of the object caused by the acceleration. This was also necessary for determining the type of test equipment that would be required for field testing.

Brett *et al* [2] experimented with a metal cylinder placed under shock loading as a result of underwater explosions, and obtained results which gave credibility to the amplitudes and periods of typical accelerations of such a metal object.

Brett *et al* [2] performed seven tests in all, of which event two had the most significant results for the purposes of this study, due to the fact that the least amount of damage was caused to the cylinder. This is important, because, if damage occurred, the accelerometer fixed on the inside of the cylinder would register a different value to when no damage occurred.

As will be seen later in this study, the equipment (electronics containers) used by the author of this study was designed to not be stressed beyond the elastic properties of the electronics container when subjected to shock loading. Brett *et al.* [6] established that the acceleration on an object as a result of an explosion of 5 gram PE4, at a stand-off distance of 300 mm, is 38 700 g (see Table 1, Event 2).

Table 1: Acceleration measurements by Brett *et al* [2]

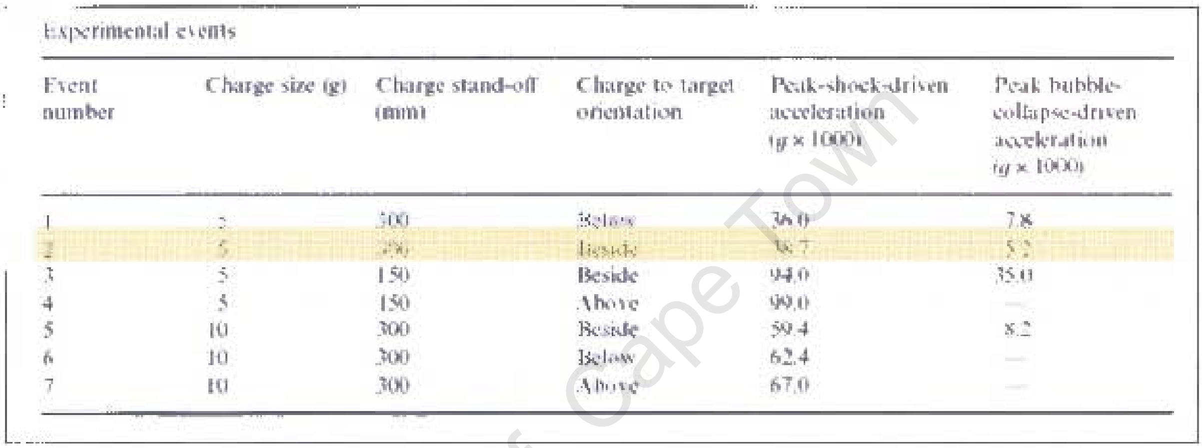

Experimental events

Event number	Charge size (g)	Charge stand-off (mm)	Charge to target orientation	Peak-shock-driven acceleration (g × 1000)	Peak bubble-collapse-driven acceleration (g × 1000)
1	2	300	Below	36.0	7.8
2	5	300	Beside	38.7	5.2
3	5	150	Beside	94.0	35.0
4	5	150	Above	99.0	—
5	10	300	Beside	59.4	8.2
6	10	300	Below	62.4	—
7	10	300	Above	67.0	—

Unfortunately, the time-axis measurements taken by Brett *et al.* [6] for event 2 were not very clear, but an approximation could be established (see Figure 20).

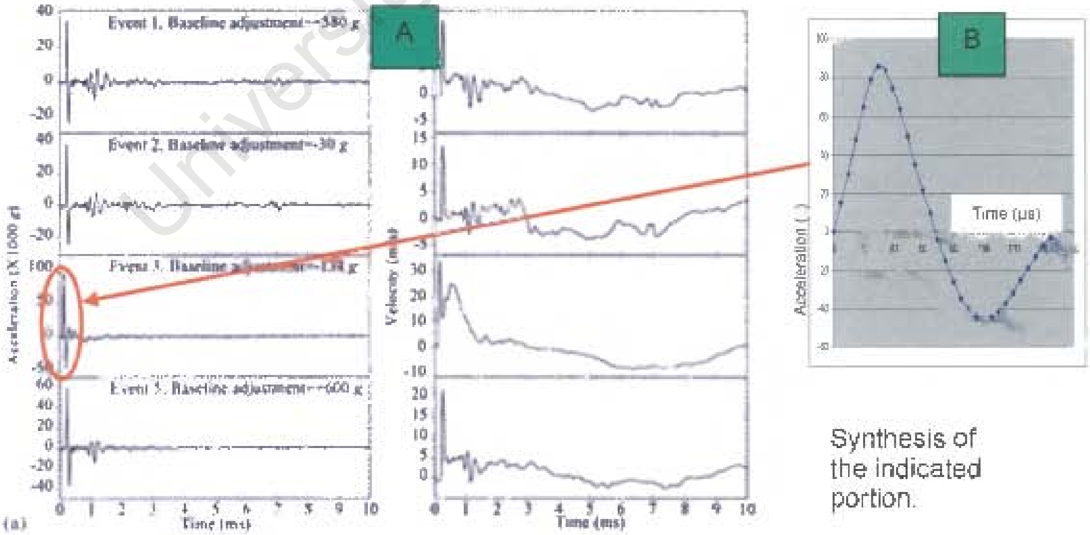

Synthesis of the indicated portion.

Figure 20: Acceleration and velocity curves from Brett *et al* [2].

Figure 20 shows that the peak acceleration is very short in comparison to the velocity, and the velocity is positive as well as negative at times, meaning that the hydrodynamic effects after the two peak periods caused the cylinder either to slow down, or to move in the opposite direction.

Consider Equation 22 and assume that the initial condition of the object was stationary. This means that $u=0$, and the subsequent displacement would be:

$$s = \frac{1}{2}at^2 \tag{23}$$

Where:
s = distance (displacement) in m
t = time in seconds
a = acceleration (m/s^2)

The average displacement was calculated by approximation, assuming that the average value of the first peak acceleration in Figure 20B was 50 000 g, and this acceleration was maintained for 60 µs. Inserting these approximations into Equation 23, we get:

$$s = \frac{1}{2}50000*9.81*(0.00005)^2 \tag{24}$$

$$\therefore s = 0.6mm \tag{25}$$

The result was an approximate displacement of 0.6 mm. After 60 µs, the acceleration was zero, which meant that the velocity was constant at that point. This meant that the object kept on moving, and the negative part of the acceleration curve during the following (approximately) 70 µs, caused the object to slow down, and possibly to stop. This means that the displacement (in this specific case) would be more than 0.6 µs, and was estimated to be 1 mm.

The significance of this calculation is that the displacement of the electronics container which was used for this study was also predicted to be in the order of 1mm, due to the fact that the mass was approximately the same as the mass of the object used by Brett *et al* [2]. Therefore, when shock/acceleration mitigating actions were planned, the size of the damping materials could be relatively small to allow for movement of only one, or perhaps (in worst cases) several millimetres.

Looking ahead at some results of the field work for this study (e.g. Figure 80), the peak acceleration period of the electronics container (object of this study) correlates very closely with the 60 µs per half period, as was measured by Brett *et al* [2].

3.1.3. Variables to consider

Note: if the contained electronics did not accelerate at all, no movement would have been experienced, and no damage would have occurred. This means that one of the solutions to be found is a method to preclude the acceleration of the container from the contained electronics, or to reduce it to below the damage threshold.

If this statement were true, it means in theory that, if all components inside the container had no mass, or all components were accelerated exactly at the same rate (by absolute rigid fixing methods), no damage would occur. In most cases, however, not only the electronics are contained in the container, but also some mechanical moving parts. At most, a combination of solutions will have to be found, if a solution of the rigidly mounted electronics only were to be attempted. Suspension methods should rather be considered.

Considering the mass of the container and Equation 22, acceleration will be smaller when the mass is increased. This is not a viable solution, due to the fact that the mass specifications of the electronics container will be fixed for a certain application.

The strength of the container itself (for obvious reasons) also plays a major role in the damage affected on the contained parts/components. For this study, and to limit the number of variables, it will be assumed that the container is physically unaffected during and after the explosion (no physical damage).

It must be accepted that each solid state electronic component, although rigidly mounted in its packaging, has many components internally, constructed by micro silicon layers of differing types and dimensions. The characteristics of these materials determine the functions of the component. It is readily understood that these materials, each piece being of different mass to its neighbour, may, under conditions of severe acceleration, alter the internal structure of the electronics. The level of the severe conditions causing internal damage is an unknown quantity at this stage.

3.1.4. Other possible causes of damage

Consider again the shock wave moving through the water in the far field, and passing by an object with a length measurement of 120 mm (see Figure 21). The physical size of the enclosure used for this study is presented relative to a shock wave in the far field which was generated by an explosive charge (Plastic X) of 17.568 kg at a standoff distance of 3.5 m at a depth of 19.85 m.

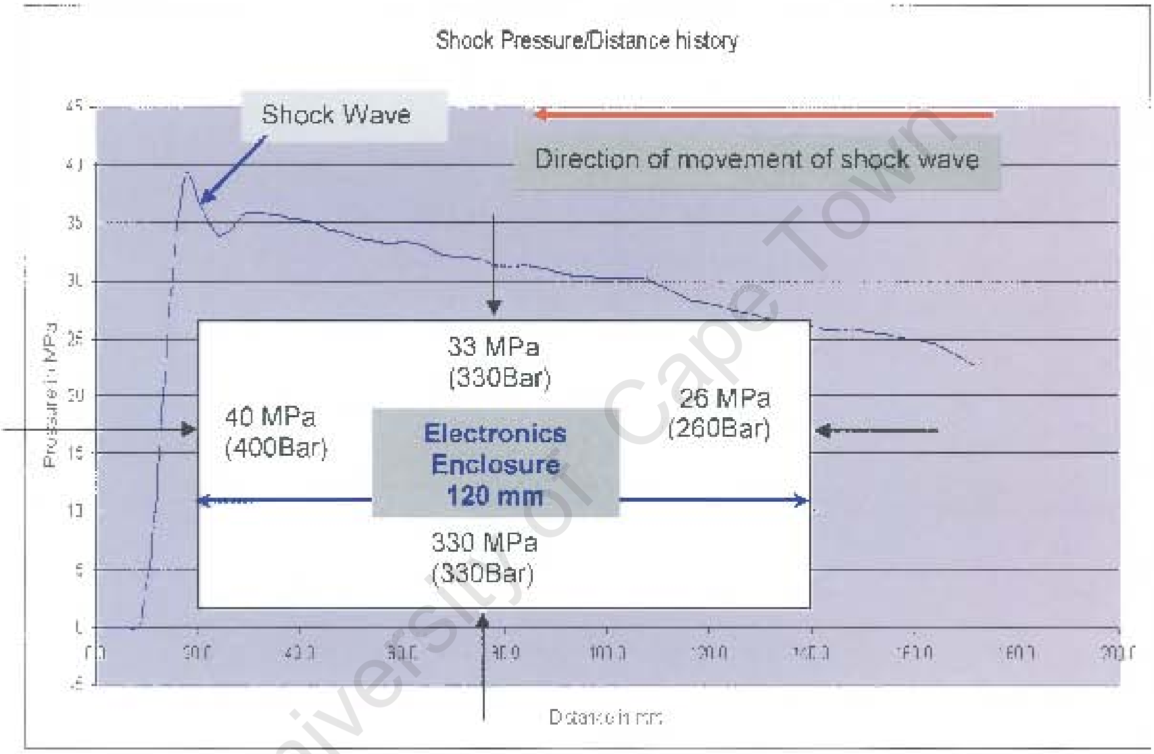

Figure 21: **Typical shock loading of electronic equipment**

From Figure 21, it is clear that when a shock wave passes over an electronics container and reaches the stage shown in this figure, the pressure around the box is in excess of 200 Bar. This is for the short duration of approximately 100 µs, after which the exponential decay of the rarefaction pressure continues to lower levels.

The consideration is that, although these pressures are present for a short while, they will initiate a crushing effect. It is predicted that the time that the pressures are prevalent will not be enough to complete the crushing effect. The hypothesis is therefore formulated as follows:

3.2. Hypothesis

Damage to electronic equipment as a result of underwater explosions is caused by the phenomenon of acceleration of the container housing the electronics.. Minimising the acceleration may avoid damage and provide a solution to the problem.

Qualification: Shock loading (as a result of an underwater explosion) of an electronics container causes the electronics container to accelerate. The acceleration of the container is passed on to the contained components via their mounting methods. Each component (whether electronic or mechanical) has a different mass, and therefore a different inertia. In an attempt to resist the perpetuation of the acceleration to all parts within, each component-inertia tends to exert different forces on its mountings. If the force amplitudes are high enough, the breaking/shearing strengths of either the component itself or its fixing mechanics is exceeded, and permanent damage occurs.

It was necessary to establish whether this hypothesis was credible before elaborating tests were performed to prove the hypothesis. The suggested plan of action was set out as follows:

From the foregoing discussions only, it was necessary to:

1. Confirm the environmental parameters prevalent in the water near the electronic equipment and their influence on an object when (and after) an explosion occurs, by measuring the acceleration.
2. Establish the environmental effect of the above parameters on the container of electronics. Using the information obtained in this study, the parameters could be used to simulate the acceleration and displacement effects on an object.
3. Determine a suitable solution and test the solution to the extent that it can be classified as a technology by which electronics could be protected against underwater explosions.

3.2.1. Postulation 1

> *It is postulated that there is an electronics Circuit Card Assembly acceleration damage threshold, above which the components will be physically damaged, and below which the components will not be damaged (see* Figure 22*).*
> *This damage threshold is dependent upon the type of components used.*

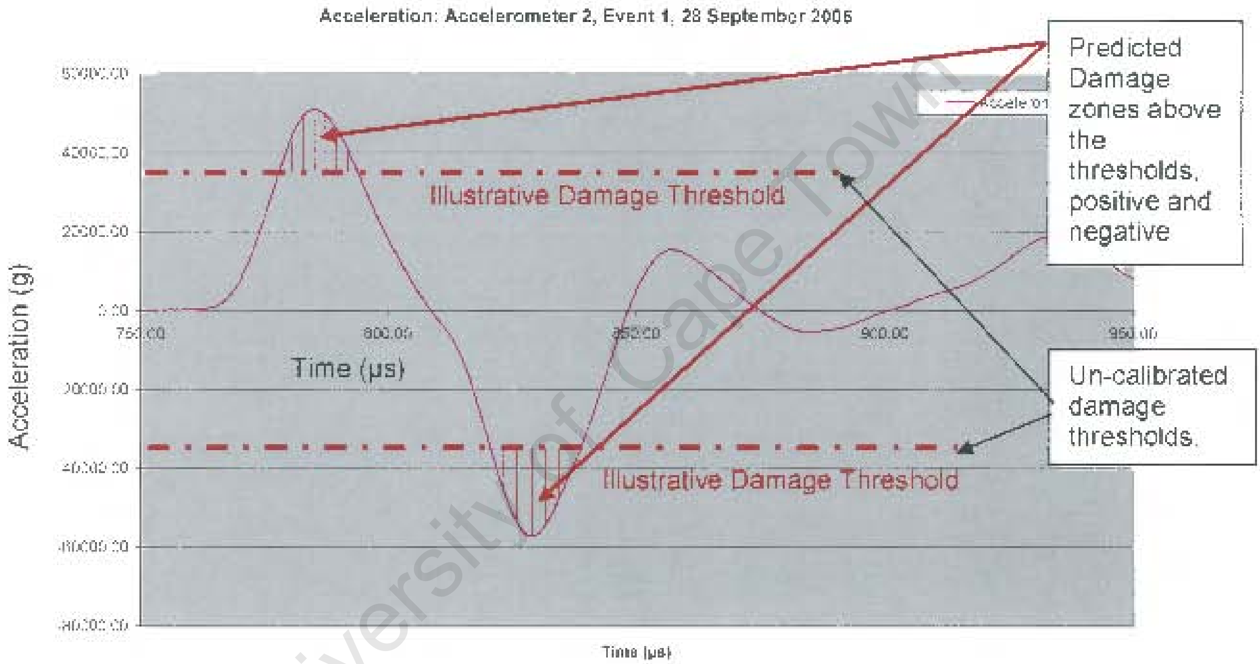
Acceleration: Accelerometer 2, Event 1, 28 September 2006

Predicted Damage zones above the thresholds, positive and negative

Un-calibrated damage thresholds.

Figure 22: Typical acceleration of an object caused by an underwater explosion

3.2.1.1. Description

In broad terms the above postulation means that in specific cases of electronic designs, component usage and PCB layout design, there is an acceleration threshold above which electronic component damage would be expected. Below that threshold, no physical damage is expected. This also means that the threshold changes for each design/component, and it is assumed that the mechanical design does not influence the result.

If this postulation were true (and assuming that no mechanical components caused collateral damage), it could be concluded that the only environment that would have to be reduced (to below a specific threshold) to prohibit electronic damage, would be the phenomenon of acceleration.

3.2.2. Postulation 2

It is postulated that, if the acceleration on the PCB is reduced (by means of a damping method such as "soft" mounting methods) to below the damage threshold, no damage would occur.

An experiment was devised to determine, visually only, whether there was enough evidence to support the postulation or not. If there were positive evidence, then further tests would be devised to confirm the findings, which could lead to the definition of damping design criteria.

It was foreseen that the first experiment may produce positive results, but that these results might not be conclusive because of the choice of soft mounting, which has a limited capability to reduce acceleration. It was also foreseen that experiments would have to be conducted with different types of soft mounting methods, to be able to establish the dynamic range of the damping effect of the chosen material and the effectiveness of the damping characteristics.

The ultimate goal was to conduct a number of experiments, which would indicate a choice of mounting methods that would be successful for the protection of electronics in a blast shock environment as produced by a 40 kg charge at a stand-off distance of 4 m, thus withstanding a pressure shock wave of 44.75 MPa (see Appendix 1).

3.2.3. Consideration of a possible solution

According to the hypothesis, a solution could be found when a suitable damper of acceleration is used between the source of the acceleration and the electronics contained within the electronics unit (see Figure 23).

Refer to Equation 21, and assume that the shock wave exerts a force on the electronics container depicted in Figure 23, causing it to accelerate. A good example of the mathematics that follows was obtained from Ogata [17:83]. The mathematics below is not to be attributed to the author.

The acceleration of the electronics CCA of mass m is investigated. The mathematical model of the damping system of Figure 23 is derived from the schematic diagram of the equivalent spring-mass-dashpot system shown in Figure 24. The acceleration of the electronics container will be measured, and is therefore assumed to be a known quantity. Consequently, it can be assumed, for this mathematical model that the electronics container is without mass. The initial condition for time $t < 0$ is static (no movement).

In the system presented in Figure 24, the following status is denoted:

$u(t)$ is the displacement of the container, and is also the input to the system.
$y(t)$ is the displacement of the electronics CCA, and is the output of the system.
b is the viscous friction coefficient of the dashpot.
k is the spring-constant.

Assume that the friction force of the dashpot system is proportional to $\dot{y}-\dot{u}$
Assume the spring is a linear spring and the spring force is proportional to $y-u$
At time $t=0$ the container is moved by the force of the shock wave.

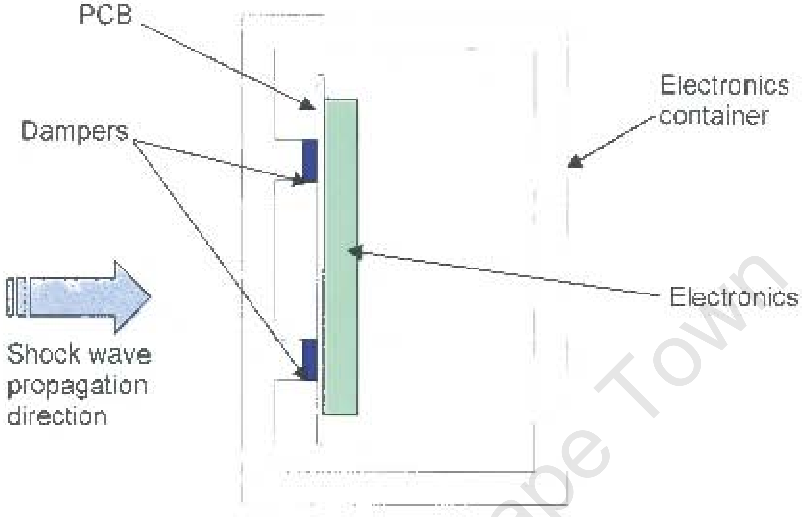

Figure 23: **The submerged electronics container with PCB mounted on dampers**

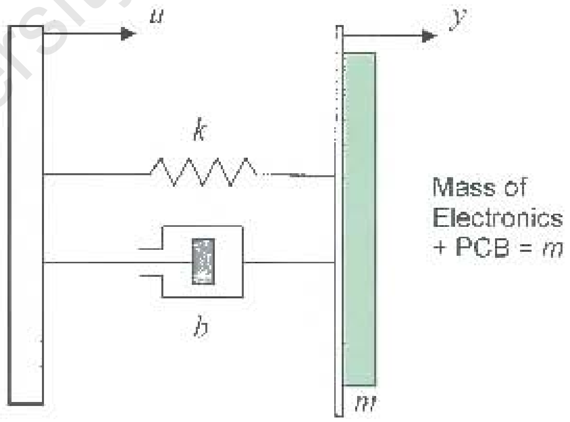

Figure 24: **Mathematical schematic equivalent of the damping system**

In Newton's second law, shown in Equation 21, m is a mass, a is the acceleration of the mass, and $\sum F$ is the sum of the forces acting on the mass.

Applying Newton's second law to the schematic diagram (Figure 24), we obtain:

Mass*acceleration of electronics CCA =
Viscous force + spring force

Taking direction of the forces into consideration, we get:

$$m\frac{d^2y}{dt^2} = -b\left\{\frac{dy}{dt} - \frac{du}{dt}\right\} - k(y-u) \qquad \text{-------------------} \quad \mathbf{26}$$

$$\therefore m\frac{d^2y}{dt^2} + b\frac{dy}{dt} + ky = b\frac{du}{dt} + ku \qquad \text{------------------------} \quad \mathbf{27}$$

This is the mathematical model of the system. To be able to do mathematical simulations with specific inputs, it is useful to obtain the transfer function of the system. Taking the Laplace transform of each term of Equation 27 results in the following:

$$\mathscr{L}\left[m\frac{d^2y}{dt^2}\right] = m\left[s^2Y(s) - sy(0) - \dot{y}(0)\right]$$

$$\mathscr{L}\left[b\frac{dy}{dt}\right] = b\left[sY(s) - y(0)\right]$$

$$\mathscr{L}\left[ky\right] = kY(s)$$

$$\mathscr{L}\left[b\frac{du}{dt}\right] = b\left[sU(s) - u(0)\right]$$

$$\mathscr{L}\left[ku\right] = kU(s)$$

Set the initial conditions equal to "0": $y(0)=0$, $\dot{y}(0)=0$, and $u(0)=0$. The Laplace transform can be written as:

$$\left(ms^2 + bs + k\right)Y(s) = \left(bs + k\right)U(s)$$

The transfer function is the ratio of Y(s) to U(s), therefore:

$$G(s) = \frac{Y(s)}{U(s)} = \frac{bs + k}{ms^2 + bs + k} \qquad \text{-----------------} \quad \mathbf{28}$$

This transfer function as given by Ogata [17:84] contains both the spring constant and the damping (viscous friction) coefficient. The mass of the electronics CCA is known. To design the damping system shown in Figure 23, the author chose to follow an empirical method to obtain the constants of a certain damping device, which may be suitable for this purpose.

This transfer function can be applied to a simulation process (with an acceleration of the container as input, and the acceleration of the CCA as the output) when constants b (damping coefficient) and k (spring constant) are known.

When it is assumed that the spring constant is much less than the damping coefficient, Equation 28 can be simplified as follows:

$$G(s) = \frac{Y(s)}{U(s)} = \frac{1}{\frac{m}{b}s + 1} \quad \text{-------------------} \quad 29$$

or

$$G(s) = \frac{Y(s)}{U(s)} = \frac{bs}{ms^2 + bs} \quad \text{-------------------} \quad 30$$

giving a solution of one pole at $-\frac{m}{b}$ ------------------------------ 31

When *m* (mass of the CCA) is known, *b* (the damping co-efficient) can be calculated by empirical methods for simulation purposes.

The ideal method of determining both the damping coefficient as well as the spring constant would be by measurement of the chosen damping system. This measurement is, however, not easily performed due to the fact that the damping coefficient is a value associated with the resistance to velocity. Another reason is that the damping coefficient and the spring constant forms part of the same material, and while measuring one parameter, the other parameter influences the measurement. The test equipment to perform the measurement of the damping coefficient was not available to the author of this dissertation, and hence the simulation of the damping system was not performed for this study. This was also the case for the transfer function given by Equation 46 on page 172.

3.2.4. Scaling Factors

The original scenario was to have moored sea mines spaced at typical distances of 5 m from each other. Those mines are armed with 40 kg and more (up to 200 kg). They are typically launched from submarine tubes, so they are typically cigar-shaped, 0.5 m in diameter, and approximately 3 m in length. The mass of the armed floating section is typically 300 kg in the case where a payload of 200 kg is carried, and the floating section floats horizontally at depths of typically 20 m.

When a charge of 200 kg is detonated, it produces a shock pressure pulse that moves spherically outward. This shock pressure pulse is typically 25 GPa (Cooper [6: p259] for Pentolite) at the boundary between the explosive charge and the sea water. This peak pressure then reduces in relation to the outward motion of the shock wave to typically 63 MPa when the shock wave had moved 5 m (Equation 3 transferred from Cole [5]).

This pressure exerts a force on the neighbouring mine during the time that the shock wave passes over the mine, causing this neighbouring mine to accelerate. This acceleration is passed onto the electronics that are contained within the neighbouring mine, causing electronic damage.

The force is not known (because of the impracticality of the measurement process), but from the literature on scaled tests (Brett *et al* [2]) it was assumed that the acceleration of the neighbouring mine would be in the order of 80 000 g for a very short (50 µs half sine) period.

The mass of the test unit that was used by this study, was approximately 2 kg, and was accelerated (first experiment on page 98) between 50 000 g and 60 000 g (see Figure 84: half sine 50 µs) using a 30 gm Pentolite charge at a standoff distance of 675 mm. The pressures produced (measured 20 MPa at standoff distance of 733 mm, see Table 22), equated to 200 kg at 13.5 m. This scaling of the test unit was deemed to be a good representation of the full scale mine. The acceleration was estimated to be slightly too high, but the mass could be increased when necessary, reducing the acceleration according to Newton's second law.

Chapter 4

4.1. SELECTION OF MEASURING EQUIPMENT

Various factors have to be taken into account when equipment is selected to measure the effects of underwater explosions on an enclosure unit.

From the chapter on the Literature Study, it is clear that the pressure shock wave resulting from an underwater explosion causes an object located in close proximity to the blast to accelerate. Therefore there are two phenomena to measure, i.e. the shock pressure at the point where the object is located, and the acceleration of the object.

The selection of the measurement equipment (to measure both the shock pressure and the resultant object acceleration) is discussed in this chapter. Additionally, the expected characteristics of the phenomena are examined closely to determine the required characteristics of the measurement equipment.

The characteristics of the pressure shock wave suggest that a rather fast rising edge (measured to be 6 µs in the far field, and faster[5] in the near field) should be taken into consideration. The discussion in Chapter 2 revealed that the measurement of 6 µs rise time is not a true representation of the actual rise time, but that the output of the sensor is in the region of 6 µs due to the physical construction of the sensor. The electronic measurement equipment should therefore cater for the output of the sensor.

All equipment for measuring is limited by a frequency bandwidth characteristic. A general rule is that the more amplification one requires, the less the equipment bandwidth would become. Some techniques are used to refine and counteract the limitations of bandwidth, and the more expensive equipment models of the same manufacturer invariably have wider bandwidths.

4.1.1. Pressure Sensors

To measure the pressure history of explosions, two Tourmaline piezo-electric sensors with built-in charge amplifiers, specially designed for measuring underwater explosion pressure shock waves, were purchased. The specifications are attached (see Appendix 2). Two models were purchased, i.e. one 138A10, and one 138A50. The only difference between the two sensors involved the sensitivities. These are listed in Table 2.

Table 2: Pressure Sensor sensitivities

Model	Calibrated Sensitivity (mV/MPa)	Max Pressure (kpsi)	Max Pressure (MPa)
138A10	73.57	10	69
138A50	12.32	50	345

---

[5] The varying propagation velocity in the near field is discussed in Chapter 2. This propagation velocity has an influence on the measurement of the rise times, which is also discussed in Chapter 2.

An RG58C/U co-axial cable of 25 m in length was attached to each sensor via connectors at both ends. To measure the explosion result, these sensors and cables were connected to a PXI-format DAQ card, with the capability of measuring 4 channels, with each channel sampling at 2 MS/s. The memory was able to store up to 1 second of data samples. The expected rise times of the explosions (from Chapter 2) was 6 µs. This means that, if these explosions exhibited similar characteristics, 12 samples could be obtained on the rising edge with the use of this specific A/D card, which is deemed to be adequate. There is ample reason to believe that the slope of the rising edge of a shock wave will increase in the near field to approximately 1 µs at distances that are applicable to the closest stand-off distance of the electronic enclosure (40 kg charge at stand-off distances of approximately 2 m). In this case, there will be two samples on the slope, which is marginal for statistical resolve.

4.1.2. Custom Synchronisation Equipment

Synchronisation of the measurements with the time of explosion is very important due to two factors.

Firstly, the A/D card is memory limited to record only 2 000 000 samples in each channel, which translates to 1 s of recording time at a sample speed of 2 MS/s. Recording of data during this 1 s window is difficult without an accurate means of synchronisation. Secondly, recording the time taken for the shock wave to reach the sensors is necessary to determine the average velocity of the shock wave. This characteristic of the shock pressure is important in the prediction of the acceleration of an object in close proximity to the blast, due to the fact that the shock pressure velocity is related to the resultant acceleration of the object under discussion.

An electronic circuit was designed to supply a synchronisation pulse for the measurement equipment to synchronise with the time of the explosion. The synchronisation pulse was fed into the digital synch-pulse port of the A/D card. The characteristics of this synch pulse were measured, and are shown in Figure 25. The period of the pulse was approximately 1 s, although only the rising edge of the synchronisation pulse was used by the A/D measurement equipment to synchronise measurements with the explosion.

It was also the intention to determine the exact moment when the detonator functioned. For this purpose, a series resistor of 0.1 Ohm was introduced into the firing line. The purpose was to measure the Voltage drop caused by the firing current into the detonator, and the change in Voltage drop when the detonator functioned. Figure 25 shows the synchronisation pulse, as well as the voltage across the Drain-Source of the firing Field Effect Transistors (FETs) (see schematic diagram - Appendix 3).

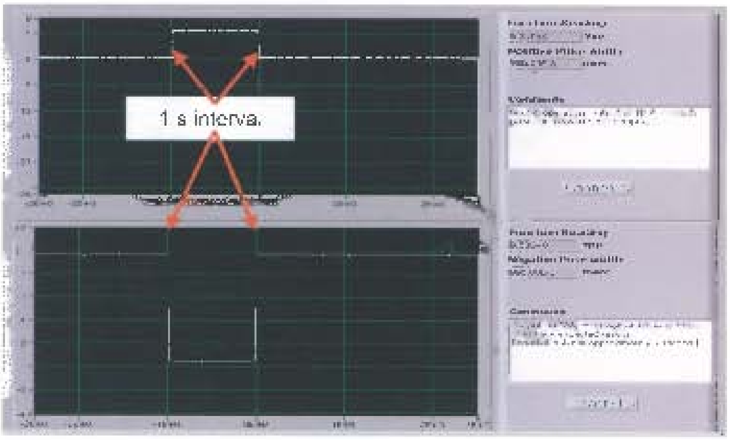

Figure 25: **The synchronisation pulse.**

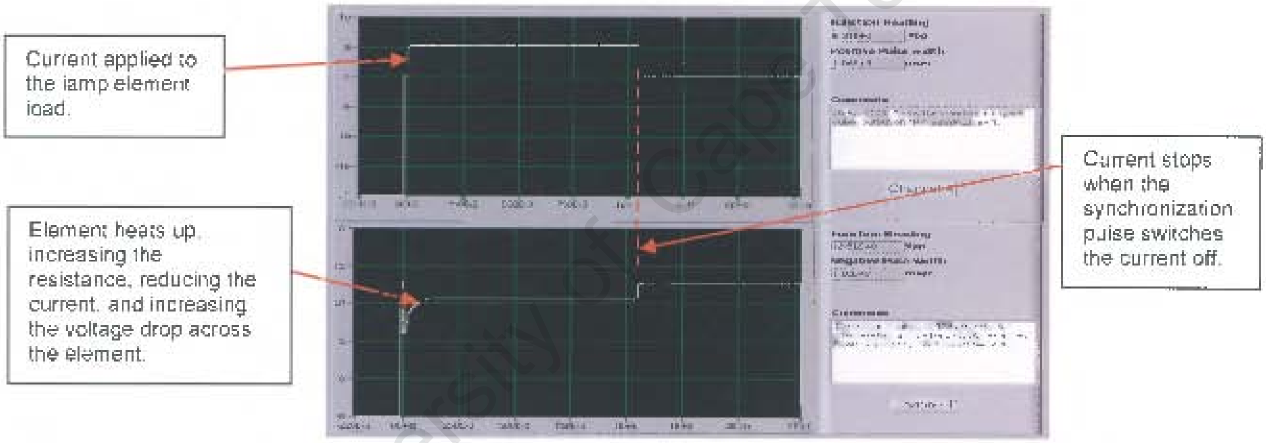

Figure 26: **The load voltage with a lamp as a load**

Figure 26 shows the voltage on the output terminals, with a 0.1 Ω resistor in series with the load. This is for testing whether the moment when the detonator functions can actually be detected accurately. From Figure 26 it is clear that this test setup will indeed show when the detonator functions, by the rising edge when the current drops to zero.

Practical results were obtained by firing the detonator in sea water when the detonator was inserted into a 30 gm Pentolite charge (see Figure 27).

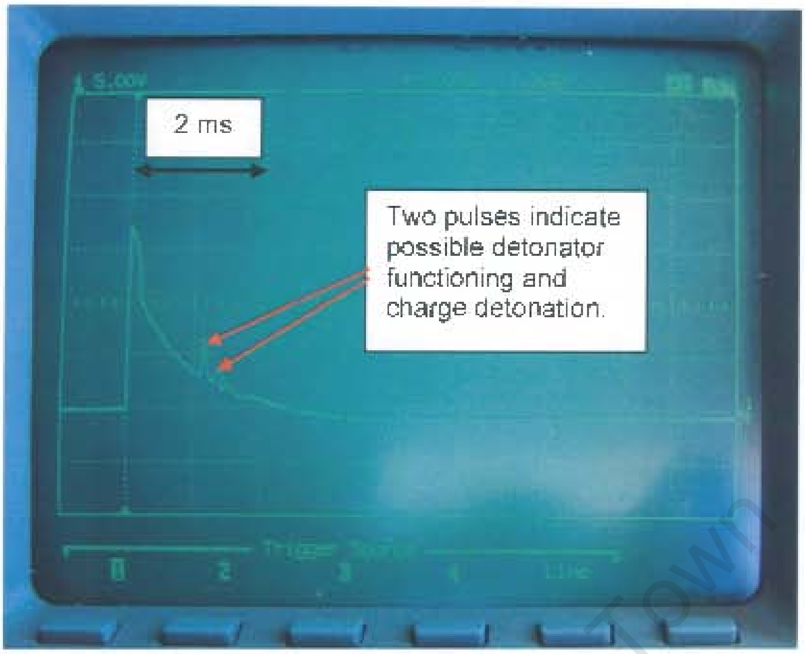

Figure 27: **Measured detonator current**

The rising edge of the detonator current pulse was used as an input to the synchronisation circuitry. The result was that the rising edge of the current pulse triggered the digital circuitry, which also produced a rising edge within fractions of a microsecond (44 ns, as shown in Figure 28), which was used to trigger the measurement cycle of 1 s.

The result obtained and illustrated in Figure 27 suggests that an accurate indication (within a few microseconds) of the moment that the charge was detonated could not be determined by using this method. Two pulses showing detonator current disturbance (shown in Figure 27) could have been due to the functioning of the detonator, and the detonation of the charge. The disturbance was probably caused by ionisation of the water in the immediate proximity of the two detonator wires. This, however, could not be verified at the time, and a different synchronisation method had to be investigated.

4.1.3. Bandwidth Requirements

When purchasing the additional equipment, it is necessary to establish the maximum bandwidth of the equipment, and the effect that bandwidth limitation will have on the measurements. The following paragraphs deal with the question of bandwidth concerning the equipment that introduces the bandwidth problem, i.e. the A/D card, and the signal conditioner. These test equipment units are arranged in tandem, and the tandem arrangement therefore has to be investigated after considering each unit individually.

4.1.3.1. A/D Card

To explore the limitation effect of the bandwidth characteristic of the A/D card, a square wave was produced by a signal generator with rising-edge-times much greater than the A/D card's ability to follow the signal due to its bandwidth limitation. The A/D card can measure voltages ranging from a DC level to a bandwidth-limited high-cut-off frequency.

A generator frequency of 100 kHz (square wave) was chosen, at amplitude 2 Vp-p. This signal was fed into the input port of the A/D card, and the A/D card was set at a sampling rate of 2 MS/s.

The input signal is shown in Figure 28a. Figure 28b is a time-amplified version of Figure 28a for measuring the rise time of the leading slope more accurately.

Figure 28: Test input signal

The leading edge of the generated signal was measured, using a 100 MHz oscilloscope, to be 44 ns (see Figure 28b).

The A/D card has the characteristic that, if a full-scale-amplitude of 10 V is chosen, the bandwidth is 1 MHz. If a full-scale-amplitude of 2.5 V is chosen, the bandwidth is 600 MHz. This characteristic is the result of the standard concept of the "gain-bandwidth" product.

The input signal was applied to the A/D card at the full scale of 10 V, and measurements were taken. Then the input signal was applied at full scale of 2.5 V, and measurements were taken again. In both cases, the amplitude of the input signal was kept at 2 Vp-p.

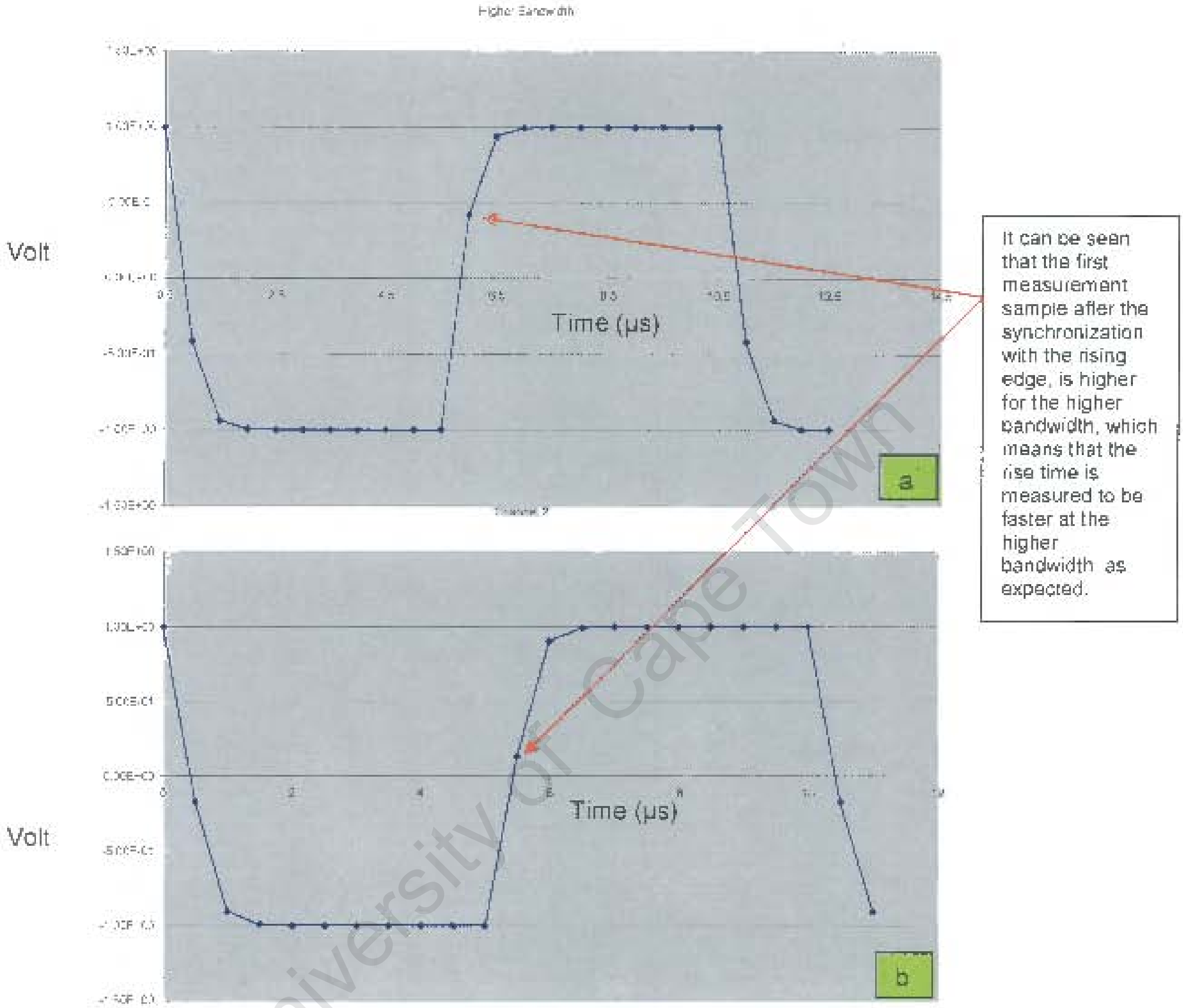

It can be seen that the first measurement sample after the synchronization with the rising edge, is higher for the higher bandwidth, which means that the rise time is measured to be faster at the higher bandwidth as expected.

Figure 29: **A 100 kHz square wave measured at higher bandwidth (top = 1 MHz), and lower bandwidth (bottom = 500 kHz)**

From these two measurements (see Figure 29), it can be seen that the rising edge starts the rising process (bottom edge of rising pulse) and shows no "rounded shoulder", but when the input signal approaches its peak, the measurement "shoulders" are rounded. This is consistent with low-pass bandwidth limitations.

Applying this bandwidth limitation effect to a square wave, such as in Figure 29, the result is quite predictable, and it may not present a problem when measuring lower frequencies. Applying a shock wave to this limiting feature, however, may present problems, due to the fact that the peak amplitude of a shock wave is reached in microseconds, but the pulse starts to drop "immediately" upon reaching its peak. It is therefore necessary to investigate the response of the measurement system to a typical explosion shock waveform. But it is necessary to first determine the filter order of the A/D card, before such an attempt is made.

Signal Conditioner

It was the intention to measure the explosion pressure pulses with the use of the pressure pulse sensors (as before) and using a "conditioning amplifier" or "signal conditioner" to supply the constant current to excite the sensors (which have built-in charge amplifiers), and to condition the signal for recording purposes.

In discussions with the supplier on the signal conditioners that are compatible with the sensors, it was found that there are various models that can be purchased.

Some signal conditioners have only unity-gain amplifiers. They have bandwidths of 1 MHz each. Some signal conditioners have the ability to amplify the signals by X1, X10 or X100. These conditioners have bandwidth limitations in the order of 100 kHz, which means that they may not be able to measure the rising edge and amplitude of a shock pressure pulse correctly. The effect of these limitations on the pressure pulse is unknown at this stage, and it therefore becomes necessary to investigate the effect of bandwidth quantifiably, or to be able to make the correct choice by simulation. A simulation process to determine the effect of bandwidth limitations on the measurement end result was attempted in this study.

4.1.3.2. Signal Conditioner and A/D Combination

The combination circuit that was considered was the cascaded signal conditioner and A/D card (see Figure 30).

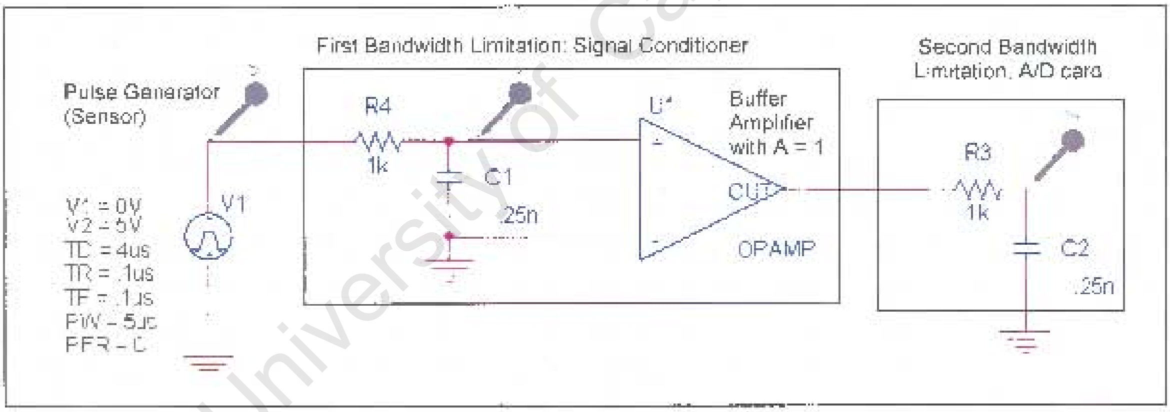

Figure 30: **Combined circuit to be simulated, in simplified first-order filter notation**

4.1.3.3. Analysis of Bandwidth Limitation

Each of the devices connected in series (the signal conditioner and the A/D card) had a bandwidth limitation. The A/D card had a bandwidth of 1 MHz, and the best signal conditioner, supplied by ICP, had a bandwidth of 1 MHz (@ unity gain).

The bandwidth of the A/D card was known, and the step response had been determined by actual measurements. The first task, therefore, was to determine the order of the low-pass characteristic of the A/D card, and then to extrapolate the findings to the signal conditioning equipment. The method was to simulate a step-function stimulus on various orders of low-pass filters, and then to compare the response with the actual measurement of the step-response of the A/D card shown in Figure 31. The response that compared best with the measured result was to determine the order of the filter of the A/D card.

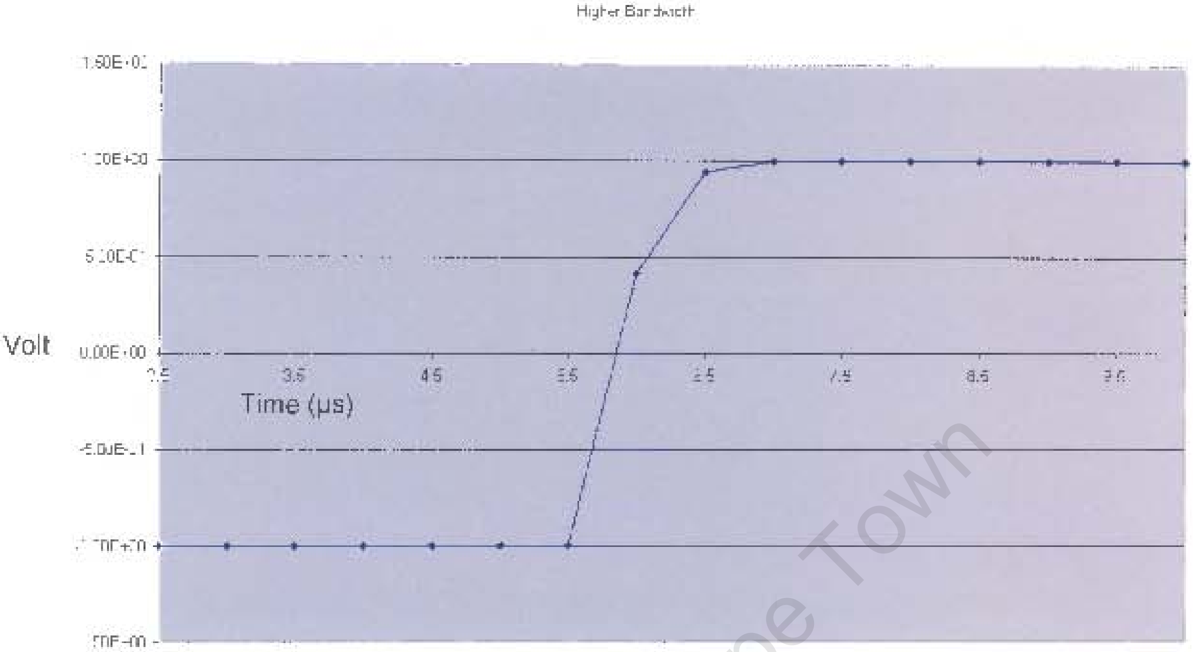

Figure 31: Actual measured result with the A/D card of a step function input

Nilsson and Riedel [16: p666] showed that the low-pass frequency of a simple (first-order) R-C circuit, is:

$$\omega_c = \frac{1}{RC}$$

$$\therefore 2\pi f_c = \frac{1}{RC} \qquad \text{------------} \qquad 32$$

From Equation 32, the values for R and C can be calculated for a low cut-off frequency of 1 MHz. The values of R = 1000 Ω and C = 0.159 nF were calculated and applied to the simulation process.

It had to be considered that the bandwidth of the test equipment (the A/D card in this instance) would not be a first-order filter, but rather a second or third (or nth) order filter. The first task was to simulate this filter, as well as various orders of the same filter, and then to compare the result to the measured response of the A/D card.

Nilsson and Riedel [16: p742] have indicated that the result of cascading identical low pass filters (see Figure 32), will sharpen the bode-plot (see Figure 33), but the resultant low cut-off frequency will still be at the original frequency.

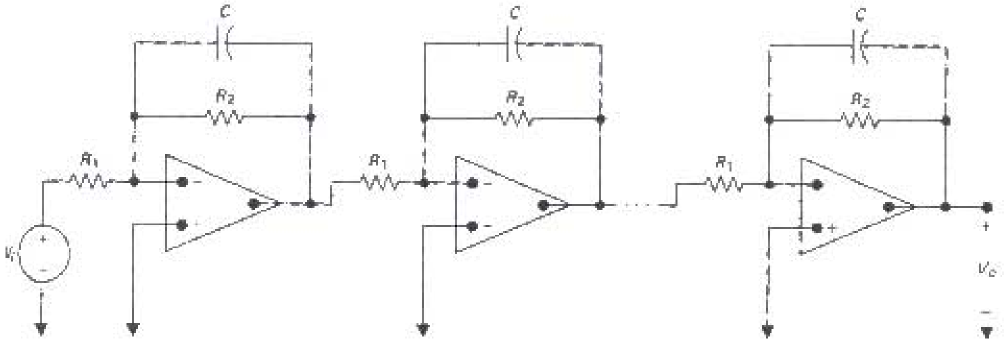

Figure 32: **From Nilsson and Riedel [16: p743]: the cascading of low pass filters**

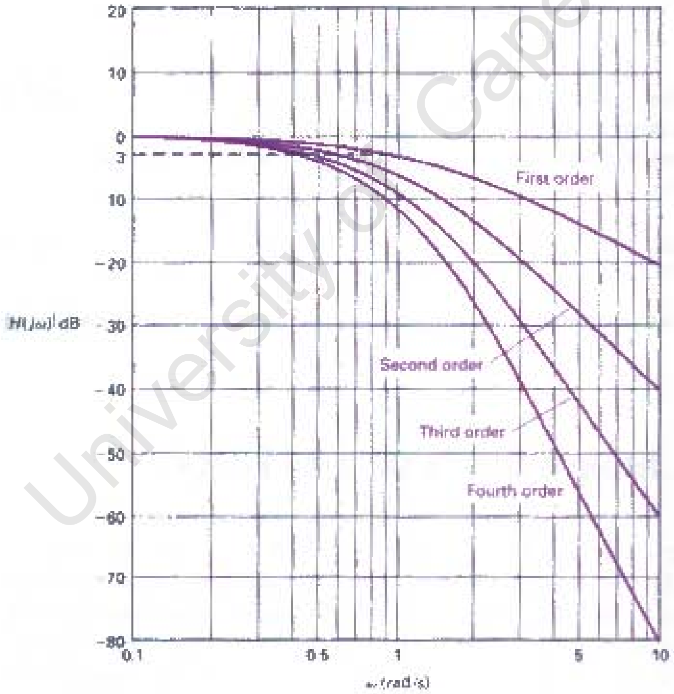

Figure 33: **From Nilsson and Riedel [16: p742]: the bode result of the cascading of low pass filters**

A simulation of the circuit up to the third order (yellow measurement point) in Figure 34 was done first, to find the best fit for the measured result of Figure 31.

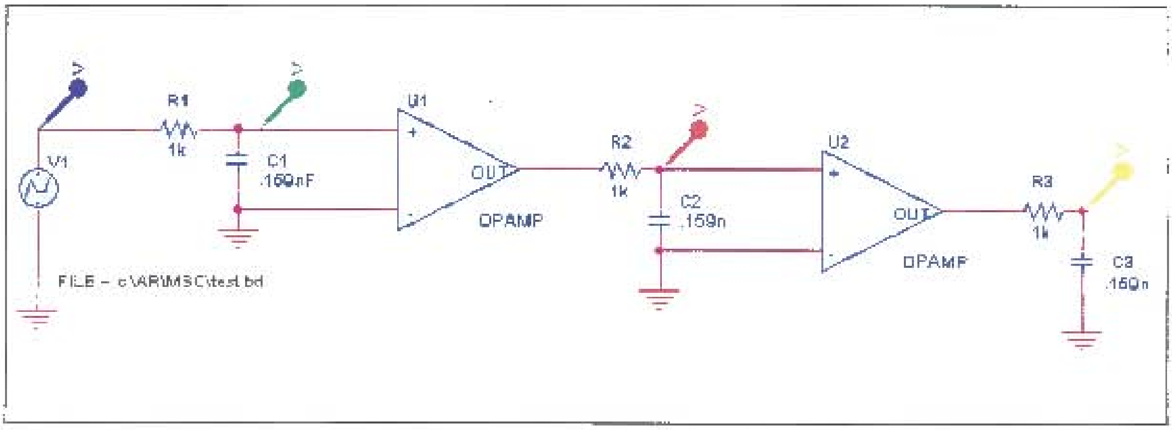

Figure 34: The cascaded identical 1 MHz low pass filters

The simulation result was superimposed on the measured result, and is shown in Figure 35.

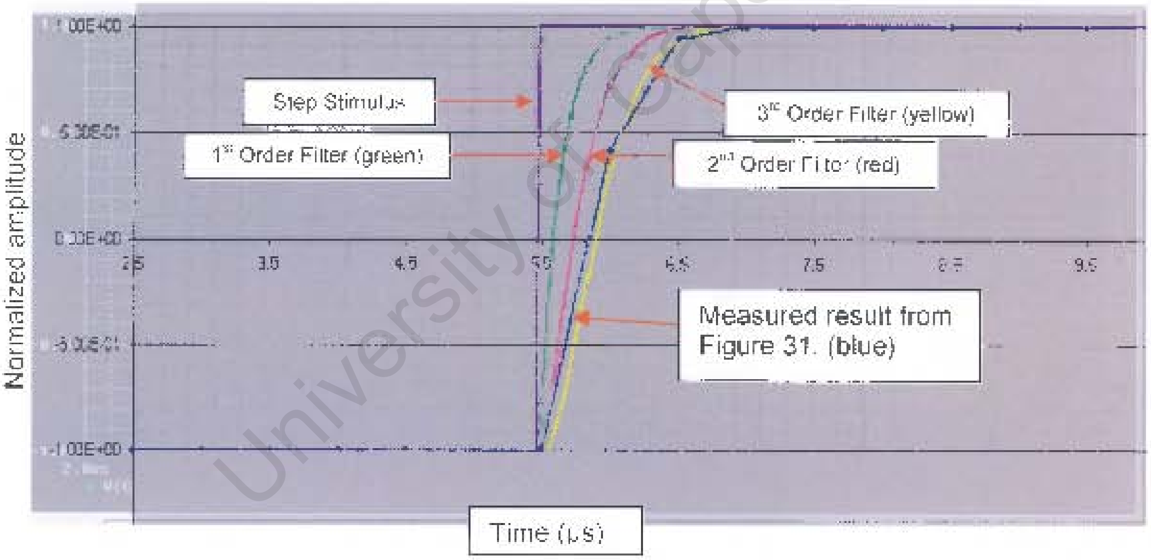

Figure 35: The simulated result superimposed on the measured result

Figure 35 clearly shows that the third order filter was the best fit for the measured result, and that it could be concluded that the A/D card low pass filter was a third order filter.

The order of the low-pass filter in the signal conditioner was unknown. It was considered fair to assume that the signal conditioner would also have a third order response. (The conditioners were not available to measure the bandwidth at that stage). It was possible to expand the simulation circuit of Figure 34 to a sixth-order filter (Figure 36 = two third-order filters cascaded), and to apply an actual measured pressure shock wave (as supplied by Ström & Janzon [20]) as a stimulus (Figure 37).

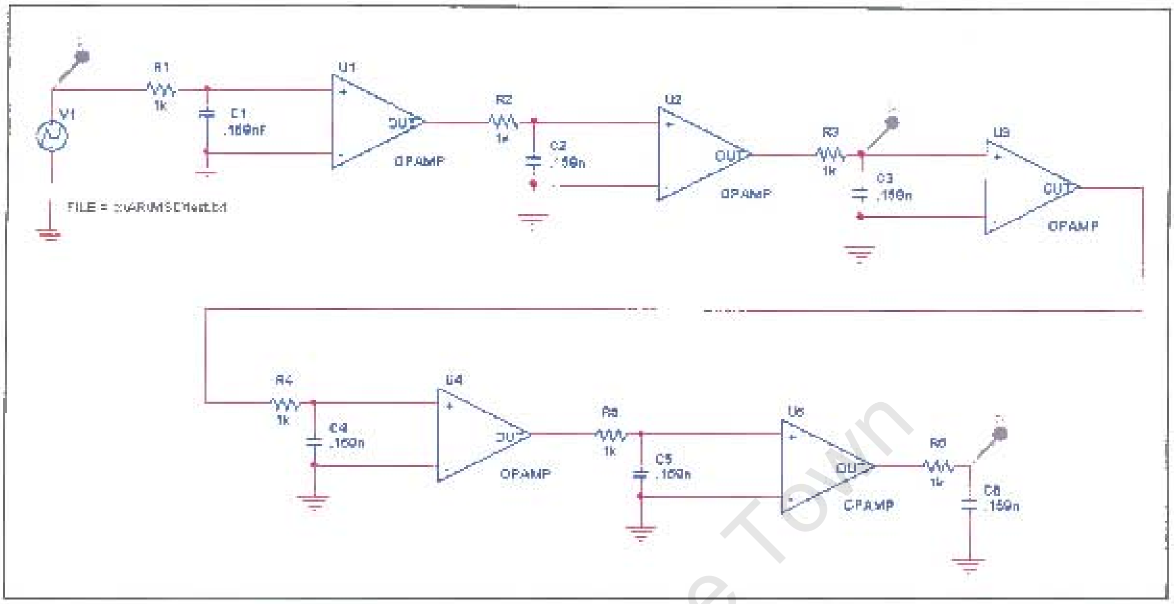

Figure 36: **The complete cascaded 6th-order 1 MHz filter**

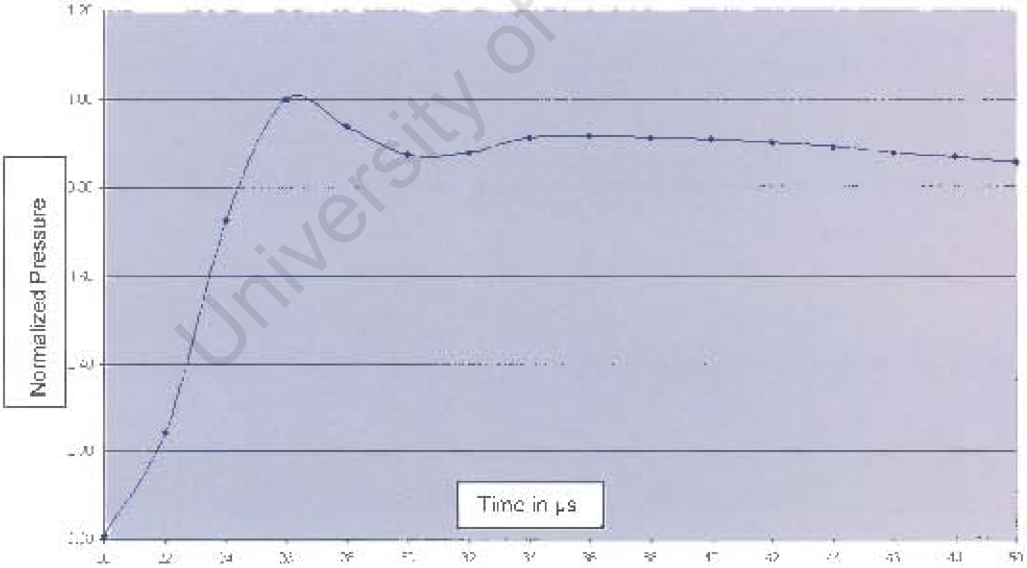

Figure 37: **Typical measured (normalised) shock wave, to be used as simulation stimulus**

The data points of the actual shock pulse measurement of Figure 37 was taken as an input stimulus for the simulation model (Figure 36), resulting in the output response shown in Figure 38.

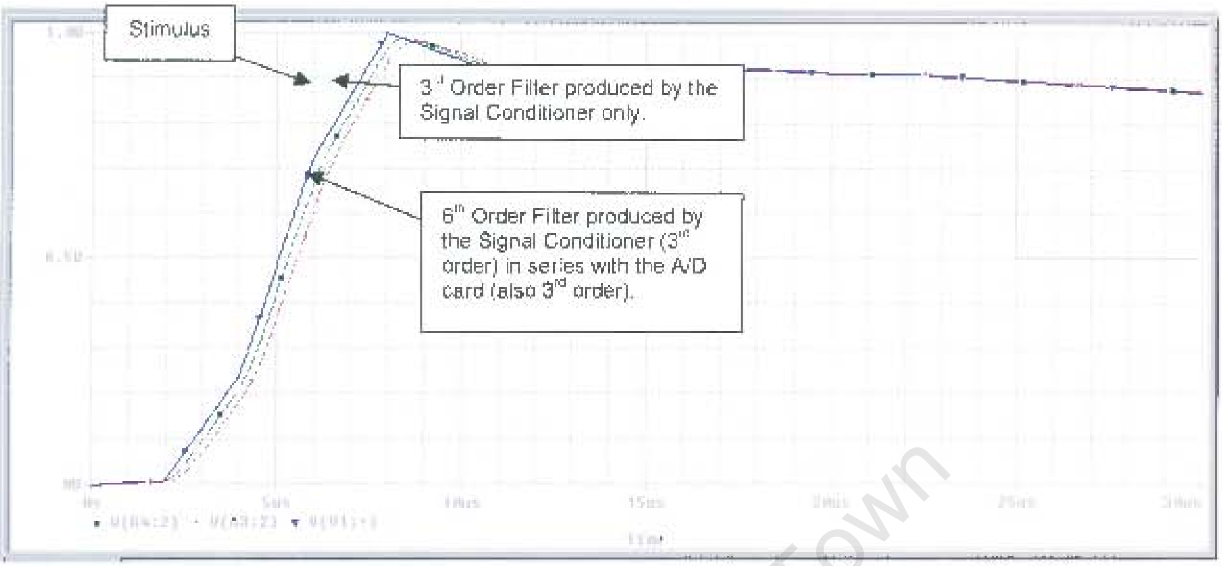

Figure 38: **Simulation results with actual measured data used as input stimulus**

From this simulation, it is clear that the influence of the specific bandwidth limitations that the instruments would introduce into the measured result were not significant. It can be seen that the peak amplitude as well as the time delay of the result varied very slightly compared to the actual stimulus, and thus the result was a fair reproduction of the stimulus. The filtered peak voltage differed from the input signal by approximately 1% and after 13 µs there was hardly any difference between stimulus and response.

It could therefore safely be said that, if the measurements in Figure 38 were correct, then the series bandwidth limitations as would be introduced by the signal conditioners plus the A/D card, (6^{th} Order Filter), would not influence the measurements adversely.

4.1.3.4. Measured Response of the Signal Conditioner and Sensor

4.1.3.4.1. Sensor Simulation Circuit

Experiment: Determine the response of the sensor simulating circuit, in combination with the signal conditioner.

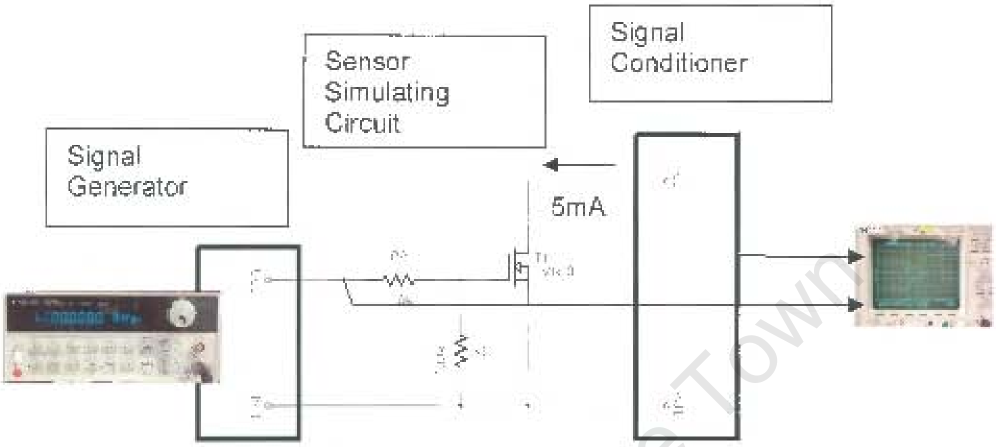

Figure 39: **Test set-up to test the Signal Conditioner response using an excitation current of 5 mA**

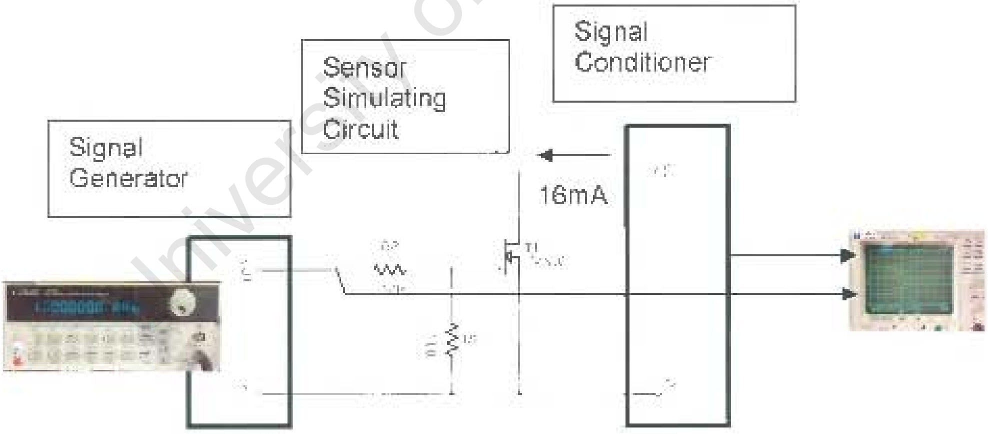

Figure 40: **Test set-up to test the Signal Conditioner response using an excitation current of 16 mA**

The signal generator was connected to the circuit shown in Figure 39 and adjusted to produce a 1 kHz square wave with 50 % duty cycle, between 0 V and 5 V. The signal conditioner was adjusted to deliver a constant current of 5 mA to the sensor simulator shown in Figure 39. The oscilloscope probe (Channel A) was connected to the output of the signal generator, and the oscilloscope Channel B was connected to the output of the signal conditioner. The result is shown in Figure 42. The measured result showed that the input signal changed much faster from one level (5 V) to the next level (0 V) than the output (-12 V to +12 V) as measured at the output of the signal conditioner. This indicates that the combined effect of the sensor simulator and the signal conditioner introduced a slew reduction to large signal amplification. The FET produced the inverted response seen in Figure 42, as was expected. Notice also that the change in output was linear between -11 V and +11 V. This was due to the fact that the FET (with output impedance consisting of a resistance, $R_{DS\text{-}ON}$ and a capacitance C_{DS}) had an output-impedance that is dominated by C_{DS} (see Figure 41).

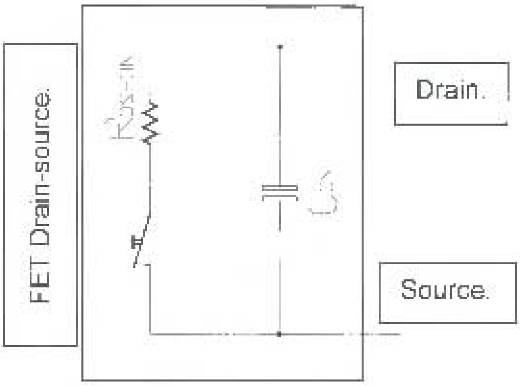

Figure 41: Output impedance characteristics of an FET

Note: $R_{DS\text{-}ON}$ is the resistance measured between the Drain and the Source of the FET when the FET is switched ON.

The output from the signal conditioner to the sensor is a constant current (set to 5 mA in the case of Figure 39, and to 16 mA in the case of Figure 40). This means that $R_{DS\text{-}ON}$ (typically 0.3 Ohm) does not play a significant role in this measurement, because the current source (signal conditioner) has a much larger internal resistance (typically 1 MΩ) compared to $R_{DS\text{-}ON}$. The capacitance of the FET in combination with the capacitance of the oscilloscope probe is thus the dominant load impedance of the sensor-simulator on the signal conditioner, and therefore the typical linear response shown in Figure 42 is obtained.

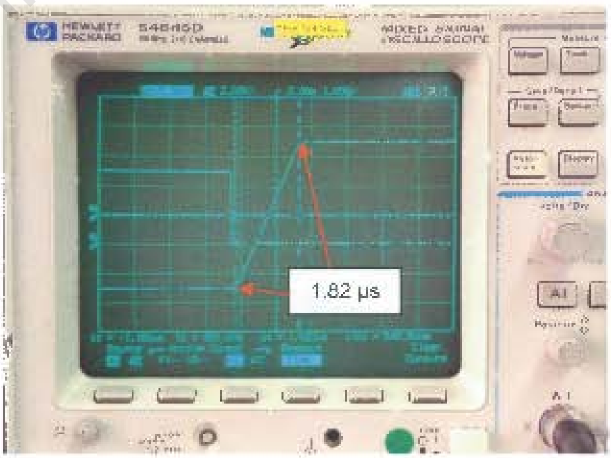

Figure 42: Test results showing the slew action of the signal conditioner with a constant current of 5 mA

To demonstrate the effect of the capacitive impedance of the sensor simulation circuit of Figure 39, the signal conditioner source current to the sensor was adjusted to 16 mA. In practise, relatively long cables are used to connect the sensors with the measuring instrumentation. These cables have a certain amount of capacitance, which is simulated by the test circuit shown in Figure 39. A good cable to use would be one with a very low capacitance. To overcome the effects of the cable capacitance, the sensor-excitation current from the signal conditioner can be increased.

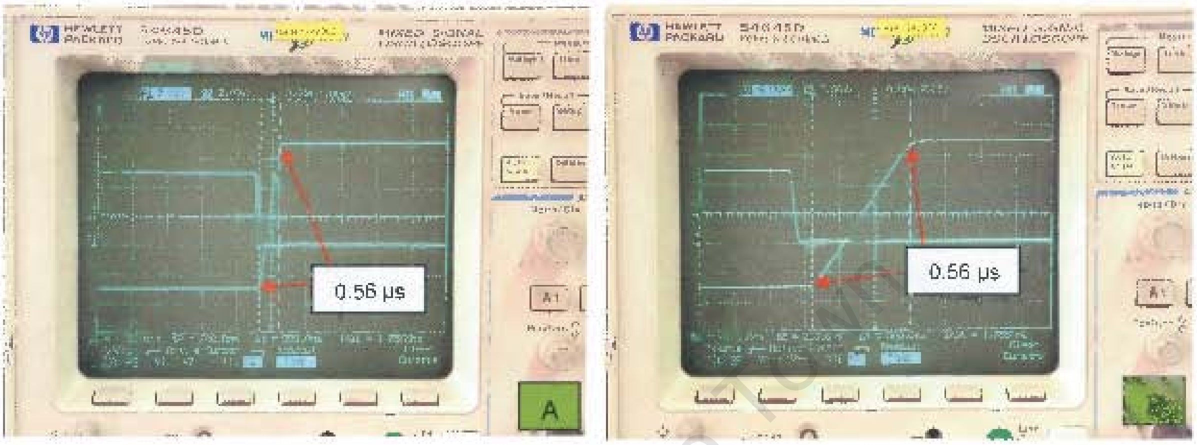

Figure 43: Test results showing the slew action of the signal conditioner with a constant current of 16 mA

The results of this experiment show clearly that the slew-rate response of the sensor-signal-conditioner setup was improved by increasing the current, which proves that the capacitive effect of the cables would be reduced when the sensor-excitation current is increased.

As expected, the rate of change in V_{CE} was much faster than in the case of a source current of 5 mA, confirming (and validating) the finding that this waveform was caused by the capacitance of the FET in combination with the capacitance of the oscilloscope probe. The slope rate was measured to be 20 V in 400 ns = 50 V/µs or 0.02 µs/V.

4.1.3.5. Signal Conditioner Response

Experiment: To determine the large signal response of only the signal conditioner, the test setup of Figure 39 was used, but the output from the signal conditioner was compared to the input to the signal conditioner. The graphical results are shown in Figure 44.

Figure 44B is a time-stretched-out version of Figure 44A to enable visualising clearly that the rising edge changed from -12 V to +12 V within 1.5 µs. To see the difference between the input and output signals, the one signal was offset manually with respect to the other. Notice that there is no visually detectable difference between the input and output signals. This means that a linearly varying large signal input that changes more slowly than a rate of 16 V/µs (or 0.0625 µs/V) will be reproduced without any distortion by the signal conditioner.

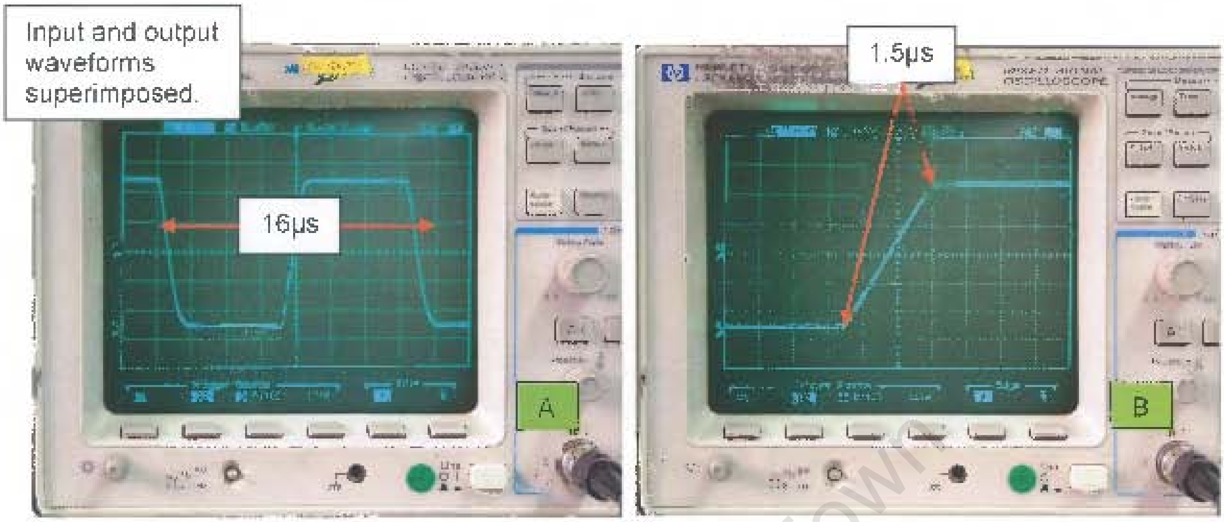

Figure 44: **Output signal compared to the input signal of the signal conditioner**

The small-signal response of the signal conditioner was tested using an altered version of the sensor-simulation circuit, as shown in Figure 45.

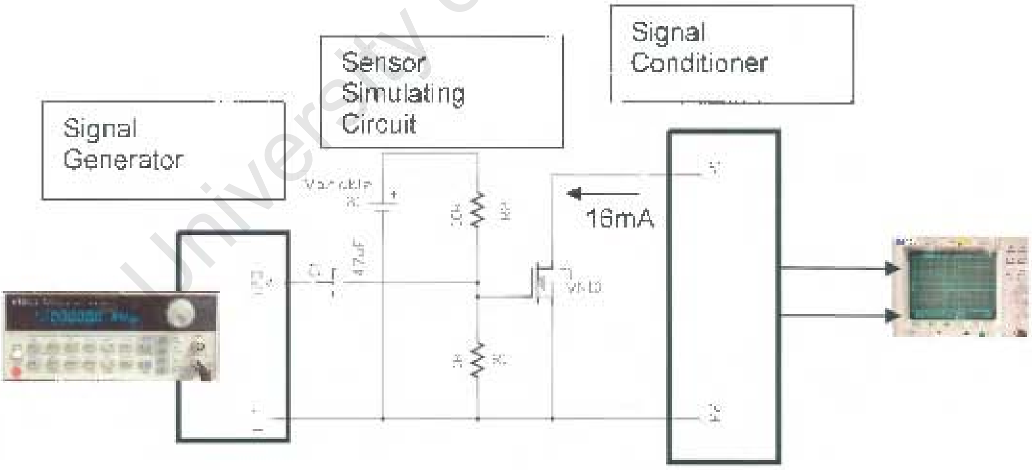

Figure 45: **Circuit for small-signal response testing**

The signal generator was adjusted to deliver a pre-programmed arbitrary signal with a fast rising edge, and an exponential decay. This signal represented a typical shock wave response. Unfortunately the capacitive properties of the sensor-simulating circuit changed this ideal waveform to a filtered version which had slower-changing properties. The input and output waveforms were compared, and shown in Figure 46A. The amplitude change from a maximum value to a minimum value, was 6 μs, (repetition period = 30 μs) which is equivalent to a shock pressure response in the far field. The output response was superimposed with the input waveform, and it can be seen that the result showed no visual difference.

A sine-wave of frequency close to 1 MHz (830 kHz) was measured in Figure 46B. The input to the signal conditioner and the output from the signal conditioner are superimposed in Figure 46B. It can be seen that a very slight phase difference was noted between input and output signals, but no amplitude difference was detected. This means that the signal conditioner performed very well with a 1 MHz signal.

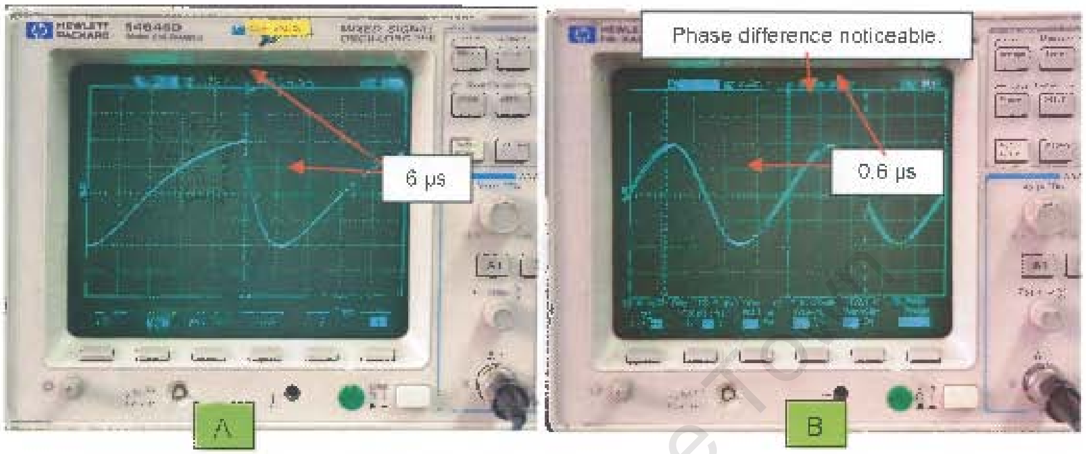

Figure 46: Comparison of the output response of the signal conditioner to an arbitrary asymmetrical input waveform, as well as a Sine waveform

The performance of the signal conditioner in response to the signal generated by an accelerometer was tested experimentally to verify the performance, and to predict what the outcome would be when an underwater explosion would not be directed exactly to the centre of the electronics enclosure. The accelerometer was fixed onto an Aluminium enclosure, offset to one side as shown in Figure 47.

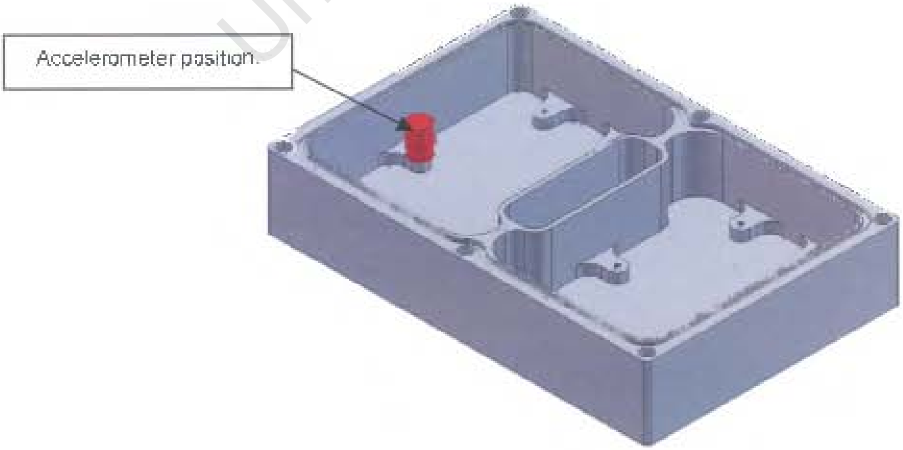

Figure 47: Accelerometer position in the Aluminium enclosure

The enclosure was accelerated using hammer impact (see Figure 48). Two points of impact were used, one directly adjacent to the point where the accelerometer was fixed for Event 1, and at the centre of the enclosure for Event 2. The acceleration measurement for Event 1 is shown in Figure 49, and the acceleration measurement for Event 2 is shown in Figure 51. Note that the acceleration for Event 1 started with a positive acceleration, as would be expected. The acceleration for Event 2 started with a negative acceleration, which did not amount to much before the value changed to a positive value. which was in the same amplitude region as for Event 1. This is because the hammer impact on the off-centre position of the enclosure caused the enclosure to have a slight rotational acceleration due to inertia, which was overcome and dominated by the overall acceleration caused by the direction of impact of the hammer.

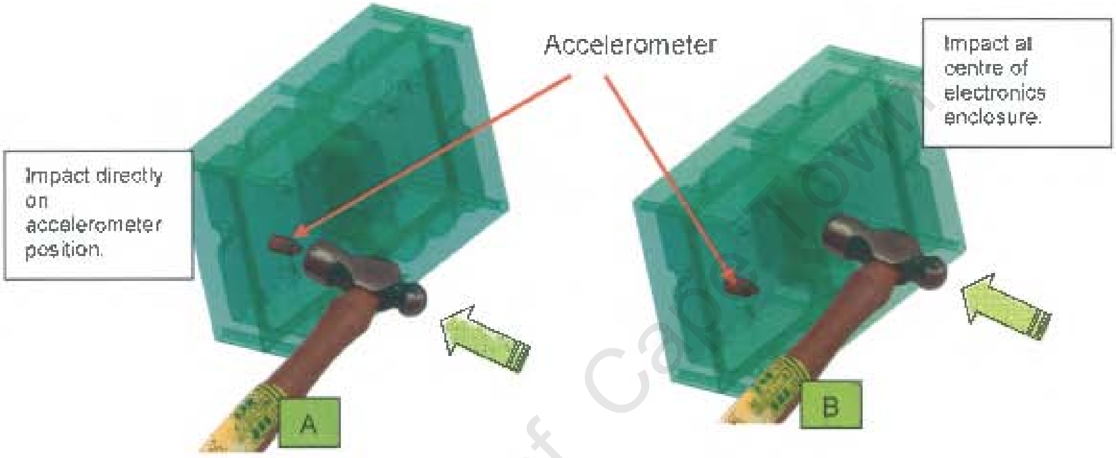

Figure 48: **Impact positions for Event 1 (A) and Event 2 (B)**

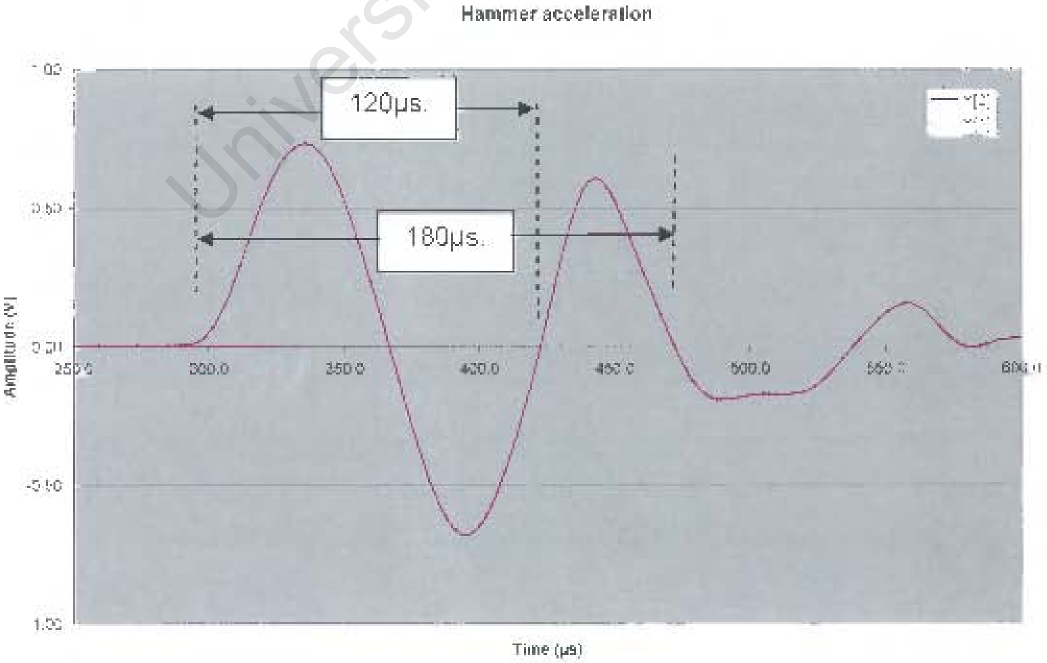

Figure 49: **Acceleration for Hammer event 1**

The oscilloscope recorded both the input and output of Event 1 to the signal conditioner as shown in Figure 50. These two signals were superimposed, with a very slight offset to show the two signals separately. Note that the waveforms of the two superimposed signals are exactly equal. This means that no distortion was added by the signal conditioner due to bandwidth limitations (low pass filtering effects). The recording equipment also recorded the measurement with no distortion, which means that the highest frequency component of the acceleration was unaffected by the measurement equipment. The conclusion can be drawn that the measurement equipment was adequate for measuring the acceleration which displays characteristics of the nature of this experiment.

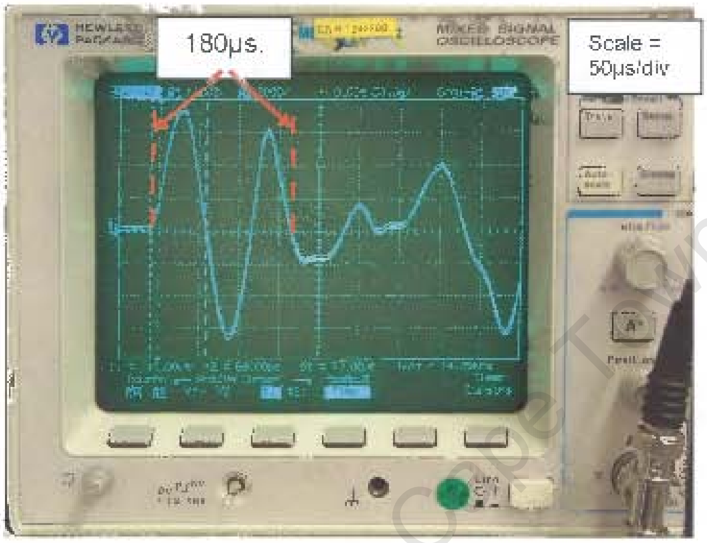

Figure 50: **The 100 MHz oscilloscope response to the input and output measurement of the hammer acceleration, Event 1**

Figure 51 shows the result of Event 2, where the impact was at the centre of the electronics container. Note that the first recorded impulse is negative, relative to Event 1. This means that the acceleration was in the opposite direction to the direct impact of Event 1, due to the swivel movement caused by an offset impact.

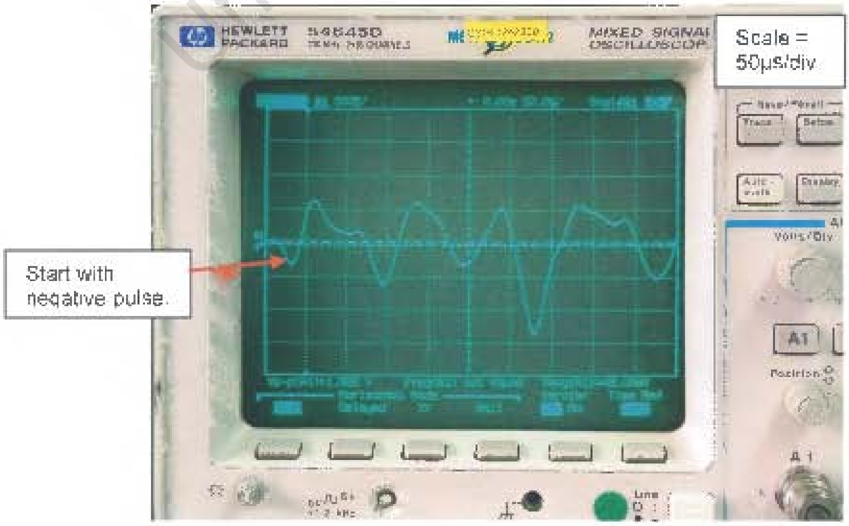

Figure 51: **Acceleration for Hammer event 2**

4.1.3.6. Validation of the measurement equipment

The conclusion that could be drawn from the foregoing empirical analysis was that the equipment that were selected for the experiments in Chapter 5 met the requirements of the expected signals that were to be measured: The bandwidth of the equipment matched the requirement of the expected signals, and the sampling rate of the DAQ equipment was adequate for the expected rate of change of the signals.

Chapter 5

5.1. MEASUREMENTS and ANALYSES

5.1.1. Experiment 1: Initial Experiment to determine general parameters

The previous chapter pointed out that acceleration is the phenomenon to be counteracted to ensure successful protection to electronics contained in a mechanical housing. It is thus obvious that acceleration measurements are to be taken and analysed in an attempt to find a solution to the problem.

From the calculations in the previous chapter, and Equation 28, it was clear that the solution concerning the required hardware would have to be some method of damping (shock acceleration filter), and that, if the correct damping could be found, the probability of damage would be minimised. The strategy that this experiment followed was to select any cost-effective damper, and to place 16 CCAs at various distances and orientations from a single blast (with and without damping for the purpose of comparison), and to analyse the results in terms of electronic damage.

The author of this dissertation had no previous experience of the measurement of underwater explosion effects, and an experiment was devised to produce initial (pre-measurement) information about the effects of underwater explosions on objects such as electronic containers in close proximity to a blast. Due to the author's inexperience, and considering the cost of sensors, it was advisable to perform the first experiment without instrumentation.

5.1.1.1. Purpose

This first experiment was aimed at gaining hands-on experience with respect to finding a convenient size of scaled explosive mass in relation to the wall thickness of the Enclosure at convenient scaled standoff distances. No sensors were used, due to the uncertain variables.

Further to the above purpose, additional investigations were done, e.g. to determine the effect of cost-effective damping methods on a CCA under blast conditions. This was a first-test ball-park estimation experiment and was intended to establish whether there was visible improvement when using standard dampers (e.g. grommets) as a mounting method, instead of a rigid mounting method.

The choice of "grommets" as a mounting method stems from the calculation (see paragraph on Acceleration and Displacement Prediction on page 46) that a relatively small (from 0.75 mm to 1.5 mm) displacement was predicted during the high damage-acceleration time. The method chosen for this experiment was to select Neoprene grommets as a mounting method for 50% of the CCAs, and no damping for the other 50% of the CCAs. Statistical information was not expected as an output of this experiment. Therefore the physical arrangement was to have both a "soft"-mounted as well as a rigid-mounted PCB in the same enclosure, and to subject it to exactly the same acceleration within practical limits.

It was acknowledged that, if positive results accumulated from this experiment, further experiments could be devised to confirm the findings statistically. Simulation would also be required to confirm the findings, and to quantify the damping constants of the mounting methods.

5.1.1.2. The UUT

The most cost-effective damping method seemed to be to use of "off the shelf" Neoprene grommets (see Figure 52).

Figure 52: Grommet mounting method

The electronics enclosures that were used for this experiment are shown in Figure 53. Two identical PCBs were mounted onto one side of the enclosure, and two identical PCBs were mounted to the other side of the enclosure. A CCA on each side made use of Neoprene grommet mountings (see Figure 52). The enclosure was closed up with the soft-mounted CCAs on the same side.

Figure 53: The electronics shown in an opened enclosure unit

Four of these enclosures (each containing four identical PCBs) were mounted at various distances from the charge. After the explosion, the enclosures were recovered, opened, and visual findings noted.

5.1.1.3. Component Choice

The components were chosen to represent a wide range of component types. Some were chosen to be small outline SM components which are predicted to withstand the shock environment better, and some were chosen to represent components which would most probably fail under shock conditions. These latter components typically were the white Burgess switches, the crystal, and the socket-mounted ICs. The component choice was varied to assist with the determination of a damage threshold.

It was expected that the ICs would not withstand the forces that are apparent in the accelerations near an explosion, and would be removed from the sockets. The removal of the ICs would probably dampen the effect of the shock, and it was expected that the ICs would still operate after the blast, if replaced in their original sockets.

It was also expected that the crystals would sustain internal damage to the extent that they would not operate, or they would operate at a different frequency.

It was expected that the military standard switches would withstand the shock environment much better than the commercial switches.

It was expected that the soft-mounted FETs and regulators would withstand the shock environment, due to the fact that the soldered wires would provide enough flexibility to absorb the shock effects.

It was expected that the LEDs would withstand the shock, due to their well-known rigid construction.

5.1.1.4. Physical Test Set-up

Four Aluminium enclosures, each containing four identical CCAs, were tied down with cable-ties on a relatively "soft" frame of PVC piping (see Figure 54).

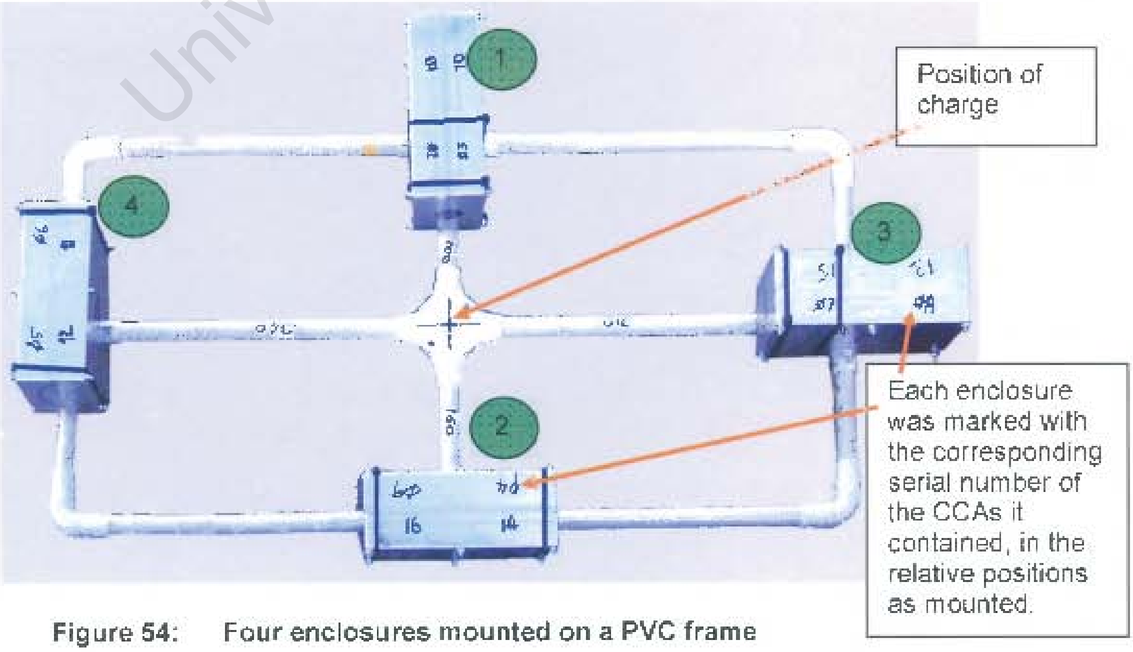

Figure 54: Four enclosures mounted on a PVC frame

A 29.2 gram Pentolite charge was placed at the centre of the frame (see Figure 55). Adding the detonator explosives, this totalled 30 gram of explosives.

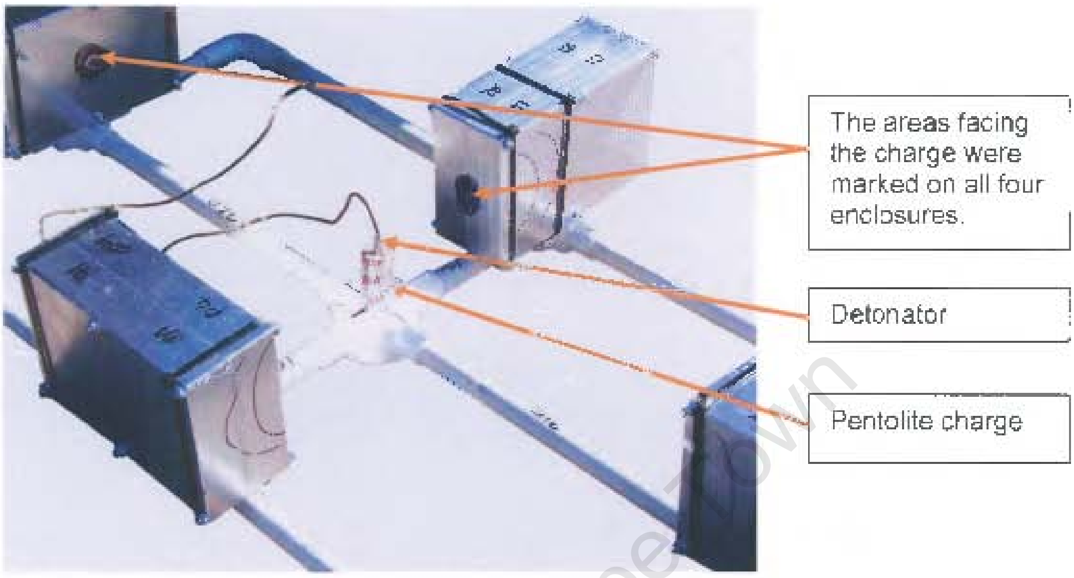

The areas facing the charge were marked on all four enclosures.

Detonator

Pentolite charge

Figure 55: **The position of the charge, relative to the enclosures**

The frame was then turned upside down, and suspended from a crane at a depth of 2 m (see Figure 56). The frame and enclosures were covered loosely with a net for easy recovery after the explosion.

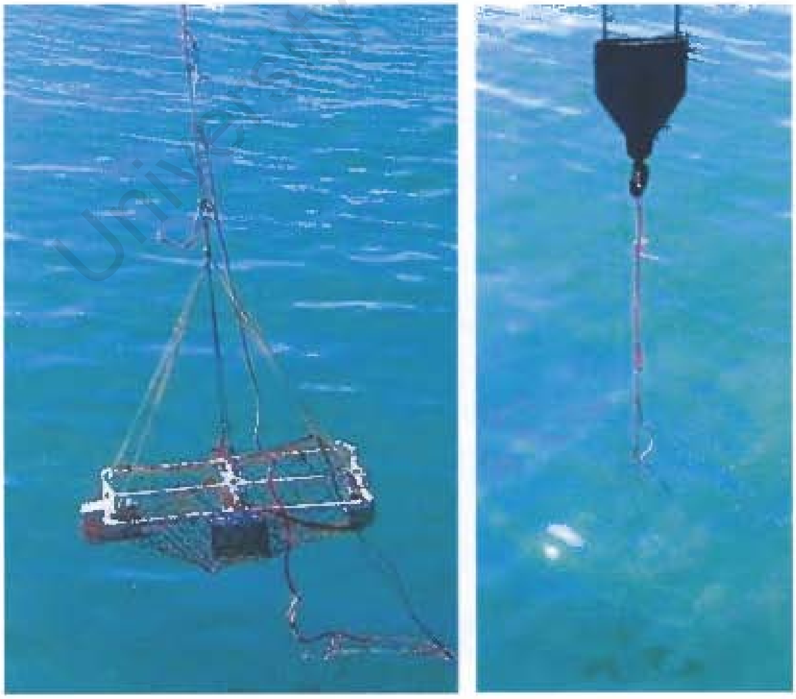

Figure 56: **The test setup suspended below the water surface, at a depth of 2 m**

The charge was then detonated from a safe distance and the four enclosures were recovered, still in the net. The frame was damaged beyond repair, as was expected.

5.1.1.5. Results and Analyses

The results are grouped into four sections, each relative to a specific distance from the blast. The closest electronics container was placed with its face 100 mm from the blast, and numbered enclosure 1. The furthest container was 360 mm from the blast, and numbered enclosure 4.

5.1.1.5.1. Enclosure No 1 at 100 mm from the blast

This container sustained fatal damage to that face which was closest to the blast (see Figure 57).

The PCBs contained within this housing, serial numbers 01, 02, 03 and 10, are shown in Figure 58. This housing was drenched in seawater as a result of the damage sustained on the mechanics, and the components were broken to the extent that the circuit had no chance of operation, and it served no purpose to re-test the circuits.

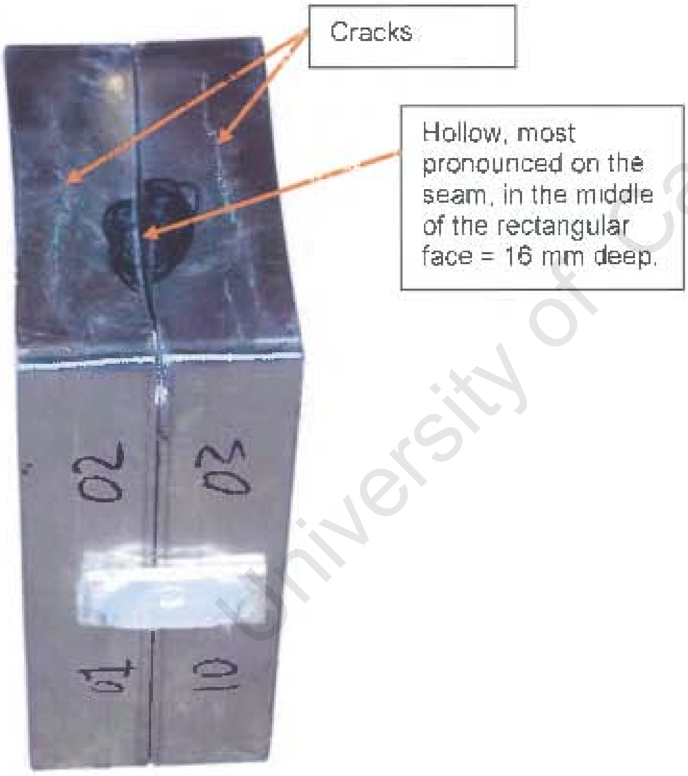

Figure 57: The housing with marked face closest to the blast at 100 mm

The peak pressure at the surface of this specific enclosure was calculated to be between 180 MPa and 200 MPa, according to calculations from Cole [5]. The standoff distance of 100 mm was less than 10 charge radii, and therefore the equations by Cole [5] would have been inaccurate, and the peak pressure predicted to actually be more than 200 MPa. Therefore this peak pressure equated to a 40 kg charge at a standoff distance of *less* than 1.15 m (which is closer than the target user requirement of 4 m or 22 charge radii).

An interesting observation was that the plastic deformation of the battery housing was in the opposite direction to the plastic deformation of the blast impact face (see Figure 57). This damage was caused by the fact that the enclosure movement was forced in one direction by the blast, and the battery housing inertia resisted the motion, causing a *relative* movement (with consequent plastic deformation) of the battery housing in the opposite direction. It is clear that the battery did not cause this battery-housing deformation, because both the opposing side walls were deformed approximately equally (see Table 3).

Table 3: **Deformation quantities of the battery housing**

Sidewall No	Deformation of top of the sidewall (in mm)
1	4
2	3.9
10	5
3	5.9

Table 4: **Deformation of the shock-loaded areas.**

Sidewall No	Deformation of the sidewall face (in mm)
2a	16
3a	15

The deformation illustrated that this phenomenon was in fact the primary cause of all electronic component breakages, and supported the hypothesis (in the relevant chapter on page 43) that high acceleration of the main object (housing) and the translation of the acceleration to the mechanical and electronic components, would be the primary cause of physical failure.

Mounted without grommets.

Note 1: Plastic deformation in different directions.

Mounted with grommets.

Note 2: Evidence of possible collateral damage, (components bend in unexpected direction), see Figure 61.

Figure 58: Damage to the electronics, 100 mm from the blast

In comparison to other results, it also supported (to a certain extent) the postulations on page 52 of this study, that there is a threshold below which no permanent deformation occurs. The inertia of a component (mass = inertia = resistance to movement) tends to force relative movement between the component and the PCB on which it is mounted, tearing it off from the PCB.

As a result of this observation, the solution would quite obviously be to use "soft" mounting methods for mounting those extremely inert components.

A conclusion that pertains to this specific container was drawn that none of the circuitry was expected to function, due to ingress of sea water, plus the fact that components were broken. Two types of switches were used, white (not MIL-STD, Burgess), and brown (MIL-STD, used in other military applications).

In both cases, the grommet-suspended PCBs were the closest to the explosion. It was therefore not possible, in this specific case, to conclude whether the grommets had the desired damping effect. When looking at the FETs driving the LEDs (see Figure 59) on PCB No.01, it is noticeable that the FETs are bent further than the FETs on PCB No.02, which was closer to the explosion. The grommet-suspended results gave plausible indication that the damping-effect was evident. The non-MIL-STD Burgess switches were damaged beyond repair, except in the cases where they were situated on the grommet-mounted PCB (see Figure 60 and Table 5). This was further evidence that the grommet-mounted PCBs had succeeded in damping the electronic components more effectively.

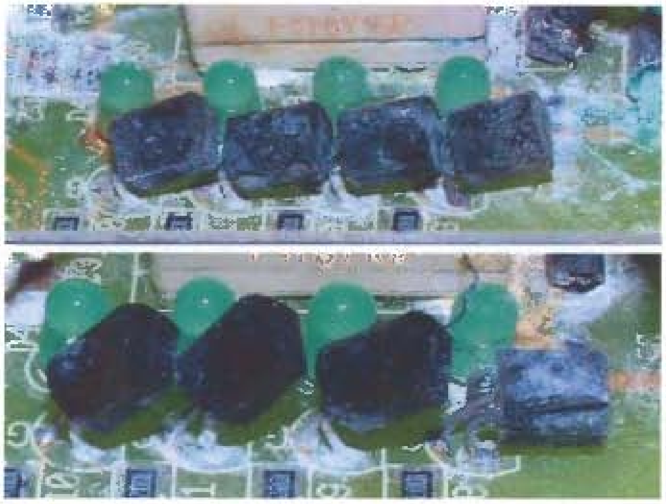

Card 01 furthest, but mounted without grommets.

Shock Direction

Card 02 nearest, but mounted with grommets.

Shock Direction

Figure 59: **Comparing shock acceleration on FETs at 100 mm from blast**

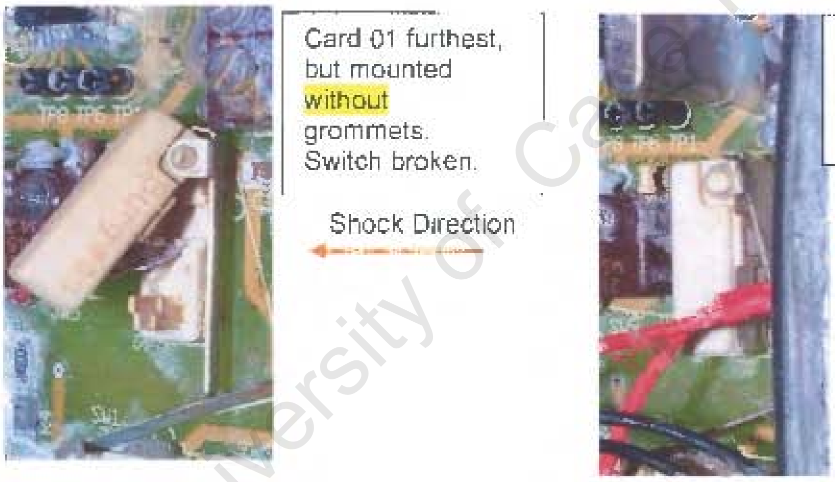

Card 01 furthest, but mounted without grommets. Switch broken.

Shock Direction

Card 02 nearest, but mounted with grommets. Switch in tact.

Shock Direction

Figure 60: **Comparing shock acceleration on switches at 100 mm from blast**

Table 5: **Damage to switches, side impact, 100 mm from blast**

Switch Type	Orientation 1	Orientation 2
Burgess Switches:	Narrow end towards explosion	Long end towards explosion
	4 visibly slightly broken (non-operational)	4 broken
Honeywell 21SX39-T Switches	1 visibly broken (3 were operational)	1 visibly broken (3 were operational)

A conclusion was drawn that the Honeywell MIL-STD switches withstood shock better than the commercial Burgess switches, as had been expected.

Table 6: Damage to general components, side impact, 100 mm from blast

General Components	Remarks
DIP Integrated Circuits	All DIP ICs were removed from the sockets
SM ICs	No SM ICs were removed from their soldered positions
Test Points	2x Test Points were removed from the PCBs

From Table 6, it was clear that more components sustained damage (for example the test points) than would be expected. This means that the standoff distance was too small.

Further Observations

There was evidence that collateral damage had been caused by the ICs which were removed from their sockets during the acceleration stages caused by the blast, and then impacted on components in the vicinity (see Figure 61). One LED and one FET was (most probably) struck by the accelerating IC. and bent in the opposite direction to what was expected. The LED that was struck by the IC was bent over and struck another LED, which then shattered (see Figure 61).

Figure 61: Collateral damage

5.1.1.5.2. Enclosure No 2 at 160 mm from the blast

This enclosure contained CCA numbers 04 and 09. The charge size was 30 gram. At a distance of 160 mm the peak pressure was predicted to be between 108 MPa and 115 MPa. This was equivalent to a charge size of 40 kg, at a standoff distance of 1.8 m.

This enclosure was mounted with its (electronic) most susceptible face towards the blast, with cards 04 and 09 closest to the blast within the container.

Cards 04 and 09

Figure 62 and Table 7 and Table 8 show the results of this experiment (160 mm from the blast).

Blast on bottom face of PCB

Figure 62: Cards 04 and 09 after the blast

Table 7: Faults on Card 04: Soft-mounted on grommets

Comp ID	Fault	Comments
C7. C13	Broken off from PCB (On Bottom of PCB)	SM capacitors on the face of the PCB nearest to the explosion. PCB moved away from capacitors.
SW5	Broken in half	Does not operate, but PCB connection still OK
ICs	Removed from the sockets	When replaced, the circuit was still operational, except for SW5.

Table 8: **Faults on Card 09: Hard mounted onto enclosure**

Comp ID	Fault	Comments
C14, C11, R14	Broken off from PCB (On Top of PCB)	SM capacitors and resistor on the face of the PCB furthest from the explosion. PCB whip-lashed.
C10, C13. C7, C6, C5	Broken off from PCB (On Bottom of PCB)	SM capacitors on the face of the PCB nearest to the explosion. PCB moved away from capacitors.
R19, R22, R16, R21, R24, R12, R23, R15	Broken off from PCB (On Bottom of PCB)	SM resistors on the face of the PCB nearest to the explosion, and mounted near mounting screw. PCB moved away from resistors.
ICs	Removed from the sockets	Circuit will not operate, due to SM components and switches broken or removed.
SW1, SW5, SW6, SW7	Broken	Beyond operation

These PCBs were the only instances in this experiment of the SM (surface mount) resistors and capacitors having broken away and being catapulted from their mounting positions. Although there was less damage to the soft-mounted PCBs, even they lost 2 components by this means, which meant that the Neoprene grommet solution was not ideal in this instance, in which the shock wave propagation direction was perpendicular to the PCB, and this stand-off distance was maintained. This gave cause for further investigation.

Figure 63: **Surface Mount capacitors broken away from their soldered positions**

A close-up photograph was taken of one specific PCB in which a SM capacitor was removed only partially from the PCB (see Figure 63).

Cards 14 and 16

The results for cards 14 and 16 are shown in Figure 64 and Table 9 and Table 10.


Blast onto top face (component side) of PCB

Figure 64: Cards 14 and 16 after the blast

Table 9: Faults on Card 14: Soft mounted on grommets

Comp ID	Fault	Comments
ICs	Removed from the sockets	When replaced, the circuit was still operational.
LEDs	One LED (red) was non-operational	When another LED was soldered in parallel to this LED, the circuit was again fully operational.

Table 10: Faults on Card 16: Hard mounted onto enclosure.

Comp ID	Fault	Comments
C4, C3, C11, R14	Broken off from PCB (On Top of PCB)	SM capacitors and resistor on the face of the PCB nearest to the explosion.
R20, R15	Broken off from PCB (On Bottom of PCB)	SM resistors on the face of the PCB furthest away from the explosion, and mounted near mounting screw.
ICs	Removed from the sockets	Circuit would not operate, due to SM components and switches broken or removed.
SW1, SW7	Broken	Commercial switches only, broken beyond operation

Further observations

The cards that were mounted with grommets sustained the least damage. In fact, when the ICs were replaced onto cards 04 and 14, (soft-mounted), both circuits operated correctly, except for the broken switch, SW5.

The hard-mounted card (09), sustained more damage: all four switches were broken, and a number of SM resistors and capacitors were removed from the PCB. The SM components which were removed were from both sides of the card. It is probable that the high perpendicular acceleration and deceleration that the card experienced during the shock period was adequate, due to inertia, to overcome the bond strength of the surface-mounted capacitors and resistors.

The shock was damped by the enclosure (as could be seen from the indentations on the battery compartments), and thus the other hard-mounted card (card 16) lost only 6 SM components, compared to card 09, which lost 16 SM components.

5.1.1.5.3. *Enclosure No 3 at 310 mm from the blast*

The charge size was 30 gram. At a distance of 310 mm the peak pressure was predicted to be between 51 MPa and 54 MPa. This was equivalent to a charge size of 40 kg, at a standoff distance of 3.4 m.

This enclosure was mounted with its (electronic) least susceptible side towards the blast, with cards 07 and 15 closest to the blast; see Figure 65 and Figure 66 as well as Table 11 to Table 14 for the results.

Cards 07 and 08

Figure 65: Cards 07 and 08 after the blast

Table 11: **Faults on Card 08: Soft mounted on grommets**

Comp ID	Fault	Comments
General	No faults	Complete circuit was operational.

Table 12: **Faults on Card 07: Hard mounted onto enclosure**

Comp ID	Fault	Comments
ICs	Only one (counter) IC removed from the socket	When IC was replaced, only the oscillator circuit was operational. The µP circuit was non-operational.
µP circuit	Does not operate	XTAL bent slightly towards the shock, uncertain if this is the cause of µP malfunction.

Cards 13 and 15

The results for cards 13 and 15 are shown in Figure 66, as well as in Table 13 and Table 14.

Figure 66: **Cards 13 and 15 after the blast**

Table 13: **Faults on Card 13: Soft mounted on grommets**

Comp ID	Fault	Comments
ICs	8-Pin IC was moved slightly, but still made contact.	The complete circuit was operational.

Table 14: Faults on Card 07: Hard mounted onto enclosure

Comp ID	Fault	Comments
ICs	Both ICs were removed.	After re-insertion of the ICs, the complete circuit was operational.

Further observation

All components were unbroken. Exception: card 07, which malfunctioned for some unknown reason. Further investigation is required to identify the cause.

5.1.1.5.4. Enclosure No. 4 at 360 mm from the blast

The charge size was 30 gram. At a distance of 360 mm (from Appendix 2) the peak pressure is calculated to be between 43 MPa and 46 MPa. This is equivalent to a charge size of 40 kg, at a stand-off distance of 4 m.

This enclosure was mounted with its (electronic) most susceptible face towards the blast and cards 11 and 12 were the closest to the blast, see Figure 67 and Figure 68, as well as Table 15 to Table 18 for the results.

Cards 11 and 12

Blast on bottom face of PCB.

Figure 67: Cards 11 and 12 after the blast

Table 15: Faults on Card 12: Soft mounted on grommets

Comp ID	Fault	Comments
General	No Faults	Circuit fully operational.

Table 16: Faults on Card 11: Hard mounted onto enclosure

Comp ID	Fault	Comments
ICs	Both ICs were removed.	When ICs were replaced, only the oscillator circuit was operational. The µP circuit was non-operational.

Cards 05 and 06

Figure 68: Cards 05 and 06 after the blast

Table 17: Faults on Card 05: Soft mounted on grommets

Comp ID	Fault	Comments
ICs	Both DIP ICs were removed.	After re-insertion of the ICs, the complete circuit was operational.

Table 18: Faults on Card 06: Hard mounted onto enclosure

Comp ID	Fault	Comments
ICs	Both DIP ICs were removed.	When ICs were replaced, only the oscillator circuit was operational. The µP circuit was non-operational.

Further Observation

After re-insertion of the ICs, both the soft-mounted PCBs were fully operational. Both the hard-mounted PCBs had faults on the µP circuitry, in that no function was detected.

5.1.1.6. Simulations

The result for Enclosure No. 1 as was reported on Page 82 and the result for Enclosure No.2 as was reported on Page 86, are summarised as follows:

1. The surface area that faced the shock loading at a standoff distance of 100 mm, suffered severe damage due to the enclosure being deformed into its plastic region. A "dent" was created on the said surface.
2. Enclosure No. 2 which was positioned at a standoff distance of 160 mm, did not display any visual deformation after blast loading.

These large variation in the results were unexpected and difficult to explain. Due to the difficulties of interpretation, Snyman [19] performed a simulation on Autodyne of the two instances discussed above.

Snyman [19] used Autodyne for simulation. He used the Euler solver for the water and explosive charge and the Lagrange solver for the Aluminium box. The mesh for the computation of the 100 mm and 310 mm standoff distance is shown in Figure 69.

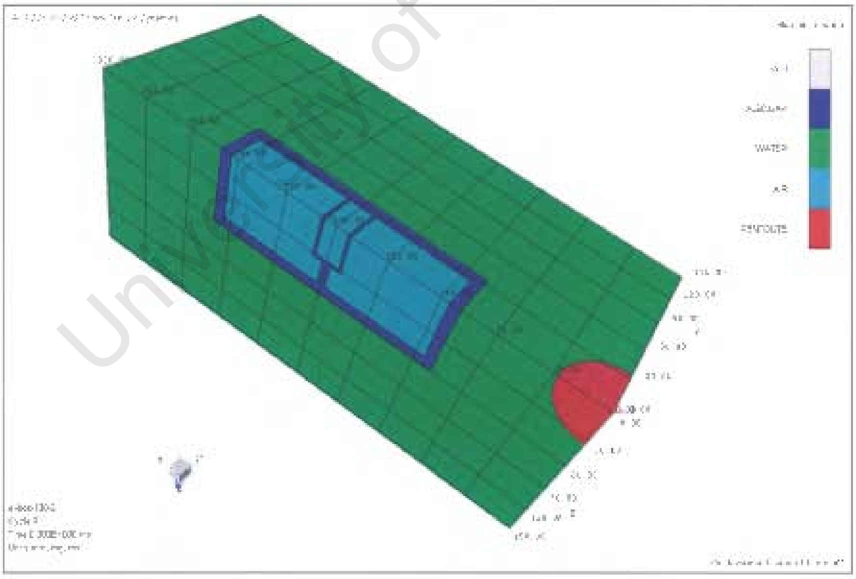

Figure 69: The computational model used for the 100 mm and 310 mm (courtesy of Snyman [19])

The result is shown in Figure 70. Visual inspection shows remarkable correlation of the permanent deformation, yet the depth of the "dent" was calculated by simulation to be 11.3 mm, which is below the measured depth of 16 mm. The deformation is therefore under-predicted by simulation.

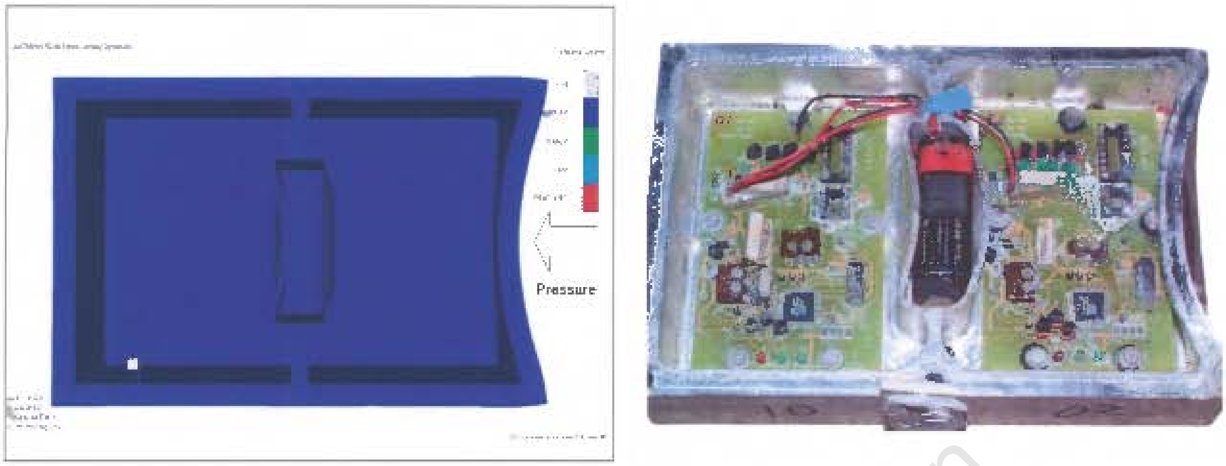

Figure 70: **Comparison of the simulation result with the empirical result of Enclosure No. 1 after shock loading**

The walls of the battery compartment were permanently deformed in the opposite direction due to inertia, which is demonstrated clearly in Figure 71, supplied by Snyman [19].

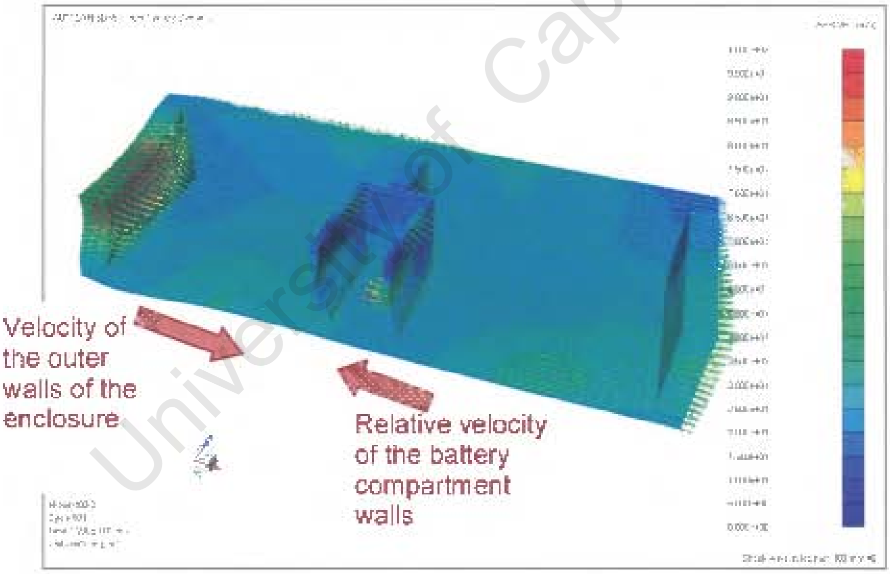

Figure 71: **The velocity distribution of the enclosure at 120 μs after the collision with the shock wave**

The simulation (of the blast using the enclosure which was positioned at 160 mm) showed negligible permanent deformation. This fact correlated well with the experimental result.

5.1.1.7. Conclusions

1. From the evidence produced by this experiment alone, it is clear that the soft-mounted PCBs survived the shock of the explosion better than the hard-mounted PCBs, although undue damage was still sustained. There is thus ample motivation for doing further investigations to improve and optimise the soft mounting method.
2. Simulation results with respect to permanent deformation of the enclosure showed remarkable correlation with the empirical result. The conclusion was that there was a threshold in the near field of the explosion where parameters of the blast phenomenon (which included the bubble and the temperature gradients) interacted non-linearly with the material of the structure to cause permanent deformation or rupturing.
3. A significant result is that of CCA numbers 04 and 09. It is clear that:
    a. The soft-mounted CCA sustained damage to the SM components on one side of the CCA only. This means that the acceleration of that CCA only just exceeded a damage threshold for SM components.
    b. The rigidly mounted CCA sustained SM damage to both the top and the bottom areas of the CCA. This means that the damage threshold was exceeded for SM components, both in the positive and negative halves of the acceleration curve. Although the acceleration is not known at this stage, this evidence supports the postulation of this study.
4. The soft-mounted PCBs that were positioned in enclosures further away from the explosion survived the shock better than the soft-mounted PCBs closer to the shock, as expected.
5. On the evidence that only two SM components were removed, and one switch broken at the experimented 160 mm stand-off distance (card 04), it is concluded that it is quite possible to harden electronics against shock caused by a 40 kg charge and at the required stand-off distance of 2 m, which produced the same amount of shock as in the case of card 04. The condition for this finding is that the "soft" electronic components that are prone to damage, and which have been included to find the damage threshold, should be hardened by replacement with either surface mounted components, or design changes should include other components which would withstand the shock loading.
6. When comparing enclosures 2 and 4 (see Figure 54), in both of which the most susceptible axis of the PCBs were facing the blast, it was found that the soft-mounted PCBs contained in enclosure 2 sustained damage whilst the soft-mounted PCBs in enclosure 4 sustained no damage. This supports the postulation as described on page 52.
7. On the evidence from the SM components that were dislodged from the PCBs (cards 04 and 09), it was concluded that the grommets used in this experiment, were too hard. It seems as if a softer compound grommet or softer mounting of another material is required, with enough translation potential, to protect components against tearing from the PCB in the most susceptible axis.
8. The ICs mounted in sockets have shown a larger degree of rigidity than expected. In 7 instances, the ICs were still positioned in the sockets.

9. No conclusion could be drawn concerning the crystals, due to the impossibility of examining them internally. The evidence revealed that only two crystals were dislodged from the PCBs, which is much better than expected. However, 3 µP circuits were not able to function, for no apparent physical reason. The faulty crystals may or may not be the cause of dysfunction. Further investigation is required.
10. The MIL-STD switches withstood the shock environment much better than the commercial switches, as expected.
11. The plastic FETs and regulators as mounted freely on the three wire terminals withstood the shock environments, as expected.
12. One LED failed, which, due to the proven reliability of this type of component, was not expected.

5.1.2. Experiment 2: First experiment which included Accelerometers and Pressure Sensors

5.1.2.1. Purpose

The purpose of this specific experiment was to measure the acceleration of the enclosure when it was subjected to blast loading, and at the same time to measure the acceleration of the contained CCA, which was mounted on grommets. The acceleration attenuation was to be calculated and a conclusion drawn concerning the efficacy of the grommets for safeguarding the electronic components against failure due to acceleration effects. The experiment made use of a scaled blast, using a 30 gm charge, and a typical stand-off distance of 750 mm.

5.1.2.2. Equipment

A bought-in signal conditioner was used in conjunction with all four sensors. The equipment list was as follows:

a. PXI computer with a fast independent four-channel A/D conversion card with interface connection box.

b. Custom detonator-computer synchronisation box.

c. 1x Tourmaline blast pressure sensor with sensitivity 0.5 mV/psi, with a 20-m low noise cable.

d. 1x Tourmaline blast pressure sensor with sensitivity 0.1 mV/psi, with a 20-m low noise cable.

e. 2x PCB accelerometers with identical specifications, with 20-m low noise cables.

f. Mounting frame and cables.

g. 100 MHz Storage Oscilloscope for measuring the synchronisation pulse.

5.1.2.3. Sensor Mounting Arrangement

The two accelerometers were mounted inside the electronics container (Figure 72).

Four identical CCAs were used in one enclosure. Two CCAs were mounted onto one side of the enclosure, and two CCAs were mounted to the other side of the enclosure. Neoprene grommet mountings were used for one of the CCAs on half of each enclosure. The other two CCAs were mounted firmly onto the Aluminium casing. The enclosure was closed up in such a manner that the soft-mounted PCBs were opposite each other (see Figure 72).

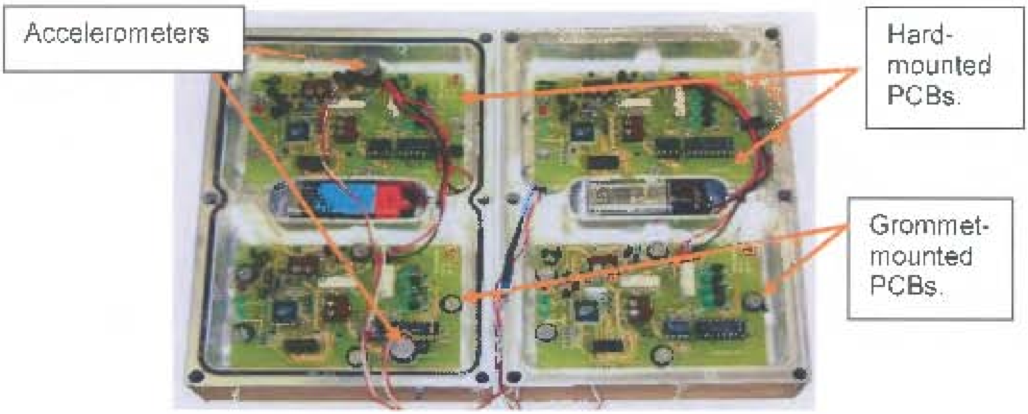

Figure 72: **Accelerometer mounting positions in the enclosure**

One of the two identical accelerometers was mounted firmly onto the container through the PCB, with a fastening torque of 1 Nm. The other accelerometer was mounted onto the PCB (using a nut to fasten the accelerometer) of a grommet-mounted CCA, with a torque of 1 Nm. The orientations of both sensors were such as to produce a positive voltage when the direction of the acceleration was in the direction of the movement of the shock wave. This catered for a shock wave direction as indicated in Figure 73.

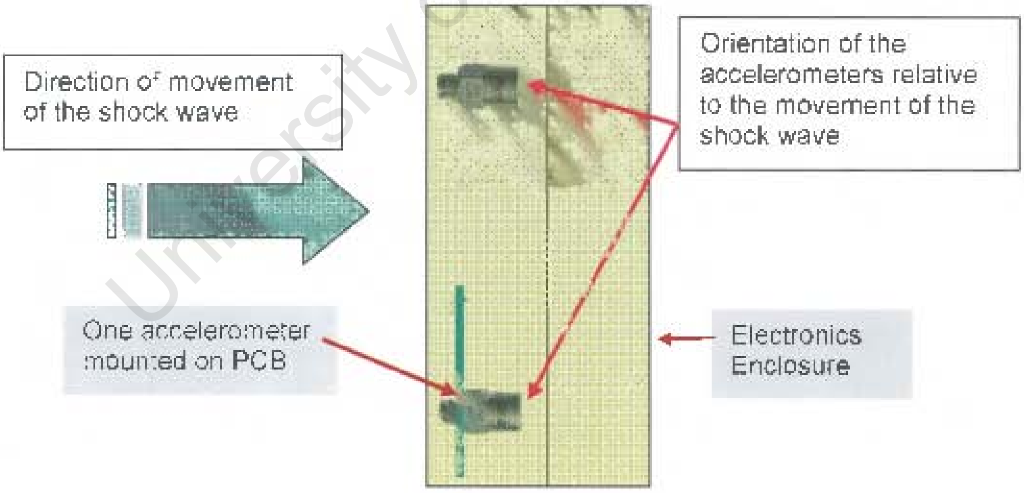

Figure 73: **Accelerometer orientation relative to the direction of the shock wave's movement**

The electronics enclosure containing the accelerometers was mounted onto a collapsible PVC frame. The shock pressure sensors were mounted onto the frame in such a manner that the shock wave would reach the enclosure before it reached the sensors, but also in such a manner that reflections from the enclosure could not interfere with the pressure measurements (see Figure 74).

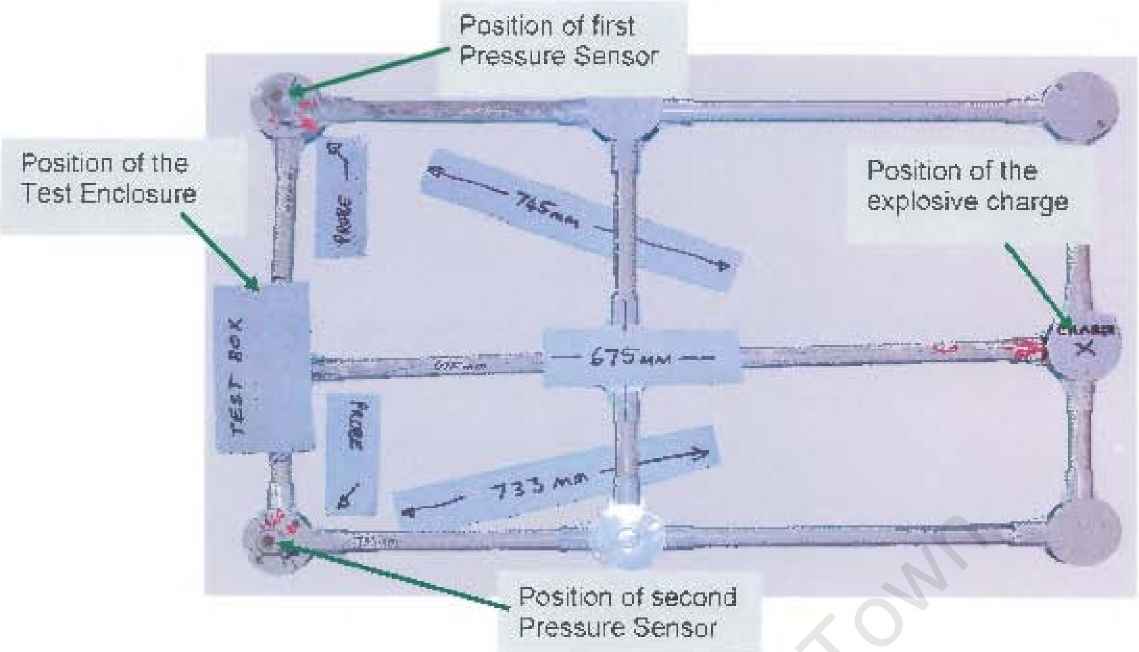

Figure 74: **Illustration of the frame, showing the mounting positions of the sensors, test Enclosure, and the explosive charge**

The sensors were not mounted symmetrically, in order to measure the propagation velocity, and verify this information with the theory.

5.1.2.4. Custom Synchronization Equipment

The custom firing and synchronisation equipment (Figure 75) used in the previous experiment (page 78), was used unmodified in conjunction with the IMPI military firing unit. The synchronisation equipment senses the positive rising edge of the current passing through the detonator. This produces a TTL-compatible signal with which the PXI computer synchronises the measurement period of 1 second to capture the complete blast event. Various tests were conducted to ensure that the synchronisation equipment was functional.

Figure 75: **The Custom Synchronisation Unit**

5.1.2.5. Physical Test Set-up

One Aluminium enclosure containing four identical PCBs was tied down with cable-ties on a relatively "soft" frame of PVC piping (see Figure 76).

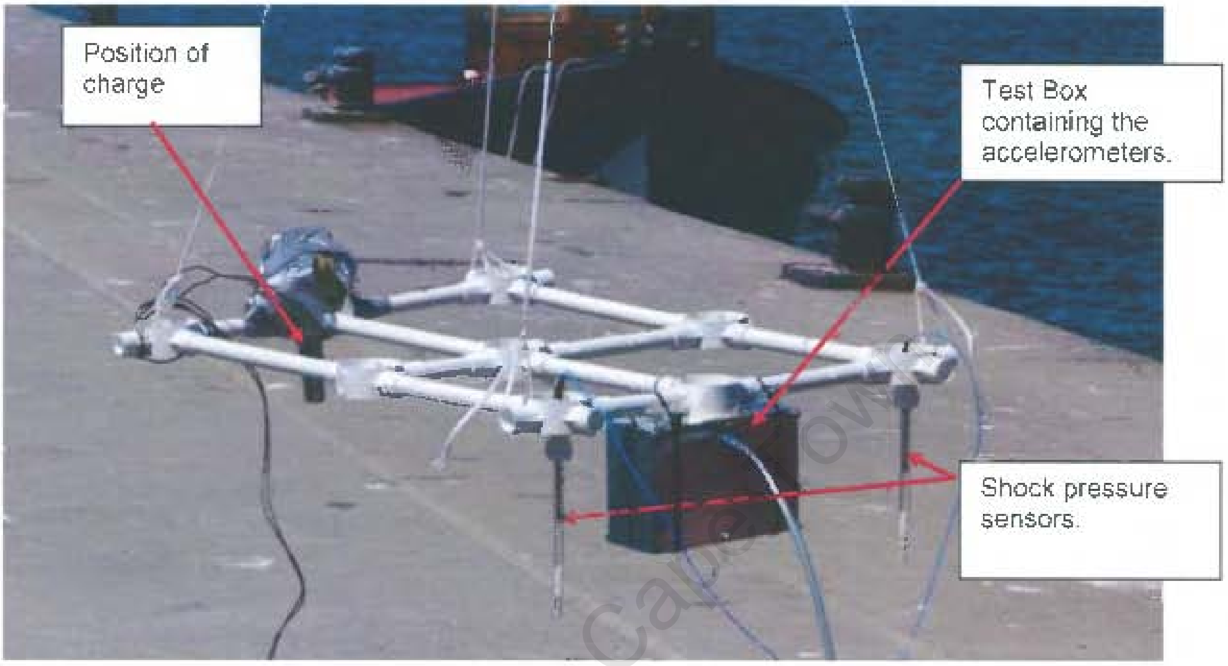

Figure 76: **The enclosure mounted on a PVC frame with the charge and sensors in position**

A 29.2 gram Pentolite charge was placed at the indicated position on the frame. With the detonator explosives added to the Pentolite charge, the total charge weight was 30 gram.

The frame was then turned upside down, suspended from a crane (see Figure 77) and lowered to a depth of 2 m below the surface of the water. The enclosure was covered loosely with a net for easy recovery after the explosion.

A period of two minutes was allowed for the sensors to settle, to obtain a steady state for the test setup below the water. Continuity between the signal conditioner and the sensors was checked.

The charge was then detonated from a safe distance, and the enclosure plus sensors were recovered. The frame was damaged beyond repair, as expected, but the sensors and wires were 100% intact.

It was expected that the impact of the shock on the frame would have an effect on the measurement of accelerations, because the electronics enclosure was not completely isolated from the frame. It was fastened by cable ties, and nested on sponge rubber. The effect was expected to be insignificant due to the fact that it would occur before the shock wave arrived at the enclosure. Sound travels faster in materials of higher density, thus the shock travelling through the frame, would reach the electronics enclosure before the shock wave travelling route through the water.

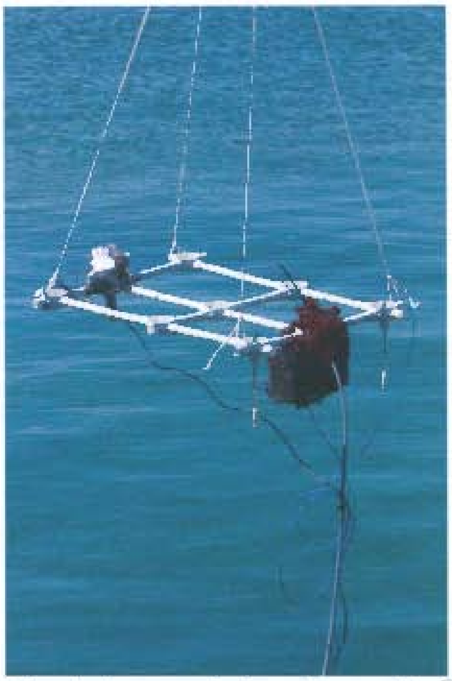

Figure 77: **The test setup being lowered to below the surface of the water, to a depth of 2 m**

5.1.2.6. Results and Analyses

5.1.2.6.1. Damage Assessment

The test box was opened after the first blast, and the CCAs were tested. The results are given in Table 19 and Figure 78.

Table 19: **CCA test results after Event 01**

CCA number	Remarks
No 05 (Soft mounts)	The microprocessor circuitry was faulty. All other components were unaffected, and the ICs were still in the sockets.
No 06	The microprocessor circuitry did not function. One IC was removed from its socket, whilst the other IC was still in its socket. All other components were unaffected. When the loose IC was replaced, the circuit that it was part of was operational.
No 11	Both socket-mounted ICs were displaced from the sockets. When they were replaced into their sockets, the complete circuit, including the microprocessor, was operational.
No 12 (Soft mounts)	All ICs were intact in the sockets, and the full circuit was operational.

Notes: From the results of the previous experiment (page 78), it was found that the microprocessor crystals of CCAs 11 and 06 were faulty. These crystals were replaced after the experiment, using a strain-relief technique. The original crystals of CCAs 05 and 12 were kept unchanged for this experiment, and the traditional mounting technique was used. After this experiment, both the crystals of CCA numbers 05 and 06 were faulty. After replacement of the crystals, all circuits were again fully functional. No conclusion with respect to the crystal mounting method is possible from this result, because one traditional and one strain-relieved crystal were faulty. Both the crystals of the CCAs which were mounted closer to the explosion, were affected adversely.

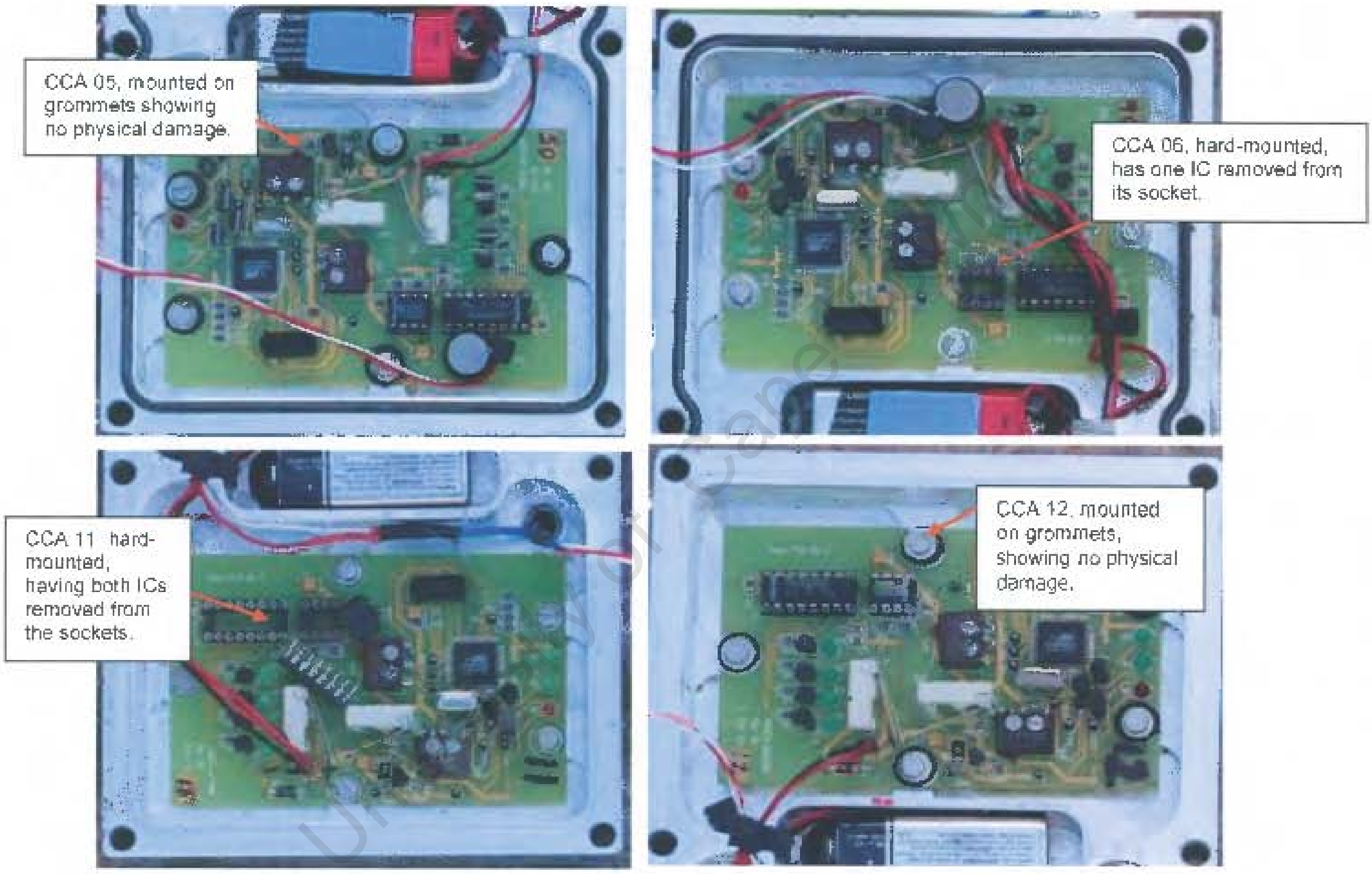

CCA 05, mounted on grommets showing no physical damage.

CCA 06, hard-mounted, has one IC removed from its socket.

CCA 11 hard-mounted, having both ICs removed from the sockets.

CCA 12, mounted on grommets, showing no physical damage.

Figure 78: The four CCAs after Event 01

Field replacement of the crystals was not possible. Only the ICs were replaced into their sockets, and the enclosure was again assembled for the second test. It was noticed that the IC insertion was not met with the regular physical resistance, indicating that less force would be required to extract the ICs under shock conditions. This was due to the numerous times (wear on the pins and sockets) that the ICs were replaced, while using the same components that were in the sockets on previous occasions.

A second blast was obtained with the same setup as for Blast 1, to obtain comparative data. The second blast results are shown in Figure 79 and Table 20.

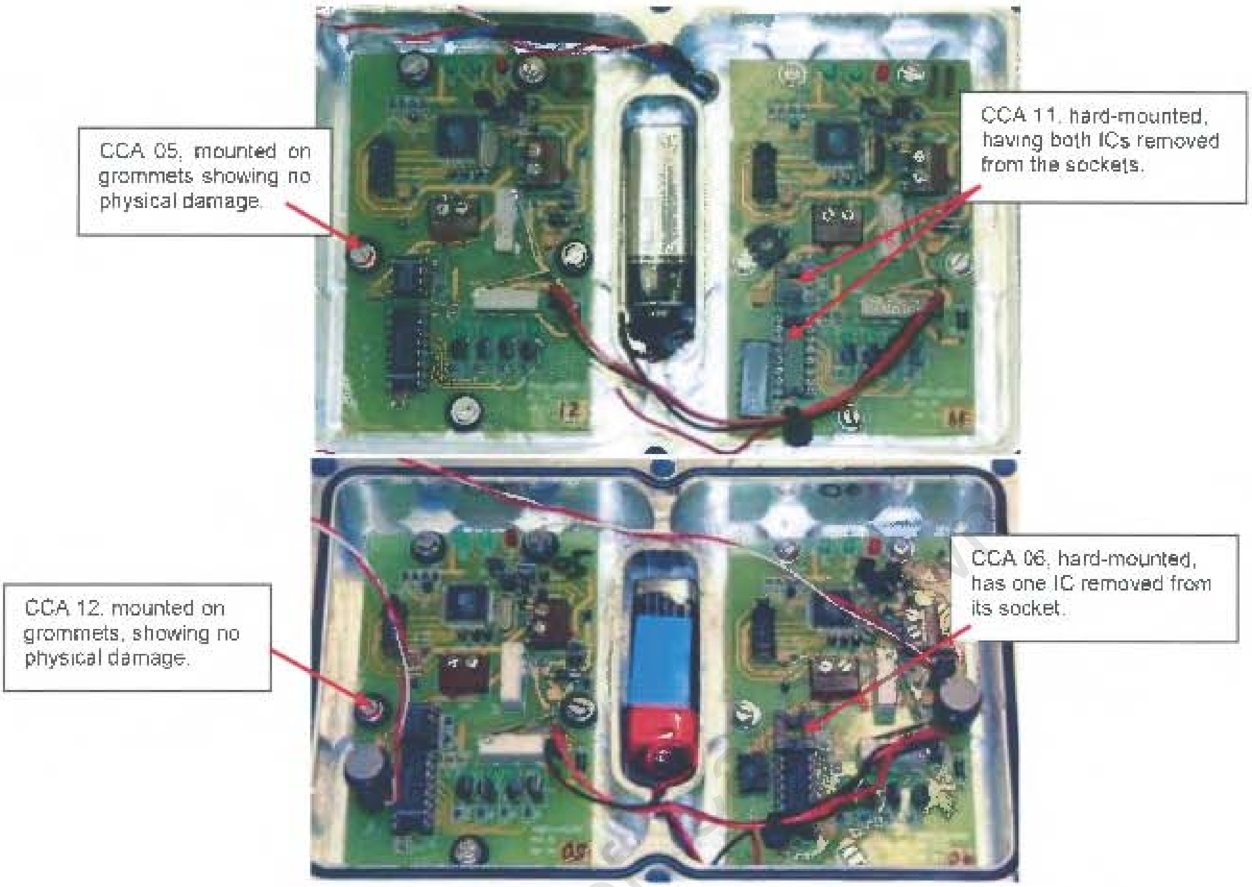

CCA 05, mounted on grommets showing no physical damage.

CCA 11, hard-mounted, having both ICs removed from the sockets.

CCA 12, mounted on grommets, showing no physical damage.

CCA 06, hard-mounted, has one IC removed from its socket.

Figure 79: The CCAs after Event 02

Table 20: CCA test results after Event 02

CCA number	Remarks
No 05 (Soft mounts)	The microprocessor circuitry was faulty (un-repaired from Event 01). All other components were unaffected, and the ICs were still in the sockets.
No 06	The microprocessor circuitry did not function (un-repaired from Event 01). One IC was removed from its socket, whilst the other IC was still in its socket. All other components were unaffected. When the loose IC was replaced, the circuit that it formed part of was operational.
No 11	Both socket-mounted ICs were displaced from the sockets. When they were replaced into their sockets, the complete circuit, including the microprocessor, was operational.
No 12 (Soft mounts)	All ICs were intact in the sockets, and the full circuit was operational.

The above result is exactly the same as for Event 01.

5.1.2.6.2. Measurement Results

5.1.2.6.3. Acceleration Measurements during Event 1

Accelerometer 1 was mounted on the PCB, and Accelerometer 2 was mounted on the enclosure. As can be seen in Figure 80, the resultant output of Accelerometer 1 is an amplitude-reduced, phase-shifted response relative to Accelerometer 2. Compare this result with the simulated result from the report [1] in Figure 81 and Figure 84. From this result, the empirical damping factor can now be determined, if required for further simulation.

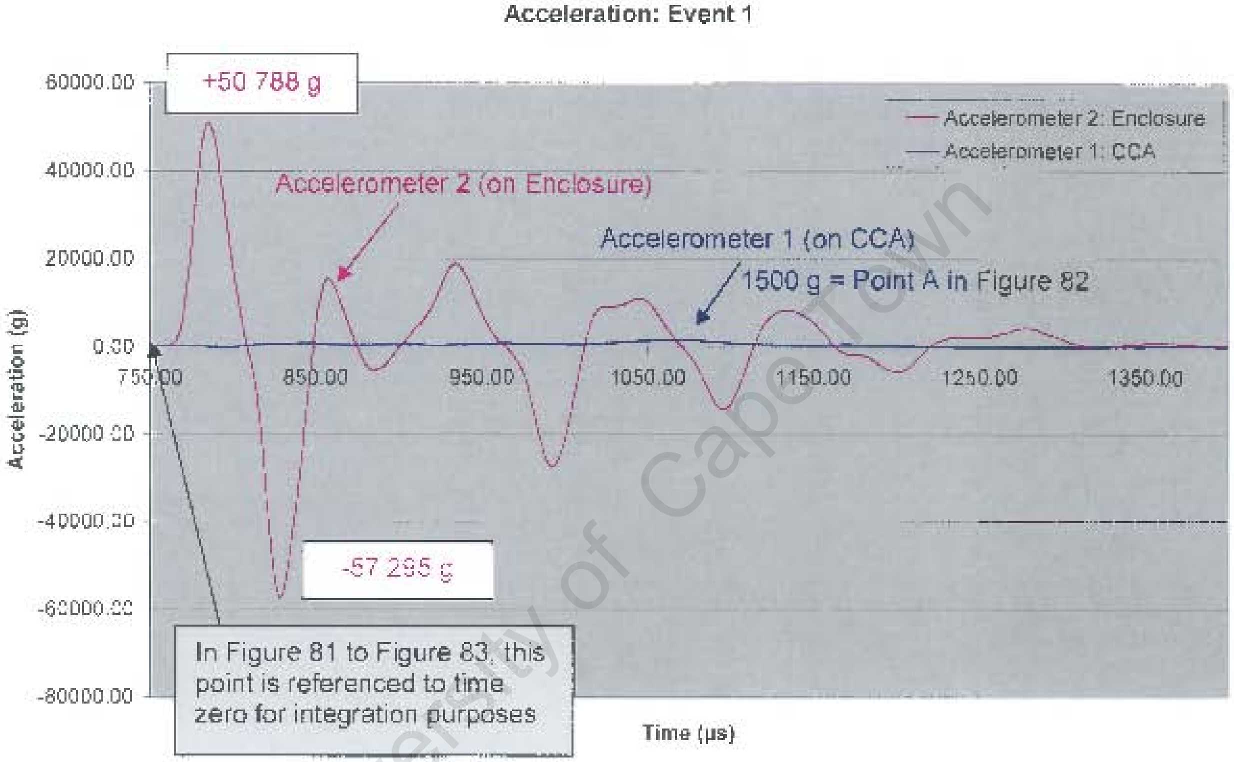

Figure 80: **Acceleration results for both sensors for Event 01, over the first 140 µs after the shock wave collision**

5.1.2.6.4. Object motion during Event 1

Enclosure motion, Event 1:

The acceleration of the electronics container that was measured during Event 1 (Figure 80) was double-integrated to find the displacement of the container. The result on getting rid of the integration constants is shown in Figure 81. This result showed that the displacement as a consequence of the shock wave collision with the Enclosure occurred approximately 1 mm after 1 ms.

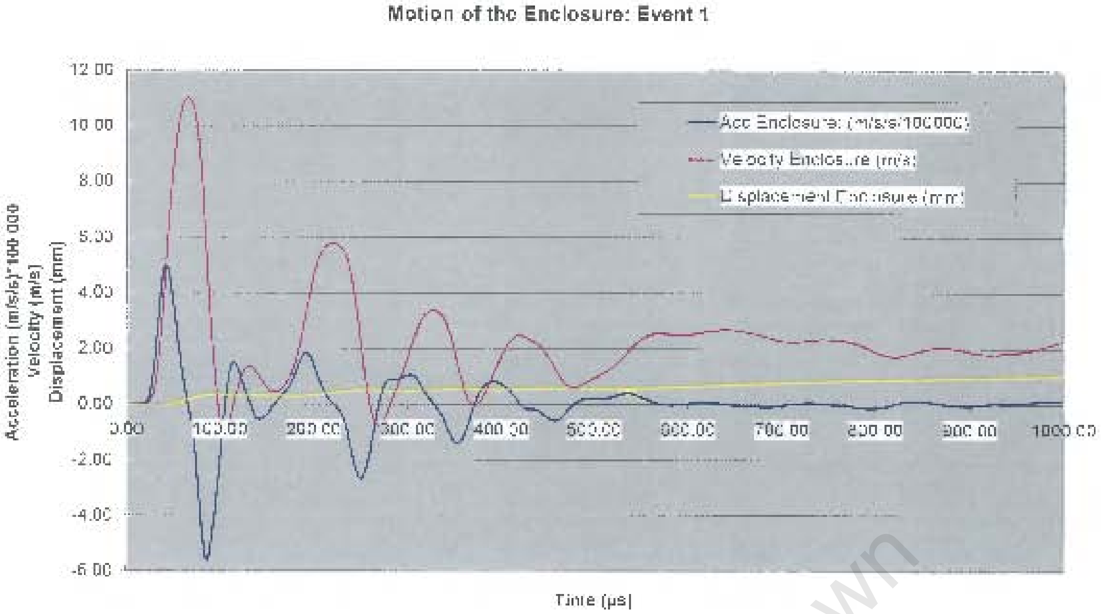

Figure 81: **Double integration of the acceleration of the electronics container, producing the displacement of the container during Event 1 over the first 1 ms period**

CCA motion, Event 1:

The double integration process applied to the acceleration of the CCA produced the motion result depicted in Figure 82.

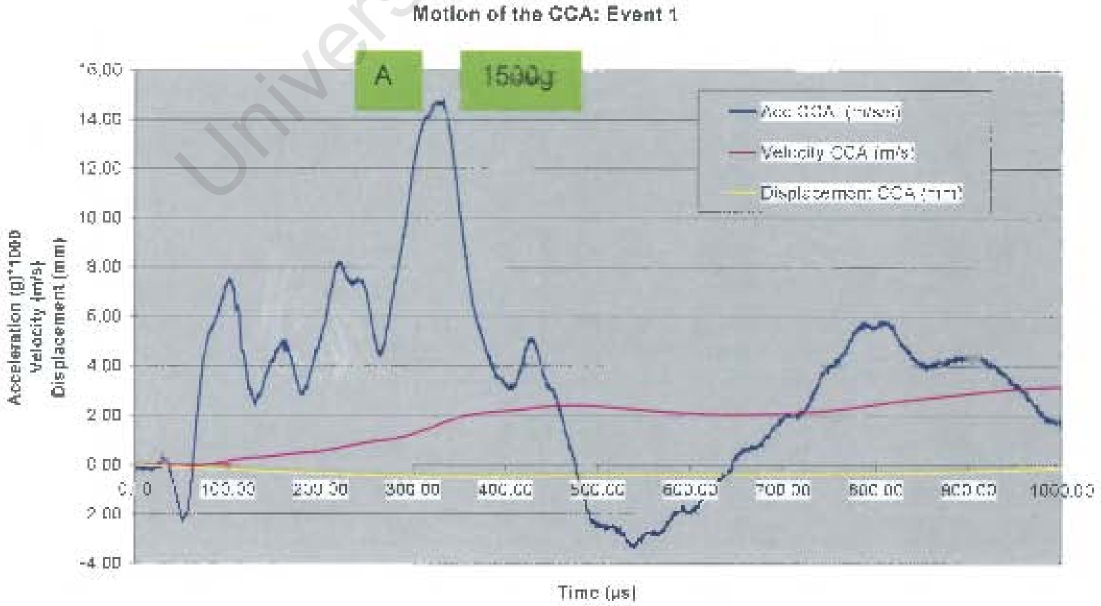

Figure 82: **Double integration of the acceleration of the electronics CCA, producing the displacement of the CCA during Event 1 over the first 1 ms period**

Over the first 1 ms after the shock wave collision with the Enclosure, the displacement was negative, due to the negative acceleration during the first 50 µs. The velocity was also negative (relatively small amount), causing the displacement to be negative. On face value, it would be expected that the acceleration of the CCA would start with a similar polarity to the acceleration of the Enclosure. However, if the shock front collided with the Enclosure at an angle slightly offset from zero degrees, a swivelling effect would be experienced by the Enclosure.

The two accelerometers were offset by approximately 50 mm on the horizontal plane, and this had the result that the offset shock front changed the polarity of the offset accelerometer. This effect was also demonstrated in Figure 51 in which a laboratory setup with a hammer providing the acceleration is shown. The inertia of the Enclosure (approximately 2 kg) caused the relatively long time delay to obtaining a positive displacement.

Relative Displacement, Event 1:

The relative displacement between the Enclosure and the CCA over a period of 16 ms is shown in Figure 83. The fact that the shock front collided with the Enclosure at a slightly offset angle caused the large relative displacement between the Enclosure and the CCA (4.1 mm – see yellow curve in Figure 83).

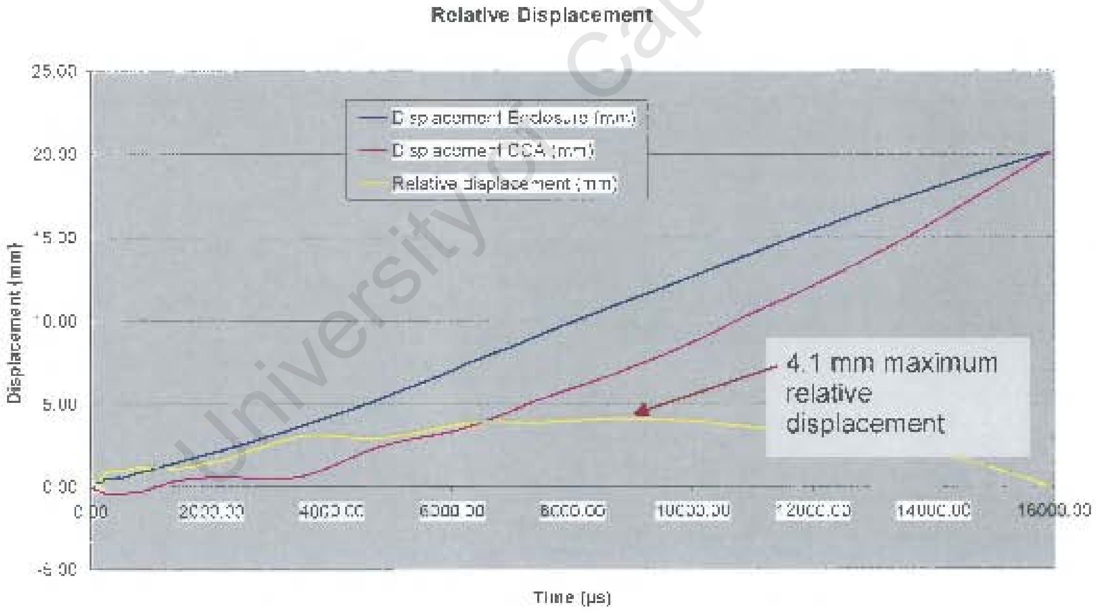

Figure 83: **The relative displacement of the Electronics Container, relative to the CCA, using grommet suspension during Event 1 over the first 1 ms period**

5.1.2.6.5. Acceleration Measurements during Event 2

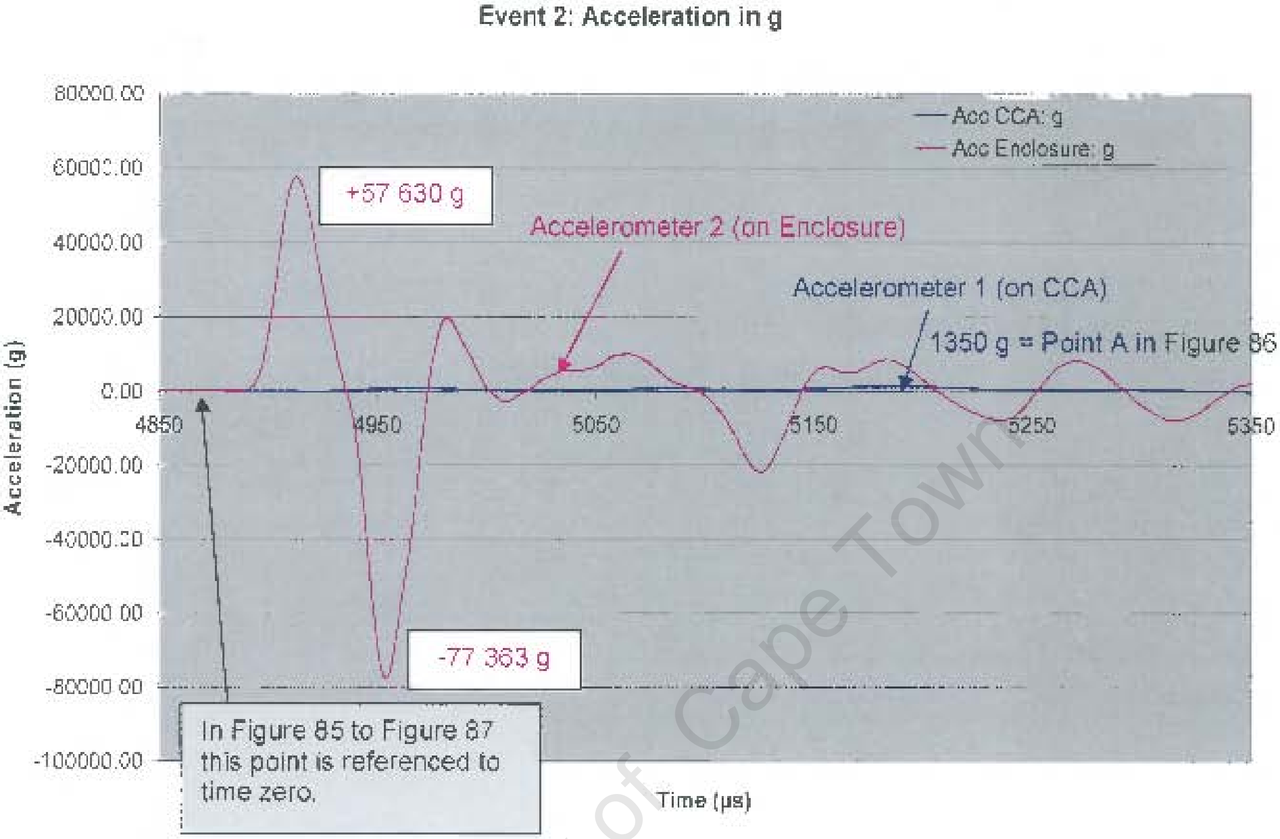

Figure 84: **Acceleration results for both sensors for Event 2 over the first 140 μs after the shock wave collision**

5.1.2.6.6. Object motion during Event 2

Enclosure Motion, Event 2:

The acceleration that was measured on the CCA during Event 2 (Figure 85) was double-integrated to find the displacement of the CCA. The result obtained after elimination of the integration constants is shown in Figure 85. This result shows that the displacement as a consequence of the shockwave collision with the Enclosure, which was passed onto the CCA, occurred approximately 0.5 mm after 1 ms.

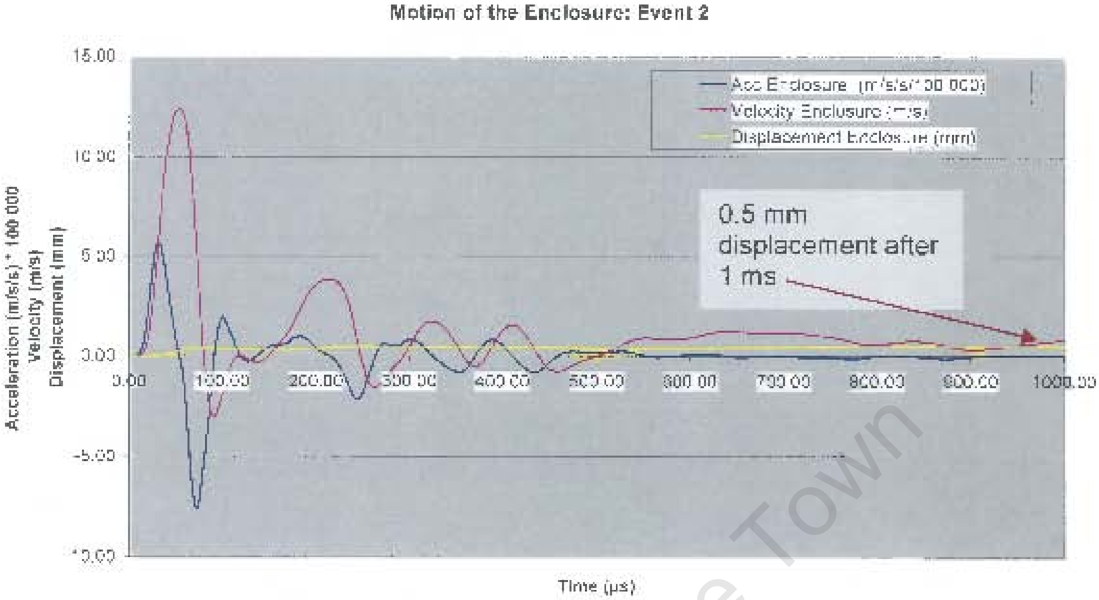

Figure 85: **Double integration of the acceleration of the electronics container, producing the displacement of the container during Event 2 over the first 1 ms period**

CCA motion, Event 2:

The double integration process applied to the acceleration of the CCA produced the motion result as shown by Figure 86.

Over the first 1 ms after the shock wave collision with the Enclosure, the displacement of the CCA was negative, due to the negative acceleration during the first 50 µs. The velocity was also negative (relatively small amount) causing the displacement to be negative. Similar to Event 1, the shock wave incident angle was slightly off-zero with the result that a swiveling effect was most probably experienced by the Enclosure.

The two accelerometers were offset on the horizontal plane by approximately 50 mm, and the offset shock front consequently changed the polarity of the offset accelerometer. The inertia of the Enclosure (approximately 2 kg) caused the relatively long time delay in obtaining a positive displacement.

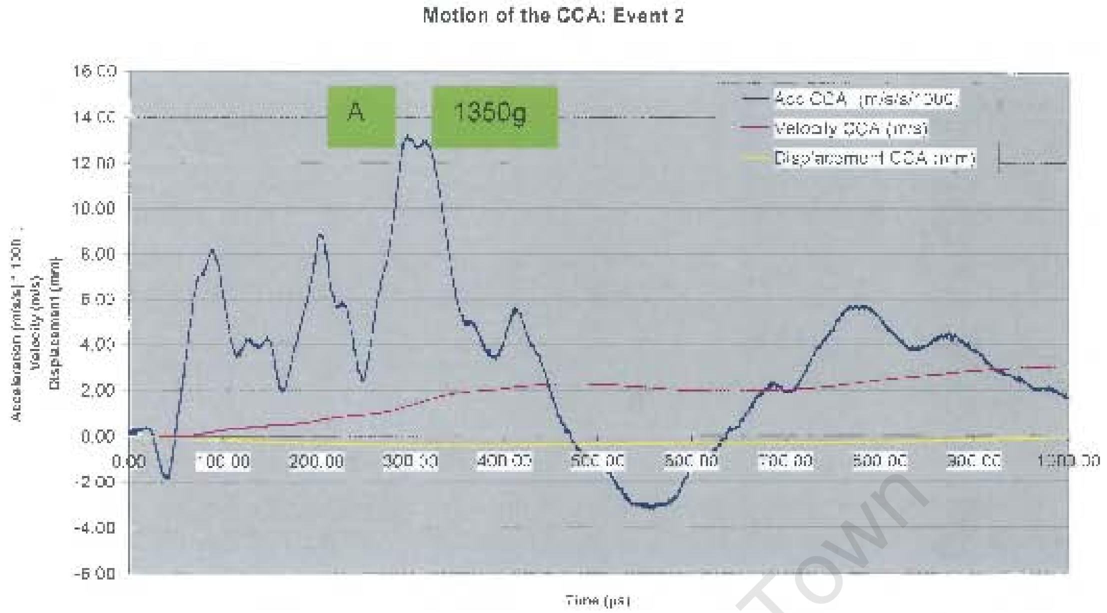

Figure 86: **Double integration of the acceleration of the electronics CCA, producing the displacement of the CCA during Event 2 over a period of the first 1 ms.**

Relative Displacement, Event 2:

The relative displacement between the Enclosure and the CCA over a period of 16 ms is shown in Figure 87. During Event 2, the maximum relative displacement (yellow graph) was approximately 0.9 mm, and it occurred during the first 1 ms of the event.

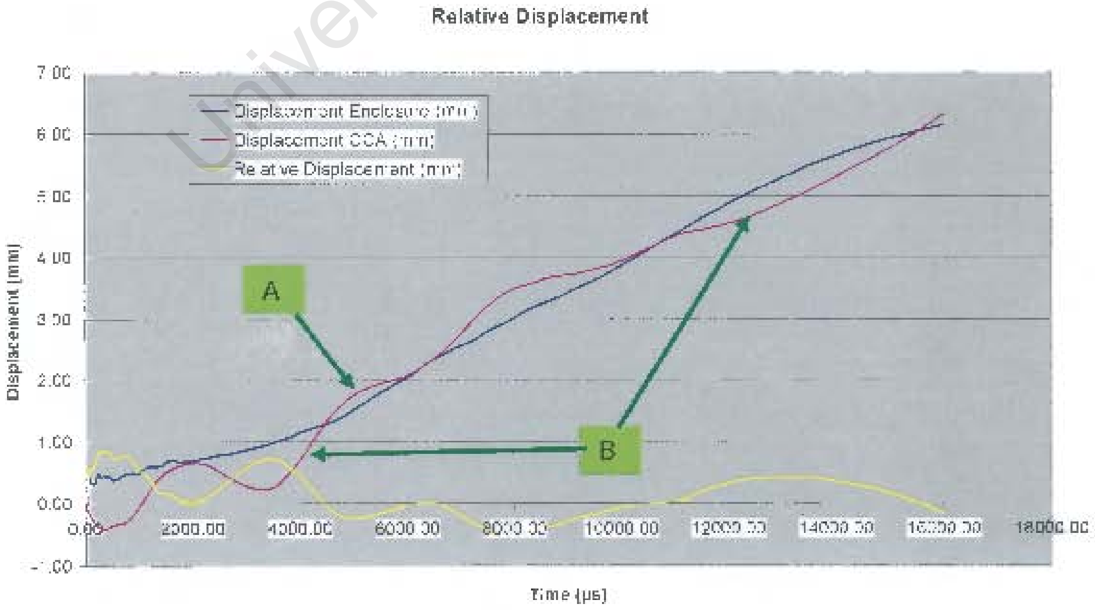

Figure 87: **The relative displacement of the Electronics Container, relative to the CCA, using grommet suspension during Event 2 over the first 1 ms period**

5.1.2.6.7. *Summary: Acceleration Results*

The two acceleration results (Event 01 and 02) were similar, as tabulated in Table 21. In both cases, the negative half cycle of the accelerations was larger than the positive half cycles, but the net displacement was in the direction of the positive acceleration. The attenuation produced by the damping effect of the grommets was therefore calculated in dB relative to the acceleration positive half cycle.

Table 21: Maximum accelerations.

Blast number	Maximum Pos Acceleration Enclosure	Maximum Neg Acceleration Enclosure	Maximum Acceleration measured on CCA	Attenuation
01	50 788 g	-57 295 g	+1500 g	15.82 dB
02	57 630 g	-77 363 g	+1350 g	16.30 dB

The acceleration attenuation is the amplitude portion of the damping co-efficient (*b*) of Equation 31. The phase relationship is not discussed in this study, because it was postulated that the amplitude of the acceleration was the phenomenon that caused the damage.

Result of the spring effect of the PCB

The spring effect of the PCB (manufactured from FR4 fibre glass composite material) on which the electronic components were mounted, has not been discussed before. It is necessary to investigate the movement of the accelerometer that was mounted on the PCB to explain the cyclic nature of the CCA displacement curve as shown in Figure 83 and Figure 87.

In both the foregoing Figures it could be seen that the Enclosure started moving in the direction that the shock waves were moving at the point of collision. The inertia of the CCA working in concert with the damping effect of the grommets, as well as the spring effect of the PCB, caused the displacement of the CCA to introduce a time constant, bringing the CCA into motion at a delayed time. The inertia of the CCA and the stiffness (spring constant) of the PCB then caused the CCA to overshoot the position of the Enclosure at point A, in Figure 87. At point B in the Figure, the Enclosure passed by the CCA, relative to its motionless position. This means that the stiffness of the PCB played a large role when the grommets were used. The damping effect of the grommets, plus the damping effect of the PCB, contributed to the overall damping effect. However, the combined damping did not allow enough reduction in acceleration to have precluded damage, as noted in Table 19. The conclusion could be drawn that the grommets were not the ideal solution to the damping problem under shock loading.

5.1.2.6.8. Pressure Measurement Analysis

Event 1 Shock Pressure

The pressure measurement results are shown in Figure 88 and Figure 89.

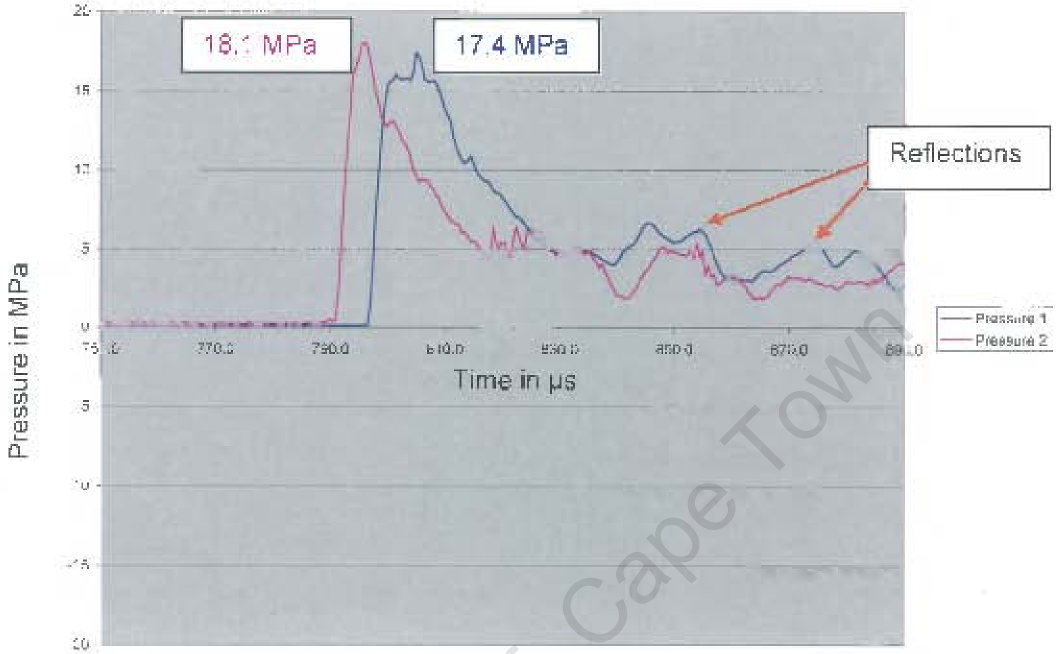

Figure 88: Two shock pressures measured during Event 1

Event 2 Shock Pressure

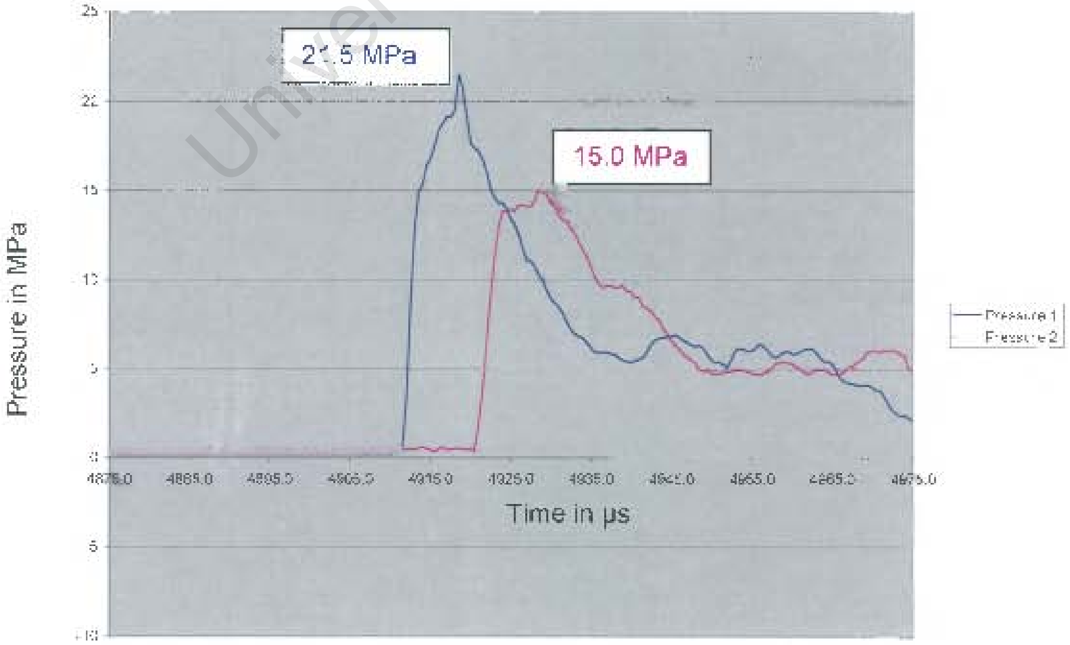

Figure 89: Shock pressures measured during Event 2

5.1.2.6.9. *Summary: Pressure results*

Pressure measurements are discussed here only to confirm that the pressures were in relation to the values that would be expected for a 30-gram explosive charge. The measured maximum pressures are shown in Table 22 and Figure 90.

Table 22: Maximum pressures.

Event/sensor number	Maximum Pressure (MPa)	Calculated Maximum Pressure (MPa)	Standoff Distance (m)
1/ Sensor 1	18.1	19.48	0.733
1/ Sensor 2	17.4	19.13	0.745
2/ Sensor 1	21.6	19.48	0.733
2/ Sensor 2	15.0	19.13	0.745

Sensor 1 denotes the sensor closest to the blast, and sensor 2 denotes the sensor furthest from the blast.

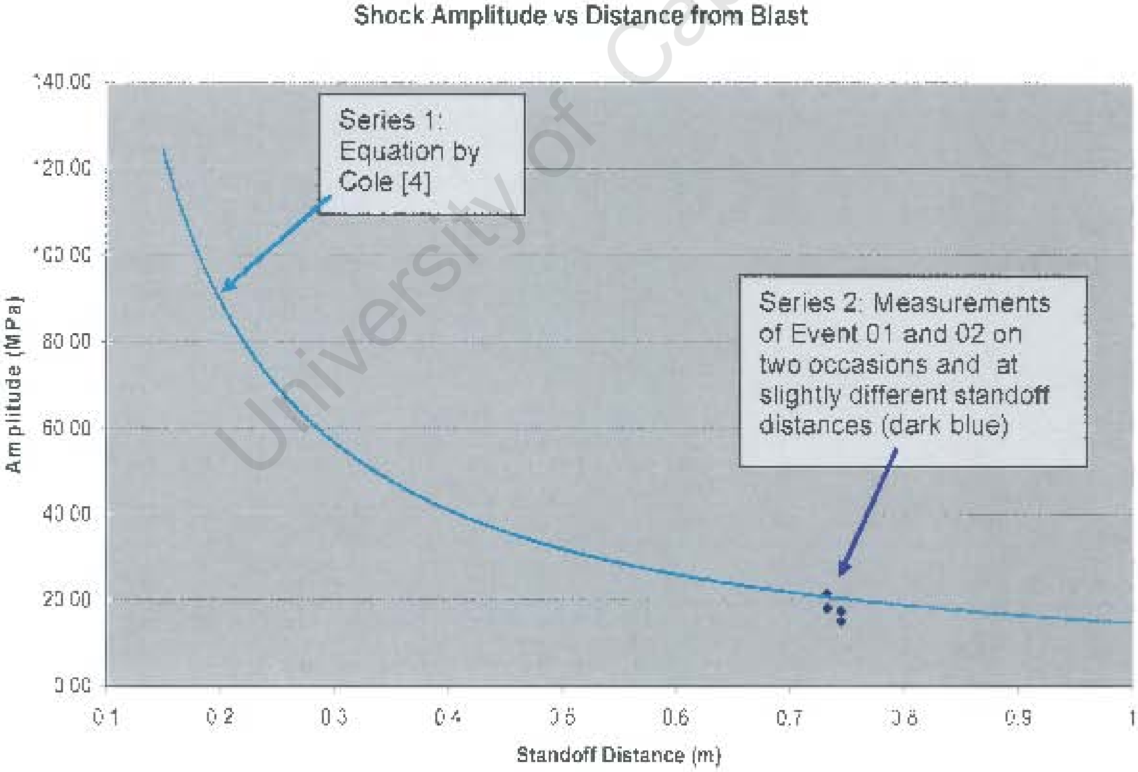

Figure 90: Calculated and measured maximum blast pressures

The results of the measured peak pressures did not follow the traditional shock pressure curvature of a typical blast closely, as would be expected (see Figure 88 and Figure 89). The abnormality could possibly have been due to a small amount of movement of the sensor during the shock wave measurement. Other reasons for this may be reflections or other interactions, and were not researched as part of this study because it was not important to this research. What was important was the fact that the measured pressures (see series 3 in Figure 90) correlate with the theoretical values to the extent that confidence was established in the acceleration measurement values.

5.1.2.6.10. Bubble measurement

The measurement duration was extended in time to capture the bubble's effect on acceleration and pressure, as shown in Figure 91, and the bubble pressure effect is tabulated in Table 23.

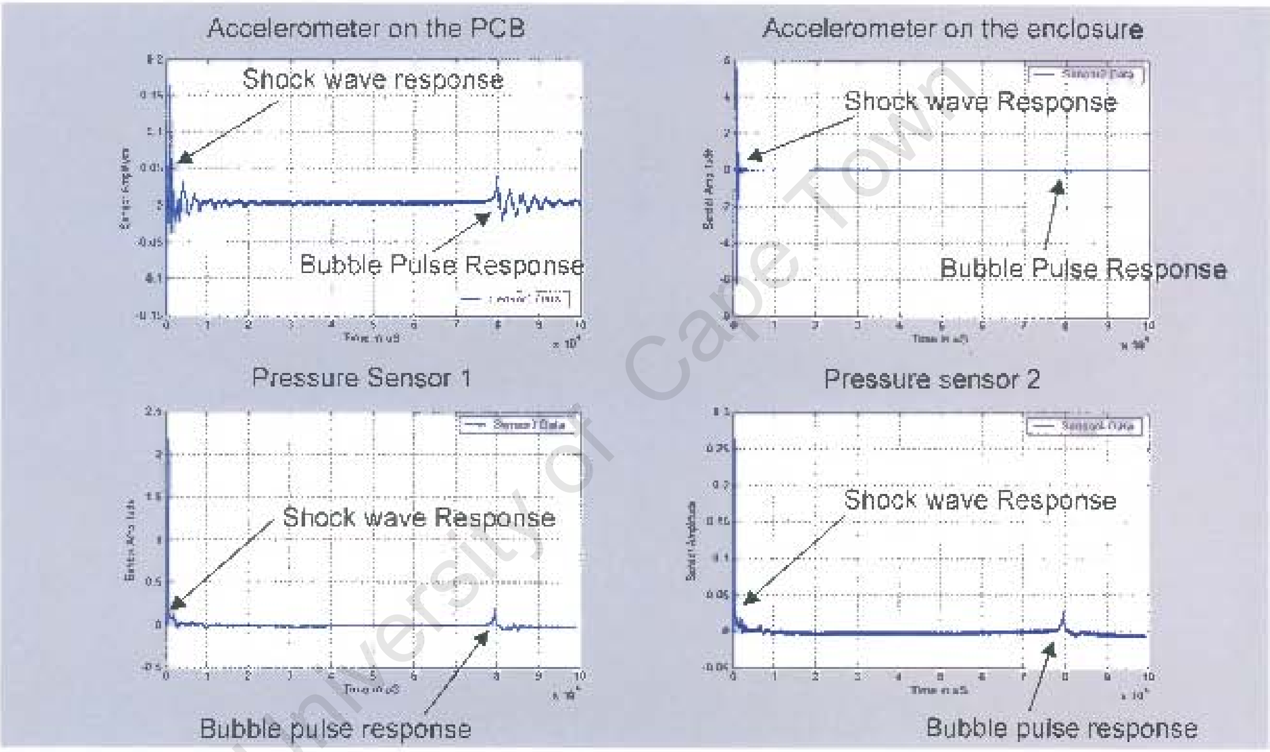

Figure 91: The bubble pulse influence on pressure and acceleration

Table 23: Bubble pressure and accelerations as a result of the bubble pulse

Blast number 01	Maximum Bubble Pressure (MPa)	Maximum Acceleration (g)
Pressure Sensor 1	2.7	
Pressure sensor 2	1.9	
Accelerometer 1 (on PCB)		385
Accelerometer 2 (on enclosure)		1256

Note: The bubble period was measured to be approximately 80 ms (see Figure 91), which correlates well with the Bubble Period calculated from Equations given by Brett [1], see Equation 33.

$$T_{bubble} = KW^{\frac{1}{3}} / (Z+33)^{\frac{5}{6}} \tag{33}$$

Where K = a constant specific to a given explosive type = 4.268 for TNT
W = the equivalent mass of the explosive charge in lb. TNT
Z = the water depth in feet

Using Equation 33, and substituting 30 gm Pentolite (equivalent to 0.0746 lb of TNT) into W, 2 m (or 6.6 ft) into Z, and using K = 4.268 for TNT, the Bubble Period was calculated to be 84 ms. This confirmed the measured disturbance at 80 ms as being the first bubble pulse.

Although the bubble pulse produced much less (approximately 1/10) pressure when compared to the initial shock wave, the acceleration on the PCB was only reduced to 25% of the acceleration caused by the shock wave. This was as a result of the longer period of the bubble pulse as compared to the shock wave, overcoming the inertia with time.

5.1.2.7. Problems encountered

The problems encountered during this exercise are listed as follows:

a. There was not sufficient shade on the jetty to be able to see the details on the oscilloscope and computer screens. Make-shift screening methods were used and these were just adequate for seeing the details only, but not of adequate standards conducive to good experimentation.

b. The lack of shade, as well as lack of a proper equipment-safe workspace, contributed to the fact that the oscilloscope measurements could not be seen or photographed, and was therefore omitted. The time of detonator function could therefore not be taken. The variance in time from moment of measurement-initiation to time of arrival of the shock wave at the accelerometers could be the variance in detonator function time, but this statement could not be resolved due to this specific lack of information.

c. Due to time required for setup, only two valid explosion events were possible.

d. There is evidence that the connection between the Pressure Sensor and the cable was momentarily disrupted after the collision with the shock wave. See pressure measurement over expanded time frame in Figure 92.

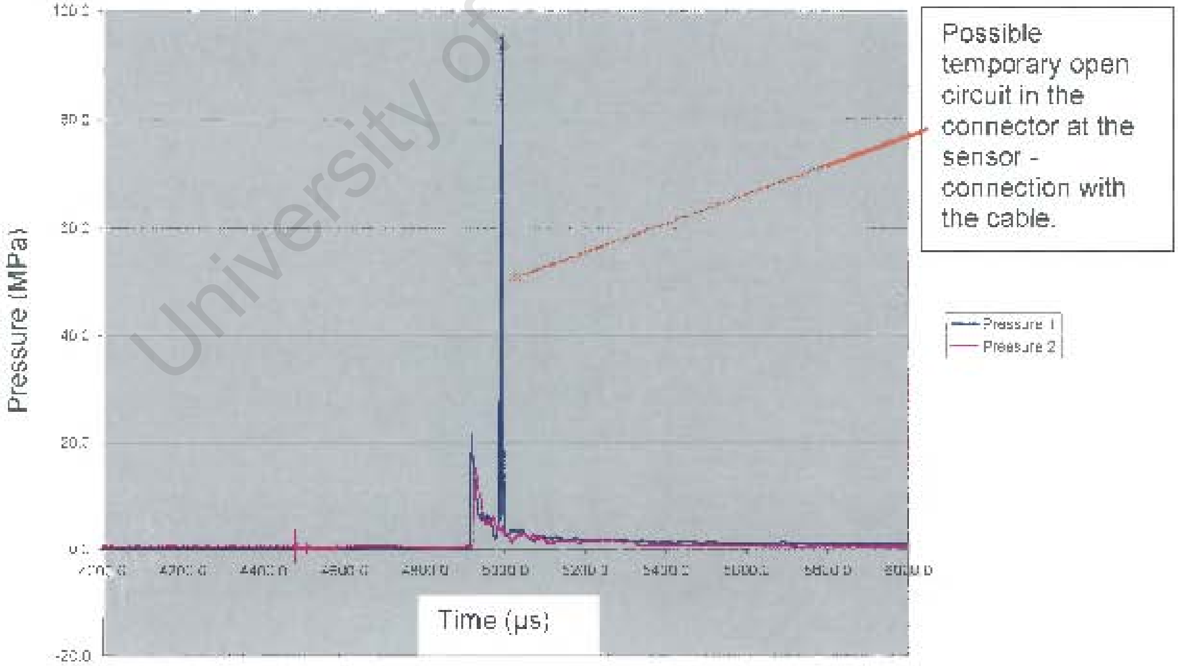

Figure 92: Pressure measurements over expanded time frame

5.1.2.8. Conclusions

5.1.2.8.1. Displacement analysis

It was predicted in Chapter 3 that the movement of the enclosure during the shock wave acceleration peaks would be relatively small. In fact, the movement during the first acceleration peak was predicted to be in the order of 1 mm. This led to the design-conclusion that damping mechanisms could physically be relatively small, allowing for the movement of approximately 1mm, hence the choice of grommets as damping mechanisms.

The relative displacement between the electronics enclosure and the CCA during the first peak acceleration period was less than 1 mm in Event 1 (Figure 83), and less than 0.5 mm during Event 2 (Figure 87). This meant that the damping mechanism was, as had been predicted, a means to allow "soft" movement of the enclosed electronic units to protect the electronics from damage. The choice of a grommet, which in general allows movement of <1 mm, is not regarded as the best solution for the acceleration rates greater than those experienced in these experiments.

5.1.2.8.2. General

a. The pressure measurements were within expected limits, but could be done more accurately if the test set-up were to be improved. The pressure amplitudes correlated very well with the empirical values of Cole [5], and therefore it was concluded that complete detonation had occurred.

b. The acceleration measured on the enclosure was within expected limits when compared to the measurements by Brett *et al* [2].

c. There was a drastic reduction in acceleration between the enclosure and the grommet-mounted CCA. Although there was not enough statistical evidence to guarantee that the present acceleration reduction of approximately 16 dB (Table 21, last column) would repeatedly be achieved in practise, both the tests yielded results which were within the same amplitude ranges. This also means that there is no statistical evidence to the contrary. Although a degree of credibility is evident, further tests are suggested.

d. From the repeated failures of the crystals only, it was evident that crystals provided the weak link in the chain with respect to this specific environment. It is suggested that an alternative time pulse generator be used in the electronics hardening process.

e. The repeated finding that some ICs were displaced from their sockets indicated that this also constituted a weak link in the chain under the prevailing conditions. It is suggested that the ICs be soldered directly onto the PCB as an electronics hardening action.

f. Apart from conclusions d and e, above, the other components on the PCBs were unaffected by the blast-events during this experiment. The achievement at this stage, (taking into account that the crystal can easily be replaced by components of the same type as have been used in this test unit, and that the ICs can easily be soldered directly), is that the electronics as used in the test unit would be immune against a blast caused by a charge of 40 kg at a distance of 8 m. Although the general target user requirement mentioned on page 18 is 5 m, the accelerometer amplitude measurement capability is only 100 000 g. At the presently scaled distance, accelerations close to 100 000 g have already been measured. Moving the test unit closer to the blast may result in damage to the sensors.

5.1.2.9. Recommendations

a. To design an improved frame on which the sensors could be mounted so that minimal sensor movement would be allowed during the arrival of the shock pulse, and for one subsequent second.

b. To repeat the same tests and then to correlate the findings with previous measurements.

c. To repeat the tests and measure acceleration only on the dampened PCBs to enable the target distance (40 kg at 4 m) to be achieved.

5.1.3. Experiment 3: Second Experiment which included Pressure Sensors and Accelerometers

5.1.3.1. Purpose

This experiment followed on from the first experiment (on page 98) to gain statistical data on the accelerations that may be expected vs. the stánd-off distance.

In the previous experiment, it was found that the frame was damaged beyond repair, and therefore a more durable frame was constructed for further experimentation. The main aim of this interim experiment was to establish whether the newly designed frame would withstand the rigour that was expected in the next experiment, which used an up-scaled charge (390 gm in stead of the 30 gm used in the previous experiment).

5.1.3.2. Equipment

The equipment list was as follows:

h. PXI computer with fast independent four-channel A/D conversion card with interface connection box.

i. Custom detonator-computer synchronisation box.

j. 1x Tourmaline blast pressure sensor with a sensitivity of 0.5 mV/psi, with a 20 m low noise cable.

k. 1x Tourmaline blast pressure sensor with a sensitivity of 0.1 mV/psi, with a 20 m low noise cable.

l. 2x PCB accelerometers with identical specifications, with 20 m low noise cables.

m. Custom-made Aluminium mounting frame and float.

n. 100 MHz Storage Oscilloscope for measurement of the synchronisation pulse.

5.1.3.3. Accelerometer Mounting Arrangement

The same electronics enclosure used for the previous experiment was used for this experiment, and the accelerometers were positioned at exactly the same positions (see Figure 93).

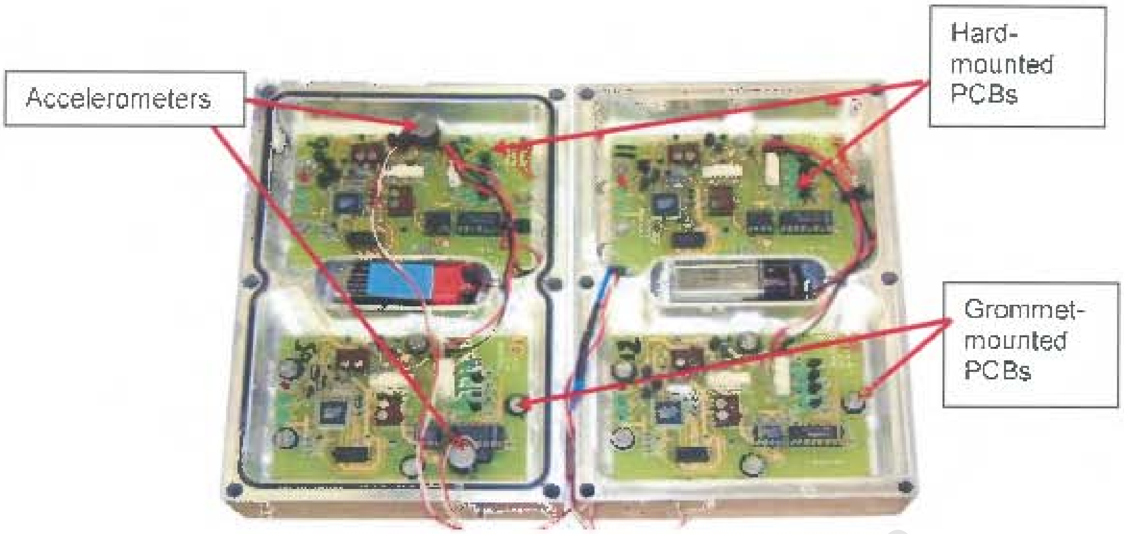

Figure 93: **Mounting of the accelerometers**

The assembled unit containing the accelerometers and the electronics was fastened onto the frame end using duct tape. The electronics unit was seated on sponge rubber, to minimise any high amplitude movements of short duration of the frame being passed on to the accelerometers (see Figure 94).

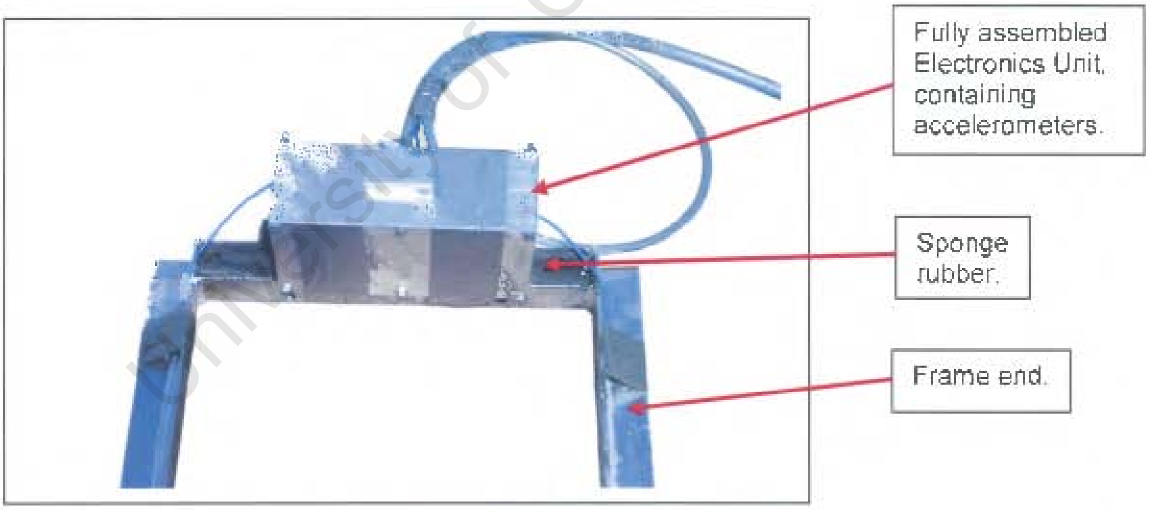

Figure 94: **Electronics unit mounted on the frame end.**

5.1.3.4. Pressure Sensor Mounting Arrangement

The Pressure Sensors were mounted in such a manner that the two sensor elements were next to each other, to enable good comparison of pressure amplitude and waveforms. These sensors were positioned on sponge rubber, and duct taped to the frame, see Figure 95. The shock wave was expected to reach the pressure sensors uninterrupted by any hardware, see Figure 54.

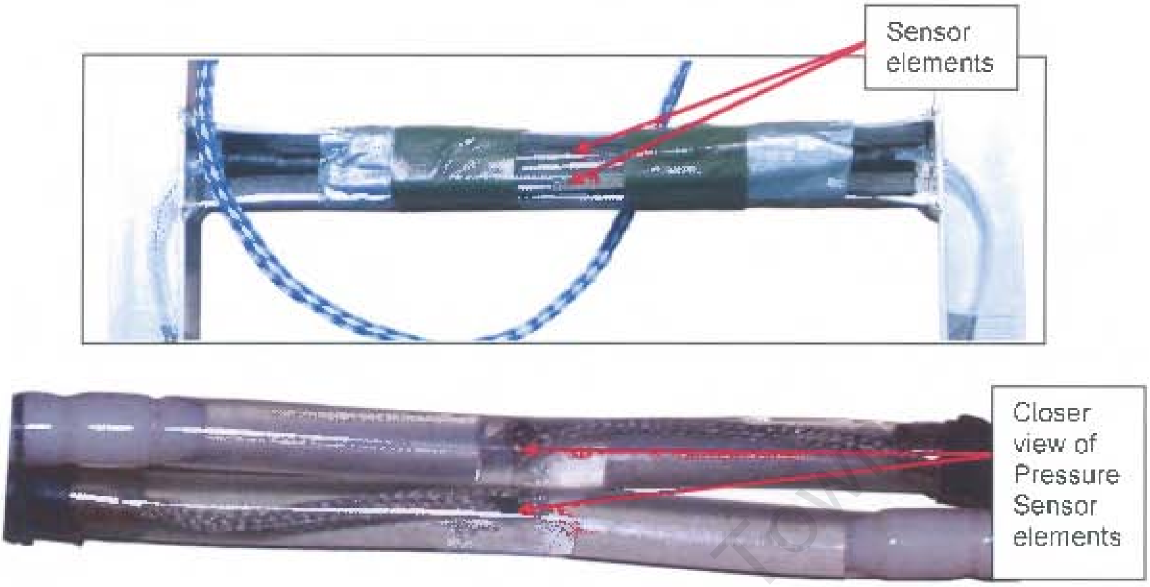

Figure 95: **Mounting arrangement of the Pressure Sensors**

5.1.3.5. Custom Synchronisation Equipment

The same custom firing and synchronisation equipment used in the previous experiment (page 98) was used in this experiment. This means that the start of the measurement cycle was synchronised with the rising edge of the firing supply current.

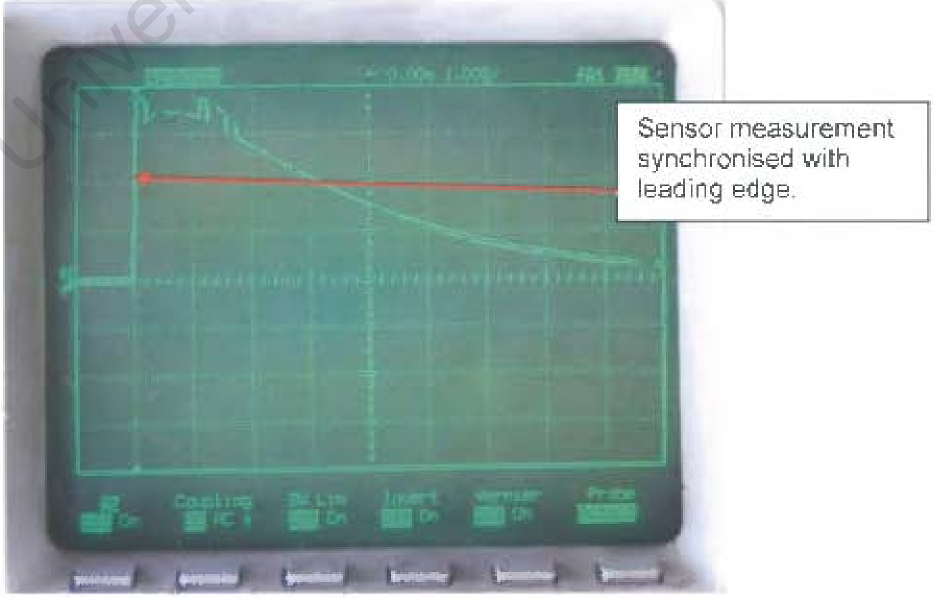

Figure 96: **Photograph of the oscilloscope measurement of the current through the detonator circuit**

5.1.3.6. Physical Test Set-up

One Aluminium enclosure containing four identical PCBs was tied down on an Aluminium frame with reinforced tape. A layer of soft sponge rubber placed between the frame and the enclosure was intended to minimise the transfer of acceleration effects from the frame to the enclosure (see the path of the shock wave in Figure 97).

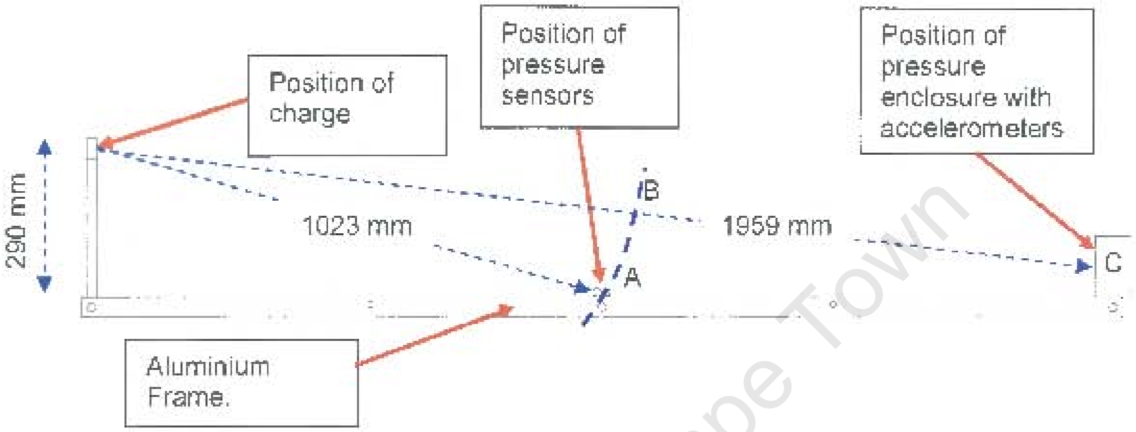

Figure 97: The enclosure mounted on an Aluminium frame - distances are for Event 1

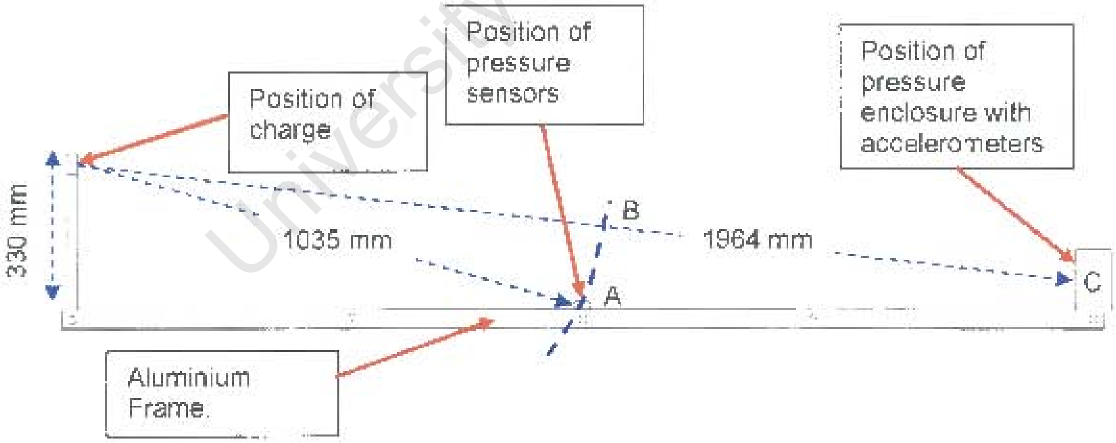

Figure 98: The enclosure mounted on an Aluminium frame - distances are for Event 2

Note: The distances that were chosen did not represent the target user requirement, due to the measurement limitation of the accelerometers. More tests are needed at a later stage. to prove that the target requirement will be met.

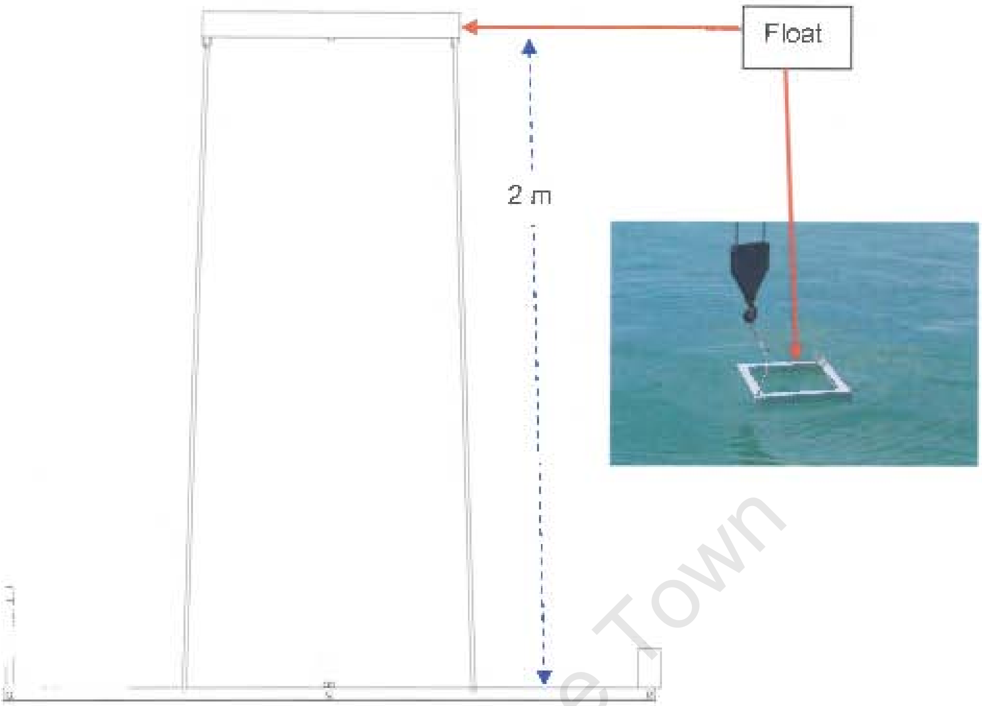

Figure 99: The complete test set-up with float

A 29.2 gram Pentolite charge was placed at the end of the frame, on a PVC holder. See Figure 54. Adding the detonator explosives to the charge explosives brought the total explosive charge mass to 30 gram.

The frame was then suspended from a crane and positioned in the water. Then the crane was removed to enable an independent test station at a depth of 2 m.

5.1.3.7. Results

5.1.3.7.1. *Raw data*

The results are shown in Figure 100, and Figure 101.

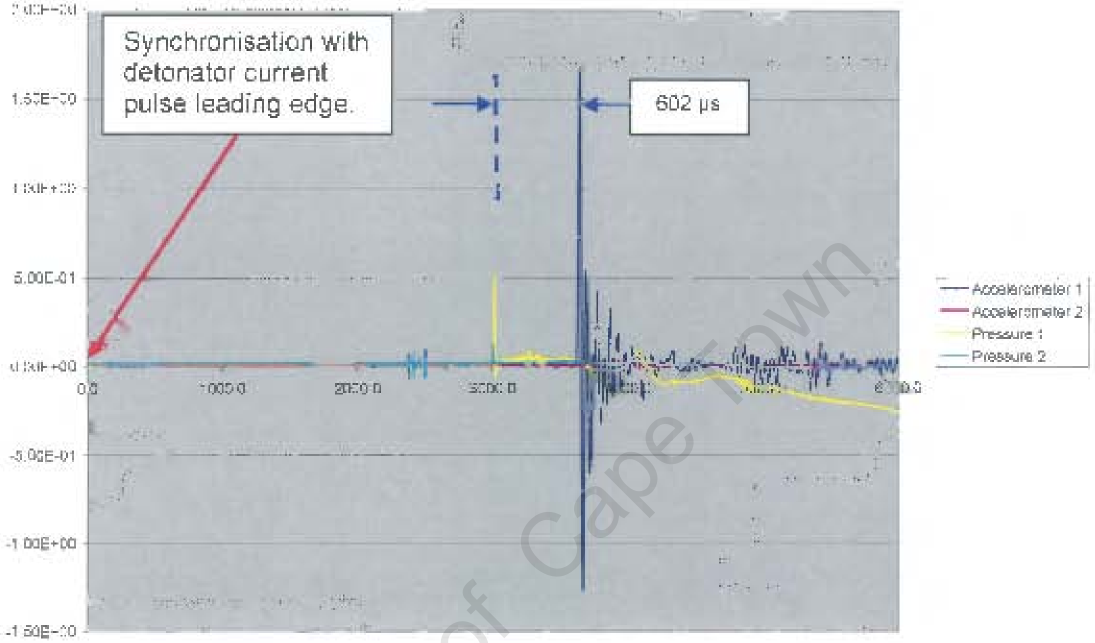

Figure 100: Results for Event 1, measured in Volts

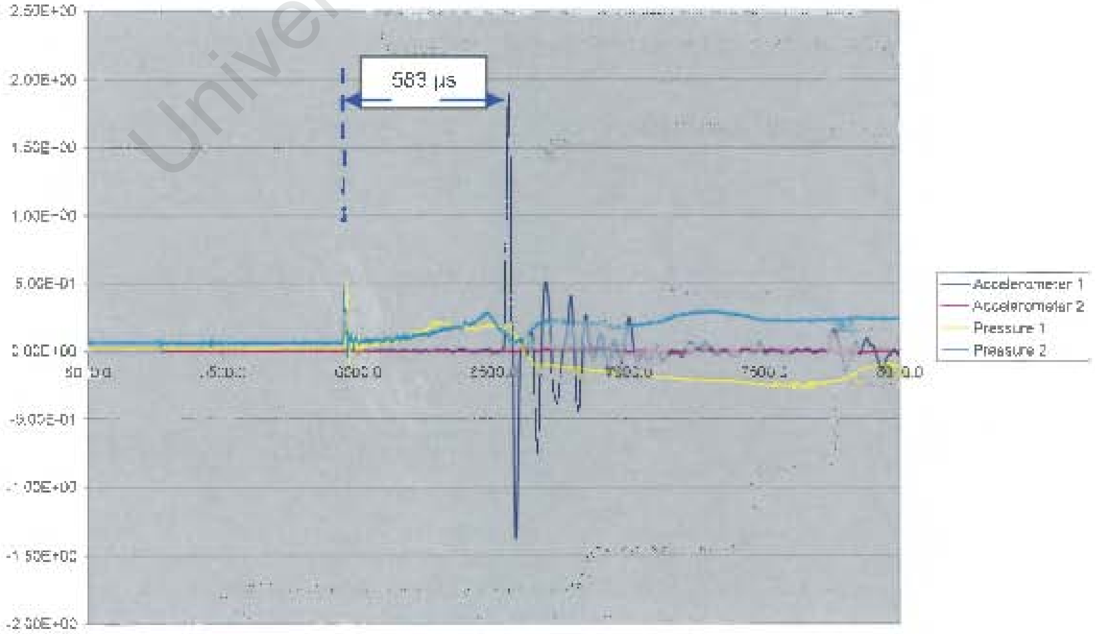

Figure 101: Results for Event 2, measured in Volts

The measurement set-up was the same for Event 1 and Event 2, except for a slightly different charge holder height above the frame. As could be seen in these two figures, the time between the measured pressure shock pulse and the acceleration, is different for the two cases. The shock wave average velocity was calculated for both cases in Table 24. The shock wave propagates spherically outwards. and could be depicted in two dimensions by the curve A-B in Figure 97 and Figure 98. The shock wave travel distance between sensors was thus the distance B-C in the same figures. The time taken for the shock wave to propagate between the sensors is equal to the time taken to travel from point B to point C. This time is shown in Figure 100 and Figure 101 as 602 μs and 583 μs respectively.

Table 24: Average shock wave velocity calculations

Blast No.	Shock wave distance between sensors, points B-C (m)	Time between sensors (μs)	Average Velocity (m/s)
1	0.935	602	1553
2	0.929	583	1593

As seen in Table 24. the average shock propagation velocity was calculated to be between 1553 m/s and 1593 m/s. This result is significant, because the velocity was greater than the small signal sound velocity in water, indicating that the sensors were positioned in the near-field[6] of the explosion.

5.1.3.7.2. *Pressure analysis*

The pressure measurements are shown in Figure 102 and Figure 103.

Note that the illustrated pressure histories per sensor are similar for Event 1 and Event 2, but that the two sensor pressure histories differ in form: Sensor 1 (in both blasts) has a "rounded" positive pulse, whilst Sensor 2 (in both blasts) has a sharp rising edge (measured at 1 μs in both instances).

---

[6] See page 40 for suggested definition of the near field.

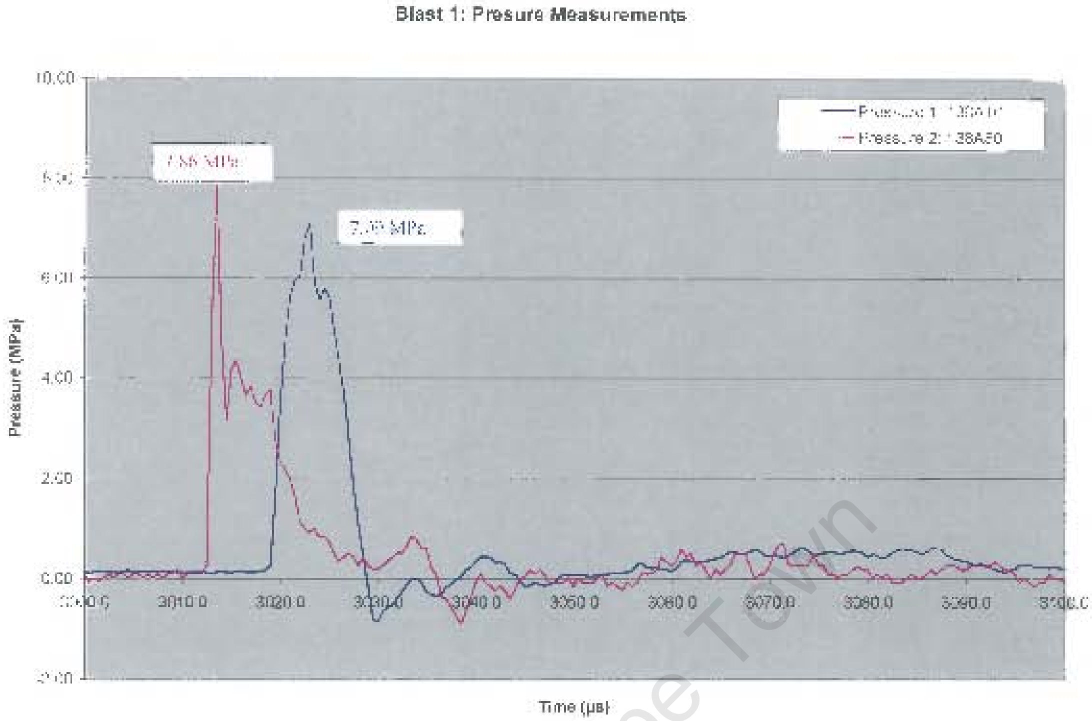

Figure 102: Event 1 Pressure histories for two sensors

Figure 103: Event 2 Pressure histories for two sensors

5.1.3.7.3. Acceleration analysis

The acceleration measurements are shown in Figure 104 and Figure 105.

The characteristics of the acceleration measurements are similar for both blasts of this experiment. These characteristics entail a large positive peak followed by a large negative peak, similar to a Sine function. Subsequently, the characteristics change according to the hydrodynamic circumstances during the specific blast period. The period of the first two halves of the characteristic curve is shown in Table 25.

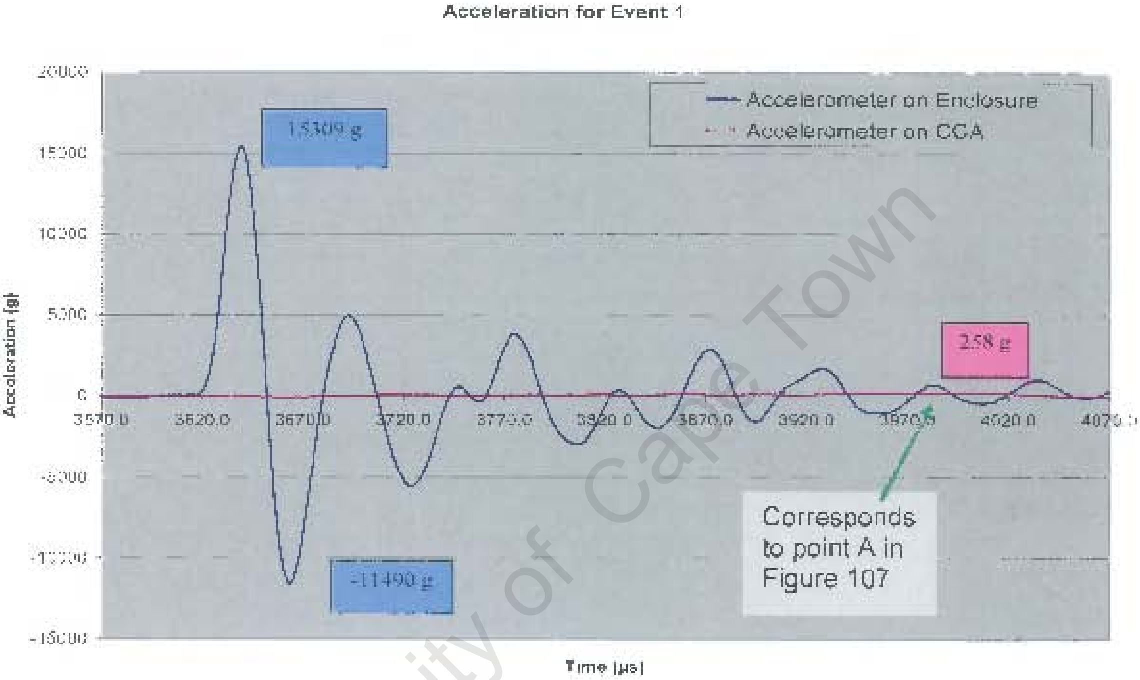

Figure 104: Accelerations for Event 1

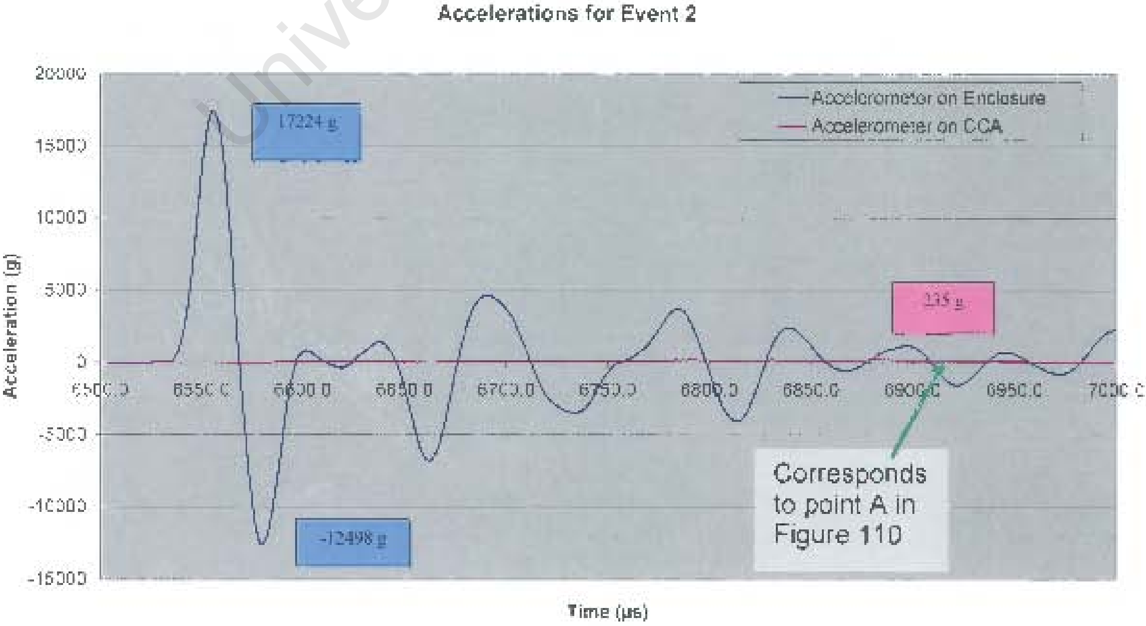

Figure 105: Accelerations for Event 2

The acceleration analysis is shown in Table 25. The attenuation is significant with regard to the reduction of the Electronics Container acceleration of 15 309 g to 235 g (to 1.54%, or by 17.7 dB) for Event 1, and 17 224 g to 210 g (to 1.22%, or by 18.7 dB) for Event 2. The full cycle period of the first cycle was approximately 60 µs for both events.

Table 25: Acceleration analysis of the second experiment, which included accelerometers

Event No	Positive Peak (g)	Negative Peak (g)	First Full Cycle Period (µs)	Max PCB acceleration (g)	Attenuation between CCA and Enclosure (dB)	Delay from pos peak on enclosure to maximum acceleration on the PCB (µs)
1	15309	-11490	62	258	17.7	342
2	17224	-12498	60	235	18.7	327

5.1.3.7.4. Displacement analysis

The displacement was calculated by double integration of the acceleration data. Figure 106 depicts the motion parameters for the Electronics Enclosure during Event 1, and Figure 107 depicts the motion parameters for the CCA which was enclosed in the Container during Event 1. The relative displacement shown in Figure 108 is the result of the displacement of the CCA subtracted from the displacement of the Electronics Container, showing that the relative displacement is less than 0.25 mm. This means that the relative movement was within the capability of the suspending grommets.

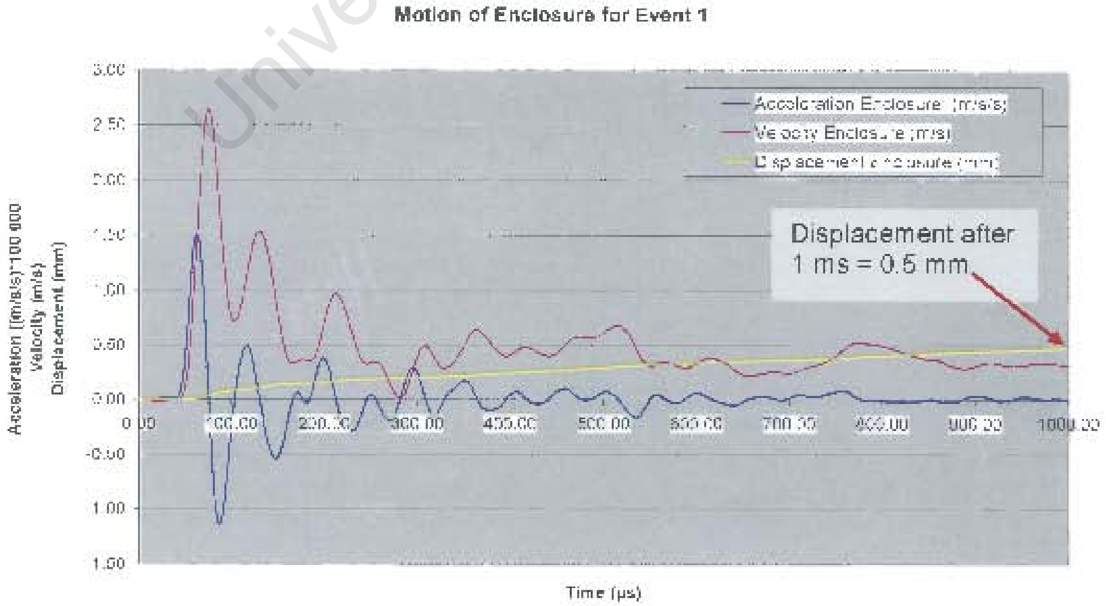

Figure 106: Motion analysis of the Electronics Enclosure for Event 1

Figure 107: **Motion analysis of the CCA contained within the Electronics Enclosure for Event 1**

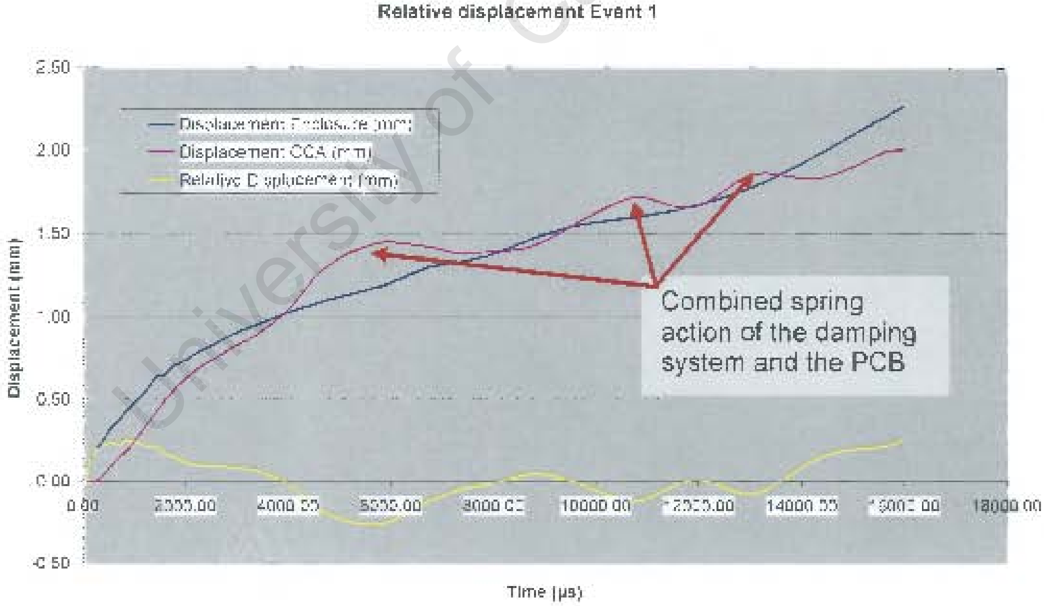

Figure 108: **Relative movement between the Electronics Container and the CCA is suspended within for Event 1**

Figure 109 depicts the motion parameters for the Electronics Enclosure during Event 2, and Figure 110 depicts the motion parameters for the CCA which was contained (suspended) in the Enclosure during Event 2. The relative displacement shown in Figure 111 is the result of the displacement of the CCA subtracted from the displacement of the Electronics Enclosure, showing that the relative displacement was less than 0.25 mm.

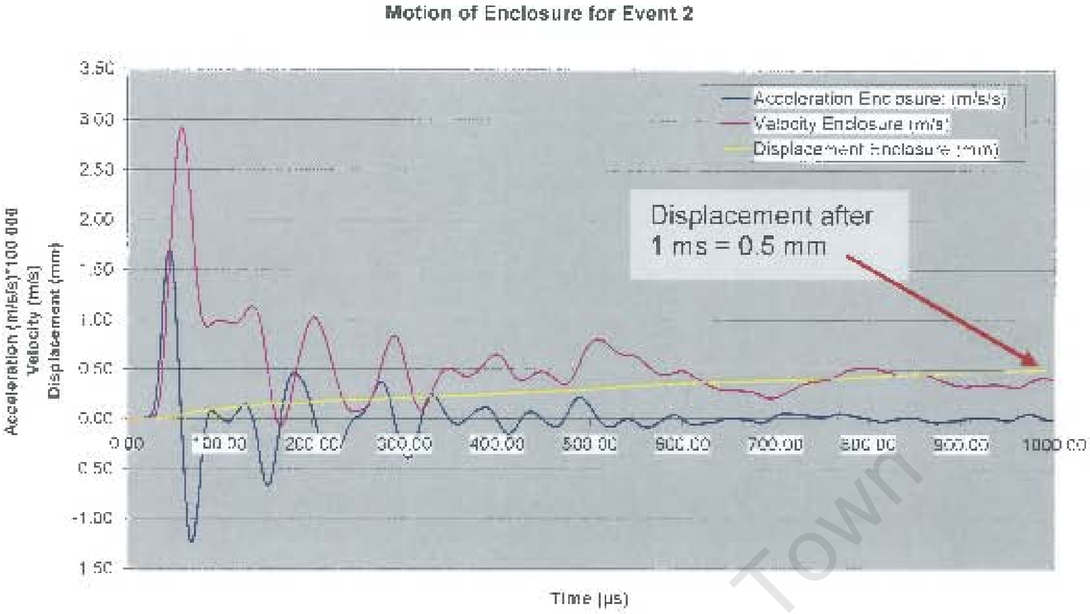

Figure 109: Motion analysis of the Electronics Enclosure during Event 2

Figure 110: Motion analysis of the CCA contained within the Electronics Enclosure during Event 2

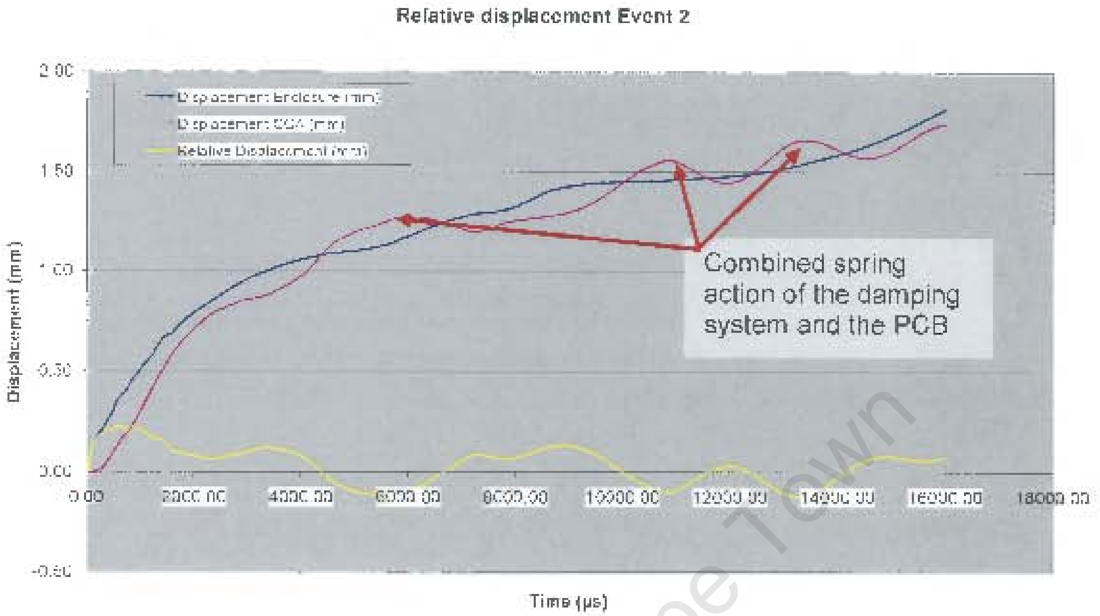

Figure 111: Relative movement between the Electronics Enclosure and the CCA suspended within it for Event 2

There is a remarkable correlation (by visual inspection) of the displacements of the Electronics Enclosure, the CCA and the relative displacements between Events 1 and 2.

5.1.3.7.5. Damage analysis

No damage was sustained during this experiment. This was significant, because parameters such as the amplitude of the acceleration of the CCA and the relative displacement between the enclosure and the CCA become part of the solution of preventing damage to the electronics.

5.1.3.8. Discussion

1. Concerning the shock wave velocity:

The shock wave velocity could not be calculated accurately near the point of the explosion, due to the fact that the time taken for the detonator to actually detonate its own 1 gram explosives and the time taken for this event to be transferred onto the main charge, and also the time taken for the main charge to actually transfer the pressure to the water, could not be determined accurately.

Event 1 revealed some activity on Pressure Sensor No. 2 (see Figure 100) voltage at 503 µs before the pressure was measured. This could be due to some form of induction into the cables by means of a phenomenon like an electromagnetic pulse (EMP), but this cause could not be confirmed. Event 2 does not have any prominent induction at a corresponding point.

The distance that the shock wave covered between the pressure sensors and the accelerometers, however, could be measured. It is simply given as 1959 mm – 1023 mm = 936 mm, due to the spherical propagation of the shock wave. The shock front velocity function is non-linear near the explosion (as measured by Takahashi [23]). Therefore the average velocity which could be calculated between the sensors would give some indication of the velocity profile. This is 936 mm / 602 µs = 1553 m/s, which is higher than the normal sound velocity in water (1450 m/s – 1500 m/s), as would be expected for sensors that are positioned in the near field.

2. Concerning the pressure measurements of this experiment:

The amplitude measurements, seen in yellow triangles in Figure 112, are about half the expected values predicted by the Cole [5] Equation, although all four measurements are very similar. This may be due to the mounting method used for this experiment, which introduces attenuation of the pressure measurements.

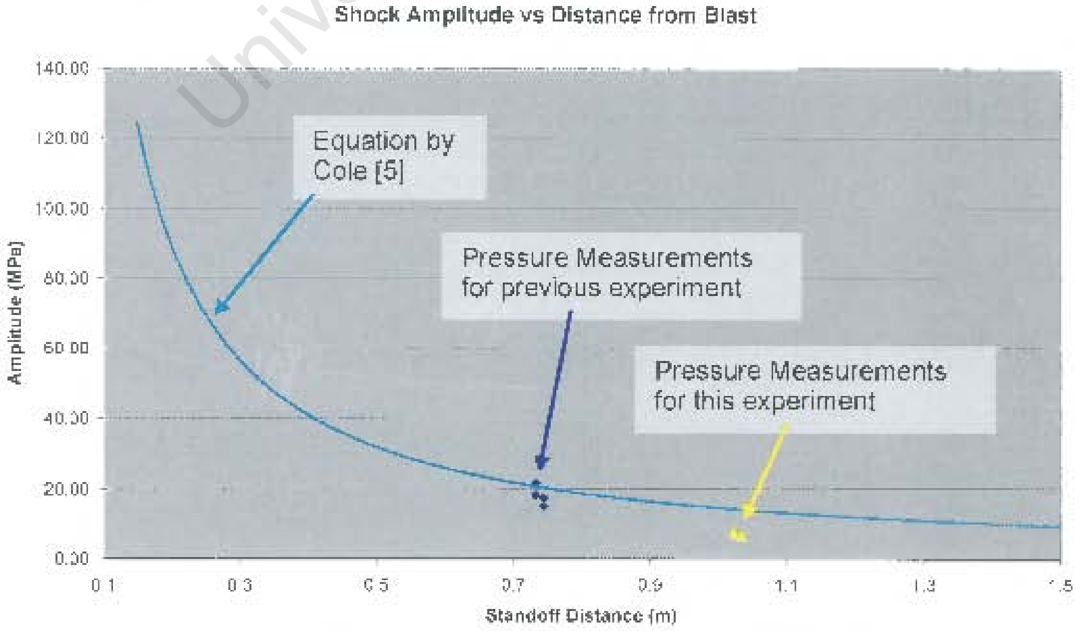

Figure 112: Amplitude measurements shown in yellow triangles.

3. Concerning the Acceleration measurements:

The hard-mounted accelerometer (on the Electronics Enclosure) measured the normal high acceleration peaks as expected, the first two peaks (full cycle) lasting between 62 µs and 60 µs for Event 1 and Event 2 respectively. The attenuation of acceleration (passed onto the CCA), is 17.7 dB and 18.7 dB for Event 1 and Event 2 respectively (Table 25).

Two experiments (four blast events) had been done using the grommet-mountings as damping material. Comparing the acceleration that had been passed onto the CCAs, it was possible to notice a distinct pattern of movement of the CCAs. The acceleration of the CCAs followed an initial increase up to a maximum at roughly 350 µs after impact, dropping down, and reaching a negative peak at roughly 550 µs after impact.

4. Concerning the displacement:

The displacement of the electronics container was compared with the displacement of the CCA to find the relative displacement. The result indicated that the displacements during Event 1 and Event 2 compare well, considering the usual integration process elimination of the constants. The relative displacement was approximately 1 mm for both the electronics container and the CCA during the blast period only. It was accepted that the bubble would have a greater effect on the displacement, which would take place at a much slower pace.

5. Concerning the electronics damage:

No damage was sustained. All four contained electronics assemblies were fully operational after both blasts.

5.1.3.9. Conclusions

a. It is clear from the discussion in paragraph 1, above, that the measured shock wave velocity is higher than sound velocity in water. This means that the measurements were done at least partly in the near field.

b. The fact that Event 1 occurred about 3 ms after the rising edge of the synchronisation pulse generated by the firing current, and Event 2 occurred at about 6 ms after a similar origin, indicated that the detonation of the main explosives for Event 2 occurred approximately 3 ms later than that of Event 1. Synchronisation by detonator current only, is therefore not considered to be good enough to determine the shock wave velocity between the first sensor and the blast position.

c. The pressure sensors could be positioned closer to the charge, because the pressure measurement in Volt at the present distances is less than 0.5 V, whilst the dynamic range of the equipment is 0 V to ± 10 V.

d. The pressure measurements measured at approximately 50 % of the values that would be obtained when the pressure sensors are positioned in an unobstructive manner. This was expected, because this experiment was designed also to analyse the time measurements to determine the effectiveness of the detonator current as a synchronisation tool.

e. The accelerometer tests yielded the expected results. The accelerometers could also be mounted at a scaled distance closer to the blast, because the maximum readings were less than 2 V.

f. The significance between the higher acceleration attenuation that was obtained during this experiment when compared to the previous experiment lies with the higher impact acceleration on the Enclosure of the previous experiment. It could be concluded that the grommet-suspension method has a dynamic range of proper function at input accelerations up to 15 000 g. Applying input acceleration beyond 15 000 g would cause the grommet to be compressed to its physical limit, and consequently a lower attenuation would be expected.

No electronic damage was sustained, due to the distance from the blast and the explosive-charge size.

5.1.4. Experiment 4: Third experiment which included Pressure Sensors and Accelerometers

5.1.4.1. Purpose

This experiment was undertaken in continuation of a series of experiments to characterise the shock waves of underwater blasts to be able to protect other electronics and explosive devices against the effects of the blast. Previous measurements were made with the use of 30 gram of Pentolite. The purpose of this specific experiment was to measure the pressure history of a blast using a larger explosive mass, i.e. 390 gram of PE9 (see Malan [4]), at a stand-off distance of approximately 0.5 m, using the traditional sensor positioning method to determine whether similar pressure histories would be obtained from the two sensors. The purpose was extended to also measure the acceleration of an Aluminium box containing electronics and the attenuation of acceleration, using a new "softer" mounting method for the CCA. On previous occasions, one of the electronic boards was mounted by means of Neoprene grommets. In this experiment, a softer sponge rubber mounting was used, to compare attenuation characteristics of acceleration with the attenuation of the grommet mounting method used in the two previous experiments.

5.1.4.2. Equipment

The equipment list was as follows:

1. PXI computer with fast independent four-channel A/D conversion card with interface connection box.
2. Custom detonator-computer synchronisation box.
3. 1x Tourmaline blast pressure sensor with sensitivity 0.5 mV/psi, with a 20-m low noise cable.
4. 1x Tourmaline blast pressure sensor with sensitivity 0.1 mV/psi, with a 20-m low noise cable.
5. 2x PCB accelerometers with identical specifications, with 20-m low noise cables.
6. Custom Aluminium mounting frame and float, adapted to couple magnetically with the mini ship target to keep the frame in position.
7. 100 MHz Storage Oscilloscope for measurement of the synchronisation pulse.

5.1.4.3. Sensor Mounting Arrangement

Two identical PCBs were mounted onto one side of the enclosure, and another two identical PCBs were mounted to the other side of the enclosure. The enclosure was closed up with the soft-mounted PCBs positioned opposite each other.

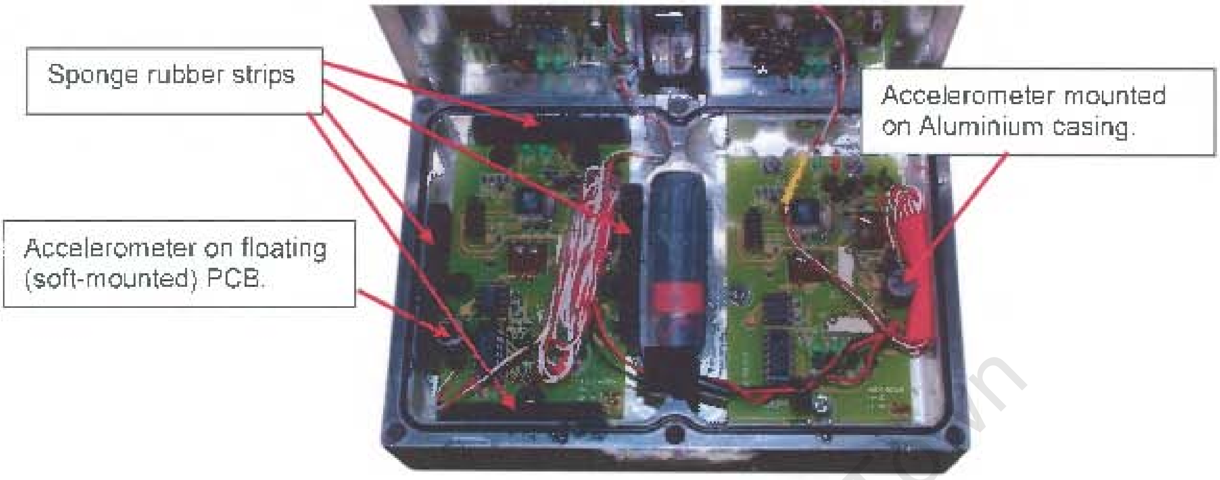

Figure 113: Soft-mounted PCB in an electronics enclosure

5.1.4.4. Custom Synchronisation Equipment

The custom firing and synchronisation equipment used in the previous experiment was used for this experiment in conjunction with the IMPI military firing unit. To summarize: This synchronisation equipment was designed to trigger a measurement cycle on the leading edge of the detonator firing current.

5.1.4.5. Physical Test Setup

One Aluminium electronics enclosure containing four identical PCBs was tied down with cable-ties on a relatively "soft" (sponge rubber) mounting arrangement on a frame manufactured from Aluminium.

The frame was suspended from a float (see Figure 114) by means of Polypropylene rope. Attached to the float were two Neoprene pipes. Each Neoprene pipe had a magnetic coupling device fitted to the front end, to enable non-solid coupling with the target.

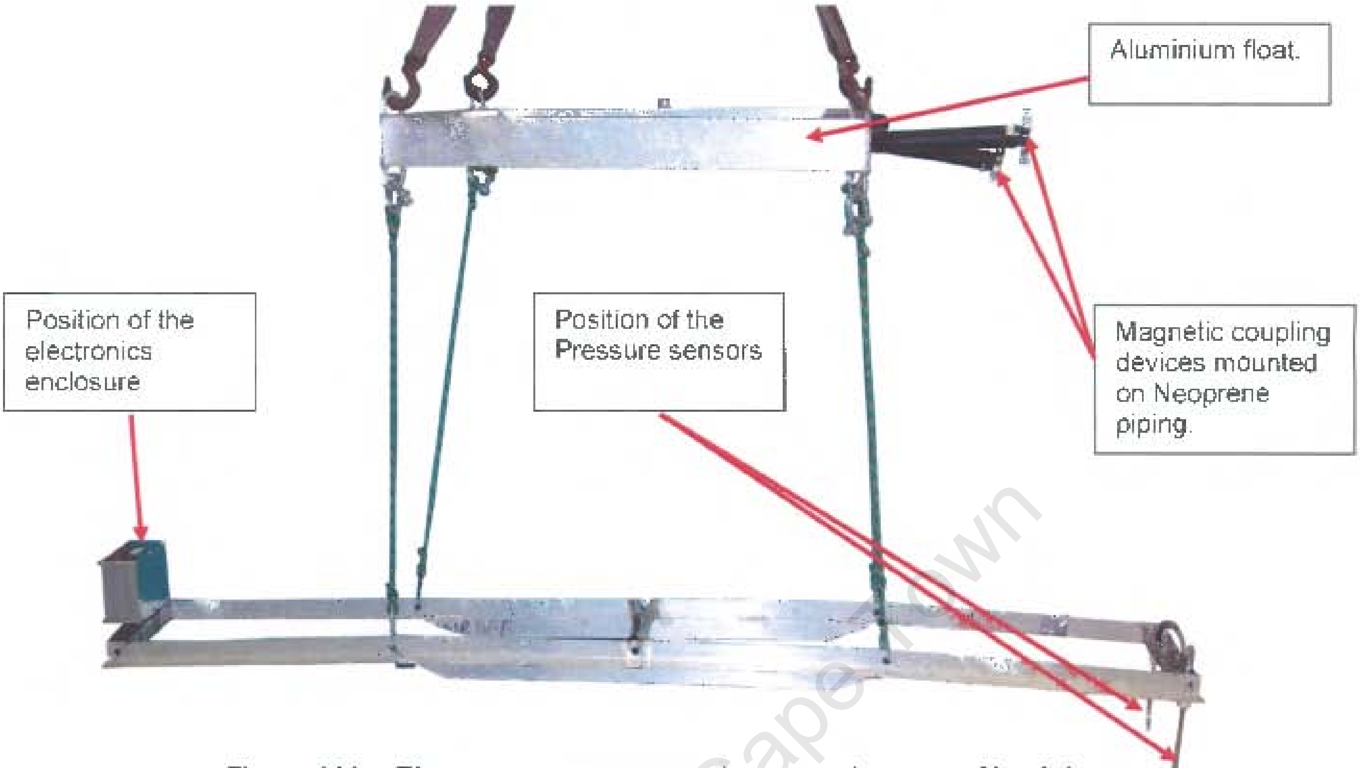

Figure 114: **The sensor arrangement mounted on an Aluminium frame**

The intended final position of the frame (containing the Pressure Sensors and the Electronics Container) relative to the target and the explosive charge is shown in Figure 115 and Figure 116.

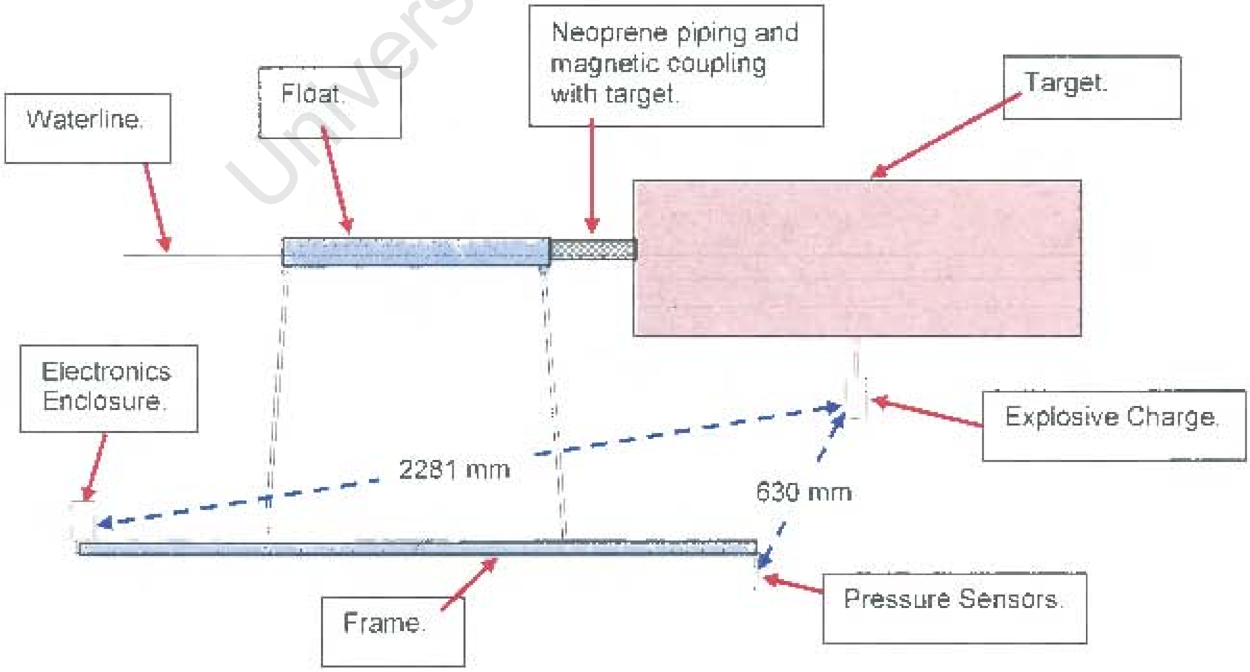

Figure 115: **Schematic drawing of the test setup**

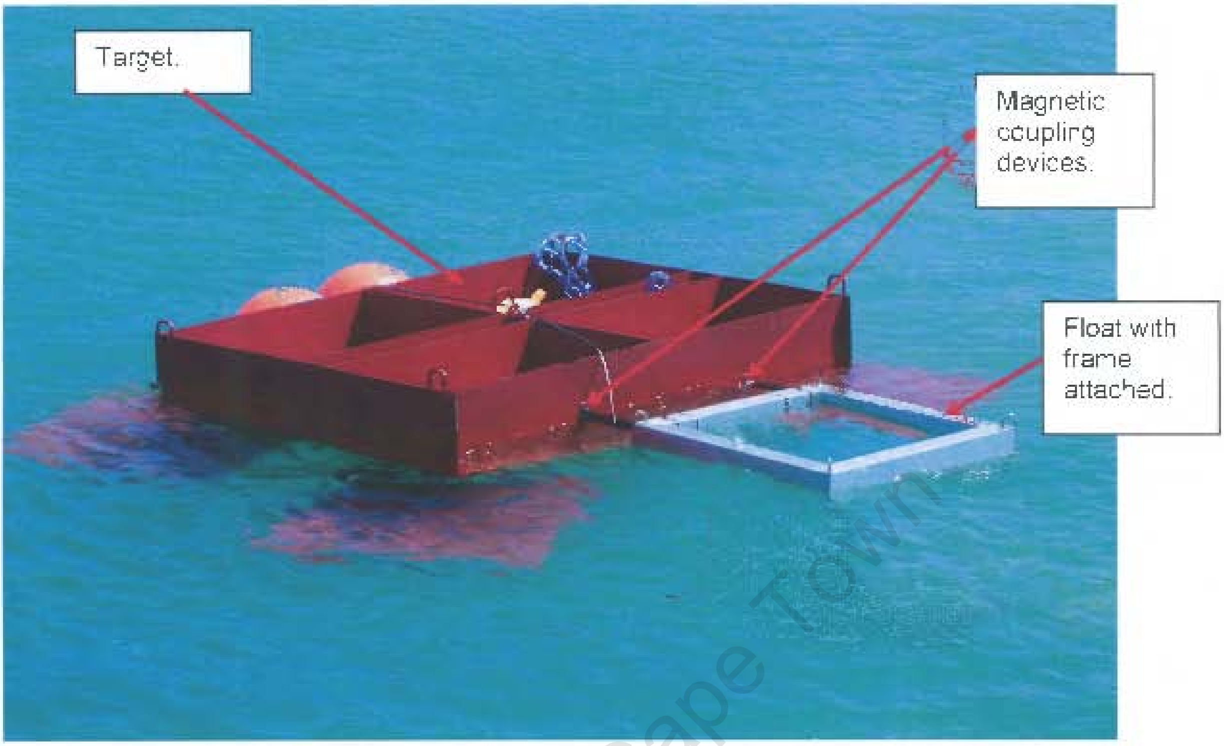

Figure 116: The completed measurement setup in the sea

A 390 gram PE4 charge was placed at the position as indicated in Figure 115, and after all measurement connections were checked the charge was detonated.

5.1.4.6. Results

The "raw" measurement results of the four sensors are given in Volts in Figure 117, to show the positions of the pressure results relative (in time) to the accelerometer measurements.

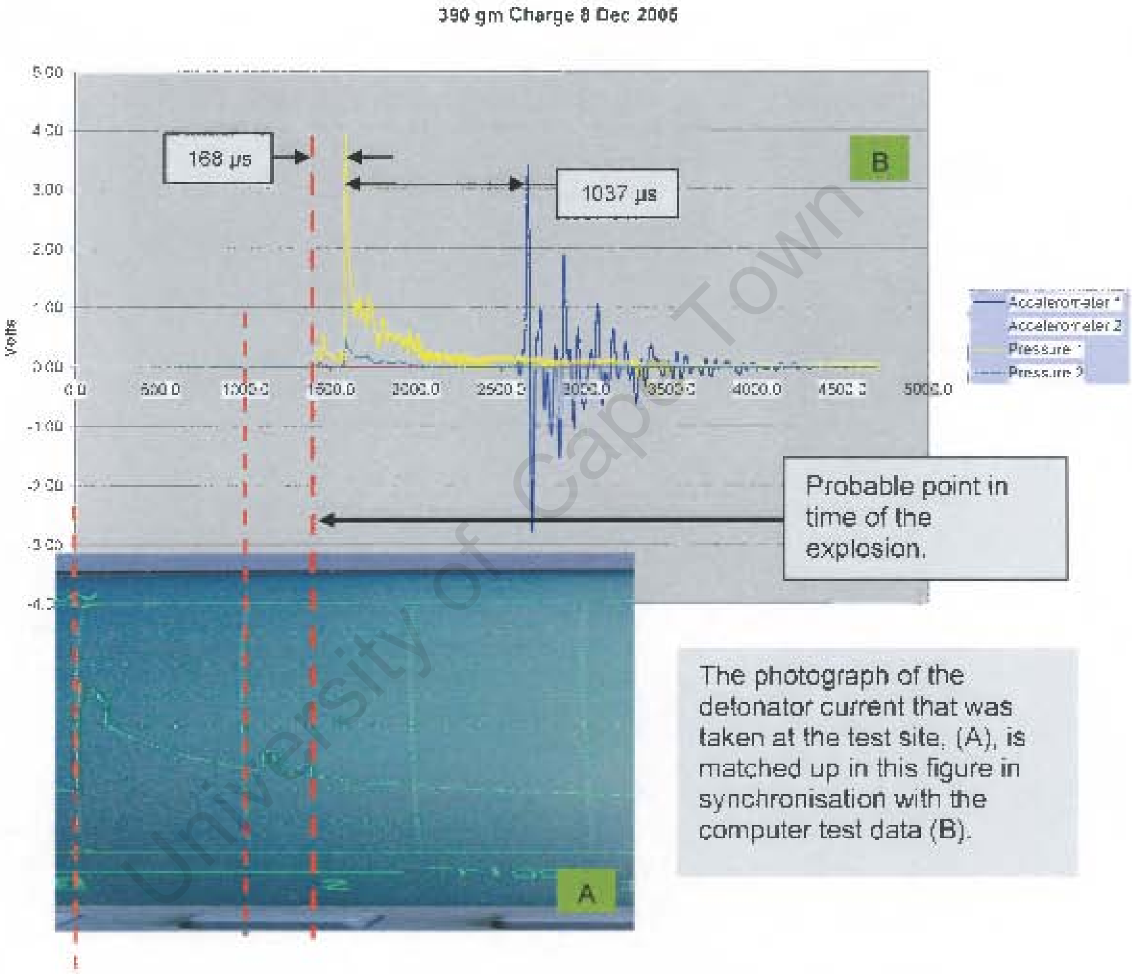

Probable point in time of the explosion.

The photograph of the detonator current that was taken at the test site, (A), is matched up in this figure in synchronisation with the computer test data (B).

Figure 117: All measurements of the four sensors in Volts, matched up with the detonator current

Synchronisation with the moment of detonation and the explosion could not be determined accurately in this experiment, due to the fact that the explosion occurred some indeterminate time after the leading edge of the detonator current. A photograph of the oscilloscope measurement of the detonator current was taken, and is shown in Figure 117. The horizontal axis of the photograph was increased to match the scale of the Voltage measurements.

An interesting phenomenon, which matches a measurement result, is seen on the detonator current curve shown in Figure 117 as the "probable point of explosion". Measurements of pressure are recorded before the actual shock pressure pulse reaches the sensors. This could be explained by the theory that an EM pulse is generated at the moment of explosion, and that this EMP causes electrical induction into the measurement (sensor) cables.

The explosion also causes ionisation of the detonator surrounds, which could explain the two prominent "humps", as seen in Figure 118, where the current increases for short periods (approximately 80 µs each). It is thought that the first "hump" is probably caused by the functioning of the detonator explosives (1 gram), and that the second "hump" is caused by the functioning of the explosives of the main charge. These latter considerations are not based on facts, and therefore it is suggested that this phenomenon is further investigated in future. Figure 118 shows two scaled views of this phenomenon.

As illustrated in Figure 117, the time taken from the leading edge of the pressure shock pulse to the start of the leading edge of the accelerometer measurement was measured to be 1037 µs. In Figure 117 the distance that the shock wave travelled from the time that the pressure pulse was taken to the time that the accelerometers started reacting, is shown to be (2281 mm – 630 mm) 1651 mm, recording an average pressure pulse velocity of (1651 mm / 1037 µs) 1592 m/s, as measured between the pressure sensor distance and the accelerometers. This is higher than the expected sound velocity (1470 m/s - 1500 m/s).

Also gathered from Figure 117, (if the assumption that the time origin of the explosion as shown in Figure 117 is true), the time taken for the shock wave to reach the (first) pressure sensors was 168 µs. The calculated distance from the explosive charge to the pressure sensors was 630 mm. This translates to an average shock wave velocity of 3750 m/s. Comparing the average shock wave propagation velocity between sensors with the average shock wave propagation velocity between the moment of explosion and the first sensors, leads to the conclusion that the shock wave velocity is non-linear, and that the average shock wave velocity of this specific charge for the first half meter is more than double the speed of sound in the water.

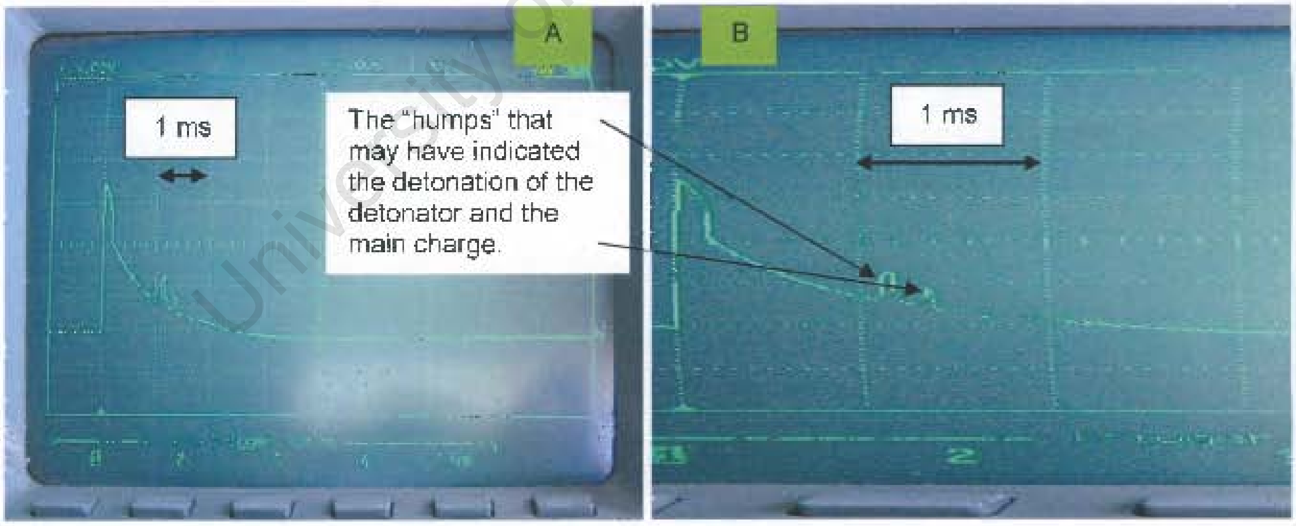

The "humps" that may have indicated the detonation of the detonator and the main charge.

Figure 118: The oscilloscope measurement of the detonator current on two time scales: B is a stretched-out version of A

5.1.4.7. Electronics damage analysis

The result of the blast effects on the electronics is shown in Figure 119 and Table 26.

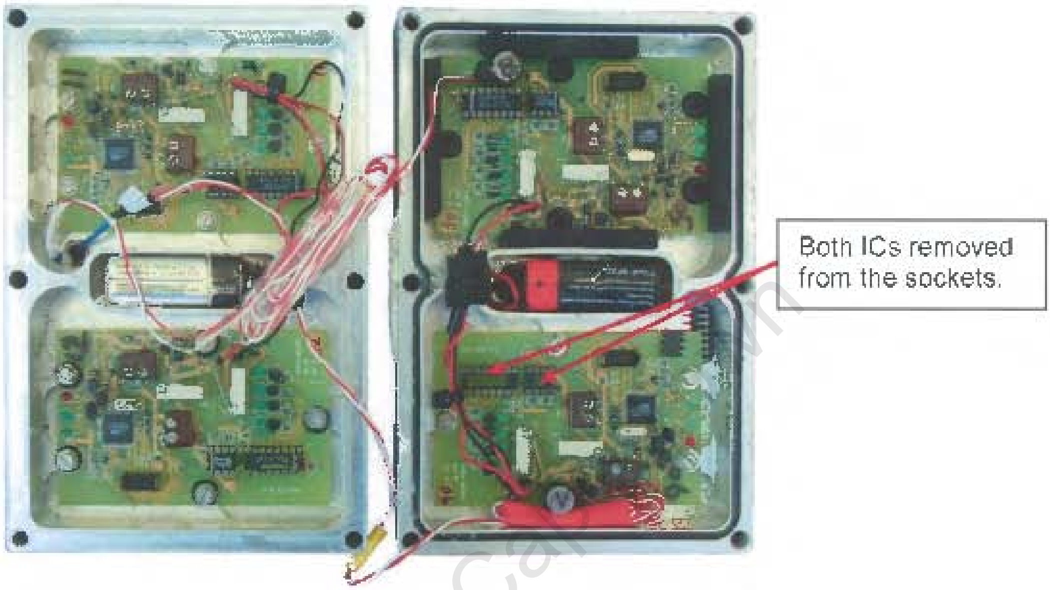
Both ICs removed from the sockets.

Figure 119: Electronics after the blast

Table 26: Electronic failure analysis

CCA Ser. No.	General Components	Remarks
05 (sponge mounted)	DIP Integrated Circuits	CCA is fully operational
	SM ICs	
	Crystal	
06 (hard mounted)	DIP Integrated Circuits	Both ICs removed from the sockets
	SM ICs	OK
	Crystal	OK
12 (grommet mounted)	DIP Integrated Circuits	CCA is fully operational
	SM ICs	
	Crystal	
11 (hard mounted)	DIP Integrated Circuits	CCA is fully operational
	SM ICs	
	Crystal	

The "soft-mounted" PCBs were in full working condition after the blast. The pressure peak at the electronics unit (stand-off distance = 2.281 m) is expected to be 15 MPa according to Cole [5] (see Figure 121). This pressure is equivalent to a 40 kg charge at a stand-off distance of 10.7 m.

5.1.4.8. Pressure measurement analysis

The measured pressures were below the expected values (Figure 120 and Figure 121 and Table 27. The reason could be that the calculated distance from the charge was smaller than the actual distance achieved during the experiment. The measured value corresponds to a stand-off distance of 0.73 m, instead of the calculated 0.63 m. This is very reasonable, given the fact that the frame (on which the sensors were mounted), was suspended by Polypropylene rope only. Movement of the frame relative to the float by 0.1 m is considered to be very reasonable.

Figure 120: Pressure history measurements

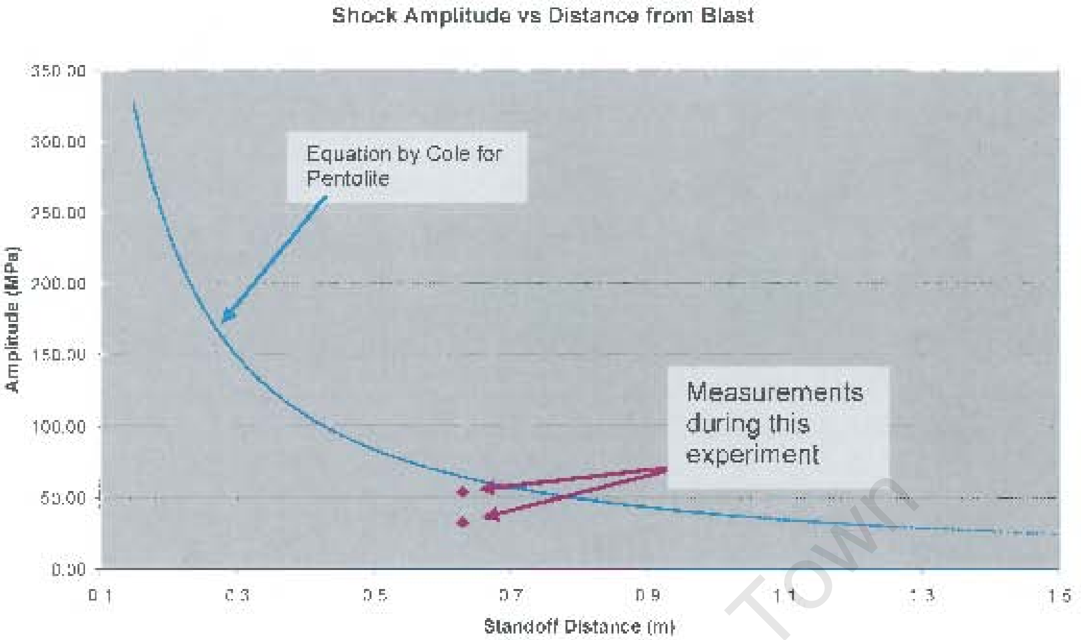

Figure 121: **Expected vs. measured pressures**

Table 27: **Pressure measurements**

	Standoff Distance (m)	Pressure (MPa)
Pressure Sensor 1	0.63	54.13
Pressure Sensor 2	0.63	32.69

5.1.4.9. Motion Analysis

The acceleration history is shown in Figure 122. The acceleration attenuation accomplished by in experiment, was 22 dB, compared to 17.7 dB and 18.7 dB (see page 128) obtained when grommet mountings were used.

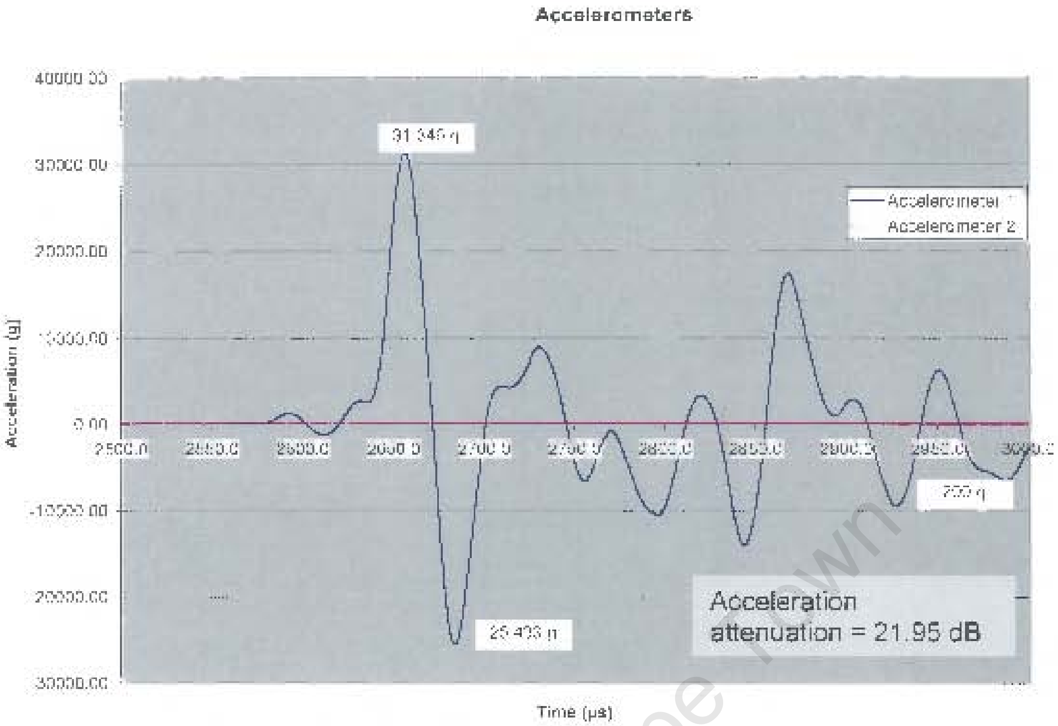

Figure 122: Acceleration measurements

The acceleration results are tabulated in Table 28, and are compared with previous results in Table 29.

Table 28: Acceleration analysis

Positive Peak (g)	Negative Peak (g)	First Full Cycle Period (µs)	Max CCA acceleration (g)	Delay from pos peak to Max on CCA (µs)
31 346	-25 433	64.5	200	321

Table 29: Acceleration analysis of previous experiment

Blast No	Positive Peak (g)	Negative Peak (g)	First Full Cycle Period (µs)	Max PCB acceleration (g)	Delay from pos peak to Max PCB (µs)
1	15309	-11490	62	259	342
2	17224	-12498	60	235	327

From the result obtained in this experiment, it was clear that the sponge rubber damping method had improved damping characteristics when compared to the standard grommet suspension method for this specific Electronics Enclosure. The attenuation for the sponge rubber mounts gave an approximate 2.5x advantage over the grommet mounts.

An interesting observation concerns the comparative period measurements: All three full-cycle periods were in the order of 60 µs, and the delays to the CCA peak accelerations were in the order of 330 µs.

The motion of the Electronics Enclosure and the CCA is shown in Figure 123. The time reference was shifted (relative to Figure 122) for clarity of reading. The velocity was obtained by integration of the acceleration, and the displacement was obtained by integration of the velocity. The integration constants were discarded. Figure 123 shows that the displacement of the Electronics Enclosure during the first 14 ms after the shock wave collided with the Enclosure. The displacement of the Enclosure was approximately 5 mm.

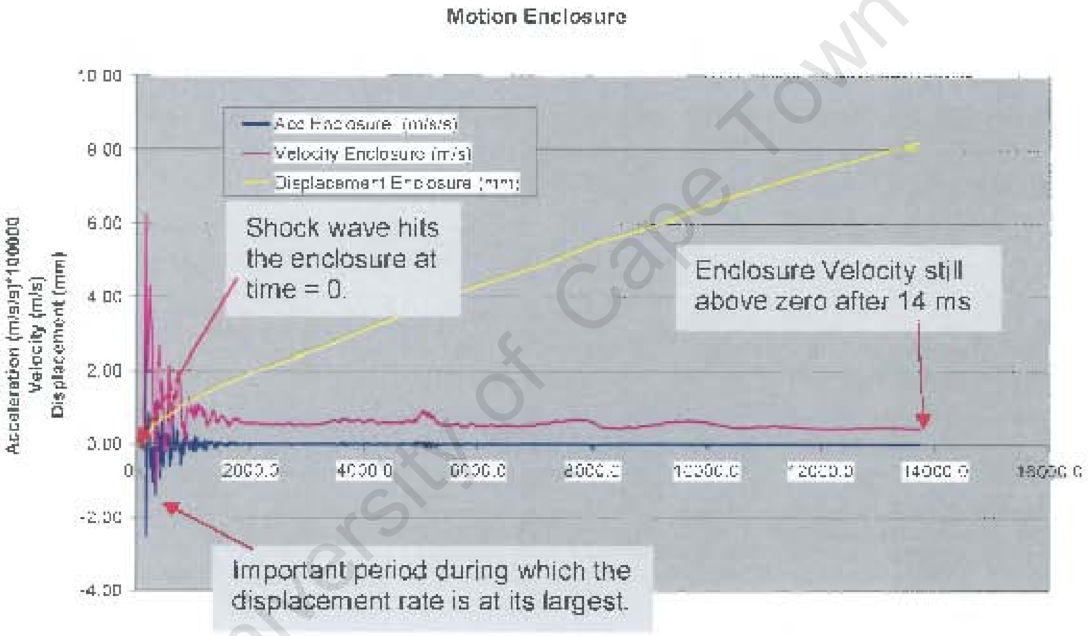

Shock wave hits the enclosure at time = 0.

Enclosure Velocity still above zero after 14 ms

Important period during which the displacement rate is at its largest.

Figure 123: The motion of the Electronics Enclosure under shock wave load

The motion of the CCA that was contained within the Enclosure, and which was suspended by means of sponge rubber (only), is shown in Figure 124. The time reference was taken to coincide with the accelerations in Figure 123, for reasons of comparison. As was expected, the acceleration of the CCA was much less than the acceleration of the Enclosure, but extended over a longer period. Consequently, the velocity and the displacement were also lower. The velocity had not reached zero during the 14 ms that is depicted by the graph, which means that the CCA had not reached its point of equilibrium, where all the oscillations that were caused by the blast had faded out. This was confirmed by the displacement graph which shows that no steady state had been reached.

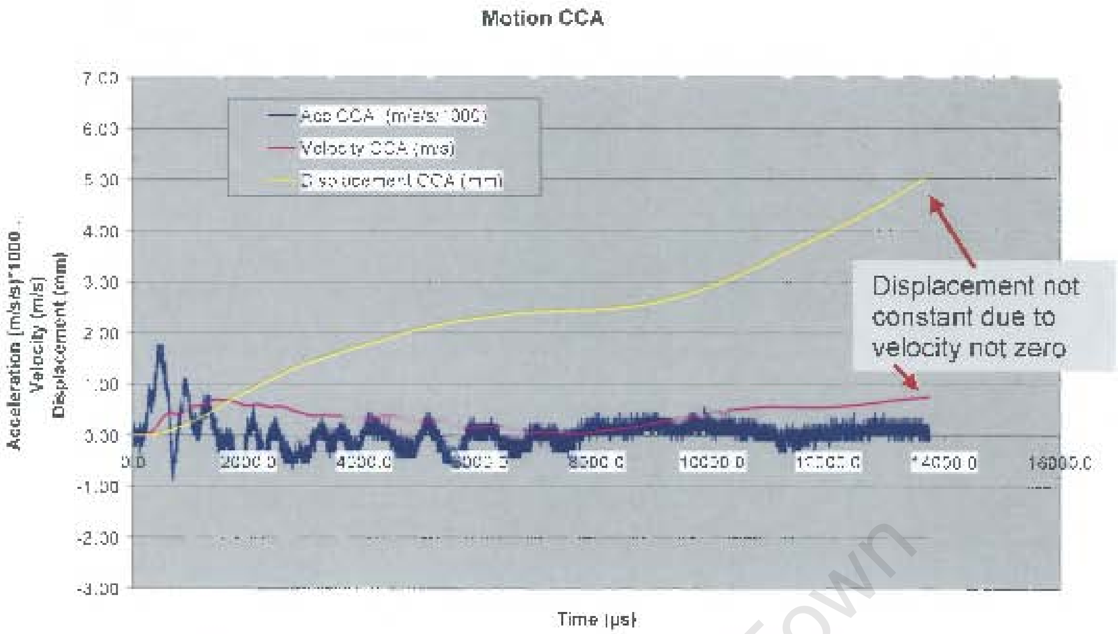

Figure 124: **The motion of the CCA contained within the Enclosure, under stress from the movement of the enclosure**

For Figure 125 the displacement of Figure 123 and that of Figure 124 were plotted together, to examine the relative movement. The resulting graph (in yellow) was the relative displacement when the displacement of the CCA was subtracted from the displacement of the Enclosure. In a steady state, this resulting displacement would be zero, and the two relevant displacement graphs would end at the same point (not zero). The relative displacement reached a maximum of approximately 4.5 mm, which is plausible due to the fact that the suspending sponge rubber allowed more movement than the grommet due to its softer structure.

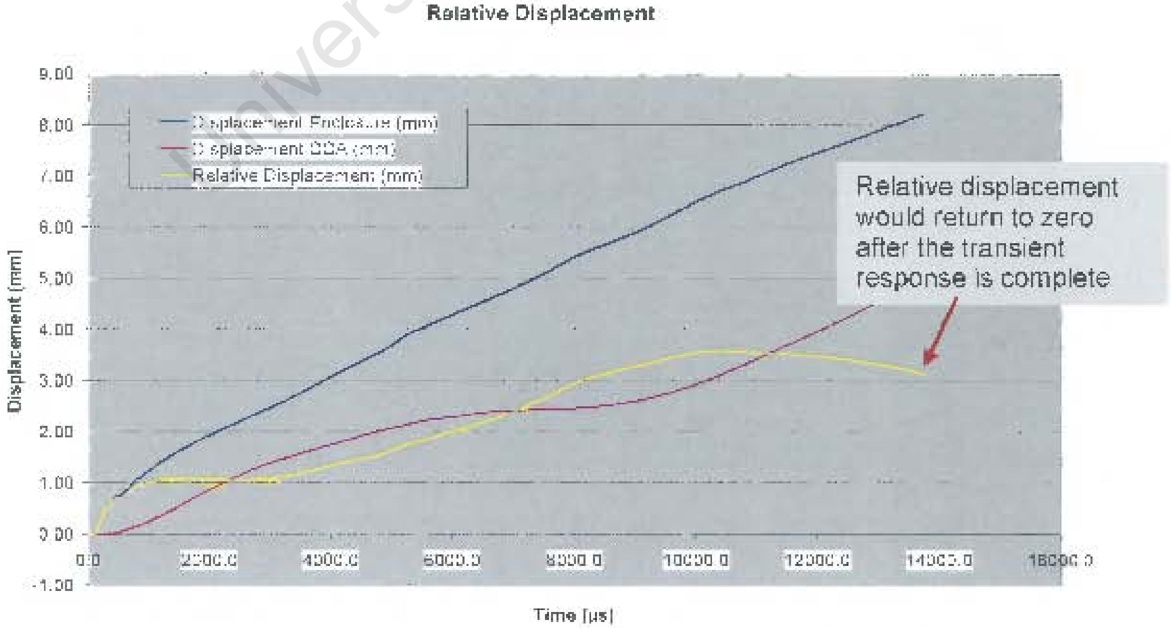

Figure 125: **The relative displacement between the Electronics Enclosure and the CCA under shock loading**

5.1.4.10. Acceleration Scaling

According to Newton's second law, it is to be expected that a linear relationship exists between force, mass, and acceleration.

Cole [5] has formulated the fact that there is a non-linear relationship between the peak shock pressure of an underwater explosion and the stand-off distance for a certain explosive mass, when detonated.

The data tabulated in Table 30 were captured during the various experiments of this project for measuring acceleration of a specific Aluminium box containing electronics, when subjected to different charge sizes and stand-off distances. The result is presented graphically in Figure 126.

Table 30: Relationship between peak pressure and acceleration

Charge size (gm)	Positive half cycle (g)	Standoff Distance (mm)	Standoff Distance (radii)	Theoretical Expected Peak Pressure (MPa)
390	31346	2281	58.8	15
30	17224	1964	119.1	6.8
30	15309	1959	118.8	6.8
30	50788	675	40.9	22.7
30	57630	675	40.9	22.7

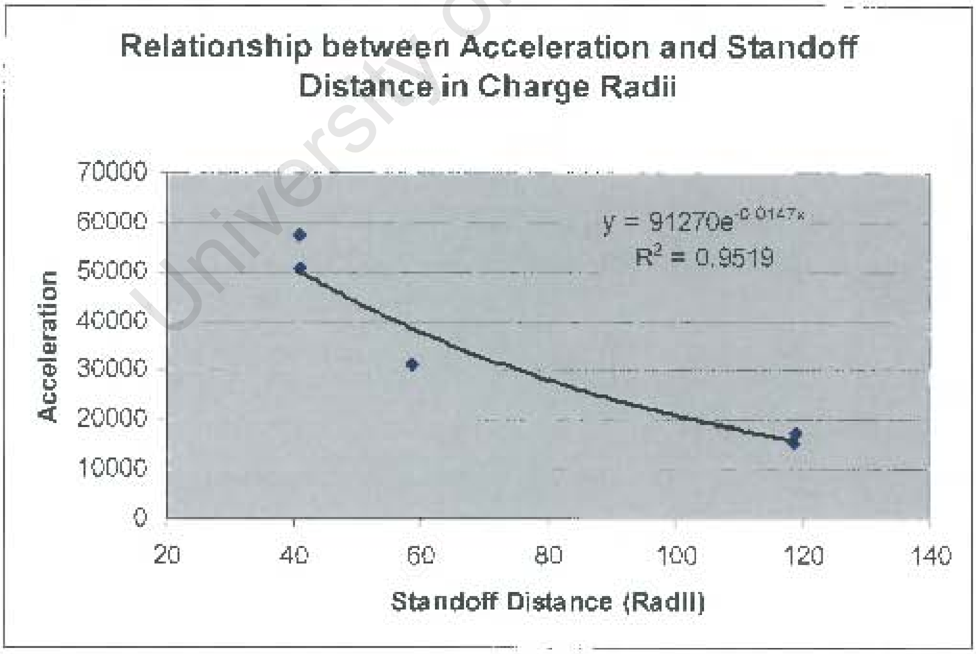

Figure 126: Relationship between peak Enclosure Acceleration and standoff distance

The data gathered from the three experiments (5 events) during which acceleration measurements were taken, were used for the investigation into acceleration scaling (see Figure 126). A trend line was drawn for a non-linear exponential option.

Although a good correlation is shown in Figure 126 ($R^2 = 0.9519$), the number of data points and the variation in acceleration measurements were considered to be not enough to determine the exponential relationship to a required degree of accuracy, especially in the region closer than 40 radii from the blast.

5.1.4.11. Conclusions

1. The result that this experiment set out to obtain had been achieved: The acceleration attenuation had been improved substantially by using the sponge rubber mounts in stead of the grommet mounts. The protection of the electronics against shock had improved, but further experiments at stand-off distances closer to the explosion are now required to determine whether the target user requirement is met.
2. The blast shock wave propagation velocity between sensors was larger than the speed of sound. This indicated that measurements were taken in the near field.
3. The pressure measurement from Pressure Sensor 2 is suspect, due to the much lower amplitudes measured. No definite conclusion could be drawn from this measurement.
4. Pressure Sensor 1 measured the peak pressure to be in the order of the value as predicted by Cole [5].
5. The acceleration analysis indicated that the first cycle acceleration characteristics were nearly identical to previously measured accelerations.
6. No conclusion could be drawn (yet) for the relationship between peak pressure and acceleration, due to the small number of data points.
7. The synchronisation of the measurements with the moment of blast had not been achieved due to the varying time between detonator current start-of-flow and detonator functioning.

5.1.4.12. Recommendations

Refer to conclusion 7 above: It is recommended that the moment of explosion of the charge is measured (possibly by light-detection techniques) to determine the reference point of measurement cycles.

5.1.5. Experiment 5: Experiment which included only Pressure Sensors

5.1.5.1. Purpose

During previous execution of the measurement of time-related incidents during underwater explosions, some difficulty was experienced with correlating the recorded data with the moment of the explosion (see paragraph on **Recommendations** on page 148).

The synchronisation was effected by measuring the current flow through the detonator. Some detonators have characteristics which would render this method practical for some applications, but the time difference between the detonator current and the actual main charge completing the detonation process mostly varied too much to take delicate measurements of, e.g., the shock wave propagation velocity in the near field.

This experiment investigated the possibility of using a photo transistor (or array of photo transistors) to sense the flash that is produced when an underwater explosion occurs. Due to the fact that light travels much faster than any other known phenomenon in a transparent medium, the measurement of the flash of the explosion was a good method for determining the moment of explosion.

To validate the measurements, the average shock wave velocity was determined through the measurement of the shock wave pressure at predetermined positions, and using the light measurement as a time marker. A good correlation between blast events would mean that a solid time marker had been obtained.

5.1.5.2. Methodology

An optical sensor was designed to give a high (10 V) voltage output when the flash of the explosion occurred. In the dark water, the optical sensor had a low voltage output (close to 0 V). The amount of light that was expected from a light flash of an explosion was not known; therefore the methodology was to include repetitions with altered designs should the first estimation be incorrect

The experiment was designed to place two pressure sensors in close proximity to a 30 gm PE4 charge, and to place the light sensor approximately 0.5 m from the charge.

Five blast events were planned to be executed, in three of which the two pressure sensors were placed at the same distance from the blast as the light sensor, and in two of which the pressure sensors were placed at greater distances from the blast.

The rationale was to calculate the average propagation velocity of the shock wave by measuring the time that elapsed from the moment of the explosion as measured by the light sensor until the time of the shock wave's arrival at the pressure sensors at two predetermined distances from the blast. The experiment would be successful if the calculation of the average shock wave velocity between the equidistant points would correlate above 99%, and the light sensor output would give a sharp rising edge <5 µs, which could be used as the time marker of the blast event.

5.1.5.3. Experimental Setup

A 30 gm PE4 charge was mounted at the centre of the bottom plate (see Figure 127). For blast events 1 through 3, the Pressure Sensors were mounted close to the outer corners of the pyramid base, while during events 4 and 5 they were mounted on the edges (see Figure 128). The position of the light sensor is shown in Figure 130.

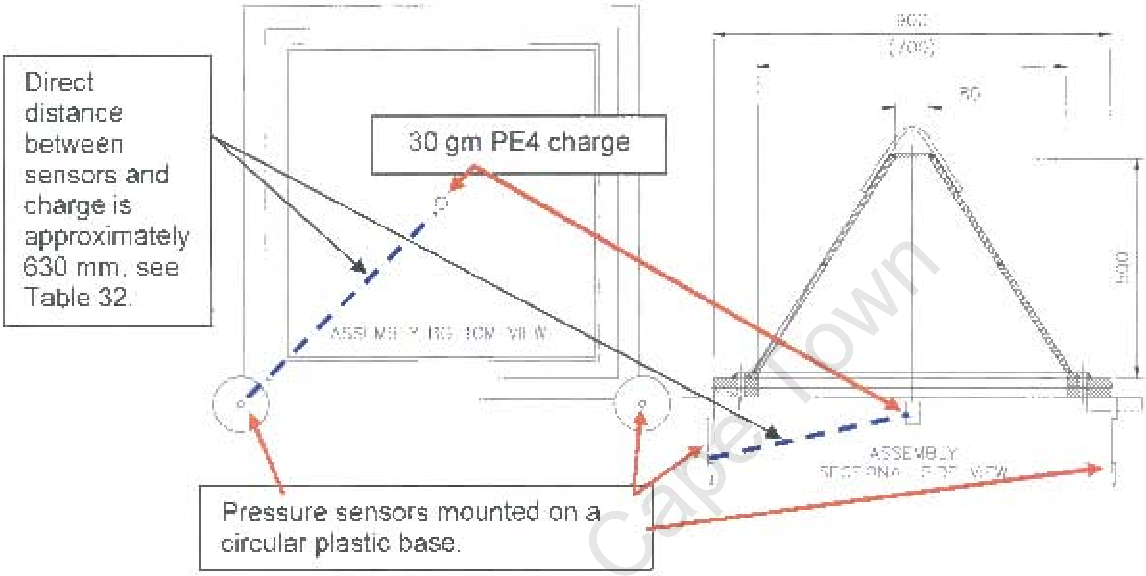

Direct distance between sensors and charge is approximately 630 mm, see Table 32.

30 gm PE4 charge

Pressure sensors mounted on a circular plastic base.

Figure 127: Mechanical details of blast events 1 through 3 for this experiment

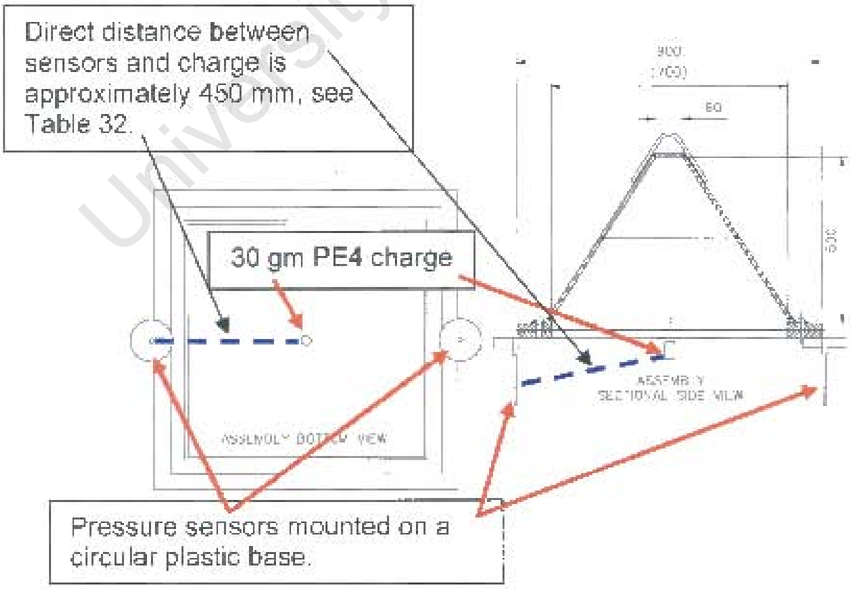

Direct distance between sensors and charge is approximately 450 mm, see Table 32.

30 gm PE4 charge

Pressure sensors mounted on a circular plastic base.

Figure 128: Mechanical details of blast events 4 and 5 for this experiment

5.1.5.4. Equipment

5.1.5.4.1. The Optical Sensor

One of the characteristics of a shock wave that is known to contribute to damage inflicted upon a blast loaded object (e.g. a ship's hull), is the speed at which the shock wave propagates. At the boundary condition, where the shock wave is transmitted from the exploded mass to the surrounding water, the speed of the shock wave is at its highest value (see Chung & Kinsey [3]). The measurement of the speed of the shock front has therefore become an important measurement quantity in the determination of resultant damage. This experiment measured the average speed of the shock wave at two stand-off distances, using a custom optical sensor to determine the time origin of the explosion by capturing (and marking the start of) the light that the burning material produces. The optical sensor consisted of a string of 12 optically sensitive transistors, connected in parallel (see Figure 129). The transistors were connected to a 20 m RG58 co-axial cable with BNC termination, and potted with Elite FR-766 polyurethane potting in a small plastic holder.

Figure 129: The optical sensor

The optical sensor was directly powered by a conditioning amplifier (model PCB Piezotronics 482A22). The conditioning amplifier supplied a constant current (limited at 17 mA) to the sensor. When the flash of the explosion occurred, the light produced by the explosion reduced the forward resistance of the parallel transistors.

The light produced by the explosion of 30 gm of PE4, at a stand-off distance of approximately 0.6 m, was expected to produce enough photons to push the sensor to its saturation limit. This was designed to produce a sharply rising leading edge when the light was applied. No small changes of light intensity were registered when the sensor was in the saturation mode. The change in current through the transistors was passed through the signal conditioner to its output as a voltage, and was measured by the DAQ equipment.

The optical sensor was placed on the side of the test sample in a position where it could sense the flash, yet not be damaged by the blast. It was secured onto the test sample, using 3M double-sided adhesive tape (approximately 3 mm thick) to enable it to tear loose without sustaining damage during the explosion. Figure 130 shows the position of the optical sensor on the underside of the test unit, relative to the charge position.

Figure 130: The position of the optical sensor relative to the explosive charge and the Pressure Sensors

The position of the pressure sensors was moved from the position shown in Figure 130 (for Events 2 and 3) to a nearer position relative to the explosive charge, as shown in Figure 131, for Events 4 and 5.

Figure 131: The new position of the Pressure Sensors for Events 4 and 5

5.1.5.4.2. *Signal Conditioner*

The pressure sensors had built-in charge amplifiers, and required special conditioning amplifiers (see Figure 132) to supply the constant excitation current for the built-in charge amplifiers, and thereby to extract the pressure measurements as were superimposed upon the excitation current signal. This signal conditioning amplifier was also suitable for supplying the drive conditions of the photo sensor.

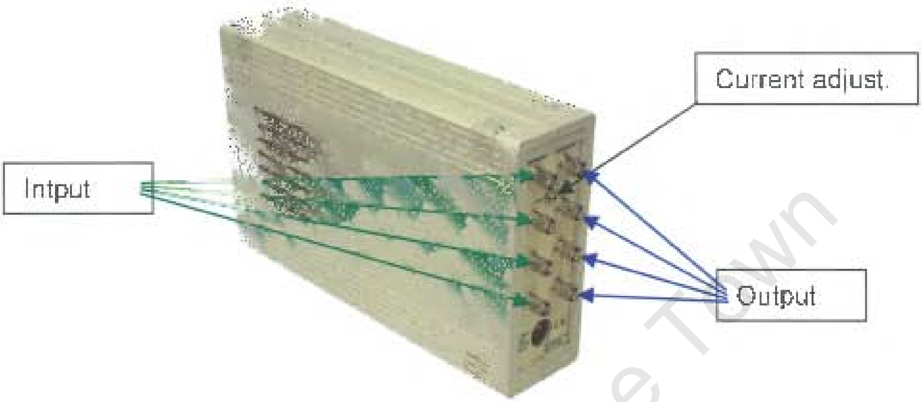

Figure 132: The 4-channel signal conditioner, PCB Piezotronics model 482A22.

5.1.5.4.3. *Pressure Sensors*

To measure the pressure amplitudes of the explosions at certain stand-off distances, two Tourmaline piezo-electric sensors with built-in charge amplifiers were used. These were specially designed for the measurement of pressure shock waves as would be produced by underwater blast. The specifications are shown in Appendix 2. Two models were used, i.e. one 138A10, and one 138A50. The only difference between the two models involved the sensitivities as listed in Table 31.

Table 31: Sensor sensitivities

Model	Calibrated Sensitivity (mV/MPa)	Max Pressure (kpsi)	Max Pressure (MPa)
138A10	73.57	10	69
138A50	12.32	50	345

An RG58C/U co-axial cable of 25 m in length was attached to each sensor via a connector at both ends. To measure the explosion pressure result, these sensors and cables were connected to a PXI-format DAQ card capable of measuring four channels, with each channel sampling at 2 MS/s. The card memory could store up to one second of data samples.

5.1.5.4.4. Custom Synchronisation Equipment

The measurement recording equipment had memory to record only 1 s of data in the four channels. Synchronisation of the fire command with the start of the measurement cycle, was essential, and had to be well within the 1 s memory limitation to be able to capture all the required data. This was obtained by means of a custom-built unit (see Figure 133) by simply measuring the current that the military SAFU supplied to the detonator when the firing command was given. When this current exceeded a predetermined threshold, a TTL trigger pulse was generated. This TTL trigger pulse was fed to the DAQ equipment as an external trigger to start the measurement cycle. The measurement cycle therefore started when the detonator current exceeded a threshold, and thus allowed enough time for the measurement of the required data. As can be derived from Table 36, the required data recording starting point ranged between 2.024 ms and 11.467 ms.

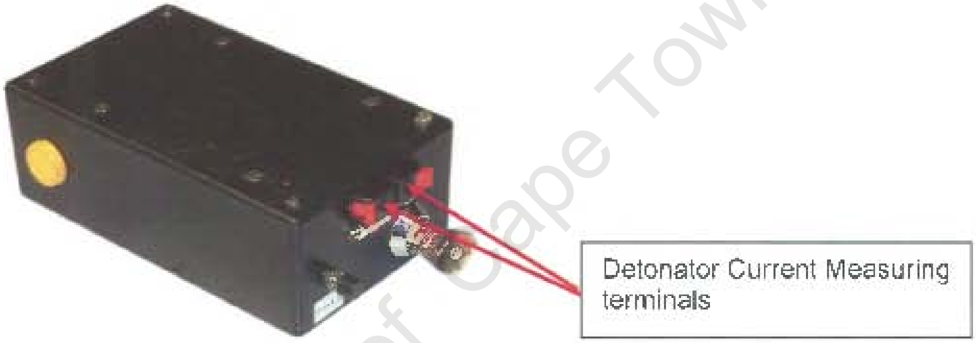

Figure 133: The custom-built synchronisation unit

The current through the detonator was measured on previous occasions during blast experiments, and it was found that the explosion occurred in a time zone of "milliseconds" rather than "microseconds". It was also found that the time taken for the explosion to occur after the detonator current was applied, varied by several milliseconds. This fact precluded this synchronisation method from being used as a time-of-explosion marker, but it was a reliable method for starting the measurement cycle.

5.1.5.5. Results and Analyses

A total of five charges were detonated for this experiment. Measurement results were obtained for four events. The first event experienced a sub-system power loss, and no data was recorded. Data for Events 2 through 5 were recorded successfully.

5.1.5.5.1. Pressure Measurements

Pressure measurements were recorded through two pressure sensors per event. For Events 2 and 3, the pressure sensors were positioned at the corners of the test jig, giving a direct (measured) linear distance from the charge to the sensors of typically between 625 mm and 635 mm (see Figure 130 for the position of the Pressure Sensors and Table 32 for actual measurements). For Events 4 and 5, the pressure sensors were moved to the centre position of the pyramid test jig edge, giving a stand-off distance of between 445 mm and 465 mm (see

Figure 131 for new Pressure Sensor positions). The peak pressure results are recorded in Table 32.

Table 32: Measurements of the pressure amplitudes as recorded for both pressure sensors during Events 2 to 5

	Peak Pressure Measurements			
	Event 2	Event 3	Event 4	Event 5
Stand-off Distance to Sensor 1 (mm)	630	625	460	445
Stand-off Distance to Sensor 2 (mm)	630	620	455	465
Measurements from Pressure Sensor 1 (MPa)	24.5	21.0	29.0	36.1
Measurements from Pressure Sensor 2 (MPa)	18.6	18.4	26.5	26.5

The peak pressures were recorded on a graph, shown in Figure 134, superimposed on a graph of the predicted peak pressures according to an Equation given by Cole [5: p239].

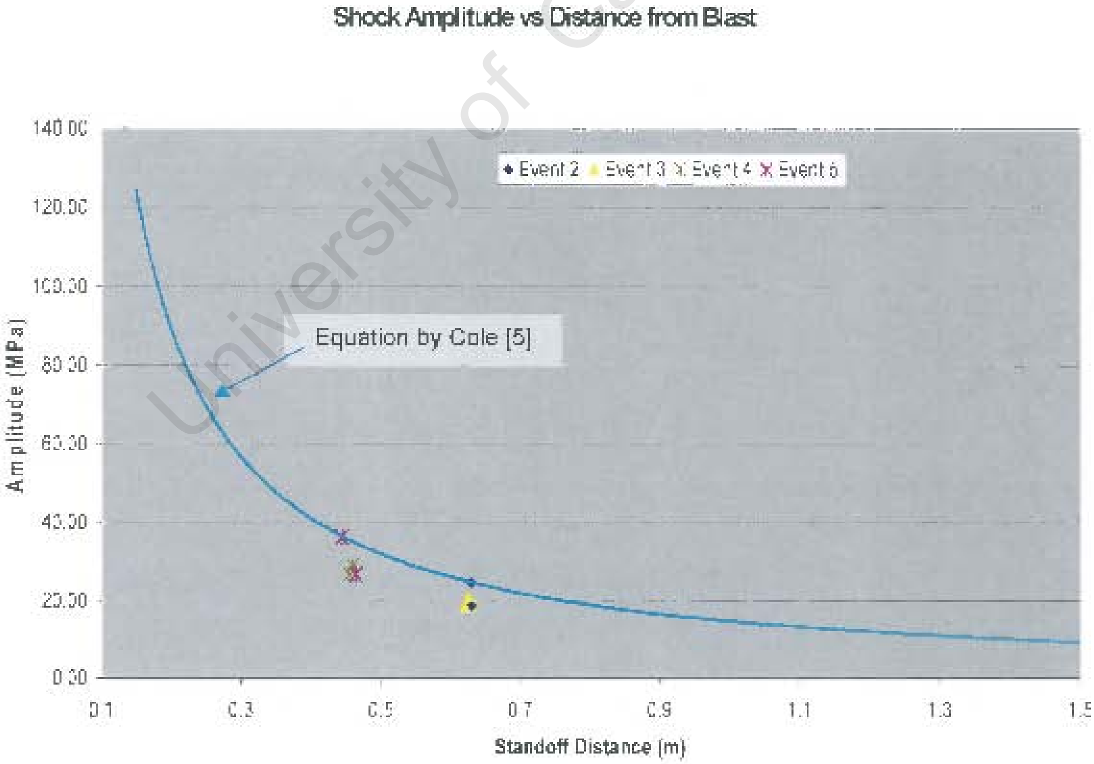

Figure 134: **The pressure results as compared to the equation given by Cole, and referenced to standoff distance in m**

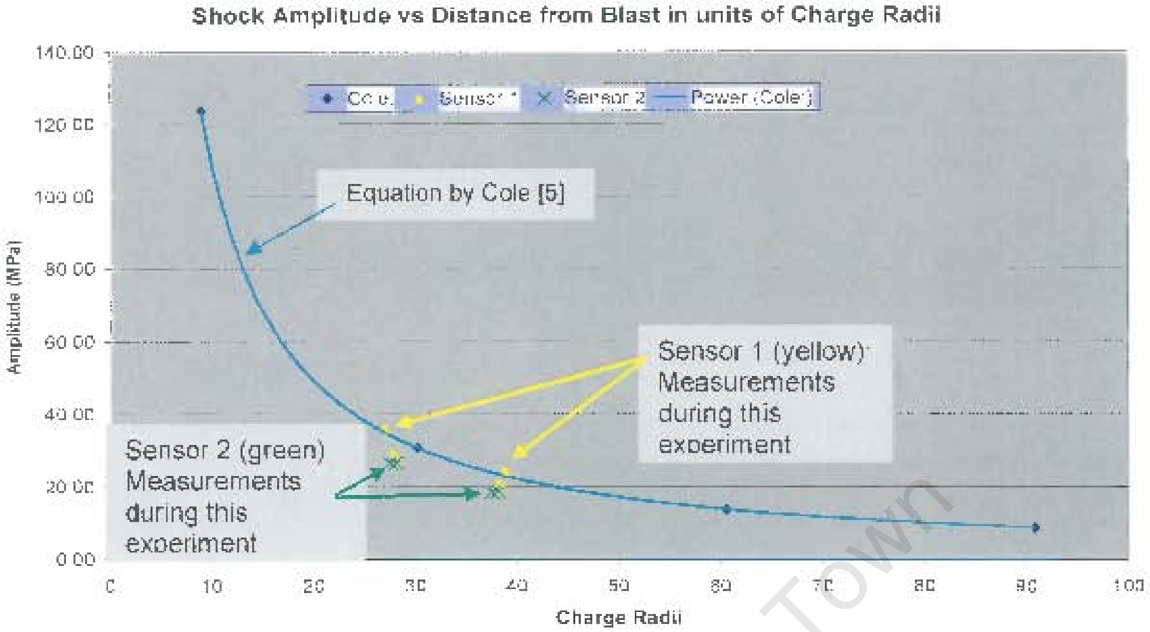

Figure 135: **The pressure results of Figure 134, with the stand-off distance referenced to the number of charge radii**

The pressure histories of the measured results are shown in Figure 136 to Figure 139. The time reference in each of these graphs is taken from the moment of explosion (t = 0) of the main charge as measured from the rising edge of the optical sensor.

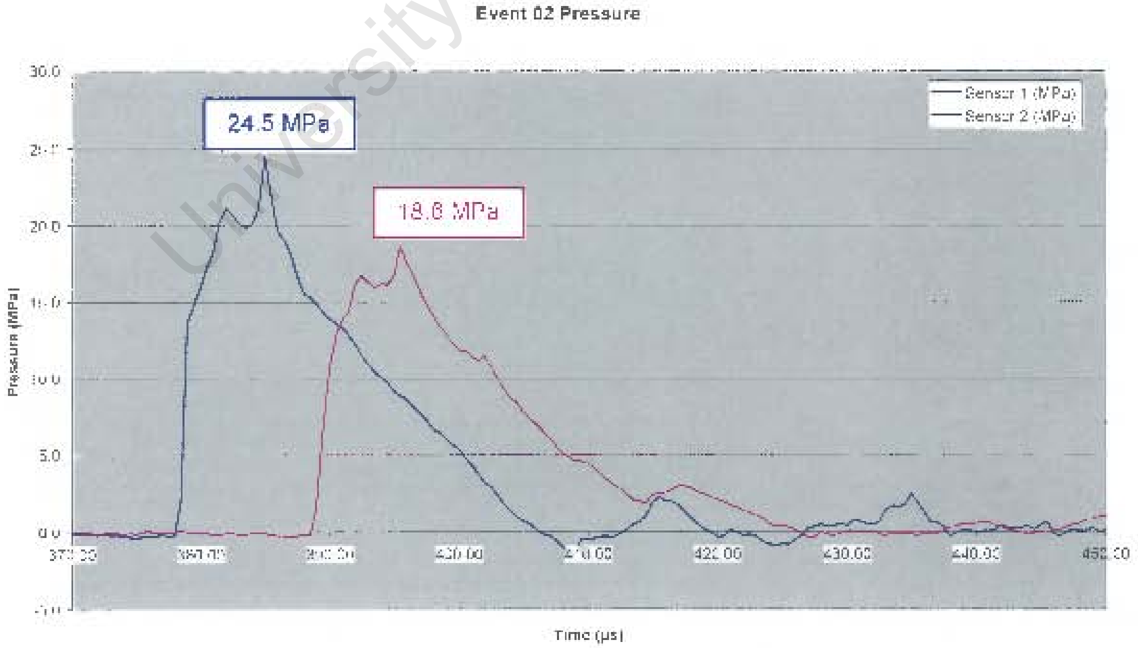

Figure 136: Pressure history of Event 2 in µs and MPa

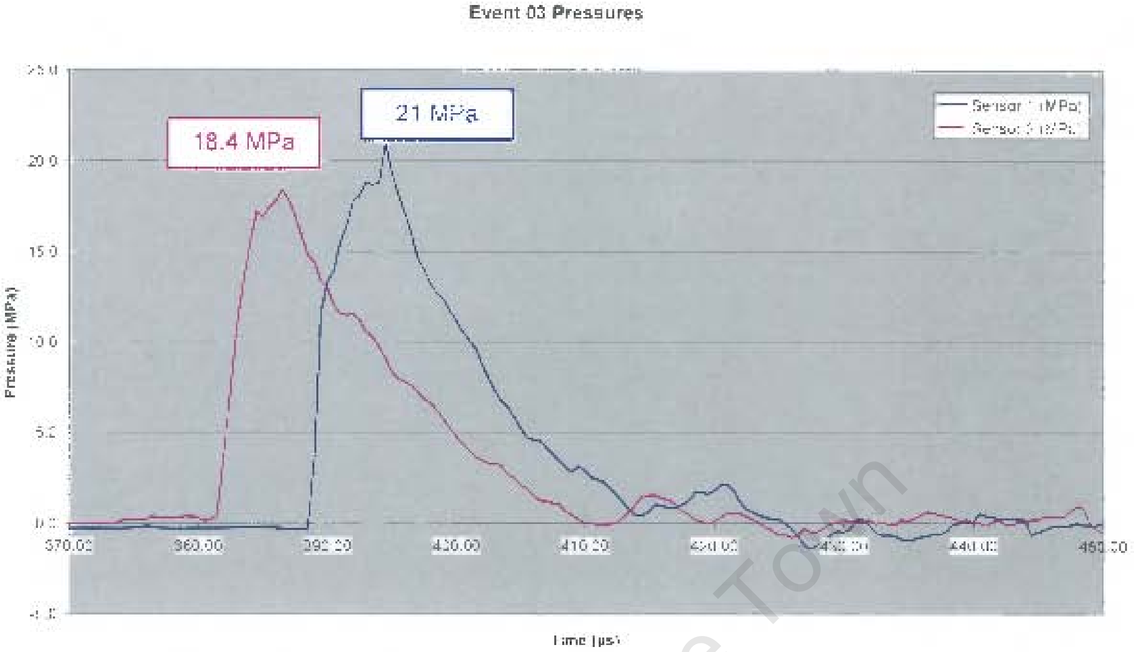

Figure 137: Pressure history of Event 3 in µs and in MPa

Figure 138: Pressure history of Event 4 in MPa

Figure 139: **Pressure history of Event 5 in MPa**

5.1.5.5.2. *Average Shock Wave Propagation Velocity*

To measure the actual time that was taken for the pressure shock wave to travel from the point of detonation to the pressure sensors, the leading slope measurement output from the optical sensor was used as t = 0. Figure 140 to Figure 143 show the time reference of explosions relative to the arrival of the shock pressure at the two pressure sensors.

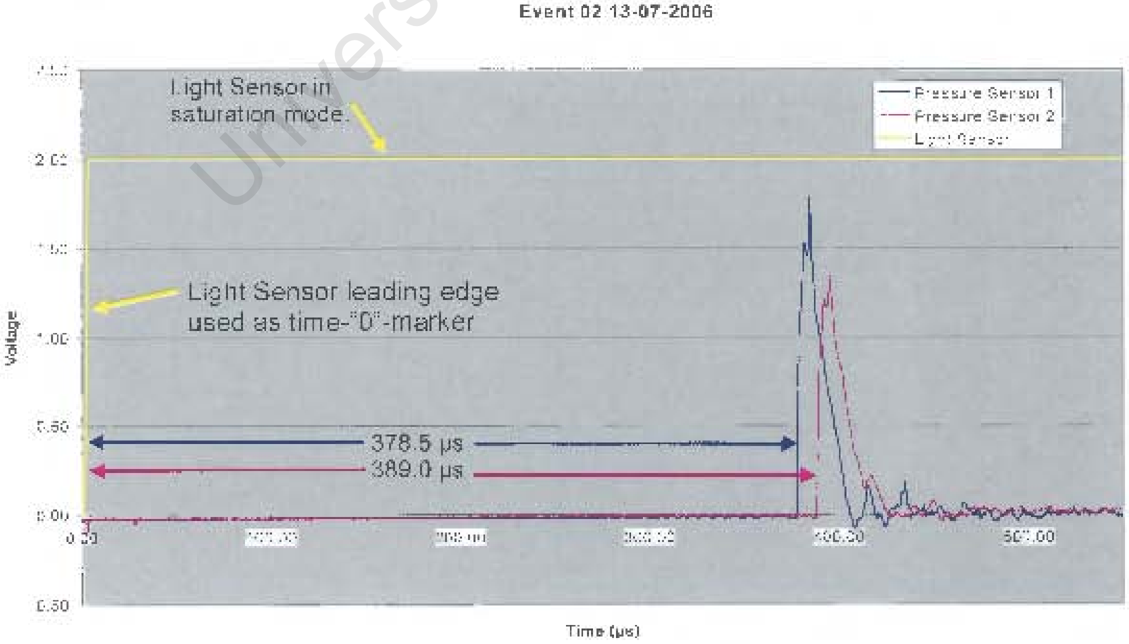

Figure 140: **Event 2 Pressures in Volt, relative to the Optical Sensor – time reference point 0 = time of explosion**

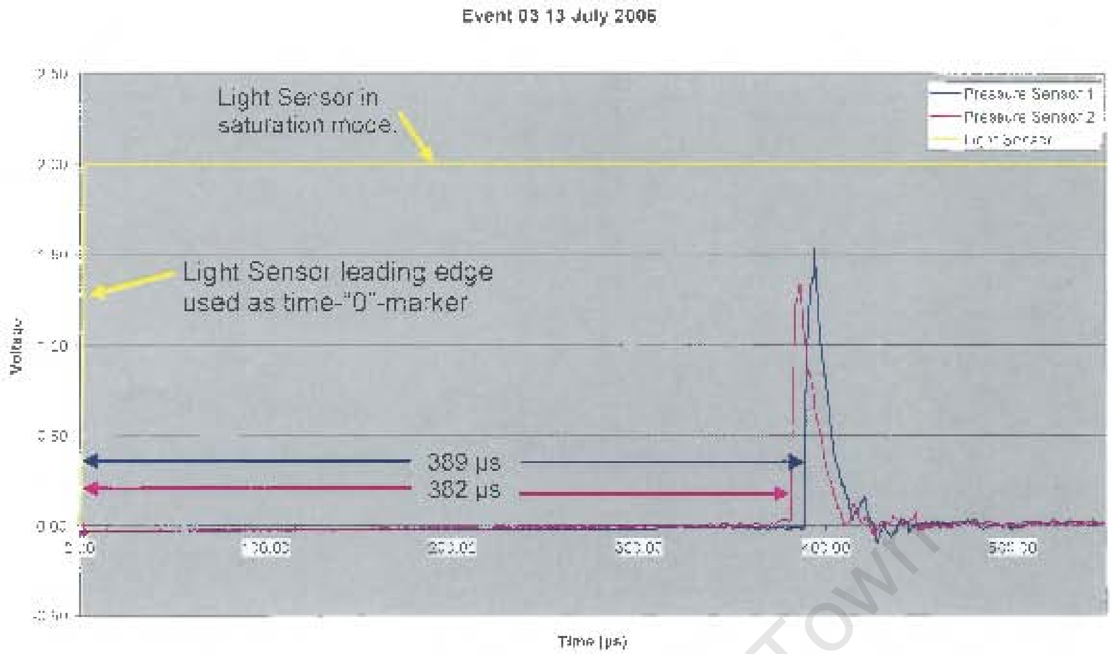

Figure 141: Event 3 Pressures in Volt, relative to the optical sensor – time reference point 0 = time of explosion

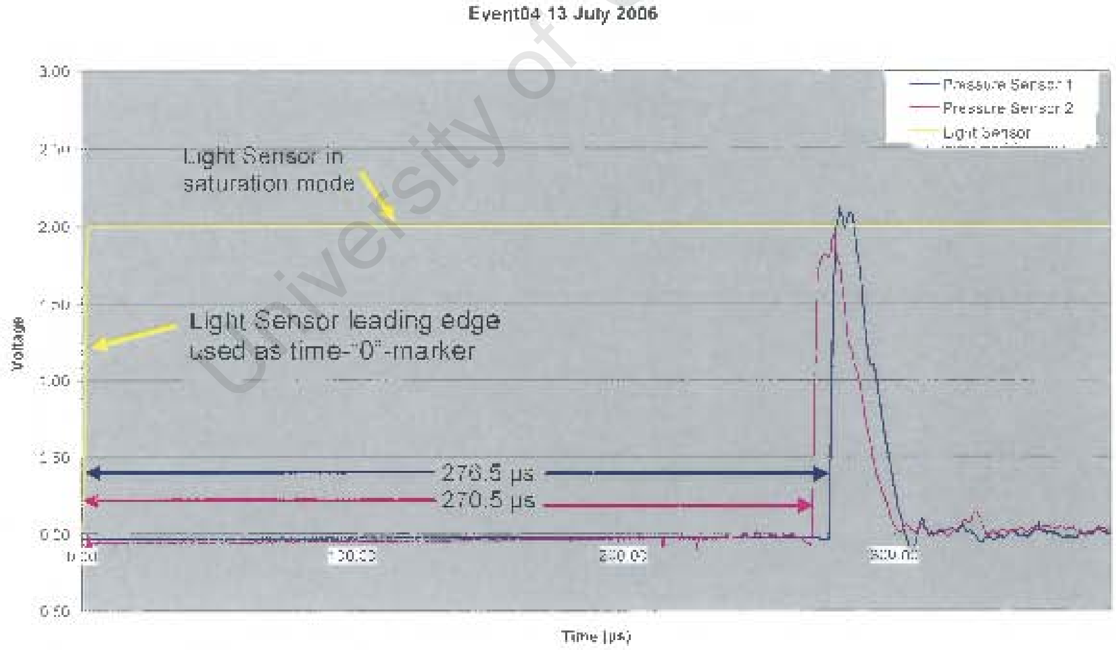

Figure 142: Event 4 Pressures in Volt, relative to the optical sensor – time reference point 0 = time of explosion

Figure 143: **Event 5 Pressures in Volt, relative to the optical sensor – time reference point 0 = time of explosion**

The linear distances measured from the charge to the pressure sensors do not represent accurate figures (to single millimetres or parts of a millimetre), due to the flexibility of the pressure sensor containment mechanics, and the fixing method allowing for the sensors to hang from a single fixing mechanism at the base of the sensor (see Figure 130). The measurements were accurate enough, however, to determine the average speed from the moment of the explosion to the moment when the shock wave arrived at the sensors. The result is shown graphically in Figure 144.

Note: The result shown in Figure 144 is an average speed at certain distances from the explosion time-origin. It must be born in mind that the speed closer to the origin is higher (Cole [5:p5]) than at the measured locations, and also that the speed function is non-linear at several charge radii from the explosive charge. The complete near-field speed function therefore cannot be derived from these measurements only. From Table 34, however, it is clear that the measurements were indicative of a near-field location of the pressure sensors. It was expected that the pressure sensitive elements would (or may) move around when the test station was submerged due to the physical flexibility of the sensors in the moving sea water. However, Figure 144 shows that there was good correlation between measurements, and that the average speed was calculated to be above 1500 m/s, therefore the average speed of the shock wave during this experiment was above the speed of sound.

The results are tabulated in Table 33. and the resulting speed calculations are tabulated in Table 34. The results showed a trend that was expected, because it clearly showed that the sensors that were positioned closer to the explosion yielded a larger average speed than the sensors that were positioned further away. The additional information that could be extracted, was that the speed of the shock wave calculated from data generated between the two sensor positions showed that the speed of the shock wave had already reduced to an average value of 1549 m/s (see Figure 132) (which was still above the speed of sound).

Table 33: **Measurements and calculations of the Pressure Sensor positions from the explosive charge, with corresponding calculated average speed**

Event No	Direct Distance to Pressure Sensor 1 (mm)	Direct Distance to Pressure Sensor 2 (mm)	Time measured to Pressure Sensor 1 (µs)	Time measured to Pressure Sensor 2 (µs)
1	630	640	Not measured	Not measured
2	630	640	378.5	389.0
3	630	620	389.0	382.0
4	460	455	276.5	270.5
5	445	465	266.5	276.0

Table 34: Speed calculations from Table 33

Event No	Average Direct Distance to Pressure Sensors (mm)	Average time to Pressure Sensors (µs)	Average speed to Pressure sensors (m/s)
2 and 3	630.00	384.63	1637.9
4 and 5	456.25	272.50	1674.3

Table 35: Average speed calculations between sensors

Average time between sensor positions 1 and 2 (µs)	Average distance between sensor positions 1 and 2 (mm)	Average speed between Pressure Sensor positions 1 and 2 (m/s)
112.13	173.75	1549.5

The peak pressure measurement results are tabulated in Table 32. The pressure results (see Figure 134) indicate that a fair comparison with the Equation for peak pressures that were defined by Cole [5:p239], had been achieved. Cole stated that his Equation for peak pressure was valid up to 10 charge radii from the blast. The distance of the pressure sensors in this experiment was >30 charge radii, using 30 gm of PE4. The graph in Figure 134 taken from the equation by Cole [5:p239], was drawn starting from 10 charge radii.

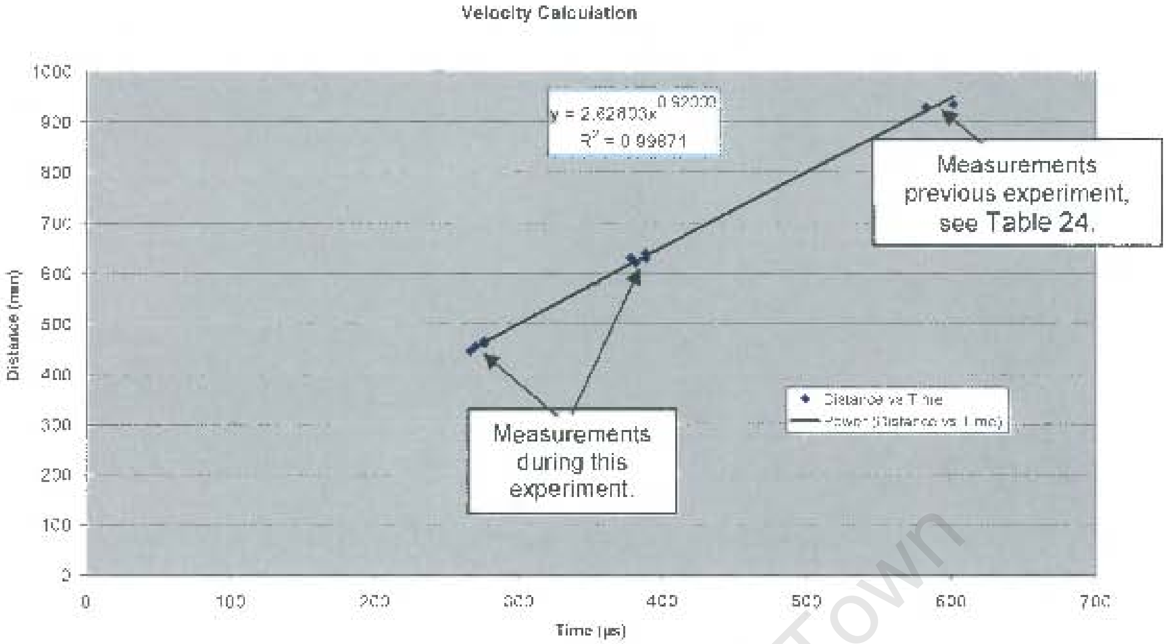

Figure 144: **A plot of the shock wave distance travelled versus the time taken for that distance travelled, taken from data of two experiments**

5.1.5.5.3. Detonator Firing Time

The detonator firing times were investigated to determine the actual time-spread from the moment that the detonator current was applied by the SAFU, to the moment of detonation, to correlate the practical findings (as used in the sea water) with the detonator specification which was obtained under laboratory circumstances (no leaking currents through sea water, etc.).

The results are tabulated in Table 36. Three of the events yielded results that were expected, i.e. that the moment of detonation followed approximately 2 to 4 ms after the detonator current was applied.

Note: This detonation time is the time of detonation of the main charge. The time taken from the moment of application of detonator current to the functioning of the detonator was not measured in this experiment.

Table 36: **Measurements taken from the moment that the detonator current is applied, to the moment of detonation of the main charge**

	Detonation Time Measurements			
	Event 2	Event 3	Event 4	Event 5
Time to Detonation (ms)	3.253	2.343	2.024	11.467
Optical Sensor Saturation Time (ms)	1.335	1.324	1.429	1.510

The graphical results are shown in Figure 145 to Figure 148. The time duration of the flash as produced by the explosion is also shown.

The result shown in the coloured (light blue) cell in **Table 36** seems to be out of line with the rest of the results (11.467 ms vs. typically 2.5 ms). An assumption could be made that in that specific case, the detonator current leaked more than usual through the sea water, causing less energy rate to be transferred to the detonator, causing a delay in the time-to-detonate. This may very well be expected to happen in practise.

Note: The optical sensor collector-emitter capacitance (C_{CE}) caused the negative slope to slew at a slower rate than the positive slope. This was due to the fact that the forward resistance reduced to a relatively small value as compared to the transistor capacitance when the photo transistors were forward biased by the application of light. This relatively small forward resistance (R_{CE}) of the switched-on transistors appear in parallel with the capacitance C_{CE}. When the light caused by the explosion was expired, the forward resistance of the photo transistors increased to a value which was very high (practically causing an open circuit). The transistor capacitance then became the dominant part of the transistor impedance, which caused the voltage to drop slower when compared to the rising slope of the measurement.

An additional "slowing down" of the reactance of the photo transistor, may have been due to the avalanche effect (started at the presence of light, and activating the photo characteristics of the transistor) which should be stopped when the light disappears, but does not stop immediately. This characteristic varies between transistor types. The uncertainty of the switch-off time caused the measurement of the "sustained light period" to be unreliable.

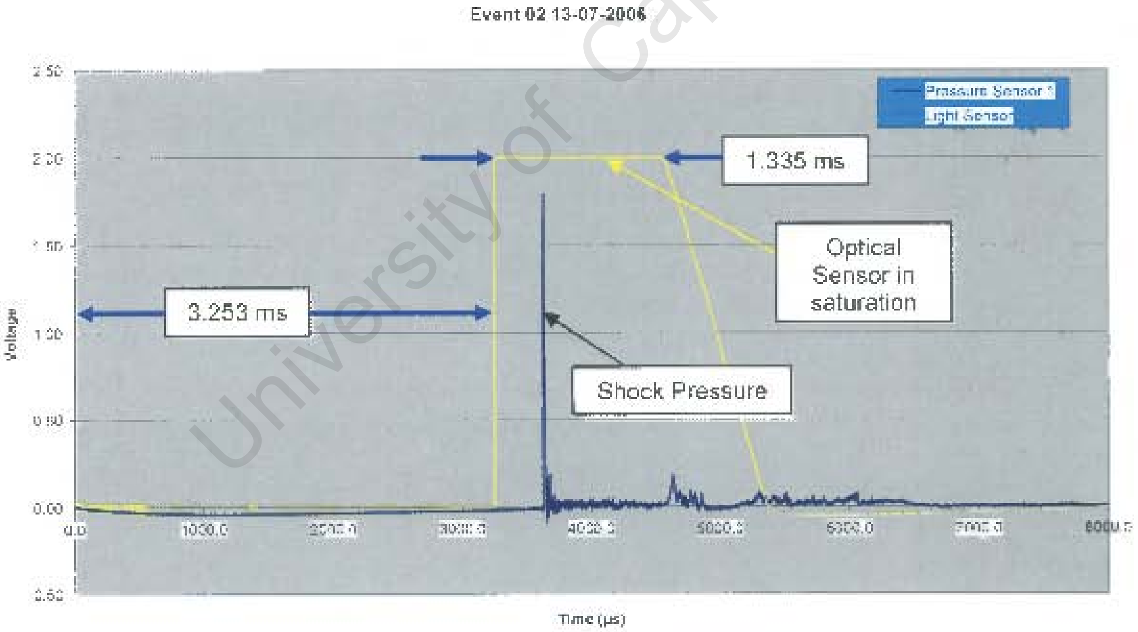

Figure 145: **Figure showing the time at which the detonator current started flowing (detonate command) with respect to the time at which the actual detonation occurred (optical sensor), and relative to the pressure pulse measured by Pressure sensor 1 (630 mm from the blast), approximately 380 µs after the explosion occurred**

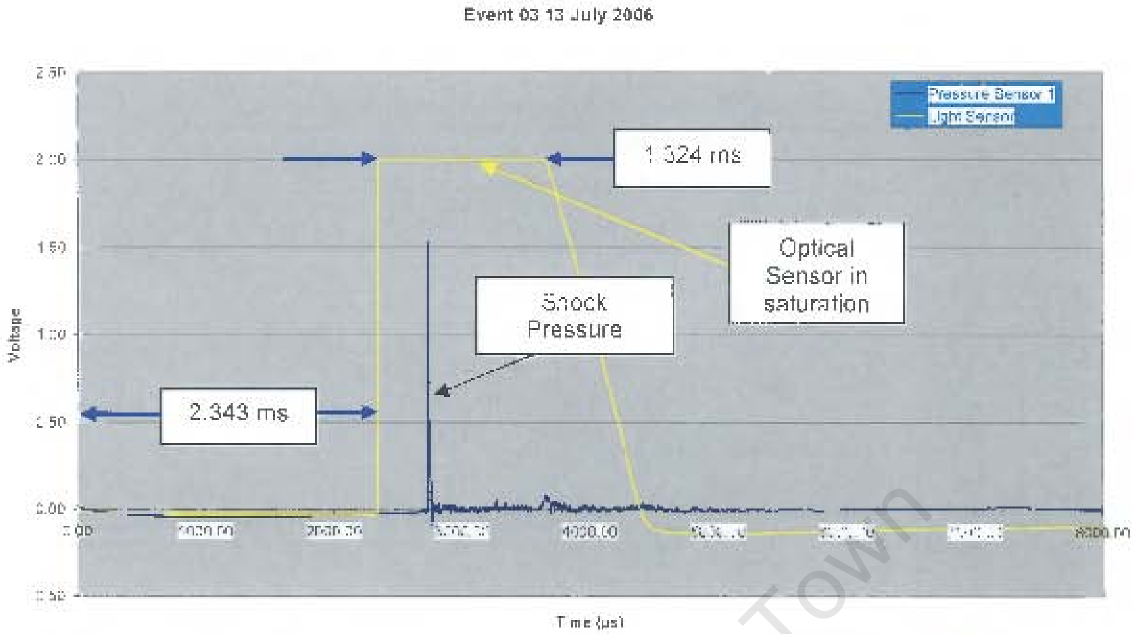

Figure 146: Figure showing the time at which the detonator current started flowing (detonate command) with respect to the time at which the actual detonation occurred (optical sensor) and relative to the pressure pulse measured by Pressure sensor 1 (640 mm from the blast) approximately 380 µs after the explosion occurred

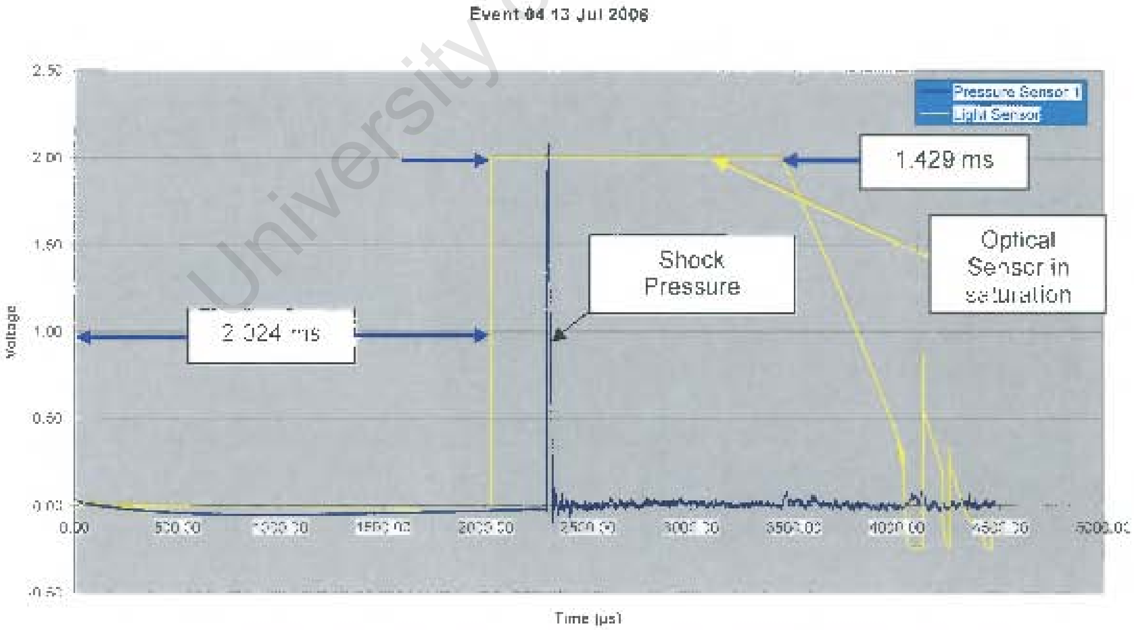

Figure 147: Figure showing the time at which the detonator current started flowing (detonate command), with respect to the time at which the actual detonation occurred (optical sensor) and, relative to the pressure pulse measured by Pressure sensor 1 (460 mm from the blast), approximately 275 µs after the explosion occurred

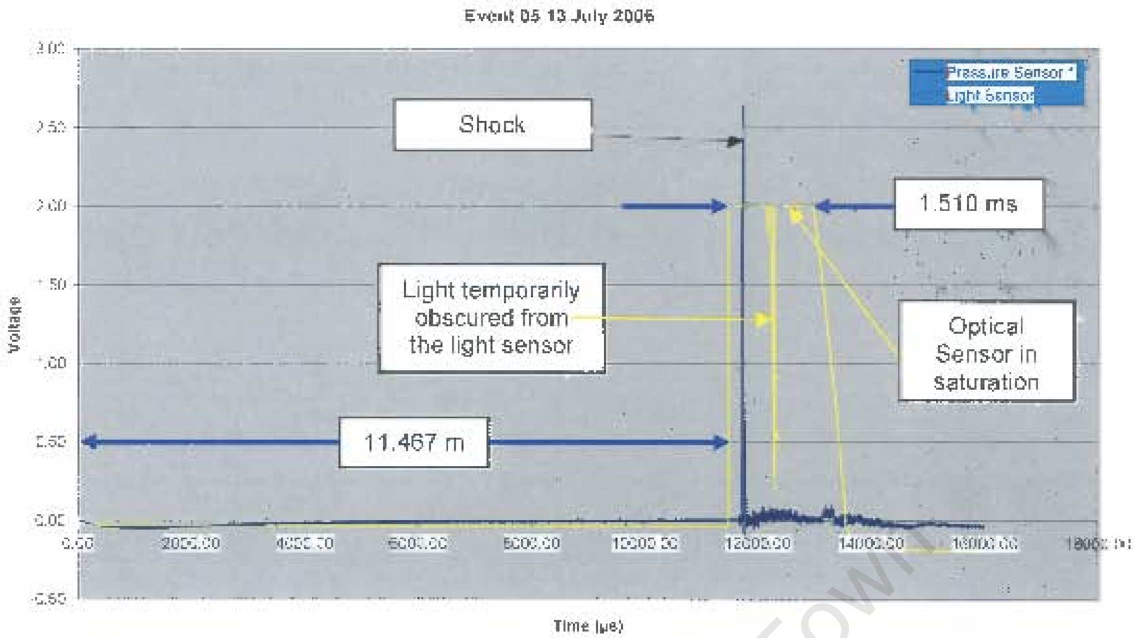

Figure 148: **Figure showing the time at which the detonator current started flowing (detonate command), with respect to the time at which the actual detonation occurred (optical sensor) and, relative to the pressure pulse measured by Pressure sensor 1 (445 mm from the blast), approximately 265 µs after the explosion occurred**

5.1.5.5.4. Sustained Light Period

An interesting aspect of the sustained light period is that it was sustained much longer than was anticipated. Table 37 records the sustained light period for this experiment. It is suggested that the reflection of light from the test specimen may have contributed to the total length of the measured light period.

Table 37 : Measured period of light caused by the explosions

Measured Light Period			
Event 2	Event 3	Event 4	Event 5
1.335	1.324	1.429	1.510

It is too soon to come to firm conclusions about the light measurement "sustained period". It is suggested to repeat the trials, but to replace the optical sensor with a much faster switching photo diode which will switch off within one or two microseconds when the light disappears, and then to compare the results.

5.1.5.5.5. Rigidity of the optical sensor

The optical sensor sustained no damage at all and laboratory tests before and after the sea trials were identical (within reason).

5.1.5.6. Conclusions and Recommendations

1. This was the first of a series of tests that would involve the use of an optical sensor to determine the point in time that could be used as a time marker for the moment of explosion. in underwater measurement-related exercises involving underwater explosions. This method proved to be reliable due to the rigidity of the sensor, the rapid initial response time, the repeatability of the results, and the good correlation of the curve-fitted graph proving the validity of the measurements.
2. The secondary information gained from this experiment, the "duration of the blast" (the "sustained light period"), was not seen to be reliable, because the phototransistors were overexposed and revealed a characteristic of switching off relatively slowly. If this period should be important, it would be advisable to use a faster photo transistor or photo diode and then to calibrate its stand-off distance in such a manner that it would not saturate during the flash period.

5.1.5.7. Summary of Pressure Measurements

A summary of all pressure measurements taken during this study is given in Figure 149. An explosive mass of 390 gm was used in one of the experiments. To be able to compare this result with the other measurements, all of which used a 30 gm explosive mass. a scaling factor was required. This scaling factor was derived as follows:

$$P_{max} = k\left({W_1^{\frac{1}{3}}}\Big/{R_1} \right)^{\alpha} \text{ for 30 gm } = P_{max} = k\left({W_2^{\frac{1}{3}}}\Big/{R_2} \right)^{\alpha} \text{ for 390 gm.} \tag{34}$$

Therefore:

$$\left({W_1^{\frac{1}{3}}}\Big/{R_1} \right) = \left({W_2^{\frac{1}{3}}}\Big/{R_2} \right) \tag{35}$$

$$\therefore \left({.03kg^{\frac{1}{3}}}\Big/{R_1} \right) = \left({0.39kg^{\frac{1}{3}}}\Big/{0.63m} \right)$$

$$\therefore \quad \left(0.31072\big/_{R_1}\right) = \left(0.7306\big/_{0.63\,m}\right)$$

$$\therefore \quad R_1 = \left(0.63 * 0.31072\big/_{0.7306}\right)$$

$$\therefore \quad R_1 = 0.268\,m \qquad \text{-----------------------------------} \qquad 36$$

The scaled stand-off distance when using a 390 gm explosive weight at a stand-off distance of 630 mm compares to 30 gm explosive at a stand-off distance of 268 mm. This value was substituted into Table 38 and Table 39 in row 3, column 4.

Table 38: Table of pressure measurements at the 138A10 (the more sensitive) Pressure Sensor

Explosive Weight (gm)	Pressure (MPa)	Distance (m)	Equivalent Distance for 30 gm	Sensor Type
30	18.1	0.733	0.733	138A10
30	21.5	0.733	0.733	138A10
390	54.13	0.63	0.268	138A10
30	24.5	0.63	0.63	138A10
30	21	0.625	0.625	138A10
30	29	0.46	0.46	138A10
30	36.1	0.445	0.445	138A10

Table 39: Table of pressure measurements at the 138A50 (the less sensitive) Pressure Sensor

Explosive Weight (gm)	Pressure (MPa)	Distance (m)	Equivalent Distance for 30 gm	Sensor Type
30	17.4	0.745	0.745	138A50
30	15	0.745	0.745	138A50
390	32.69	0.63	0.268	138A50
30	18.6	0.63	0.63	138A50
30	18.4	0.62	0.62	138A50
30	26.5	0.455	0.455	138A50
30	26.5	0.465	0.465	138A50

A graphic representation of the results in Table 38 and Table 39 is compared to the Equation by Cole [5] in Figure 149. Visual inspection revealed a good correlation between the Equation by Cole and the more sensitive Pressure Sensor. The correlation of the less sensitive Pressure Sensor was not as good.

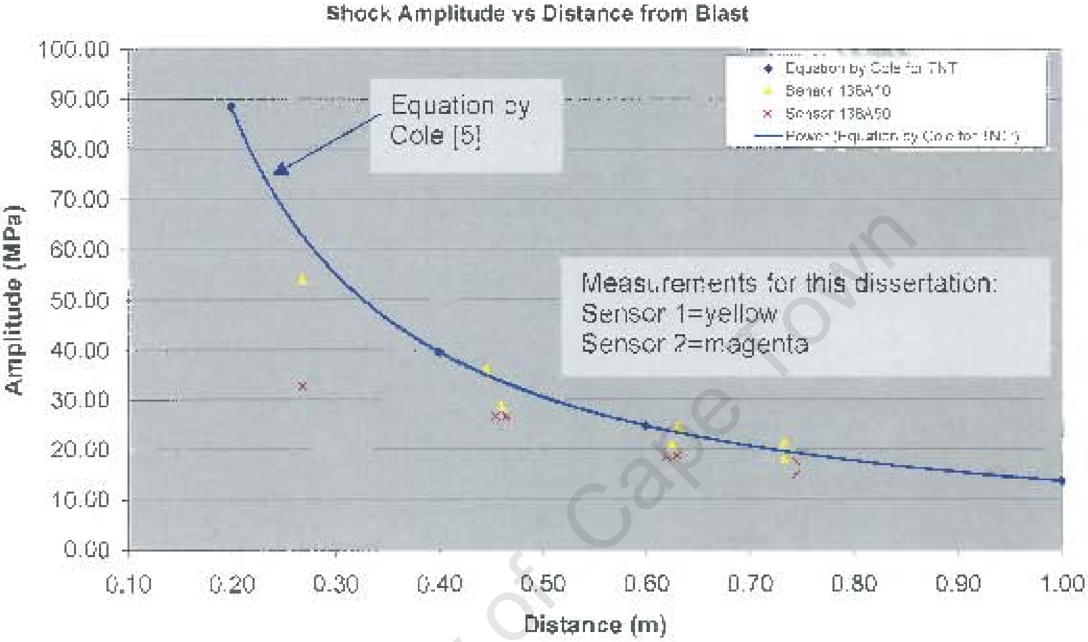

Figure 149: **Summary of Pressure Measurements for this study, compared to the Equation by Cole [5]**

5.1.6. Experiment 6: Experiment to test softer damping solution

5.1.6.1. Purpose

The foregoing experiments tested the appropriate parameters that were expected to play the major roles in the process of eliminating damage to enclosed electronics under blast loading. In broad terms, the conclusion was that:

1. The electronics would be precluded from damage if adequate damping was allowed for the CCA to filter out the high frequency components of the acceleration of the Enclosure.
2. The components on the CCA should follow certain guidelines to harden[7] the electronics against blast loading.

In this experiment, both the above conclusions were adhered to, and the purpose of this experiment was aimed at positioning the Electronics Enclosure at the target specified Standoff Distance of 270 mm from an explosive charge of 30 gm Pentolite (see paragraph "Aim" on page 18).

Damping mechanics acted as low pass filters to acceleration. The following transfer function was obtained from the simplest damping mechanism (Equation 30 repeated):

$$G(s)=\frac{Y(s)}{U(s)}=\frac{bs}{ms^2+bs} \qquad \text{-----------------------------------} \qquad \textbf{37}$$

In Equation 37, it was assumed that the spring constant was much smaller than the damping coefficient, hence the simplified transfer function described by Equation 37. The spring constant would never be zero, because then the CCA would not be returned to its original relative position to the Enclosure. The damping material will therefore have to be chosen to have a larger damping-effect, with a smaller spring-effect.

The unit step response of *G(s)* in Equation 37, is:

$$G(s)_{step}=\frac{1}{s}*\frac{bs}{ms^2+bs} \qquad \text{-----------------------------------} \qquad \textbf{38}$$

$$\therefore G(s)_{step}=\frac{b}{ms^2+bs} \qquad \text{-----------------------------------} \qquad \textbf{39}$$

It is obvious from Equation 39 that a second order low pass filtering operation would constitute an effective result. If the damping coefficient is chosen large enough, then the CCA would be accelerated at a much slower rate, and therefore transferring the energy at a lower rate. The result is that at a much smaller acceleration amplitude would be obtained, resulting in no damage effects.

When the damping material has a large damping effect (soft touch to the hand), it automatically would have the CCA move much further than when the damping effect is small,

---

[7] The term "hardening" of electronics was mentioned in the Synopsis on page 4. In this experiment, the electronics hardening suggestions that were dictated by the findings of the previous experiments were implemented.

e.g. using a grommet for the damping mechanics. Ample allowance must therefore be made for the larger CCA-travel, to avoid collision with the Enclosure.

The damping material that was used in the previous experiment will again be used for this experiment, because it was proven that the travel distance was small enough, whilst the damping-effect was large enough to obtain good results.

The purpose of this experiment was to measure the acceleration of the CCA, and to compare the result to the measured acceleration of the Enclosure. An analysis of the displacement should show that the relative movement between the CCA and the enclosure was large enough to have obtained good damping, but low enough to preclude collision between the CCA and the Enclosure. No damage should be sustained, due to enough attenuation of the acceleration transfer to the CCA.

The CCA mounting method (sponge rubber) was to reduce the acceleration transfer from the Enclosure to the CCA to below damage threshold. Acceleration will not be nullified, and therefore the component mounting method described above was intended to prohibit any collateral damage.

Figure 150 shows the internal layout of the Electronics Enclosure. Two layers of 6 mm sponge rubber were used as the damping material. See also Figure 151. The one layer was glued to the inner sidewalls. The second layer was made up from twelve blocks which were glued onto the first layer, spaced such that coverage of 50% of the damping area was ensured. The CCA was suspended between two such double layers of sponge rubber, eliminating the need to hard-mount the CCA. A layer of sponge rubber was added on the inner side panels to damp side movements (when appropriate). This double-layer suspension method was chosen to widen the bandwidth of the transfer function to ensure that damping was also obtained when the usual drop-tests were performed during the design qualification process.

Figure 150: **The Electronics Enclosure with the modifications for the double sponge rubber damping solution**

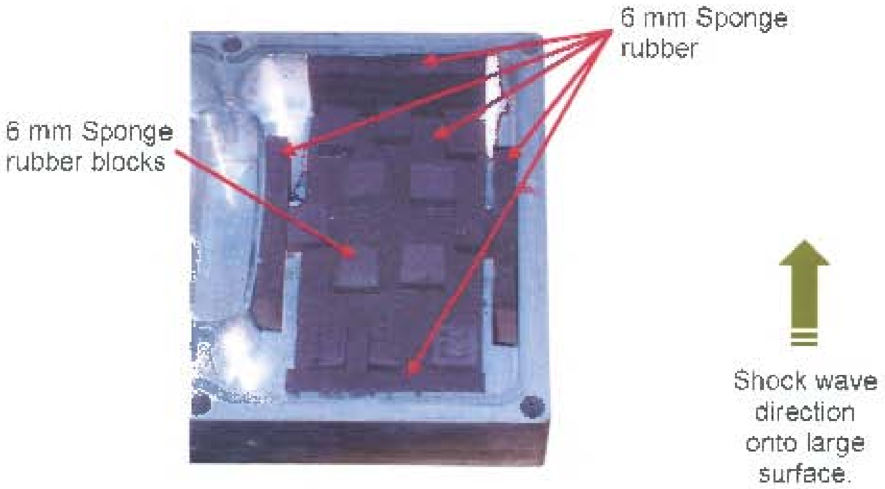

Figure 151: **The suspension method (one side).**

The transfer function of the suspension method of Figure 151 is derived as follows:

The equivalent system is approximated by a double spring-dashpot system, shown in Figure 152, assuming that the mass m_1 is zero. It is noted that the spring constant (k_2) and the damping coefficient (b_2) would be different to k_1 and b_1 respectively.

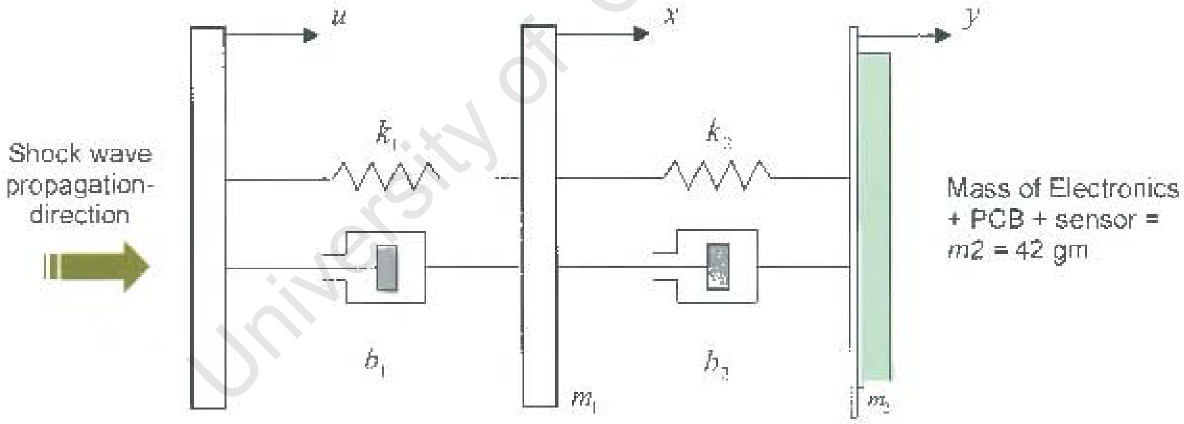

Figure 152: **The equivalent system of the double layer suspension method**

Applying Newton's second law to the system, we obtain:

Mass*acceleration of electronics CCA =
Viscous force + spring force

$$m_1 \frac{d^2 x}{dt^2} = k_2(y-x) - b_2\left\{\frac{dy}{dt} - \frac{dx}{dt}\right\} + k_1(u-x) + b_1\left\{\frac{du}{dt} - \frac{dx}{dt}\right\} \quad \text{------------------} \quad \mathbf{40}$$

And:

$$m_2 \frac{d^2 y}{dt^2} = -k_2(y-x) - b_2\left\{\frac{dy}{dt} - \frac{dx}{dt}\right\} \quad \text{------} \quad 41$$

When $m_1 = 0$, Equation 40 could be rewritten as:

$$0 = k_2(y-x) + b_2\left\{\frac{dy}{dt} - \frac{dx}{dt}\right\} + k_1(u-x) + b_1\left\{\frac{du}{dt} - \frac{dx}{dt}\right\} \quad \text{------} \quad 42$$

Taking Laplace transforms of these two equations, and assuming zero initial conditions, we obtain:

$$\left[(b_1+b_2)s + (k_1+k_2)\right]X(s) = \left[b_2 s + k_2\right]Y(s) + \left[b_1 s + k_1\right]U(s) \quad \text{------} \quad 43$$

$$\left[m_2 s^2 + b_2 s + k_2\right]Y(s) = \left[b_2 s + k_2\right]X(s)$$

$$X(s) = \frac{\left[m_2 s^2 + b_2 s + k_2\right]Y(s)}{(b_2 s + k_2)} \quad \text{------} \quad 44$$

Substituting Equation 44 into Equation 43, and taking the output versus the input, we obtain:

$$\frac{Y(s)}{U(s)} = \frac{(b_1 s + k_1)(b_2 s + k_2)}{(b_3 s + k_3)(m_2 s^2 + b_2 s + k_2) - (b_2 s + k_2)(b_2 s + k_2)} \quad \text{------} \quad 45$$

Where: $(b_1 + b_2) = b_3$ and $(k_1 + k_2) = k_3$

$$\frac{Y(s)}{U(s)} = \frac{(b_1 s + k_1)(b_2 s + k_2)}{b_3 m_2 s^3 + (b_2 b_3 + m_2 k_3 - b_2^2)s^2 + (b_3 k_2 + b_2 k_3 - 2b_2 k_2)s + k_3 k_2 - k_2^2} \quad \text{---} \quad 46$$

This constitutes the transfer function of the double-layer damping material for simulation purposes. The measurement of the parameters b_n and k_n was difficult due to the fact that the damping material inherently contained both these parameters. These parameters could not be measured separately as would be in the case of the suspension on a vehicle. The latter had a separate spring and shock absorber, making it possible to measure the one without interference from the other. The sponge rubber (by nature) has properties of a fluid, with a large viscosity. During attempts to measure the spring constant, the viscosity caused some inaccuracies, and *vice versa*. The equipment to measure these parameters were not available to the author, and thus it was decided that a separate project would be performed to determine these parameters, and then to perform the simulation as soon as the correct equipment were available. The main thrust of this study was unaffected.

5.1.6.2. Methodology

A frame (see Figure 153) was manufactured onto which the test unit (Enclosure with enclosed electronics and accelerometers) would be mounted in a moveable Enclosure clamp. The frame was designed to enable the repositioning of the test unit after each blast. A scaled test using 30 gm of explosive would be executed at a specified equivalent standoff distance of 270 mm for one of the tests, equating to a charge of 40 kg at a standoff distance of 3 m. The CCA should be tested after each blast event, and the success criterion should be that:

1. No damage would be sustained to the electronics.
2. The electronics would be fully operational after the tests.

For the latter purpose, a test point was identified which delivers a square wave when the circuit is operational. This test point was taken via an umbilical cord through a watertight gland to the test station where the accelerations were also recorded. The test point was monitored by an oscilloscope to enable on-line tests at all times.

Figure 153: The frame that was used to hold the Electronics Enclosure in position at various distances from the explosive charge.

The CCA that was used in the previous experiments was modified at a few places, according to the recommendations of the previous experiments, removing the "soft spots". See Figure 154.

These changes were:

1. The replacement of the crystal with a surface-mounted component which produced the required time base for the microprocessor.
2. IC sockets were not used for the larger ICs as before. The ICs were directly soldered into the PCB.
3. All switches were replaced by military-standard switches. All switches were orientated in a flat position, and only a thin layer (0.5 mm) of RTV adhesive was used to mount the switches. No hard-mounts (screws) were used.
4. The larger LEDs were mounted flat onto the PCB, and glued to the PCB with RTV.
5. The transistors which were mounted in the upright position were glued together after the solder operation.

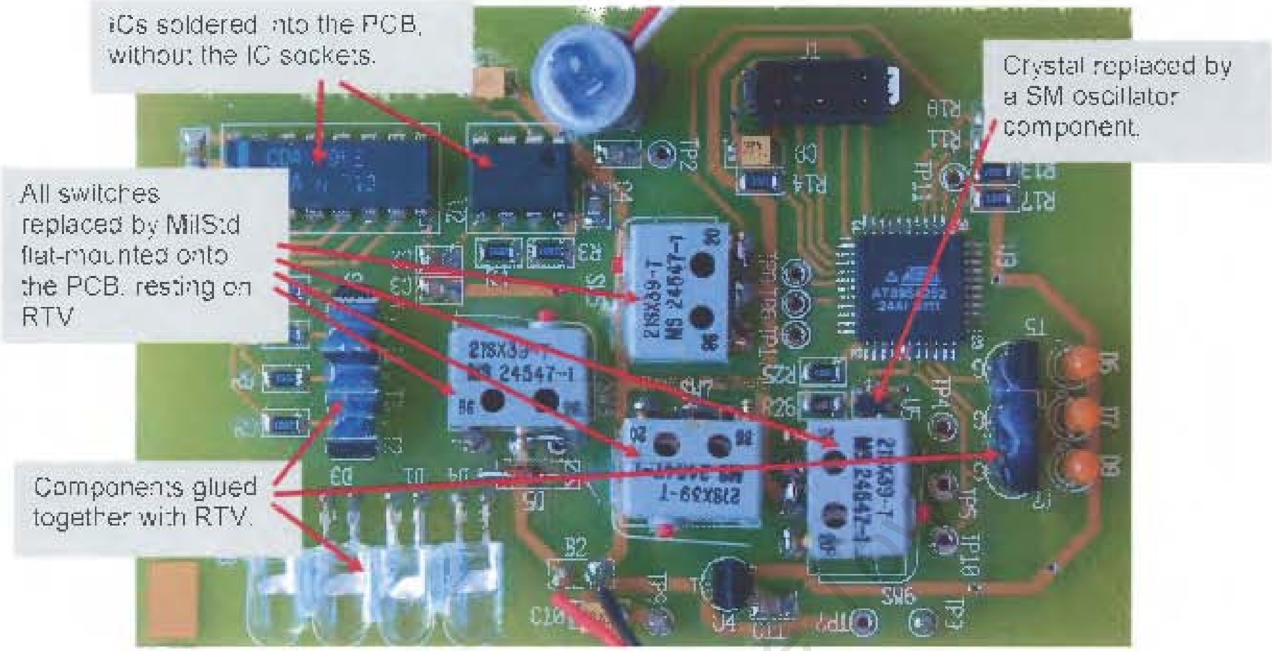

Figure 154: The modified CCA that had the soft spots of electronics replaced by alternative components

Figure 155: The position of the CCA and accelerometers in the Electronics Enclosure.

5.1.6.3. Results

Due to the restricted availability of the range-personnel, it was only possible to execute two measurement-events. Only one Pressure Sensor was used, because the second Pressure Sensor was damaged during the previous experiment.

During the first event, the Enclosure was positioned at 240 mm standoff distance from the charge, and the Pressure Sensor was positioned behind the Enclosure at 650 mm. During Event 2 the Enclosure was positioned at 350 mm from the explosive charge, and the Pressure Sensor was positioned next to the Enclosure. The distance between the centre of the explosive charge and the Pressure Sensor was measured to be 380 mm. See Table 40.

Table 40: Position of the Enclosure and the Pressure Sensor.

Event No	Standoff Distance of the Enclosure (mm)	Distance of the pressure Sensor from the Explosive Charge (mm)	Expected Peak Pressure (MPa) from Equation 3	Peak Pressures Obtained (MPa)
1	240	650	22.55	8.44
2	350	380	42.03	27.50

5.1.6.3.1. Pressure Measurements

The pressure history for Event 1 was recorded as shown in Figure 156.

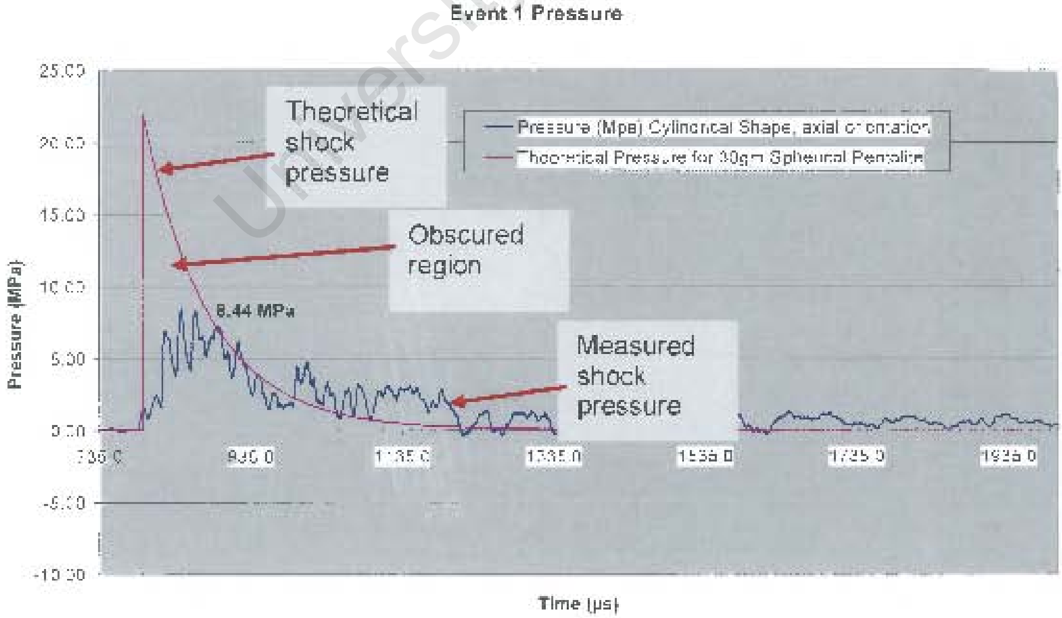

Figure 156: Pressure history for Event 1.

The pressure history for Event 2 was recorded as shown in Figure 157.

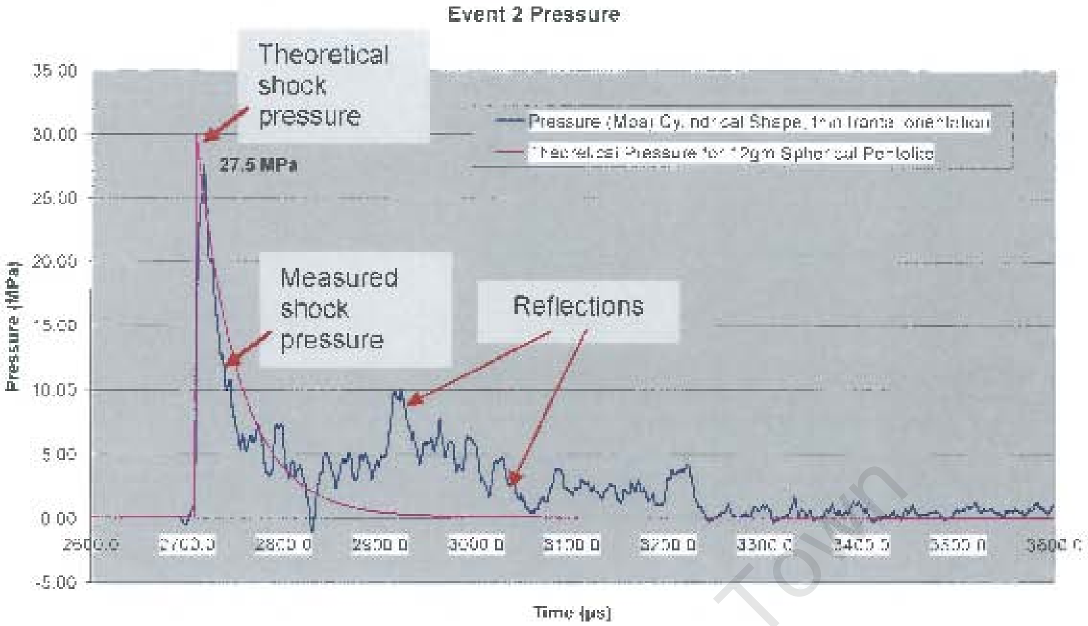

Figure 157: Pressure history for Event 2, and theoretical pressure history for 12 gm Pentolite.

The pressure history for Event 1 (Figure 156) did not follow the usual (theoretical curve in Figure 156) history format. This would be expected, because the Pressure Sensor was partly obscured from the explosive charge. The pressure history of Event 2 followed the usual history format, except that the peak pressure that was measured was smaller than the expected value, see Table 40. According to the theoretical pressure history (also shown in Figure 157), the measured value obtained was equivalent to 12 gm Pentolite, meaning that either the detonation of the charge was incomplete, or the sensor was suspect.

5.1.6.3.2. Acceleration Measurements

The acceleration results for Event 1 are shown in Figure 158, and the acceleration measurements for Event 2 are shown in Figure 159.

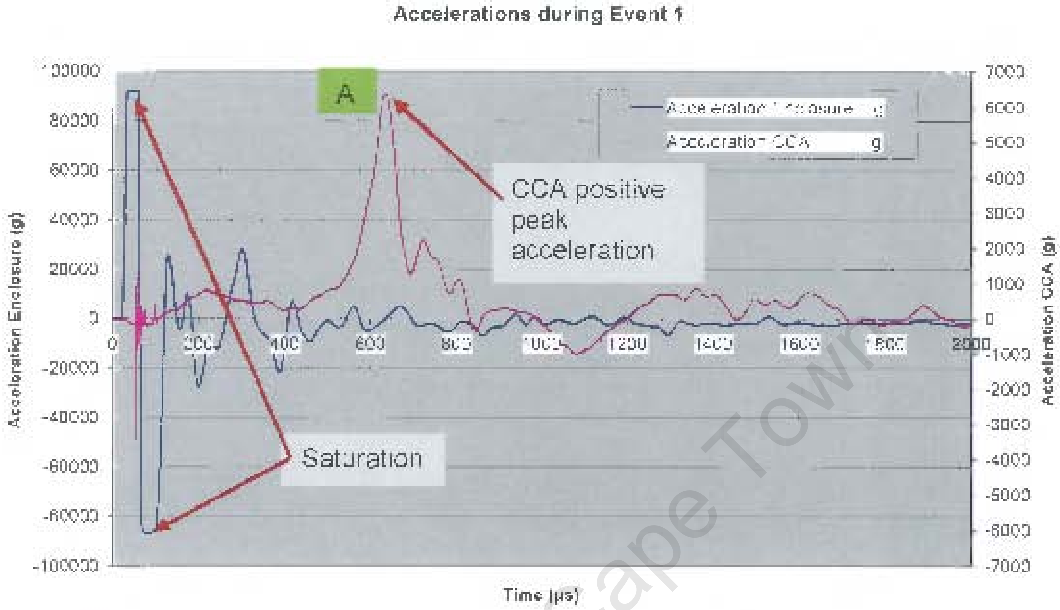

Figure 158: **Acceleration measurements for Event 1, at a standoff distance of 240 mm.**

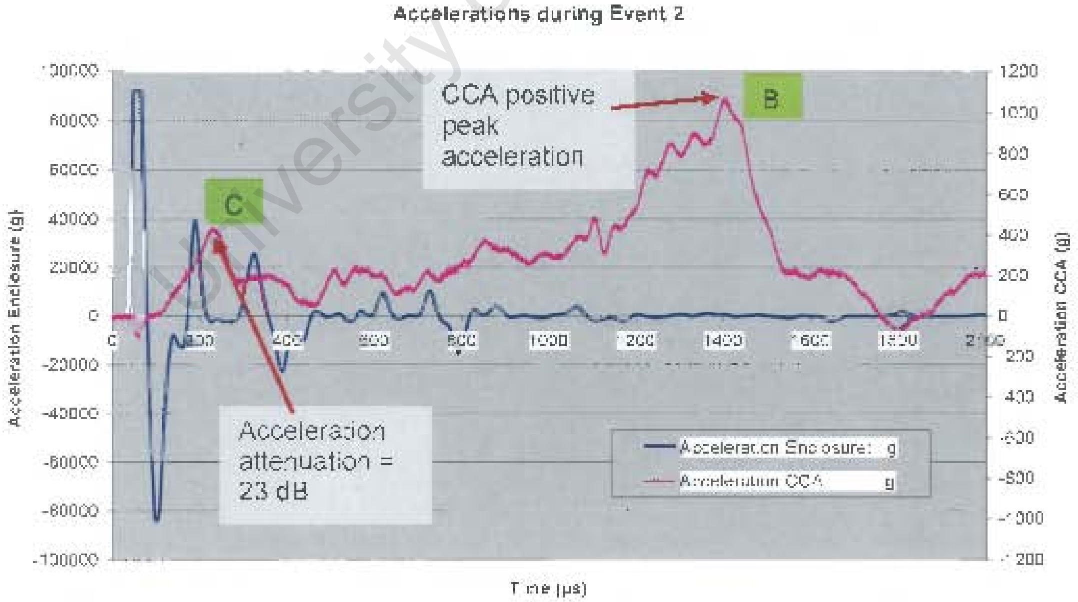

Figure 159: **Acceleration measurements for Event 2, at a standoff distance of 350 mm.**

The maximum CCA accelerations varied between 1042 g and 6238 g during Events 1 and 2 respectively.

The sensitivity of the accelerometers were too high for the chosen standoff distances, consequently the accelerometer which was mounted on the Enclosure, saturated at approximately 90 000 g. During Event 1, both the positive and the negative peak accelerations were cut off at the saturation voltage. During Event 2, only the positive half cycle was cut off at the saturation voltage due to the larger standoff distance.

The attenuation of acceleration could not be quantified exactly, due to the saturation at 90 000 g. Taking the maximum acceleration of Event 2 as 100 000 g (conservatively by extrapolation), and the peak value as 1050 g at point B in Figure 159, the attenuation is -19.79 dB. This is more attenuation than previously recorded. If the peak at point B is eliminated, then one could expect attenuation figures in the order of 23 dB, as shown in Figure 159 point C.

The accelerations measured for this study before this experiment, was summarised by Table 30 and graphically illustrated by Figure 126. Adding the acceleration-peak measurement during Event 2 of this experiment changed the curve-fitted result as shown in Figure 160. (It must be kept in mind that the peak acceleration for this experiment saturated during both Events). The curve-fitting process yielded the result that a curve with the format as described in Equation 47 was obtained.

$$Acceleration = A\left(e^{-Bx}\right) \tag{47}$$

Where *A* = 130000 g
And *B* = 0.018 (constant)
And *x* = number of charge radii

Equation 47 is depicted by Figure 160. This finding has a remarkable resemblance with the form of the shock velocity U_s in Equation 6, and confirms that there is a direct relationship between the induced acceleration of an object and the propagation speed of the shock wave.

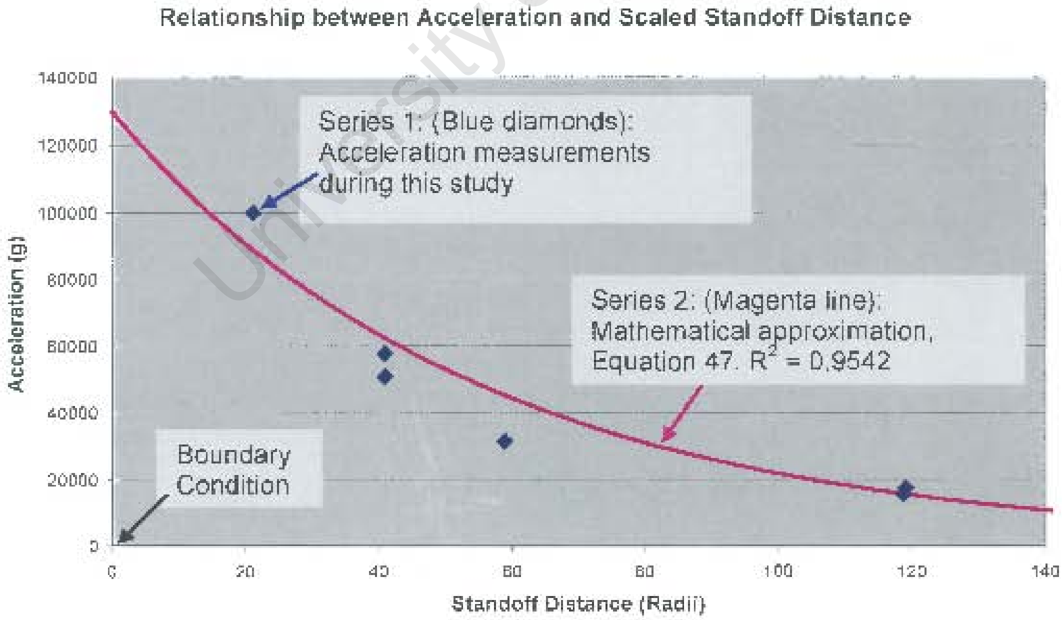

Figure 160: Relationship between peak-acceleration and standoff distance

5.1.6.4. Damage Assessment

After each test the electronics were function-tested at the test site, and it was found that these tests succeeded after both blast events. After the tests, the Electronics Enclosure was examined in the laboratory. No physical damage had occurred, and all the components were *in sito* as they were before the tests. All repeated functional tests passed. No damage had occurred.

5.1.6.5. Motion Analysis

The motion analysis was not done for this experiment because the acceleration measurement saturated during both events. The acceleration was more than the dynamic range of the measurement equipment.

It is however noticeable, on the CCA acceleration measurement, that a positive peak acceleration occurred at approximately 600 µs after the initial shock during Event 1 (see point A in Figure 158), and at approximately 1400 µs after the initial shock during Event 2 (see point B in Figure 159. This may have been attributable to the fact that a mechanical "landing" in the Electronics Enclosure (previously used for mounting purposes) was too close to the position of the CCA-mounted Accelerometer.

5.1.6.6. Conclusions

The conclusions that could be drawn from this experiment were that:

1. The accelerometers were too sensitive to measure the acceleration of the Enclosure at the selected standoff distances, and the combination of the sensor sensitivity and the dynamic range of the A/D equipment caused saturation at the points indicated in Figure 158.
2. According to the pressure measurement during Event 2, it was concluded that only a partial detonation had occurred. The close relationship between the measured history and the theoretical history (of a reduced explosive mass) was remarkable, rendering the data valid for a reduced charge mass.
3. The pressure measurement of Event 2 and the "no damage" finding indicated that the Electronics Enclosure with the selected damping mechanism protected the electronics successfully against an explosive charge of at least 12 gm Pentolite at a standoff distance of 240 mm. This was equivalent to a 40 kg charge at a standoff distance of 5.5 m.

Chapter 6

6.1. DISCUSSION and CONCLUSIONS

6.1.1. Introduction

This final chapter reviews the work undertaken to address the main aim of the thesis introduced on page 18, and by which the related sub-aims (stated on page 24) were executed to endorse the conclusion that the main aim had been accomplished.

6.1.2. Theories noted and defined

The literature was studied to note the characteristics of an underwater explosion with respect to the effect that the explosion had on objects that were positioned horizontally at standoff distances which were applicable to this study. It was found that an underwater explosion consisted of two main elements, that is, the shock wave and the bubble formation. The hypothesis of this study stated that the shock wave was the main contributor towards the damage to electronics in close proximity to the blast, and consequently the shock wave characteristics (using several sources) were noted in depth (see Equation 3 through 11). The bubble formation and collapse were thus ignored during this study.

During the literature study it became evident that the shock wave had two regions in which the propagation-velocity of the shock wave was different. These regions were called the "near-field" (near to the explosion) and the "far-field" (at further standoff distances than the near field). However, no clear definition of this characteristic was offered by the literature, and therefore a transition between the two regions was unclear. Hence the author of this thesis offered a definition (see: "Conclusions: Near Field vs. Far Field characteristic" on page 41, and repeated here for elucidation purposes) which would satisfy the requirements of this dissertation with respect to the characteristics of a shock wave which would influence a damage factor.

> Definition Offered:
>
> *In the far field, the shock wave has reached a constant velocity, equal to the speed of sound in that medium. Before this constant velocity characteristic is reached, the shock wave velocity is higher than the speed of sound, with a maximum value at the border condition (0 charge radii), and tapers down non-linearly towards the speed of sound as the standoff distance increases. This is the near field. This near field is usually defined by a number of charge radii.*

Briefly, the shock wave propagation velocity in the near field starts with a maximum (several times the speed of sound in the water, and typically 4000 – 5000 m/s) at the boundary condition. This propagation velocity then reduces by a function which approximates an exponential format, until the speed of sound is reached (see Figure 11) (the maximum amplitude depends upon the explosive pressure - P_d - and its pressure-transfer-coefficient to the surrounding water). In the far field the shock wave propagates at the speed of sound. The border between the near field and the far field is not a sharp transition, and therefore the near field definition could be terminated by the standoff distance at which the propagation velocity has reduced to within (say) 5% of the speed of sound.

The near field is significant for the purposes of defining design parameters of equipment that will be situated near imminent underwater explosions due to its non-linear nature. It is reasonable to accept that damage may also increase non-linearly in the near field, as the explosive charge is approached (standoff distance is decreased).

6.1.3. The Hypothesis

During the first experiment, the measurement results showed that more electronic damage occurred close to the blast (see the results of Enclosure No1 at 100 mm [= 6 charge radii] standoff distance on page 82), than further away (see the results of Enclosure No4 at 360 mm [= 22 charge radii] standoff distance on page 92). The damage results could not be presented in a more scientific format. because the damage could not be calculated on any acceptable scientific scale. Also, some design "damage soft spots" were deliberately introduced into the CCA-design, and some CCAs were mounted on damping material, whilst others were mounted hard against the Enclosure. The purpose was to investigate the standoff distances where:

1. Damage would occur where it was not expected, e.g. surface-mounted components being dislodged, switches physically broken, etc.
2. Damage would occur only to the "soft spots" on the CCAs.
3. No damage would occur.

From the results obtained in Experiment 1, it was reasonable to conclude that the damage to the test-electronics increased non-linearly as the standoff distance decreased.

Keeping cognisance of the fact that the water particle velocity associated with the propagation of a shock wave is directly proportional to the shock wave velocity (see Equation 7) and the speeding particles are orientated in the direction of propagation, the basis of the hypothesis of this study was established. The conclusion drawn from this statement is that the outward force which is created by the shock wave would also increase exponentially closer to the charge in the near field, and reach a maximum at the boundary condition. In the far field, the outward force would reduce proportionally with the shock-wave-generated pressure (see Equation 10) until the force would be too small to have a significant effect. (Equation 10 is valid for the condition where $P >> P_0$). This outward force, according to the hypothesis, is the cause of object acceleration. and consequently electronic damage.

The acceleration measurement results that were recorded for this study suggest that a good correlation had been found between the peak acceleration of the Electronics Enclosure and the scaled standoff distance (in charge radii) from an underwater explosion (see Figure 160). This validates a conclusion that the outward force of the explosion (and therefore the acceleration of an object on which the force is exerted) is related to the shock wave velocity.

It must also be kept in mind that the experiments for this study were conducted using a standard explosive mass of 30 gm, and that the equation for the decay function of a shock pressure pulse (see Figure 10) indicates that a larger explosive mass would sustain the particle velocity for a longer duration. This means that the shock impulse density (integral with time of the shock pressure pulse history) is also directly proportional with the acceleration, and would contribute to an Equation which would describe this conclusion.

It appears reasonable that an Equation illustrating this conclusion could be given by Equation 48 on page 182. This function includes all the properties of a shock wave that were identified in the "Research Design" (sub-paragraph "Methodology" on page 24) to have influence on the damage to enclosed electronics.

Note also that the total force ($\sum F$) on the object which would culminate in an acceleration of the object. is also dependent on the available area on which the force is exerted (force aperture – which includes the drag-coefficient). A smaller aperture leads to a smaller acceleration.

$$\sum F = m * a \quad k * U_s * P_{imp} * A \qquad \text{------------------------} \qquad 48$$

Where
F = Force exerted on the Enclosure
m = mass of the Enclosure
a = acceleration of the enclosure
U_s = Shock wave velocity
P_{imp} = Shock impulse function
k = constant
A = Aperture

$$\therefore a = \frac{k}{m} * U_s * P_{imp} * A \qquad \text{-------------------------------} \qquad 49$$

Refer to Experiment 6, Figure 156. The aperture was reduced at the position of the pressure sensor as a result of the Enclosure partly obscuring the shock wave, causing the Pressure Impulse energy to be reduced (area under the pressure-history curve).

To summarise: This study showed that there was an un-quantified relationship between the hard-mounted electronics damage in an Enclosure and the acceleration of the Enclosure. The conclusion was also that the damage closer to the explosion was not only due to the pressure, but also due to the shock wave velocity.

6.1.4. Mitigation factors

The hypothesis of this study stated that the acceleration of the Enclosure is the cause of hard-mounted electronics contained in the Enclosure. This implies that mitigation techniques should incorporate a solution to preclude (as far as possible) the transfer of the Enclosure acceleration to the contained CCA.

It was calculated as a ball-park figure that the displacement of the Enclosure would be less than 1 mm (Acceleration and Displacement Prediction on page 46) during the large acceleration period when a shock wave collides with the Enclosure. This gave rise to the conclusion that an internal (to the Enclosure) damping mechanism may be provided, which would be physically small, and therefore cost effective. As a first solution, a standard Neoprene "grommet" was used to mount the CCA, which would serve as a damper to the acceleration. However, the grommet-solution would be effective for larger distances (e.g. if the Enclosure was situated in the far field) only. Another (softer) damping mechanism was tested, and it was found (using Neoprene sponge rubber – see Experiments 4) that the acceleration was dampened more adequately than for the grommet-mounted CCAs (sponge rubber attenuation of 21.95 dB – see Figure 122 – versus grommet attenuation of 15-18 dB – see Table 21 and Table 25)

Note: The relative displacement of the CCA (relative to the Enclosure) was larger for the softer mountings (as would be expected). Care must be taken in the design of the equipment to cater for the correct expected acceleration, because a mounting method which attenuates adequately, may allow too much CCA displacement, causing the CCA to take up all the slack during blast loading, and then colliding with the Enclosure.

There is some evidence that the selected mounting method for Experiment 6 was too soft for the selected standoff distance. In Figure 158 point A and in Figure 159 point B indicated a sudden increase in acceleration which could be attributable to all the slack of the damping material being taken up. If these peak accelerations were in fact as a result of the reduced damping material slack, then it could well be envisaged that the maximum acceleration would be in the order of 400 g. This would constitute an acceleration attenuation in excess of 24 dB (assuming the saturated peak acceleration in Figure 159 would be in excess of 100 000 g), which is an improvement over the damping method of Experiment 4. Unfortunately the test range team was unavailable to execute an experiment to prove this statement.

6.1.5. Field measurements and sensors

Applied Research had been performed on the subject of safeguarding electronics that were enclosed in a watertight Electronics Enclosures against underwater blast loading. The results of the field experiments were mostly positive, see conclusions on pages 96, 117, 134, 148, 166, and 179. The following conclusions are highlighted or added:

1. *The damping solution of Neoprene sponge rubber that was used in Experiment 6 was adequate for the protection of the enclosed electronic CCA for the protection against blast loading of 30 gm at scaled standoff distances as low as 15 charge radii (240 mm for 30 gm explosive charge at a relative density of 1.6), which is within the goals for this study. A 30 gm charge produces approximately 73 MPa pressure at a standoff distance of 240 mm, which is equivalent to a 40 kg charge at a standoff distance of 2.6 m.*
2. *The acceleration that the selected Enclosure undergoes during blast loading in the near field region of 20 charge radii, (see acceleration measurements on page 177) is too high to measure using the given accelerometers (with the sensitivity of 0.073 mV/g). A possible solution is to increase the mass of the Enclosure, after all scaling factors were considered, because the force (and force aperture) is constant.*
3. *A good correlation between the explosive charge radius and the acceleration was obtained (see Figure 126) from which it could be predicted what the expected acceleration would be at specified standoff distances for a 30 gm explosive charge. Estimating that the maximum acceleration of Event 2 during Experiment 6 was 100 000 g, this point was added to Figure 126, which produced the graph shown in Figure 160. A curve (with $R^2 = 0.9542$) was fitted over the data points in Figure 160, producing an equation of:*

$$Acceleration = 130000\left(e^{-0.018x}\right) \quad \text{-------------------} \quad 50$$

Where x = number of radii
And $R^2 = 0.9542$

This curve was valid for an explosive mass of 30 gm Pentolite, an Enclosure with mass = 1.996 kg and with an aperture of (180 mm x 120 mm = 0,0216 m^2) and a *drag coefficient =1 (Enclosure facing the explosion at right angles with the shock velocity).*

4. *Only two pressure sensors were used in multiple experiments. The pressure results (see Figure 149) indicate that one sensor (the less sensitive sensor) consistently produced results which were lower than the other sensor. These readings were also consistently lower than the theoretical values indicated by Cole [5] on the same graph. This indicated that the sensor may have sustained some damage during tests prior to this study.*

5. *A method had been researched whereby the flash that was generated by the under-water explosion was recorded by means of optical transistors (see Experiment 5 on page 149), and this measurement was used to synchronise the pressure and accelerometer measurements with the moment of explosion. Although air-blast operations use the flash of the explosion for many reasons, as far as could be established, the optical transistor synchronisation method for under water experiments had not yet been published. It is recommended that further studies are undertaken to investigate the optical transistor (or optical diode) for use in underwater measurement, especially to obtain shock wave velocity. The shock wave velocity is in direct relation with the pressure (see Equation 10), and seeing that pressure measurements are difficult to obtain due to pressure sensor shortcomings, an alternative would be to determine pressure by measurement of the shock wave velocity.*

References

[1] **Brett, John M.**
Numerical Modelling of Shock Wave and Pressure Pulse Generation by Underwater Explosions
DSTO-TR-0677
DSTO Aeronautical and Maritime Research Laboratory
June 1998.

[2] **Brett, John M. & Yiannakopoulos, George & van der Schaaf, Paul J.**
Time-resolved measurement of the deformation of submerged cylinders subjected to loading from a nearby explosion
International Journal of Impact Engineering 24 (2000) 875 - 890
23 March 2000.

[3] **Chung, Michael & Kinsey, Trevor.**
Report: DSTO-RR-0134. Investigation into the Effects of Underwater Shock Waves on Simple Structures, Shielded and Bare Explosive Materials
DSTO Aeronautical and Maritime Research Laboratory, Melbourne Victoria 3001
Australia: June 1998.

[4] **Cichocki, K.**
Effects of underwater blast loading on structures with protective elements
International Journal of Impact Engineering 22 (1999) 609-617
16 February 1999.

[5] **Cole, R.H.**
Underwater explosions.
New York, USA
Dover Publications
1948.

[6] **Cooper, Paul W.**
Explosives Engineering
New York, USA
Wiley-VCH Inc
ISBN: 0-471-18636-8
1996.

[7] **Hammond, Lloyd C.**
The structural response of submerged air-backed plates to underwater explosions.
Dept of Civil Engineering
PhD Thesis: Monash University
September 2000.

[8] **Hattingh, I.J.**
CSIR Internal Report: MR010-000038-701. Test Report on the Protection of Electronic Equipment against Underwater Explosions
CSIR: 20 February 2004.

[9] **Held, M.**
Underwater Explosion Phenomena.
9th International Symposium on Military Applications of Blast Simulation
Oxford, England
September 1985.

[10] **Kira, Akio & Fujita, Masahiro & Itoh, Shigeru.**
Underwater explosion of spherical explosives
Journal of Materials Processing Technology 85 (1999) 64-68
1999.

[11] **Klaseboer, Evert & Turangan, Cary & Fong, Siew Wan & Liu, Tie Gang & Hung, Kin Chew & Khoo, Boo Cheong.**
Simulations of pressure pulse-bubble interaction using boundary element method
Computer Methods in Applied Mechanics and Engineering 195, pages 4287-4302
2006

[12] **Malan, D.F.**
JSF Test Report
CSIR Report: S378-260-722
Council for Scientific and Industrial Research
August 2002.

[13] **Malan, D.F.**
Report on Damage to Equipment
CSIR Report: MR054-000000-722 Rev 1
Council for Scientific and Industrial Research
November 2004.

[14] **Malan, D.F.**
Project UNDEX: Report on Scaled Test conducted on 8 December 2005.
CSIR Report: MR025-000000-701010 Rev 1
Council for Scientific and Industrial Research
20 December 2005.

[15] **Morrison, P.H.**
Cannon-Launched Guidance Electronics, a 9000g Challenge
Copperhead Program, Martin Marietta Aerospace
Orlando, Florida
1978.

[16] **Nilsson, J.W. & Riedel, S.A.**
Electric Circuits (Fifth Edition)
New York, USA
Addison-Wesley Publishing Company
1996.

[17] **Ogata, Katsuhiko.**
Modern Control Engineering (Third Edition)
New Jersey, USA
Prentice-Hall International
1997.

[19] **Roos, H.H.**
Evaluation of Damaged Military Equipment
CSIR Internal Report: S378-097-722
Council for Scientific and Industrial Research
July 2004.

[20] **Snyman, I.M.**
UNDEX Report On Modelling Of Underwater Blast Effect
CSIR Report: MR025-000000-701014
Council for Scientific and Industrial Research
January 2007.

[21] **Ström, Paul & Janzon, Bo.**
Report: 03-H426, Enclosure 1
FOI Report: Sweden
19 November 2003.

[22] **Swisdak, Michael M.**
Explosion effects and properties, Part II, Explosion effects in Water.
Rept NSWC/WOL/TR-76-116, Naval Surface Weapons Center, Silver Spring, Md, (AD/A-056694)
1978.

[23] **Takahashi, K. & Murata, K. & Kato, Y. & Itoh, S.**
Non-ideal detonation of emulsion explosives
Journal of Materials Processing Technology 85 (1999) 52-55
1999.

[24] **Urick, Robert J.**
Principles of Underwater Sound (Third Edition)
New York, USA
McGraw-Hill Book Company
1983.

Main Bibliography

Burdic, W.S.
Underwater Acoustic System Analysis.
NJ, USA
Prentice-Hall.
1984.

Hung, C.F. & Hsu, P.Y. & Hwang-Fuu, J.J.
Elastic shock response of an air-backed plate to underwater explosion
International Journal of Impact Engineering 31 (2005) 151-168
2005.

Ramajeyathilagam, K. & Vendhan, C.P.
Deformation and rupture of thin rectangular plates subjected to underwater shock.
International Journal of Impact Engineering 30 (2004) 699-719
14 January 2004

APPENDIX 1

GRAPHICAL PRESENTATION OF THE COLE [5] EQUATION FOR PEAK PRESSURE VS. STANDOFF DISTANCE FOR PENTOLITE.

Graph of shock wave peak amplitude relative to standoff distance, for a charge weight of 40 kg Pentolite.

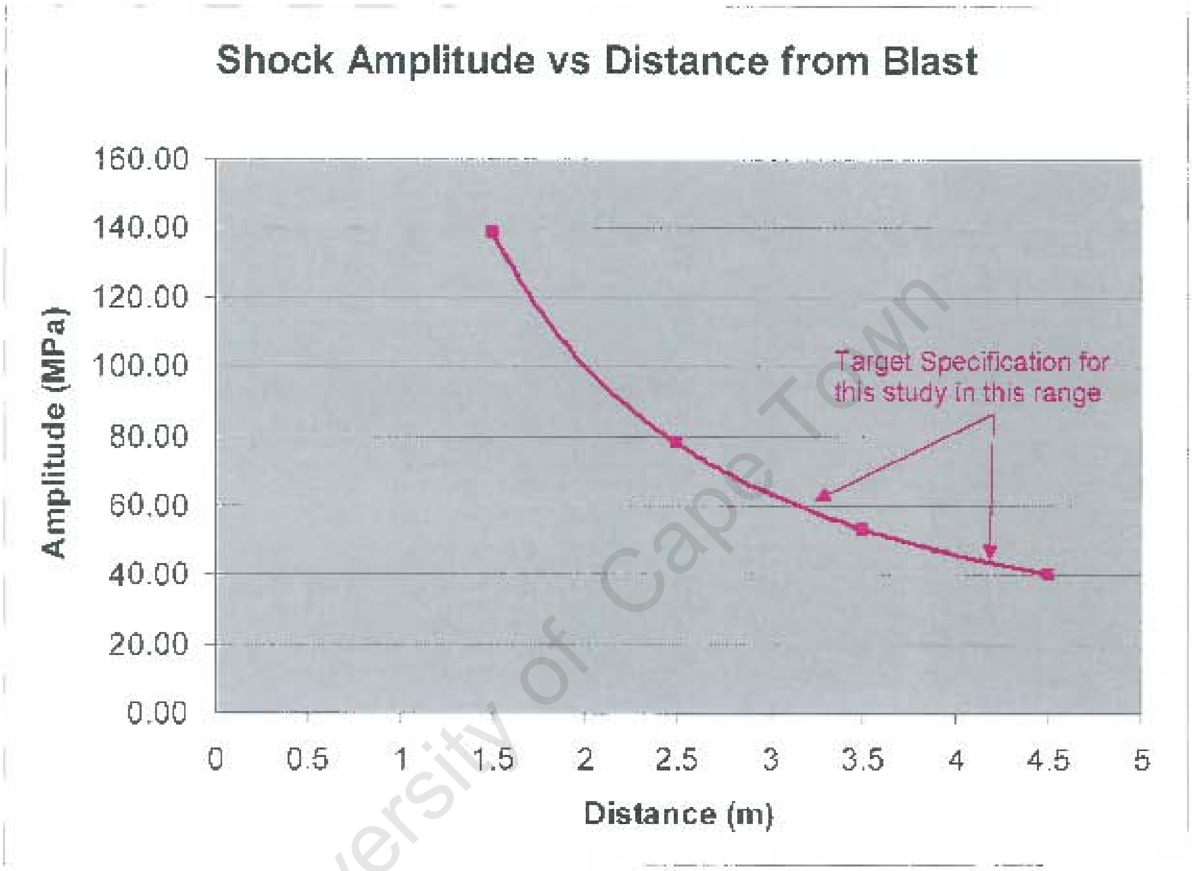

Original equation for Pentolite:

$$P_{\max} = 2.25 \times 10^4 \left(\frac{W^{\frac{1}{3}}}{R} \right)^{1.13} \quad lb/in^2$$

Where:
$P_{\max}$ is in lb/in^2,
W is in lb,
R is in ft.

Equation for Pentolite translated to the metric system:

$$P_{\max} = 54.56 \left(\frac{W^{\frac{1}{3}}}{R} \right)^{1.13} \quad MPa$$

Where:
Pmax is in MPa,
W is in kg,
R is in m.

The specification of 40 kg at a standoff distance of 4 m equates to 44.75 MPa, and thus an equivalent charge mass of 30 gm at a scaled standoff distance of 360 mm. This distance equates to 22 charge radii.

APPENDIX 2

SPECIFICATIONS OF THE TOURMALINE PRESSURE SENSORS USED IN THIS STUDY.

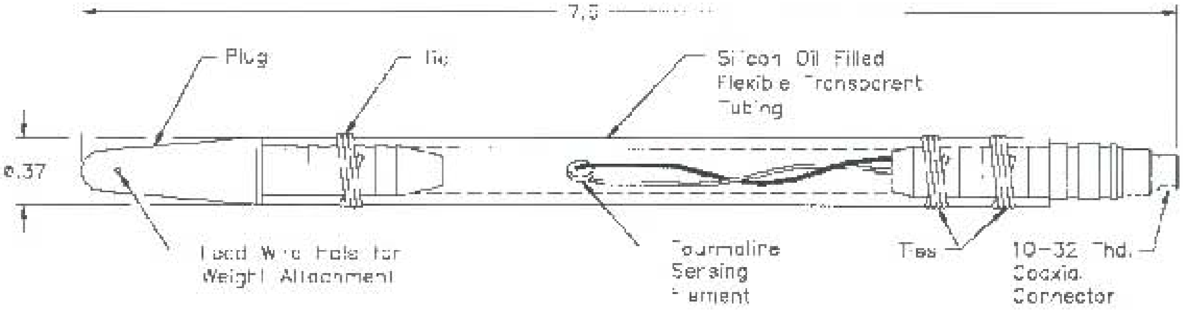

Figure 161: Model 138A Tourmaline Pressure Sensor.

	Dynamic Range (1)	psi	1 000	5 000	10 000	25 000	50 000
	MODEL NUMBERS	long short	138A01 138A02	138A05 138A06	138A10 138A11	138A25 138A26	138A50 138A51
AMPLITUDE	Sensitivity (5)	mV/psi	5	1	0.5	0.2	0.1
	Resolution	psi	0.02	0.1	0.2	0.5	1
	Range (for 5V output)	psi	1000	5000	10 000	25 000	50 000
	Range (for 10V output) (2)	psi	2000	10 000	20 000	50 000	n/a
	Maximum Pressure	psi	50 000				
	Linearity (3)	%FS	≤ 2				
FREQ RESP	Resonant Frequency	MHz	≥ 1				
	Rise Time (in water)	µs	≤ 1.5				
	Discharge Time Constant (4)	s	≥ 0.2				
	Low Frequency (-5%) (4)	Hz	2.5				
ENVIRONMENTAL	Shock (max)	g pk	20 000				
	Temperature Range	°F	0 to 100				
	Polarity (positive pressure)		positive				
	Output Impedance	ohm	≤ 100				
	Output Bias	+volts	8 to 14				
	Power Required: Voltage	+VDC	20 to 30				
	Constant Current	mA	2 to 4				
PHYSICAL	Sensing Element	material	tourmaline				
	Connector/Amplifier Housing	material	stainless steel				
	Body Housing	material	Tygon tube, nylon tie, Delrin plug (where applicable)				
	Connector	type	10-32 coaxial				
	Sealing (connector/amplifier)	type	welded/hermetic				
OPT	Water-resistant Cable	prefix	W (specify length)				

Model Number 138A10	ICP® PRESSURE SENSOR SPECIFICATIONS	Revision F ECN #: 21174

	ENGLISH	SI	
Performance			
Measurement Range (for ± 5V output)	10 kpsi	68950 kPa	
Useful Overrange (for ± 10V output)	20 kpsi	137900 kPa	[1]
Sensitivity	0.5 mV/psi	0.073 mV/kPa	
Maximum Pressure	50 kpsi	344750 kPa	
Resolution	200 mpsi	0.14 kPa	
Resonant Frequency	≥1000 kHz	≥1000 kHz	
Rise Time (Reflected)	≤1.5 μ sec	≤1.5 μ sec	
Low Frequency Response (-5 %)	2.5 Hz	2.5 Hz	
Non-Linearity	≤2.0 % FS	≤2.0 % FS	[2]
Environmental			
Temperature Range (Operating)	0 to +100 °F	-17.8 to +37.8 °C	
Maximum Shock	20000 g pk	196140 m/s² pk	
Electrical			
Output Polarity (Positive Pressure)	Positive	Positive	
Discharge Time Constant (at room temp)	≥0.2 sec	≥0.2 sec	
Excitation Voltage	20 to 30 VDC	20 to 30 VDC	
Constant Current Excitation	2 to 20 mA	2 to 20 mA	
Output Impedance	<100 ohm	<100 ohm	
Output Bias Voltage	8 to 14 VDC	8 to 14 VDC	
Physical			
Sensing Element	Tourmaline	Tourmaline	
Housing Material	Stainless Steel	Stainless Steel	
Electrical Connector	10-32 Coaxial Jack	10-32 Coaxial Jack	
Weight	0.75 oz	21.0 gm	

CE[3]

All specifications are at room temperature unless otherwise specified.

In the interest of constant product improvement, we reserve the right to change specifications without notice.

ICP® is a registered trademark of PCB group, Inc.

Optional Versions (Optional versions have identical specifications and accessories as listed for standard model except where noted below. More than one option maybe used.)

- N - Negative Output Polarity
- W - Water Resistant Cable

Notes

[1] For +10 volt output, minimum 24 VDC supply voltage required. Negative 10 volt output may be limited by output bias.

[2] Zero-based, least-squares, straight line method

[3] See PCB Declaration of Conformance PS023 for details

Entered: BLS	Engineer: RPF	Sales: DPC	Approved: MEM	Spec Number:
Date: 12/02/2004	Date: 12/02/2004	Date: 12/06/2004	Date: 12/08/2004	138-1100-80

PCB PIEZOTRONICS
PRESSURE DIVISION

Address: 3425 Walden Avenue
Depew, NY 14043
United States
Phone: 888-684-0011
Fax: 716-686-9129
E-mail: pressure@pcb.com
Web site: www.pcb.com

APPENDIX 3

THE SYNCHRONIZATION UNIT SCHEMATIC DIAGRAM

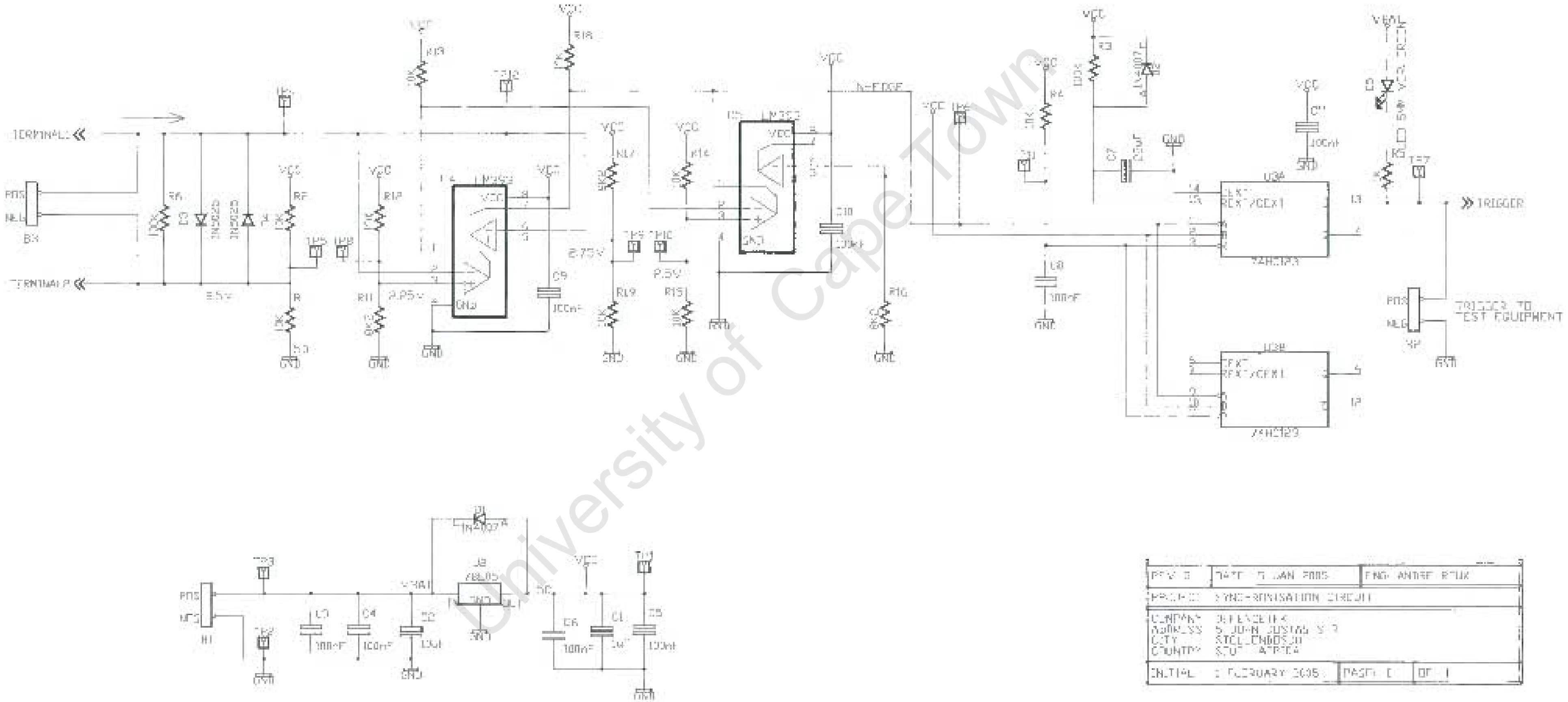

Figure 162: The schematic design of the detonator firing electronics with synchronisation to measurement equipment.

SYNCHRONIZATION UNIT CIRCUIT DESCRIPTION

This unit operates in conjunction with the IMPI™ firing unit, and provides a synchronization pulse to the measurement equipment as soon as current is detected in the detonator circuit.

The high-level principle of operation is described by Figure 163 below. The IMPI™ supplies a high voltage (from an internal capacitor) on its output terminals as soon as its firing button is depressed. This voltage is applied to the detonator via a long (variable between 100 m and 1000 m) cable. The synchronization unit is placed in series with this detonator current, and for easy operation, the synchronization unit is polarity protected, meaning that its two input terminals may be connected in either way. This is quite necessary, because the IMPI™ output terminals are not marked, and the operators of the IMPI™ may connect it onto the detonator circuit in either way, without heeding the polarity.

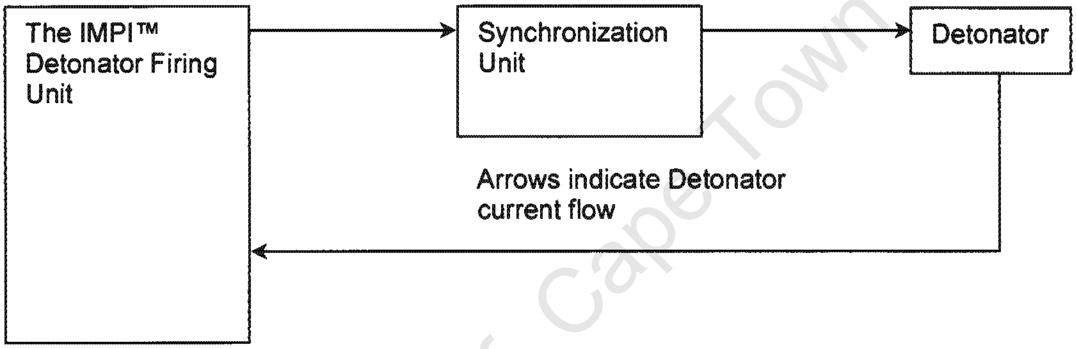

Figure 163: The high-level connection-diagram using the IMPI™ connected to the detonator via the Synchronization Unit.

The IMPI™ has its own battery, making the unit a voltage-floating unit. The synchronization unit also has an internal battery, which also makes this unit a voltage-floating unit. Two diodes connected back-to-back (D3 and D4) facilitates that the current may flow in either direction. One of the terminals are connected to a voltage divider (R1 and R2), placing the TP5 at half the VCC voltage (2.5 V). This voltage is connected through a high impedance resistor (R6 = 100kΩ) to the two input terminals of the voltage comparators in U4.

Steady state:

As there is no (or negligible) current flowing through R6, the voltage at pins U4A/p2 and U4B/p6 is also 2.5 V. The voltage divider at U4A/p3 (R11 and R12) gives a voltage of 2.25 V at U4A/p3. This means that, if the unit is at rest (no current flowing through D3 or D4, the output of the comparator (U4A) at U4A/p1 is in a LOW state (= GND) due to the voltage at pin U4A/p2 being higher than the voltage at U4A/p3. This LOW state is fed to the input of a comparator (U5A/p2). This latter comparator performs the function of a logic inverting amplifier because the voltage divider at U5A/p3 (R14 and R15) sets the voltage at U5A/p3 to 2.5V, and the input at U5A/p2 is expected to be either logic HIGH (5 V) or logic LOW (0 V). With the input of the comparator U5A at U5A/p2 in a LOW state, the output, U5A/p1, is in the high-impedance open-drain state. This means that the conductor marked N-EDGE is pulled to a HIGH state by R18, because the outputs of all the LM393 comparators are in the "open drain" configuration.

In the steady sate, the voltage at the input of the comparator U4B at U4p6 is 2.5 V. The voltage divider (R17 and R19) sets the input of the comparator U4B at U4p5 to 2.75 V. This means that the output at U4B/p7 is also in the high-impedance state with U4B/p5 (positive input) at a higher voltage than U4B/p6 (negative input). This output (U4B/p7) is also connected to the conductor marked N-EDGE.

Both the outputs (U4B/p7 and U5A/p1) of the comparators are in the now in the high-impedance state, allowing R18 to keep the conductor N-EDGE in the HIGH state.

The conductor N-EDGE is connected to the input of a mono-stable multi-vibrator (U3A), which needs a negative edge to trigger the output of U3A. In the steady state, there is no negative edge, and therefore U3A/p13 is steady at a LOW level.

Positive current flow when detonator is activated:

A positive current flow is relevant when the current is in the direction as indicated on the schematic diagram, flowing into Terminal 1. This means that the voltage across D3 rises from 0 V to approximately 0.7 V in a relatively short time. For the purposes of this circuit, the current performs a 0.7 V step function. The voltage at U4B/p6 therefore rises from 2.5 V to 3.2 V, which is higher than the comparator voltage threshold of 2.75 V. The output of U4B/p7 then flips from a high-impedance state to an active LOW, due to the fact that U4B/p6 (negative input) > U4B/p5 (positive input).

This means that the conductor N-EDGE is pulled LOW by U4B/p7, providing the negative edge that is required at U3A/p1 to trigger the mono-stable U3A at U3A/p13. This output steps to 5 V, and stays at 5 V for approximately 1 second, providing the required synchronization pulse. This mono-stable time is a function of the values of R3 and C7.

Negative current flow when detonator is activated:

A negative current flow is relevant when the current is in the opposite direction to the indicated current on the schematic diagram, therefore flowing into Terminal 2, through D4, and out of Terminal 1.

In this mode, the voltage drop across D4 (approximately 0.7 V) causes the voltage at TP4 to be 0.7 V lower than the voltage at TP5. The voltage at U4A/p2 (negative terminal of U4A) = 1.8 V, which is lower than the voltage at U4A/p3 (2.25 V). This means that the output of U4A (U4A/p1) flips to a high-impedance state, pulling the input to U5A at U5A/p2 to a HIGH state via the resistor R13. This means that U5A/p2 > U5Ap3, and therefore the output U5A/p1 is pulled into an active LOW state. This means that the conductor N-EDGE is pulled LOW, providing the required negative edge for the mono-stable U3A to activate a 1 second positive pulse at U3A/p13, which is the synchronisation pulse.

Output indicator:

LED D5 switches ON when the voltage at U3A/p13 goes HIGH, indicating when a synchronisation pulse is obtained.

Other circuits:

Comparator U5B, and mono-stable U3B are not connected to function.

U2 provides a regulated 5 V, called VCC from a 9 V battery.

APPENDIX 4

A PXI computer containing a 4-channel A/D card was used, in a configuration for measurement at 0.5μs intervals. The specifications for the A/D card, is shown in Figure 164.

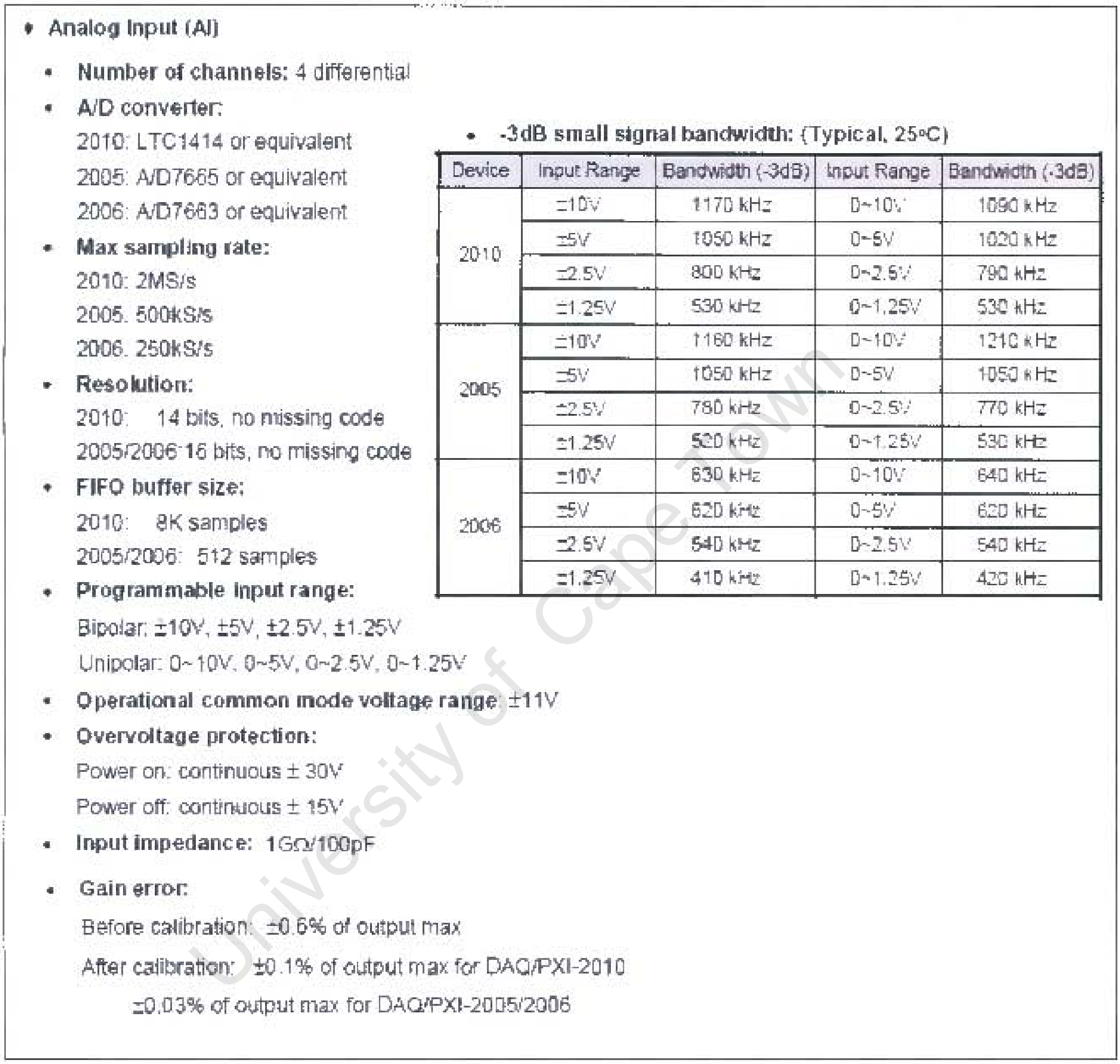

- **Analog Input (AI)**
  - **Number of channels:** 4 differential
  - **A/D converter:**
    2010: LTC1414 or equivalent
    2005: A/D7665 or equivalent
    2006: A/D7663 or equivalent
  - **Max sampling rate:**
    2010: 2MS/s
    2005: 500kS/s
    2006: 250kS/s
  - **Resolution:**
    2010: 14 bits, no missing code
    2005/2006 16 bits, no missing code
  - **FIFO buffer size:**
    2010: 8K samples
    2005/2006: 512 samples
  - **Programmable input range:**
    Bipolar: ±10V, ±5V, ±2.5V, ±1.25V
    Unipolar: 0~10V, 0~5V, 0~2.5V, 0~1.25V
  - **Operational common mode voltage range:** ±11V
  - **Overvoltage protection:**
    Power on: continuous ± 30V
    Power off: continuous ± 15V
  - **Input impedance:** 1GΩ/100pF
  - **Gain error:**
    Before calibration: ±0.6% of output max
    After calibration: ±0.1% of output max for DAQ/PXI-2010
    ±0.03% of output max for DAQ/PXI-2005/2006
  - **-3dB small signal bandwidth:** (Typical, 25°C)

Device	Input Range	Bandwidth (-3dB)	Input Range	Bandwidth (-3dB)
2010	±10V	1170 kHz	0~10V	1090 kHz
	±5V	1050 kHz	0~5V	1020 kHz
	±2.5V	800 kHz	0~2.5V	790 kHz
	±1.25V	530 kHz	0~1.25V	530 kHz
2005	±10V	1160 kHz	0~10V	1210 kHz
	±5V	1050 kHz	0~5V	1050 kHz
	±2.5V	780 kHz	0~2.5V	770 kHz
	±1.25V	520 kHz	0~1.25V	530 kHz
2006	±10V	630 kHz	0~10V	640 kHz
	±5V	620 kHz	0~5V	620 kHz
	±2.5V	540 kHz	0~2.5V	540 kHz
	±1.25V	410 kHz	0~1.25V	420 kHz

Figure 164: **Specifications of the DAQ card.**

APPENDIX 5

FURTHER DISCUSSIONS ON LITERATURE

Major Sources:

Ström and Janzon [10]

The data-sets of the measurements were given to the CSIR in two formats:

1. A short report explaining the test set-up.
2. Data files in .TXT format on a CD of the raw data as it was recorded on site.

The four pressure sensors that were used were unknown at the date of publication of this dissertation. The sampling rate was 500 Hz.

The measurements done by Ström and Janzon [10] are regarded by the CSIR (custodian of a copy of the information) to be very significant. The results obtained are the most comprehensive results of underwater blast measurement that the author could find, and the raw data was made available to the CSIR to analyze independently. The raw data was presented to the CSIR in raw (not analyzed) format, therefore this dissertation analyzes the data in detail.

One of the tests performed by Ström and Janzon [10] will be described in this literature review. Figure 165 shows the typical test set-up as used by Ström and Janzon [10].

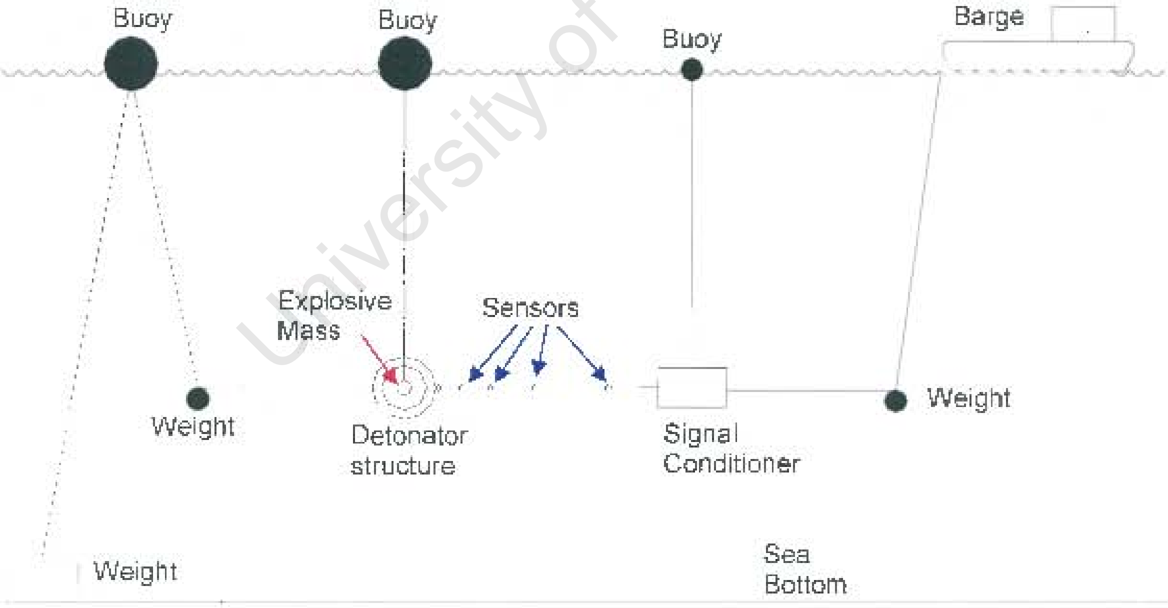

Figure 165: Typical Test Set-up in a Swedish fjord.

Four pressure sensors were positioned at various distances from an explosive charge. The distances were typically 3.5 m, 6 m, 11 m, and 20 m (see Table 43 for accurate recorded distances). As can be seen from Figure 165, the four sensors that were used were strung horizontally away from a charge, to ensure constant depth. The depth was typically 20 m, in a 40 m deep zone.

Five charges were exploded, and recordings made from all four sensors, and stored as ASCII files. One of the files (representing one of the explosions) was entered into Matlab®, and the result is shown in Figure 166. The very sharp rising pressure shock pulse can be seen, as well as the pressure effects of the bubble formation roughly 360 ms later. The five charges were of differing charge compounds and charge weights.

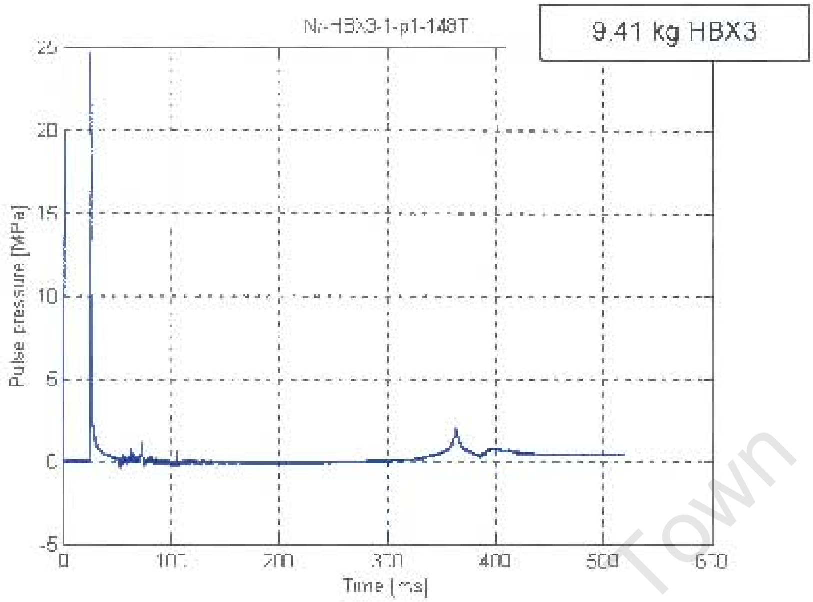

Figure 166: Plot of one of the five explosions, pressure versus time.

Some reference figures mentioned in the report by Ström and Janzon [10]:

A 9.41 kg HBX3 charge produced a 24.9 MPa pressure peak being measured 3.65 m from the point of detonation.

Quoted from Ström and Janzon [10]

- Utilizing TNT as the reference, the energy can be calculated as 2 MJ/kg.
- Theta = 0.264 ms.
- Shock energy is calculated utilizing the Equation:

$$e_{shock} = \frac{4\pi r^2}{Q}\int_0^t \rho u dt$$

- Maximum pressure is calculated as follows:

$$P_{max} = 51.175\left(\frac{R}{Q^{\frac{1}{3}}}\right)^{-1.1255} MPa$$

The graph (Figure 166) shows that the shock wave pressure pulse has a very large peak pressure, as opposed to the bubble pressure pulse which has a much lower peak pressure pulse. On face value the shock wave will have the largest probability to cause damage.

The data as supplied by Ström and Janzon [10] is discussed below in terms of the characteristics as required by the intended research methodology:

Characteristic 1: Shock Wave Propagation Velocity:

The test set-up (Figure 165) was constructed to have 4x sensors, which were placed at roughly 3.5 m, 6 m, 11 m and 20 m from the blast. The task to determine the propagation-velocity is simply to take the known distance between sensors, and divide this distance with the time taken for the shock wave to propagate between the known positions. This will give an average value of the propagation velocity.

The time-base of the pressure measurements was given as 2 μs. As can be expected, the practical placement process of the sensors could not be executed to a very high degree of accuracy, and therefore the sensor positions were recorded by Ström and Janzon [10] to be at slightly variable distances from the blast, as compared to the intended 3.5 m, 6 m, 11 m, and 20 m. This in itself does not constitute a problem, if it could be accepted that the actual distances from the blast is measured to a high degree of accuracy.

The experiment was conducted by executing the detonation of five charges, and all four sensors were activated to start measuring simultaneously. Unfortunately, from the raw data it was not possible to detect a marker, which indicates the moment of blast. This means that the position (in time and/or distance) of the first sensor cannot be determined from the raw data. This also means that. (for a first iteration approach), the position of the first sensor has to be accepted from Table 42, as 3.5 m.

Some of the data from the report by Ström & Janzon [20] is shown in Table 41. P1, P2, P3, and P4 denote the four positions of the four pressure sensors from each blast.

Table 41: Recorded sensor standoff distances from the blasts.

	No.	Type	Weight [kg]	E(s) [MJ/kg] P1	E(s) [MJ/kg] P2	E(s) [MJ/kg] P3	E(s) [MJ/kg] P4	Bubble Period [ms]
PL Blast 1	1	Plastic X	17.586	1.1573	1.0624	0.9849	0.9696	322.95
PL Blast 2	2	Plastic X	22.448	1.2626	1.0994	1.0429	0.9733	351.28
PL Blast 3	3	Plastic X	27.328	1.208	1.1398	1.1047	1.0431	370.72
HB Blast 1	4	HBX3	9.41	1.0614	1.0189	0.9878	0.958	336.82
HB Blast 2	5	HBX3	9.48	1.073	1.0009	0.9733	0.9658	339.02

For more clarity, this study will denote the five blasts as Plastic X Blast 1, Plastic X Blast 2, Plastic X Blast 3, HBX3 Blast 1, and HBX Blast 2 respectively from the top to the bottom of Table 41.

More information about the recorded standoff distances is shown in Table 42. The cell shown with a yellow background is assumed to have incorrect information. Correct information was obtained from the ASCII file containing the raw data, see Table 48, row 2.

Table 42: **Standoff distances and recorded peak pressures of five blasts.**

	No.	Distance P1 (m)	Pmax (MPa)	Distance P2 (m)	Pmax (MPa)	Distance P3 (m)	Pmax (MPa)	Distance P4 (m)	Pmax (MPa)
PL Blast 1	1	3.5	37.07	6.17	18.68	11.06	9.56	19.95	4.88
PL Blast 2	2	3.84	37.01	6.37	19.94	11.46	9.99	20.2	4.93
PL Blast 3	3	3.71	40.69	6.39	21.62	11.44	11.41	20.23	5.99
HB Blast 1	4	[8]6.65	23.45	6.37	12.81	11.39	6.62	20.23	3.51
HB Blast 2	5	3.88	22.12	6.52	12.54	11.54	6.43	20.37	3.41

A discrepancy of the data in Table 42 with respect to the raw data has been found, and Table 42 has been rewritten by the author as

Table 43, correlating the data in the table with the data contained in the raw data files.

Table 43: **Table with information taken from the raw data of standoff distances and peak pressure values of five blasts.**

	No.	Distance P1 (m)	Pmax (MPa)	Distance P2 (m)	Pmax (MPa)	Distance P3 (m)	Pmax (MPa)	Distance P4 (m)	Pmax (MPa)
PL Blast 1	1	3.5	39.09	6.17	19.28	11.06	10.34	19.95	5.04
PL Blast 2	2	3.84	39.93	6.37	20.59	11.46	10.84	20.2	5.04
PL Blast 3	3	3.71	43.31	6.39	22.33	11.44	11.93	20.23	5.99
HB Blast 1	4	3.65	24.72	6.37	13.32	11.39	7.06	20.23	3.67
HB Blast 2	5	3.88	23.37	6.52	13.11	11.54	6.6	20.37	3.53

Plastic X Blast 1 produced the pressure results as shown in Figure 167. It is important to note that the independent axis (Time) denotes the time taken from the moment of the start of the recording. It does not denote the time taken from the moment that the blast occurred.

---

[8] This cell contains information (kept incorrect in this dissertation for the purposes of accuracy of quotation), which was recorded incorrectly by Strom & Janzon [20]. The raw data confirms that this distance should be 3.65 m (see Table 43).

Plastic X Blast 2 produced the pressure results as shown in Figure 167.

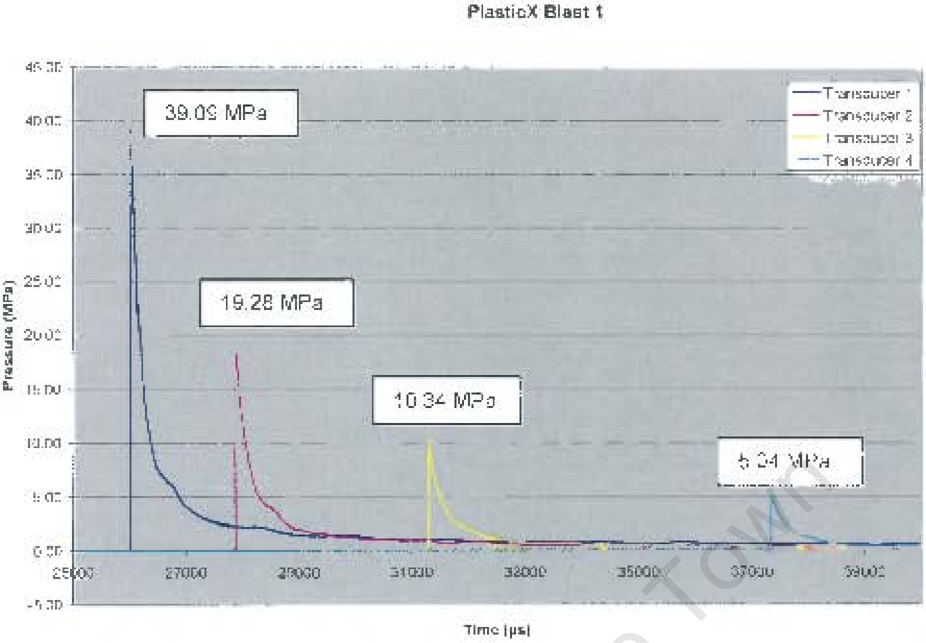

Figure 167: Pressure results from Plastic X Blast 1.

The calculation of the propagation velocity for Plastic X Blast 1 is shown in Table 44.

Table 44: Calculation of propagation velocity for Plastic X Blast 1.

PlasticX Blast 1	17.568kg			
Distance from blast from report (m)	3.5	6.17	11.06	19.95 m
Distance from blast on raw data records (m)	3.50	6.17	11.06	19.95 m
Shock Time between sensors (µs)	0	1848	3418	6038 µs
Distance between sensors (m)	0	2.67	4.89	8.89 m
Velocity (m/s)		1445	1431	1472 m/s
Distance between first and last sensor (m)				16.45 m
Time between first sensor and last sensor (µs)				11304 µs
Average velocity (m/s)				1455 m/s

Plastic X Blast 2 produced the pressure results as shown in Figure 168.

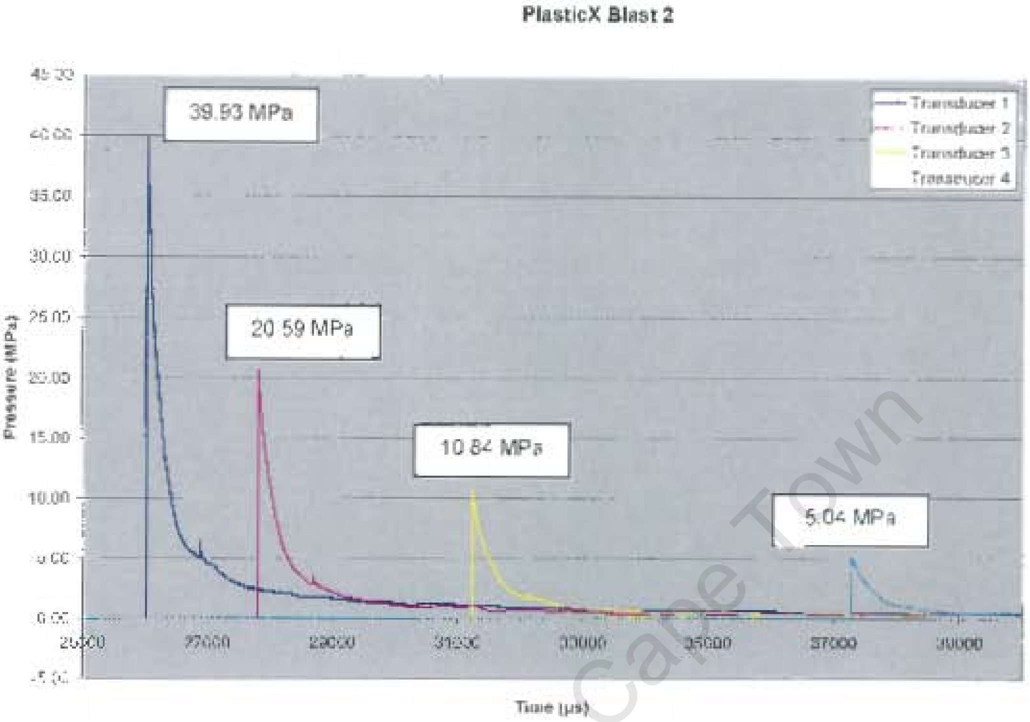

Figure 168: Pressure results from Plastic X Blast 2.

The calculation of the propagation velocity for Plastic X Blast 1 is shown in Table 45.

Table 45: Calculation of propagation velocity for Plastic X Blast 2.

PlasticX Blast 2	22.448kg			
Distance from blast from report (m)	3.84	6.37	11.46	20.2 m
Distance from blast on raw data records (m)	3.84	6.37	11.46	20.20 m
Shock Time between sensors (µs)	0	1792	3430	6028 µs
Distance between sensors (m)	0	2.53	5.09	8.74 m
Velocity (m/s)		1412	1484	1450 m/s
Distance between first and last sensor (m)				16.36 m
Time between first sensor and last sensor (µs)				11250 µs
Average velocity (m/s)				1454 m/s

Plastic X Blast 3 produced the pressure results as shown in Figure 169.

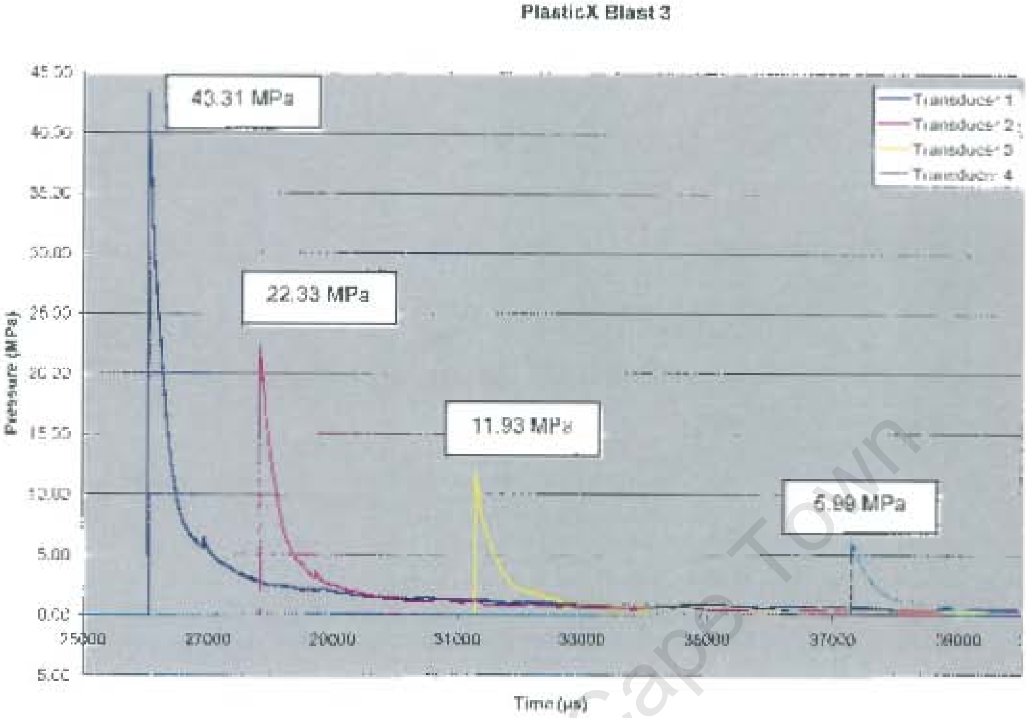

Figure 169: **Pressure results from Plastic X Blast 3.**

The calculation of the propagation velocity for Plastic X Blast 3 is shown in Table 46.

Table 46: Calculation of propagation velocity for Plastic X Blast 3.

PlasticX Blast 3	27.33kg			
Distance from blast from report (m)	3.71	6.39	11.44	20.23m
Distance from blast on raw data records (m)	3.71	6.39	11.44	20.23m
Shock Time between sensors (µs)	0	1788	3442	6028µs
Distance between sensors (m)	0	2.68	5.05	8.79m
Velocity (m/s)		1499	1467	1458m/s
Distance between first and last sensor (m)				16.52m
Time between first sensor and last sensor (µs)				11258µs
Average velocity (m/s)				1467m/s

HBX3 Blast 1 produced the pressure results as shown in Figure 170.

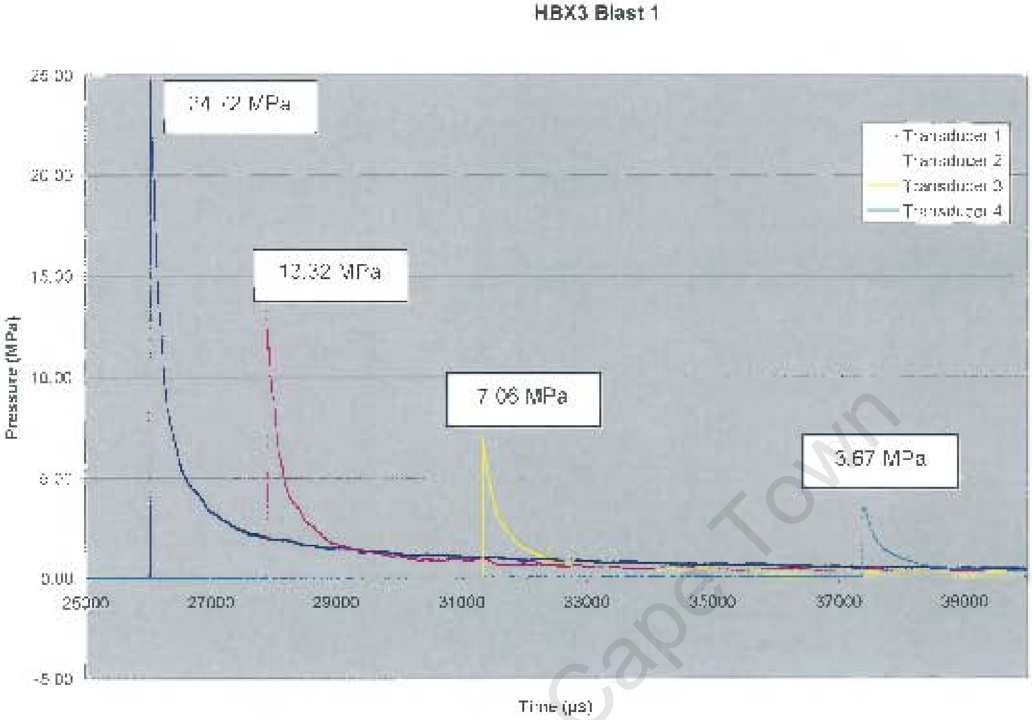

Figure 170: Pressure results from HBX3 Blast 1.

The calculation of the propagation velocity for HBX3 Blast 1 is shown in Table 47.

Table 47: Calculation of propagation velocity for HBX3 Blast 1.

HBX3 Blast 1	9.41kg			
Distance from blast from report	6.65	6.37	11.39	20.23 m
Distance from blast on raw data records	3.65	6.37	11.39	20.23 m
Time between sensors (µs)	0	1870	3446	6038 µs
Distance between sensors (m)	0	2.72	5.02	8.84 m
Velocity (m/s)		1455	1457	1464 m/s
Distance between first and last sensor (m)				16.58 m
Time between first sensor and last sensor (µs)				11354 µs
Average velocity (m/s)				1460 m/s

HBX3 Blast 2 produced the pressure results as shown in Figure 171.

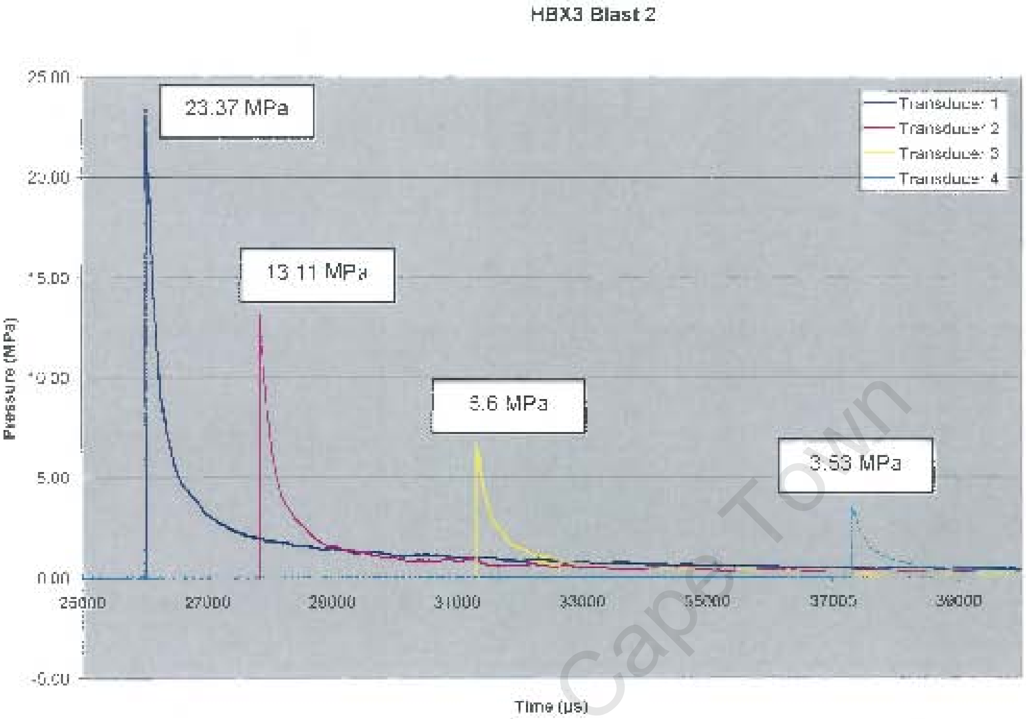

Figure 171: **Pressure results from HBX3 Blast 2.**

The calculation of the propagation velocity for HBX3 Blast 2 is shown in Table 48.

Table 48: Calculation of propagation velocity for HBX3 Blast 2.

HBX3 Blast 2	9.48kg				
Distance from blast from report	3.88	6.52	11.54	20.37	m
Distance from blast on raw data records	3.88	6.52	11.54	20.37	m
Shock Time between sensors (μs)	0	1832	3456	5992	μs
Distance between sensors (m)	0	2.64	5.02	8.83	m
Velocity (m/s)		1441	1453	1474	m/s
Distance between first and last sensor (m)				16.49	m
Time between first sensor and last sensor (μs)				11280	μs
Average velocity (m/s)				1462	m/s

Characteristic 2: Peak-Pressure Function

Figure 167 to Figure 171 show the pressure functions as measured at standoff distances between 3,5 m and 20 m from the blasts. From these figures, it can be seen that the peak pressures reduce with distance. Ström and Janzon [10] defined the peak pressure to reduce at a rate of:

$$P_{\max} = 51.175\left(R \Big/ Q^{\frac{1}{3}} \right)^{1,1255} \quad \text{MPa} \quad \text{-------------------} \quad \mathbf{51}$$

Where
R is the standoff distance in m.
Q is the charge weight in kg.

Traditionally, the equation for P_{max} is written such that the charge weight (mass) is divided by the distance. Rewriting the Ström and Janzon [10] Equation in the traditional format, we get:

$$P_{\max} = 51.175\left(Q^{\frac{1}{3}} \Big/ R \right)^{-1,1255} \quad \text{MPa} \quad \text{---------------} \quad \mathbf{52}$$

In this format, Equation 52 can be compared with the Equation offered by Cole [5], which is graphically illustrated in Appendix 1 on Page 188.

Equation 52 was superimposed graphically over actual measurements taken by Ström and Janzon [10] in Figure 172. It is clear that the theoretical Equation has slightly larger values than the actual measurements as produced by the specific HBX3 blast1. This is due to the fact that the formula was composed for a different explosive material.

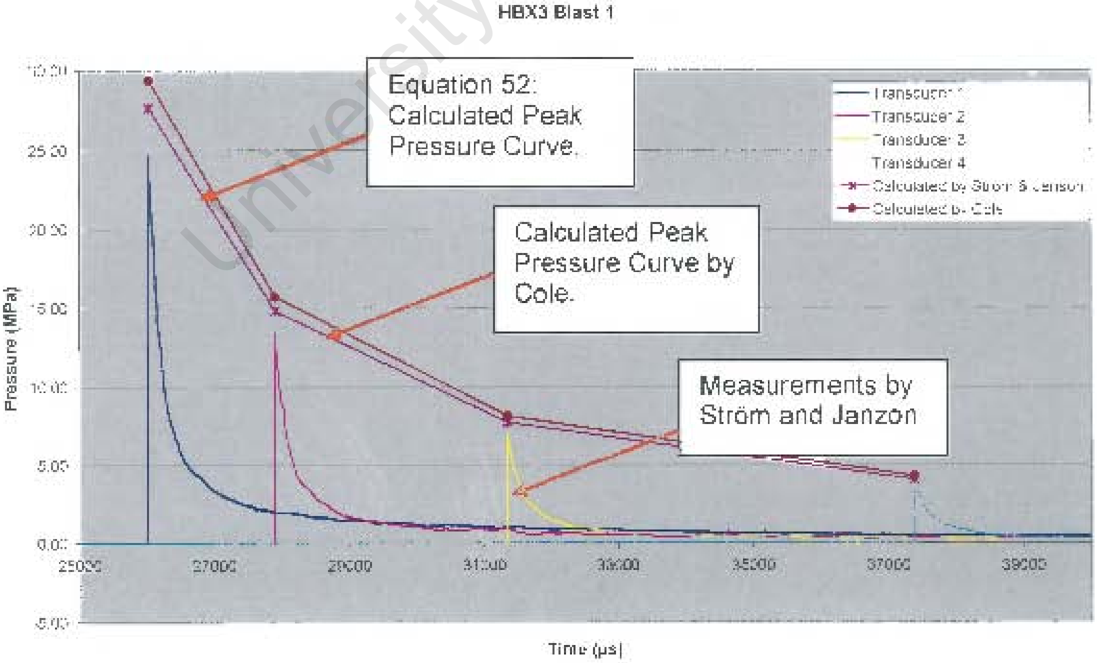

Figure 172: Equation 52 (Peak Pressure Curve) superimposed on actual pressure measurements.

In another format (for better amplitude comparison), the measured values of the two HBX3 blasts (blasts 4 and 5) are shown relative to the corresponding calculated Peak Pressure in Figure 173 A and B. It can be seen that, for both the HBX3 blasts, the measured peak pressure values are generally below the formulated curve of Equation 52.

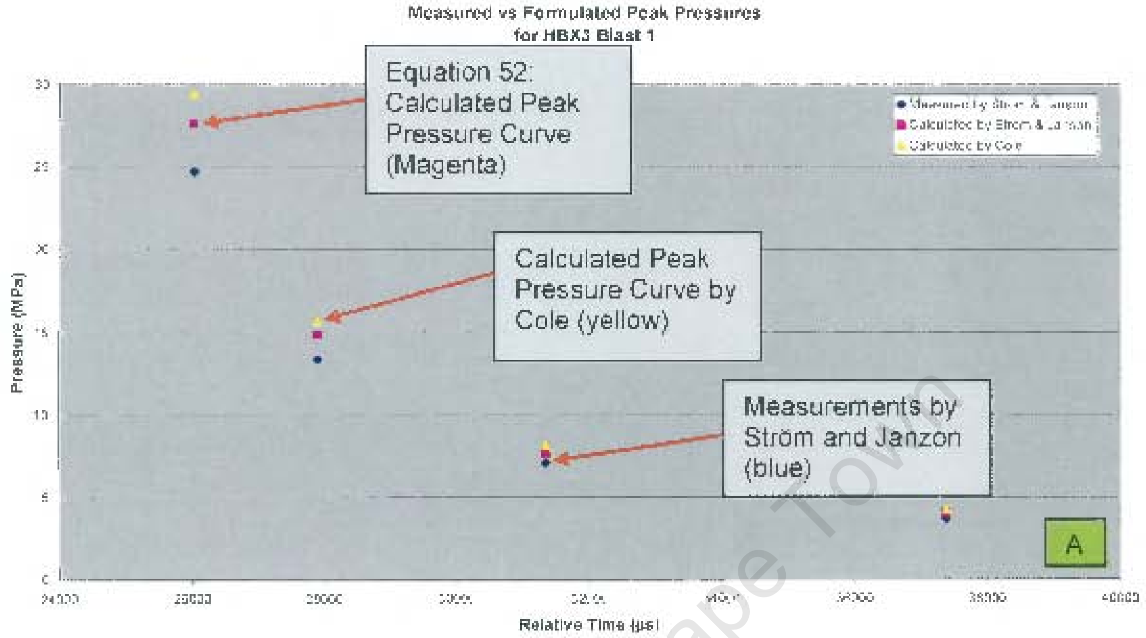
Measured vs Formulated Peak Pressures
for HBX3 Blast 1

Equation 52: Calculated Peak Pressure Curve (Magenta)

Calculated Peak Pressure Curve by Cole (yellow)

Measurements by Strom and Janzon (blue)

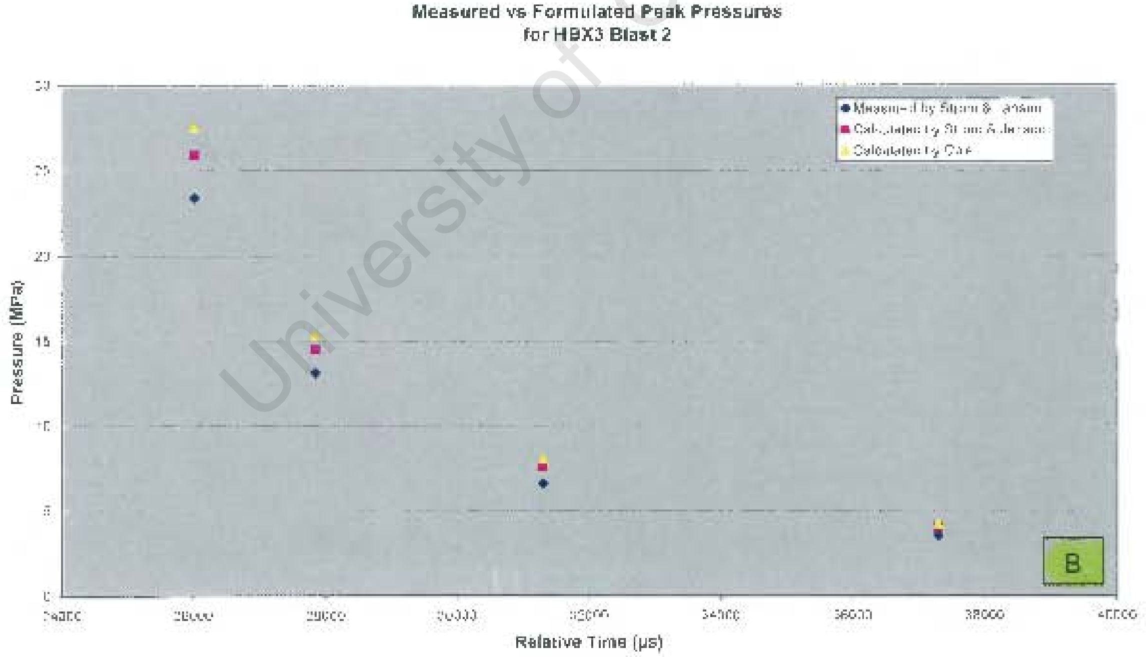
Measured vs Formulated Peak Pressures
for HBX3 Blast 2

Figure 173: Comparison of the measured Peak Pressure values against the calculated Peak Pressure values for HBX3.

The opposite finding is true for the Plastic X composition (blasts 1 to 3). Figure 174 A, B and C shows that the measured values are in fact larger closer to the blast than the calculated values according to Equation 52.

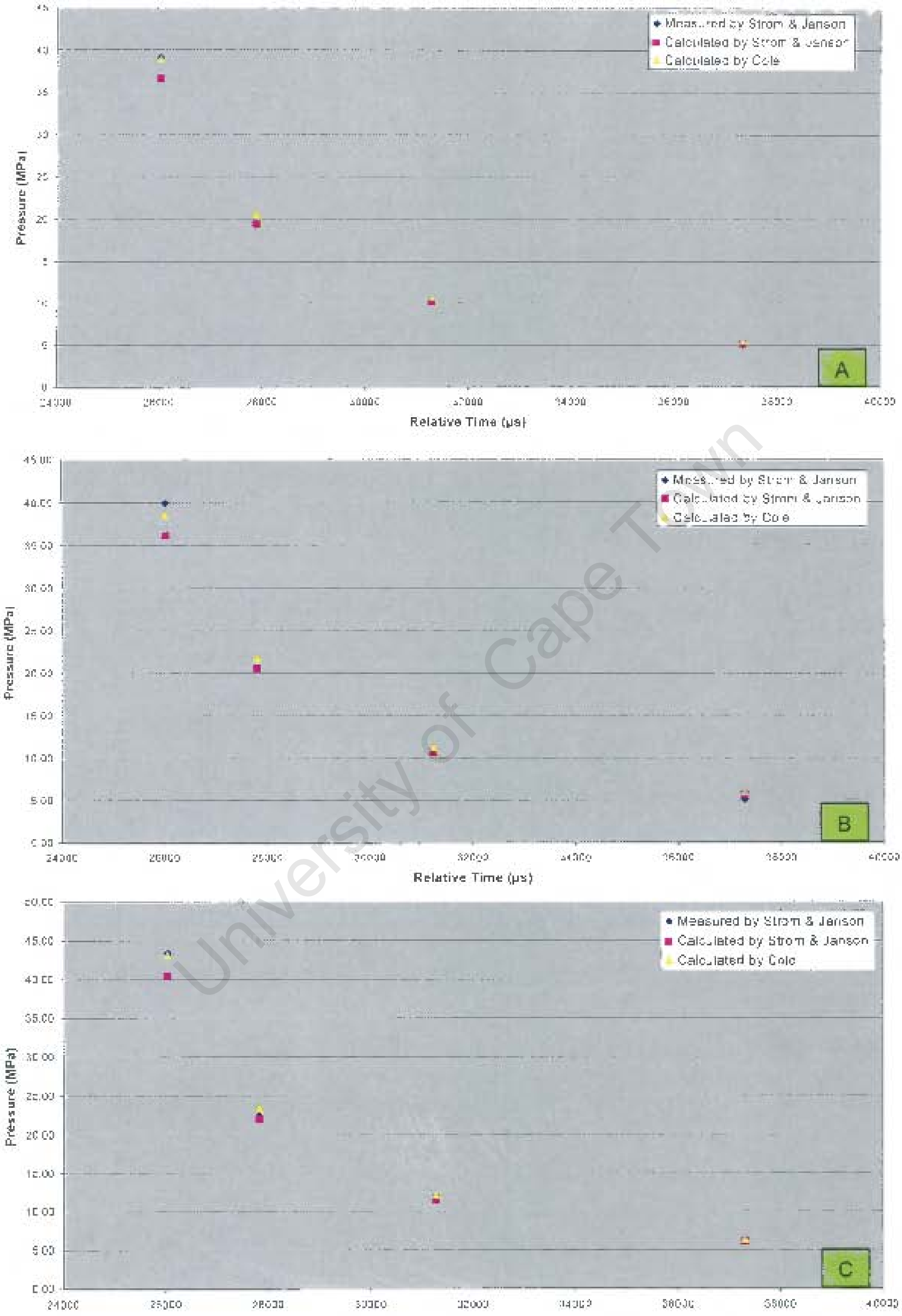

Figure 174: Comparison of the measured Peak Pressure values against the calculated Peak Pressure values for the three PlasticX blasts.

It can be seen that, for all three the PlasticX blasts, the measured values are slightly above[9] the formulated curve of Equation 52. A conclusion could be drawn that the PlasticX explosives are therefore more successful with respect to the peak pressure amplitude than the HBX3 composition.

The mathematical equation given by Ström & Janzon [20] has an asymptotic result when the distance approaches 0 m. This, in theory, means that the predicted peak pressure at the point of explosion →∞. This anomaly was discussed in paragraph on Characteristic 3: Shock Pressure Leading-Slope Rise-Times on page 207), where it was shown that the description of the leading edge does not allow infinite amplitudes at the explosion origin (boundary condition of $R \rightarrow a_0$ where a_0 is the charge radius).

Observations:

The mathematical model that is given by Ström & Janzon [20] is applicable to their own proprietary composition, called Plastic X (unpublished composition).

The mathematical Equation for each type (composition) of explosive differs with respect to the expected peak amplitude of the explosion at any given distance from the explosion. If a company produces its own composition of explosive, it will probably be required to measure a number of explosions at a given distance to determine the specific mathematical model to be used for that specific composition. This statement is general knowledge amongst explosive manufacturers.

Characteristic 3: Shock Pressure Leading-Slope Rise-Times

The interest-value of the rise-time lies in relationship of the rise-times with respect to the acceleration (that is caused by an explosion) of an enclosure containing electronics, in close proximity of the blast. This study investigates this relationship.

The main purpose of this Section was to determine the rise times of explosion shock fronts as derived from the raw data as given by Ström & Janzon [20]. Information on this topic was not readily available in the literature, except that it was referred to as "discontinuous" or "practically instantaneous". Actual values for rise times could not be found in the literature, and therefore this dissertation analyzed the data as supplied by Ström & Janzon [20]. Figure 175 shows that all normalised rise-times have approximately the same history characteristics, and for the relevant twenty measurements supplied by Ström & Janzon [20], the rise times were approximately 6 μs.

---

[9] The measure of "slightly above" refers to the influence of a combination of the constant in Equation 52 as well as the power to which the quantity in brackets are raised. Cole [5] subscribes the constant as 54.56 as opposed to the constant by Strom & Janzon [20] of 51.175. The power of the quantity between brackets is subscribed by Cole [5] as 1.13, while Ström & Janzon [20] defined it to be 1.1255. It must also be kept in mind that the type of explosive defines these two numbers. This thesis does not discern between types of explosives to an exact amount with respect to the peak pressure produced by the explosion, but rather what order of pressure (and shock wave propagation velocity) will be experienced by an object at stand-off distances of approximately 2 m from a blast of a 40 kg charge. Due to reflections from nearby objects, e.g. a ship's hull, it is expected that the peak pressure will vary by as much as 30%. The difference between quantities given by Cole [5] and Ström & Janzon [20] are negligible for the purposes of this dissertation.

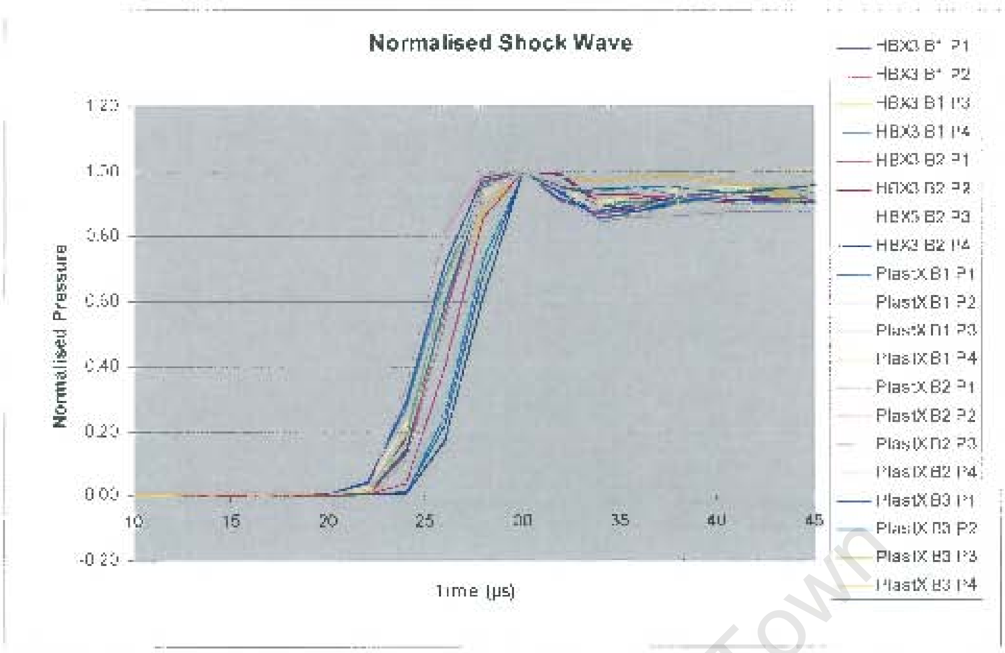

Figure 175: Rise-times vs. normalised shock at all four sensor positions.

The inclination to suspect that the similarity between these measurements was induced by bandwidth limitations of the test equipment could be discarded due to:

1. The fact that bandwidth limitation would keep the dP/dt characteristic of the waveform constant (over the linear region) for all values that the pressure slew action is faster than the bandwidth capability of the measurement equipment, and
2. The fact that this is not the case for the measurements taken by Ström & Janzon [20], because the dP/dt characteristic decreases with range, although the rise times remain constant.

It is also necessary to investigate the pressure history, not in the time dimension, but in length dimension. Cole [5] refers to this length dimension to determine the "thickness" of the shock front. Now that it is known that the shock front moves at constant velocity in the far field (at approximately 1470 m/s), and together with the fact that the rise times are approximately 6µs in the far field, the shock front thickness can be quantified for the far field as 1470 m/s x 6 µs = 8.82 mm (or approximately 9 mm to round off the result). This is significant, because now the rise times can be superimposed upon the physical dimensions of the electronics container, see Figure 19, for applications in the far field.

Figure 176 depicts the same data as was used by Figure 175, but translated into linear dimensions as a prelude to the discussion of Figure 19.

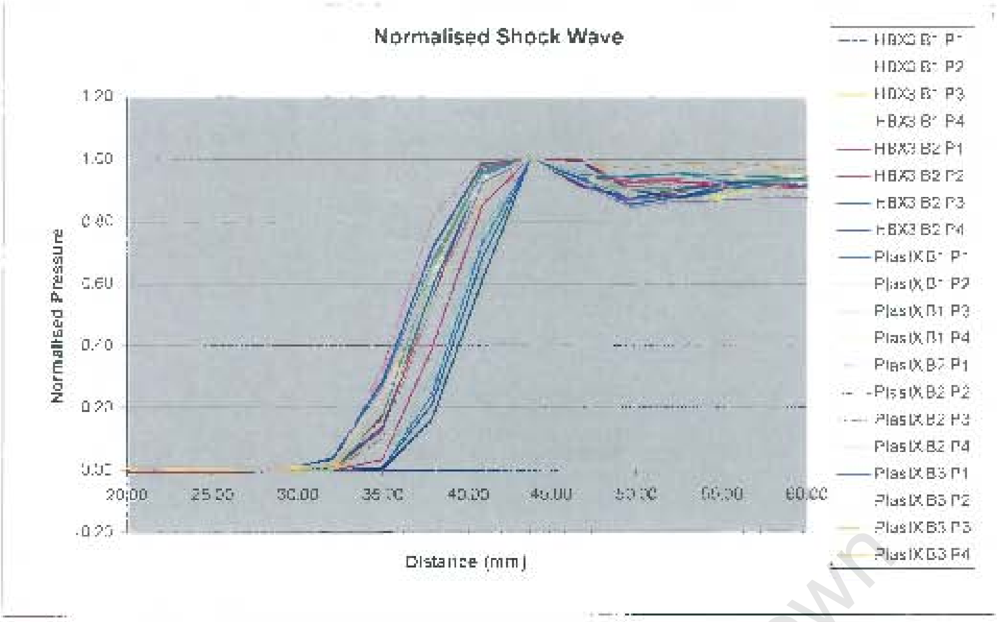

Figure 176: Incremental distance vs. normalised shock at all four sensor positions.

Discussion

The results (in all cases shown in Figure 175) illustrate that the rise times were recorded to be approximately 6 µs (or 9 mm), irrespective of peak pressure value, or distance from the blast. This observation was valid for the data as supplied by Ström & Janzon [20], i.e. for distances between 3.5 m and 20 m, relative to explosive masses between 9.5 kg and 27 kg, for the two different explosive compositions that were used.

Ström & Janzon [20] offered the explanation that the sensor width was approximately 10 mm. When a shock wave with an infinitely fast rise-time approached the sensor at a constant speed, (typically 1468 m/s), the time taken for the shock wave to completely engulf the sensor from the time that the shock front touched the sensor, was 0.01m/1486m/s = 6.73µs. If the rise-time was measured to be 6 µs, then the actual rise time would be 0.73 µs. However, the rise-times were not measured with enough accuracy to deduct an actual rise time of less than 1 µs.

Cole [5]:

The manuscript by Cole [5] gives insight into the early research years about the subject of underwater explosions. His manuscript was first published in 1946, but over the years this document remained the prime reference manual for most explorers of the subject of underwater blast.

One should realize that in the years prior to 1946, equipment was not as sophisticated as modern equipment. Keeping in mind that the Cole [5] research in many ways is still holding water, his manuscript is a remarkable achievement.

The specific characteristics that are researched by the author, is found in Cole [5:p40]:

Characteristic 1: Shock Wave Propagation Velocity

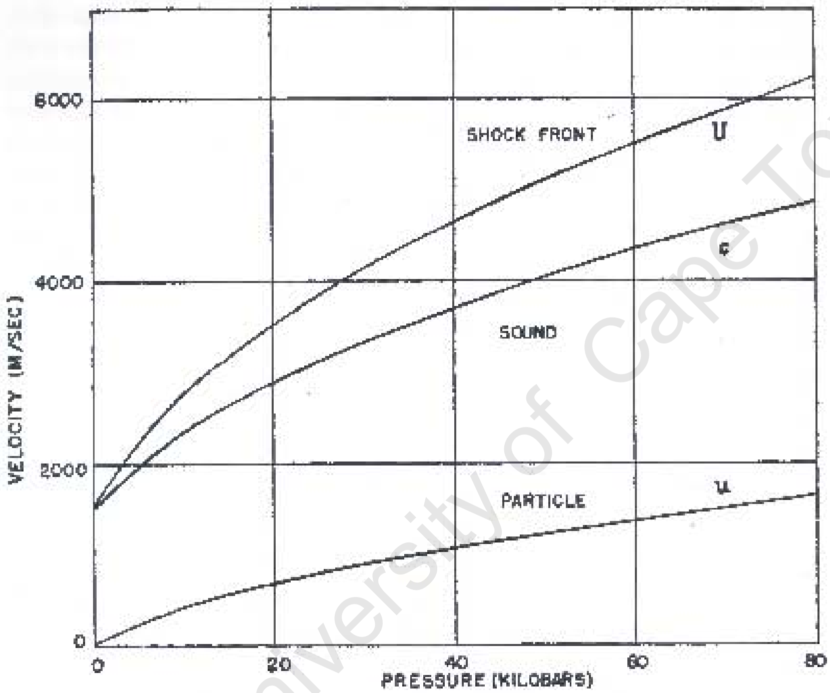

Fig. 2.3 Velocities at a shock front as a function of pressure for high pressures.

Figure 177: **Velocities at a shock front as a function of pressure.**

Cole [5:p4] reports that, if the pressure is small enough, the rate of propagation is practically independent of the magnitude of the pressure. This statement refers to pressures, which are small enough to be considered "acoustic" pressures, as could be found in the far field[10] of a shock wave. The threshold of the transition to "small enough" is not given.

Cole [5:p40] shows that (see Figure 177) the shock front propagation velocity is higher than the speed of sound for high pressures. He also reports that (Cole [5:p5]), when a blast occurs, the shock wave velocity propagation is "several times" the "limiting value of 5000 ft/s" (i.e. the speed of sound) at (and very near) the explosion. This shock wave velocity drops to the speed of sound quite rapidly as the shock wave advances outward and the pressure falls to acoustic values. Cole [5] does not give a more detailed description of the propagation velocity near the blast.

---

[10] The concept of the "near field" and the "far field" is discussed on page 40 of this dissertation.

Characteristic 2: Peak Pressure Function

Cole [5:p5] states that the pressure level in the spherical wave falls off more rapidly with distance than the inverse first power law (1/R) predicted for mall amplitudes. but eventually approach this behaviour in the limit of large distances. He also states that (Cole [5:p7]) the pressure-time curve at a given distance from the explosion will have the same general form.

Cole [5:p122] reports that it has been found that for limited ranges of the argument $W^{1/3}/R$ (where W is the weight of the explosive charge, and R is the standoff distance) the peak-pressure P_m can be approximated by power laws of the form:

$$P_{max} = k\left(W^{\frac{1}{3}}\Big/R\right)^{\alpha} \qquad \text{--------------} \quad \mathbf{53}$$

Cole [5:p122] also reports that this Equation is *"a fairly accurate expression of theoretical results between 10 and 100 charge radii"*. He plotted values for TNT on a graph, and empirically fitted a straight line of slope $\alpha = 1.16$ onto the data. He reports (Cole [5:p123]) that *"$\alpha = 1.16$ gives a good fit except for $W^{1/3}/R > 0.3$ ($R/a_0 < 25$)"*. a_0 = the charge radius. This means that a less accurate fit for α = 1.16 was experienced for standoff distances that were less than 25 charge radii.

To complete the Equation of Cole [5], the values for α = 1.13 and k = 2.16 (from Table 7.3: Cole [5:p242] for TNT, which differs slightly from α = 1.16 as reported in Cole [5:p123]) is inserted into Equation 54:

$$P_{max} = 2.16x10^{4}\left(W^{\frac{1}{3}}\Big/R\right)^{1.13} \ lb/in^{2} \qquad \text{--------} \quad \mathbf{54}$$

Equation for TNT:
Where W is in lb and R is in feet.

Cole [5:p238] also reports on experiments done with spherical Pentolite charges. His data were obtained from 47 records at 12 distances from 51 and 80-pound charges, as well as from 75 records at 4 distances from 0.5, 3.8, and 7.5-pound charges. Peak pressures were plotted against $W^{1/3}/R$ using logarithmic scales. A straight line of slope 1.13 (different from the 1.16 as shown in Equation 54) on a log-log scale fitted the data fairly well, and Cole [5:p239] reports a completed Equation for the peak pressures as generated by Pentolite charges:

$$P_{max} = 2.25x10^{4}\left(W^{\frac{1}{3}}\Big/R\right)^{1.13} \ lb/in^{2} \qquad \text{--------} \quad \mathbf{55}$$

Equation for Pentolite:
Where W is in lb and R is in feet.

This Equation for Pentolite charges can be translated into the SI (metric system) as shown in Equation 56:

$$P_{\max} = 54.56\left(W^{\frac{1}{3}} \Big/ R \right)^{1.13} \ MPa \qquad 56$$

Equation for Pentolite in SI: Where W is in kg and R is in m.

This result of Equation 56 is depicted in graphical form for Pentolite in Appendix 1. The starting point of 2 m is purposely selected to be more than 10 charge radii, because of the inaccuracies reported by Cole [5] at closer distances than 10 charge radii.

Characteristic 3: Shock Pressure Leading-Slope Rise-Times

Cole [5:p230] measures the shock wave as shown in Figure 178:

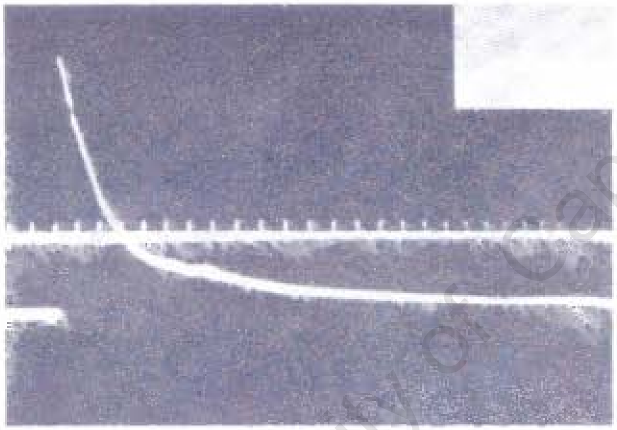

Figure 178: Pressure history as measured by oscilloscope prior to 1946.

Cole [5:p5] reports that the pressure rise is for all practical purposes discontinuous.

Characteristic 4: Shock Pressure-Time History

Cole [5:p230] reports that the pressure history that follows the initial peak pressure, decays exponentially, and the pressure shock wave can be approximated by Equation 57.

$$P = P_{\max} e^{-t/\theta} \qquad 57$$

θ is the time-constant of exponential decay, and this time-constant is given by Cole [5], (converted to SI), as shown in Equation 58:

$$\theta = 92.5W^{1/3}\left(W^{1/3}\big/_{R}\right)^{-0.22}\ \mu s \quad \text{-----------} \quad 58$$

Where:
W is in kg
R is in m

Characteristic 5: Shock Impulse Energy

Cole [5:p231] reports: *"For many purposes, the effectiveness of a shock wave depends on the time-integral of pressure, or impulse, more significantly than on the detailed form of the pressure versus time"*. In general form, this is shown in Equation 59.

$$I(t) = \int_0^t P(t)dt \quad \text{---------------------------} \quad 59$$

Cole [5:p239] experimented with a time constant θ, and derived an empirical Equation for the Impulse for an integration period of 6.7 x θ, as shown in Equation 60:

$$I(6.7\theta) = 2.18W^{1/3}\left(W^{\frac{1}{3}}\big/_{R}\right)^{1.05} \quad \text{-----------------------} \quad 60$$

Where:
W is in lb
R is in ft

Chung & Kinsey [3]

Chung & Kinsey [3] of DSTO in Australia made great strides forward in 1998 to measure the shock detonation velocity making use of optical methods (framing and streak records of a camera which is capable of 10^6 frames per second). Both the initial velocity of the shock wave and bubble formation were measured, and the results shown in Figure 179. This figure shows the rapid initial expansion of the detonating Pentolite sphere (section AB) and the shock wave (BC_1) rapidly separating from the bubble of detonation products (section BC).

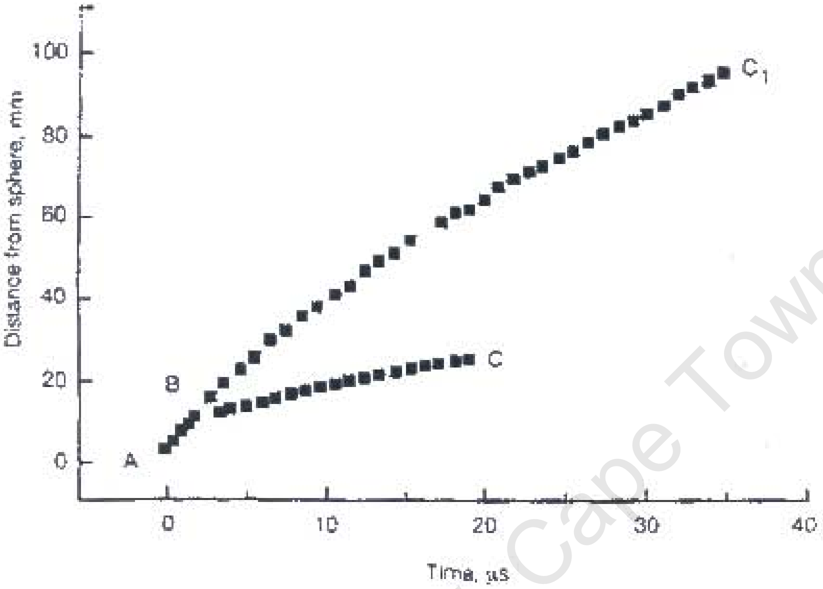

Figure 179: Expansion of the shock wave and bubble surface in the distance-time domain.

This means that, in the initial stages of the explosion (after the detonation has been completed) the bubble and shock waves are effectively moving together at the same speed, until point B is reached, approximately 2 µs after the explosion. The bubble and shock waves then separate, and the bubble starts slowing down at a greater rate than the shock wave. Chung & Kinsey [3] plotted the velocity of the shock wave against Reduced-Distance, as shown in Figure 180.

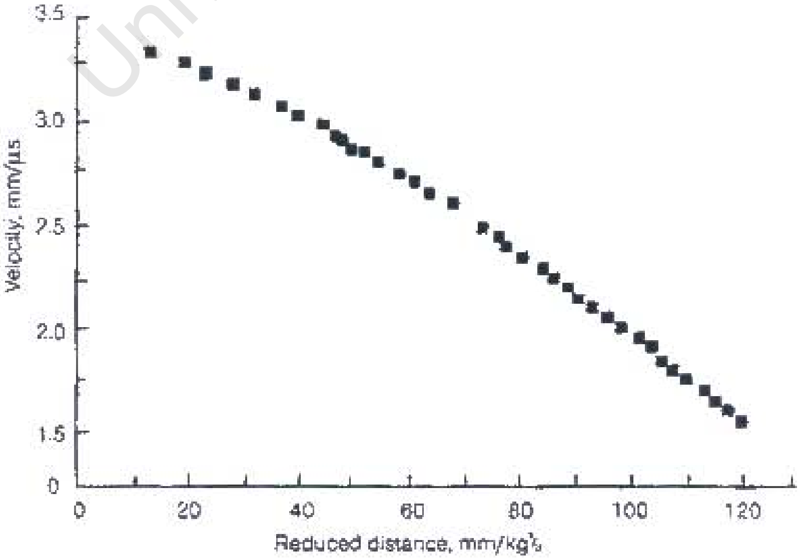

Figure 180: Variation in velocity of expansion of the shock wave, with reduced distance.

The author is of the opinion that Chung and Kinsey maintained a high degree of accuracy for this type of experiment, yet the graph shown in Figure 180 may not be entirely accurate, due to the tendency of the velocity to become less than the speed of sound when the graph is extrapolated. The expected knee in the graph may be too prominent, see Figure 181.

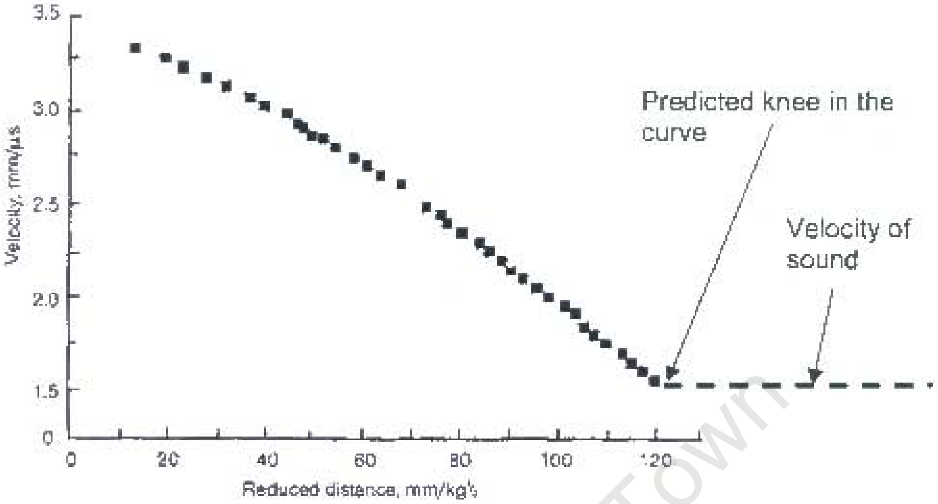

Figure 181: Sound velocity compared to shock wave velocity.

Nevertheless, it has been substantiated that the velocity of propagation of the shock wave is non-linear for ranges between the reduced distances of 12 mm/kg$^{1/3}$ (0.23 charge radii) to 120 mm/kg$^{1/3}$ (2.3 charge radii) and that the initial velocity in this segment is approximately 3.4 mm/µs. This means that the initial velocity is approximately 2.3 times the speed of sound in water, depending on the size of the charge and related pressure that is created.

Chung & Kinsey [3] also showed that the mathematical Equation which fits this velocity curve, is given by curve-fitting methods as:

$$U = 11.33\,R^{-0.37}\ mm/\mu s \qquad \text{61}$$

The correlation of the curve fitting process was $R^2 = 0.83$.

Chung & Kinsey [3] also shows that (see Figure 182) the section closer than 0.23 charge radii (12 mm/kg$^{1/3}$) the velocity follows a different curvature. In this region, the highest velocity is recorded as 6 mm/µs. This equates to 4 times the speed of sound. Although Figure 182 depicts the measurements reported for the bubble expansion, it has been shown in Figure 179 that the first portion of the curve, the velocity of the shock wave is equal to the velocity of the bubble. Therefore the first portion of Figure 182 is also valid for the shock wave.

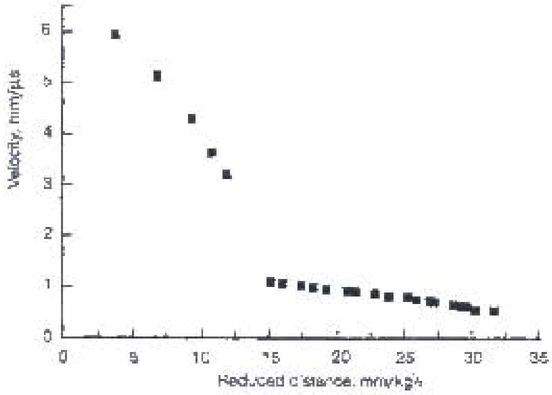

Figure 182: Variation in velocity of bubble expansion with reduced distance.

Supporting Sources

Hammond [7]

Hammond [7] set out *"to develop a numerical simulation method for predicting the structural response of submerged, air-backed plates to far-field underwater explosions and to further the understanding of the physics associated with the coupled fluid-structural response, including local cavitation-phenomena"*.

His discussions on the definition of the near field and far field of an underwater explosion are directed towards his specific application needs, and does not give the definitions in absolute terms. However, Hammond [7] indirectly supports the author's view that the definition of the near and far fields should be related to the shock wave propagation velocity Hammond [7:12]:

"The velocity of the shock wave in the near field to the underwater explosion is typically several percent greater than the acoustic wave velocity in the far field region. Acoustic wave velocities are attained at approximately twenty charge radii from the detonation centre".

Burdick [15]

Burdick [15] states that underwater sound velocity is formulated by:

$$c = 1449 + 4.6T - 0.055T^2 + 0.0003T^3 + (1.39 - 0.012T)(S - 35) + 0.017h \quad \text{-------} \quad \mathbf{62}$$

Where:
C= Velocity of Sound in m/s
T= Temperature in °C
S= Salinity in parts per thousand
h= depth in m

Using a temperature of 15 °C, a salinity of 4.8 %, and a depth of 20 m, the velocity of sound is calculated to be 1461.3 m/s. This result shows good correlation with the result obtained by Figure 8.

Cichocki [4]

Cichocki [4] was concerned about the protective capacity of containment structures subjected to impulse loading. His study was therefore somewhat different to this study, which was intent to protect much smaller objects than the structures of Cichocki [4]. However, it is of interest that his protective methods are similar to the protective methods as is suggested by this study for smaller units.

He suggested that one of the possible means of protection of important structures, was that the protective one could be placed at a certain distance from the main one, and would act as a protective shell. This protective shell can be connected with the main structure by means of diaphragms, stiffeners and other structural elements. The main purpose would be to dissipate the maximum amount of energy in the protective containment.

The correlation between the principles of the solution that this study presents for the protection of smaller units against the rigors of underwater blast loading, and the solution as offered by Cichocki [4] is in essence 100 %. This study, however, uses the protective shield as part of the functionality of the unit, i.e. the container of the electronics is designed to withstand the pressure loading, but all internal components (mechanical or electronic) are suspended by energy absorbing material.

Morrison [15]

Morrison [15] reports on a different kind of shock-acceleration, i.e. the shock produced by launching an electronics container from a cannon. What is interesting and applicable about this paper, is the description of his solution to counteract the effects of acceleration, i.e. concentrating on the mounting methods, in stead of making use of an outer structure that absorbs the shock and protects an inner structure.

One must take into account that the accelerations caused by cannon-launched missiles are much smaller than the accelerations that are considered by underwater explosions. Figure 183 shows that the peak acceleration that is experienced by the cannon-launched missile, is in the order of 9000 g. The period over which this acceleration is experienced (>10 ms) is much longer than the accelerations caused by underwater explosions (<100 µs). The acceleration impulse (integral of the acceleration over time) curve may have the same typical value.

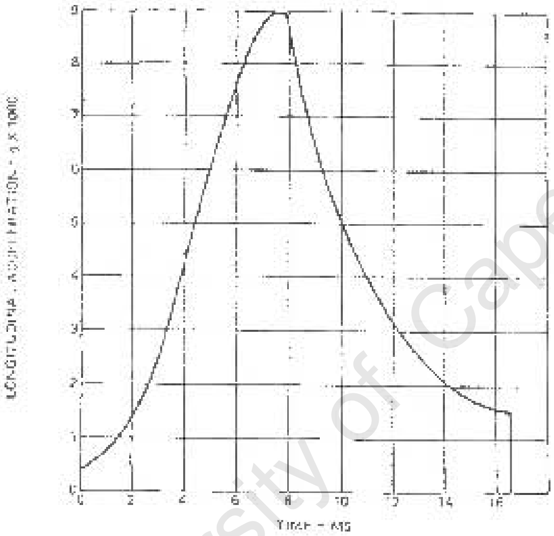

Figure 183: Accelerations caused by cannon-launched missiles, Morrison [15].

This study by Morrison [15] reports that a very careful component screening process must be adhered to before components are used in a production run. During and after production the assembled units are also subjected to more tests, to ensure reliability. In Figure 184 Morrison [15] shows the type of component screening that was done prior to assembly. Unfortunately he did not report on the failure rate of components that were subjected to the tests to enable the reader to assess how successful this pre-screening process was.

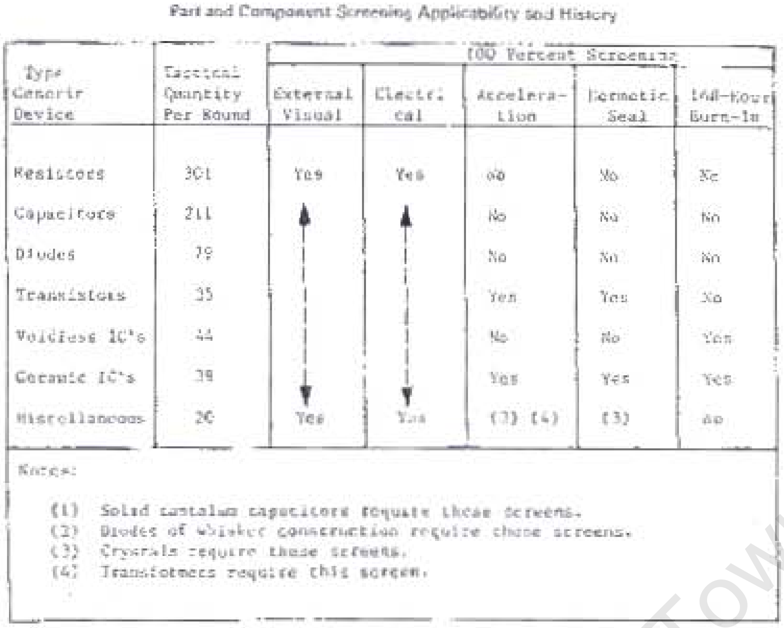

Part and Component Screening Applicability and History

Type Generic Device	Typical Quantity Per Round	100 Percent Screening				
		External Visual	Electrical	Accelera- tion	Hermetic Seal	168-Hour Burn-In
Resistors	301	Yes	Yes	No	No	No
Capacitors	211	↑	↑	No	No	No
Diodes	79			No	No	No
Transistors	35			Yes	Yes	No
Voidless IC's	44			No	No	Yes
Ceramic IC's	39	↓	↓	Yes	Yes	Yes
Miscellaneous	20	Yes	Yes	(3) (4)	(3)	No

Notes:

(1) Solid tantalum capacitors require these screens.
(2) Diodes of whisker construction require these screens.
(3) Crystals require these screens.
(4) Transformers require this screen.

Figure 184: Part and component screening reported by Morrison [15].

However, Morrison [15] did report that a "*reliability dilemma*" was encountered using integrated circuit (IC) components. "*Because of their strain rate properties, both plastic and epoxy encapsulated IC parts proved more tolerant of canon-launched environment than ceramic ICs. Nevertheless, the superior hermetic characteristics of ceramic components made them more reliable*". It must be said that this study [18] was performed in the early 1970s, and that the modern IC-packaging is much more rugged as well as more reliable. This paradox is therefore not applicable today as it was at the time of the study [18].

Morrison [15] also reported that crystal devices were found to be susceptible to launch-induced failure. However, a mounting method was found (additional support), which assisted the pass rate of crystals. This is an interesting finding, because the author of this dissertation also used crystals in high-acceleration tests (a purpose-designed soft spot because of its known failure rate under high acceleration), and found these components to sustain internal failure.

The only other device, which Morrison [15] reports that had problems during the screening process, were transformers. These transformers used a bonded cup core spindle, which had to be replaced by a solid core spindle to achieve 100 % pass rate.

Morrison [15] gave special attention to component mounting and placement methods. The fact that the acceleration loading had a specific direction in the cannon-launched missiles, the components could be placed such that the load was exerted as a compression rather than tension or shear. Figure 185 shows various preferred methods of mounting the components.

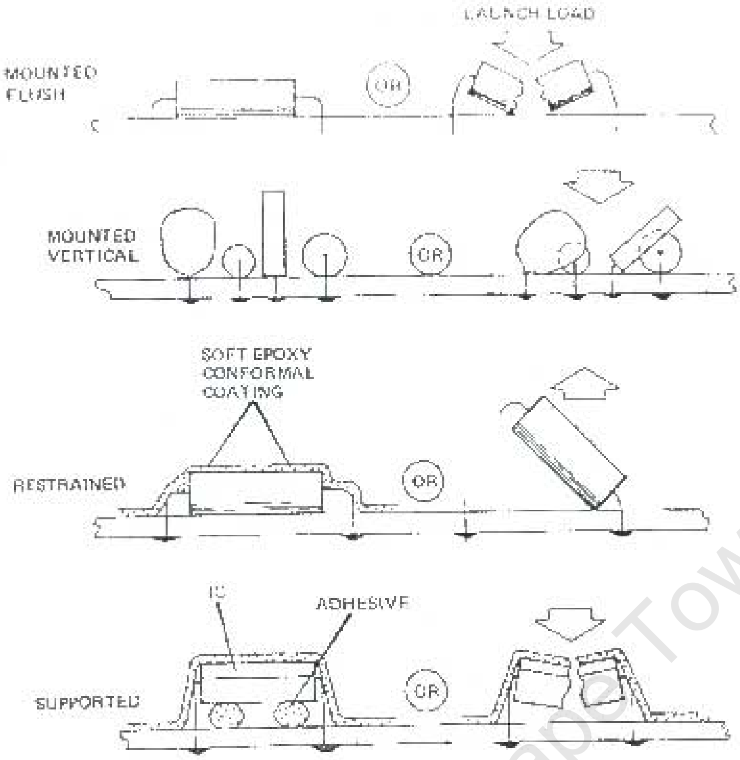

Figure 185: Suggested mounting methods prescribed by Morrison [15].

The principle of "soft-mounts" are illustrated quite well in Figure 185, and the author will show in later chapters that extensive use is made of de-localised soft mounting methods to ensure that acceleration is damped before it is passed on to the components. It must also be said that de-localised soft-mounts are more successful when the time of acceleration is relatively short, irrespective of the amplitude. De-localised soft mounting may therefore not be a good solution to the relatively long acceleration duration of the cannon-launched unit.

Morrison [15] discussed the potting principle, and found that two problems arose when the entire card was potted, i.e. the total weight increased, and acceleration became problematic (not reported why), and rework of the cards became very difficult. The author predicts that this method is contra-productive, because of the qualification and inspection of the production quality becomes extremely difficult.

Urick [23]:

Urick [23: p116] defines a "velocity profile" as "the variation of sound with depth, or the velocity-depth function".

Urick reports that a velocity profile can be obtained by velocity measuring instruments, OR by hydrographical observations of temperature, salinity, and depth.

The three parameters identified, is thus:

1. Temperature
2. Salinity
3. Depth

It is assumed (intuitively at this stage) that the "depth" parameter may in fact have a relation to DENSITY, although Urick gives non-linear curves of velocity vs. depth. The author concludes that density varies non-linearly with depth, due to factors such as salinity and temperature, both of which contribute to the density. The conclusion is thus that the density is a function of depth, salinity and temperature.

Background:

Urick states that there are four discernable layers in deep-sea waters of different velocity characteristics, i.e.:

Surface layer: (top layer), in which the velocity of sound is "susceptible" to daily and local changes of heating, cooling, and wind action. From this statement. the author identifies one distinct parameter, i.e. Temperature. Wind-action may influence temperature. and is thus not seen as a separate parameter.

Seasonal Thermo-cline layer: (below the top layer). "The word 'thermo-cline' denoting a layer in which the temperature changes with depth". He states that the seasonal thermo-cline is characterized by a negative thermal gradient (temperature and velocity) relative to depth (and varies with seasons).

Main Thermo-cline layer: (below the seasonal thermo-cline). Urick states that seasonal influence is minimal, and that the temperature actually increases with depth.

Deep Isothermal Layer: (below the main thermo-cline): In this layer, Uric states that the temperature remains "nearly constant" at 39°F (just above 4°C), and that the sound velocity increases with depth because of the effect of pressure on sound velocity.

118 / principles of underwater sound

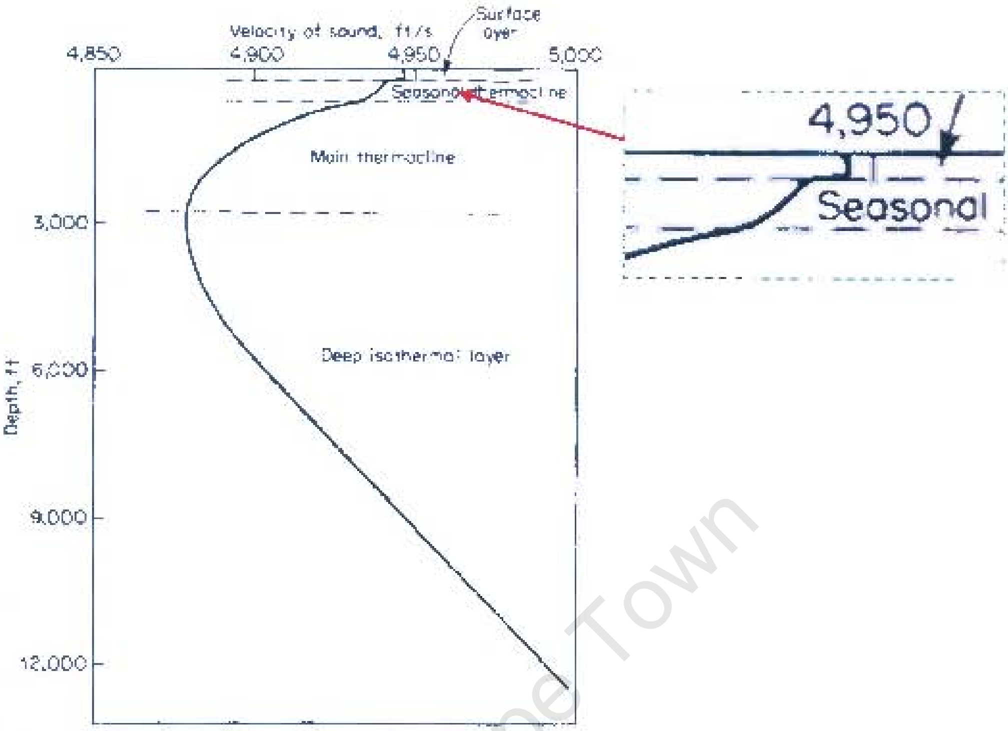

fig. 5.12 Typical deep-sea velocity profile divided into layers.

Figure 186: The different thermal layers illustrated by Urick [23: p118]

120 / principles of underwater sound

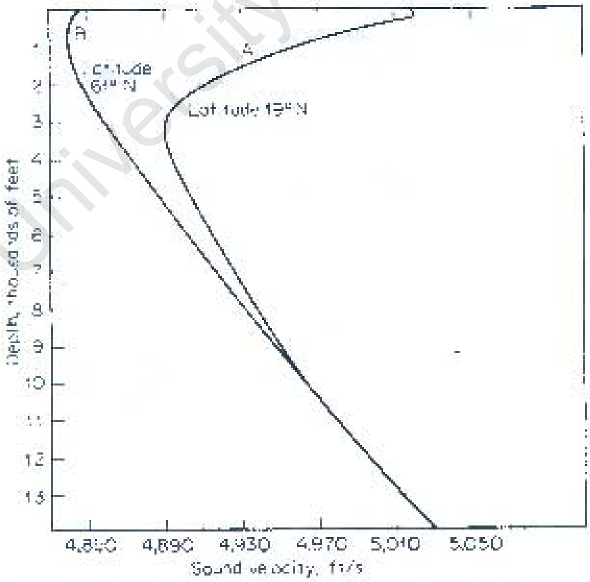

fig. 5.16 Velocity profiles in different latitudes. A: 18°50'N, 30°01'W, spring. B: 61°02'N, 34°01'W, spring. (Ref. 47, profiles 41 and 143.)

Figure 187: Graphical presentation of the sound velocity profile illustrated by Urick [23: p120]

Quantitative findings:

Urick's finding as depicted by Figure 186, is that the velocity typically changes from 4850 ft/s to 5000 ft/s in seawater. Translated to the metric system, this is 1478 m/s to 1524 m/s.

Urick [23] also showed that the sound velocity varies drastically at shallow depths measured at different locations in the world. The range is from 1440 m/s to 1540 m/s.

Conclusion:

The author draws the conclusion that the term "speed of underwater sound" relates to sound, which propagates in seawater at 1440 m/s to 1540 m/s, depending upon the density of seawater only. In the absence of any stimulus, which would increase/decrease the density of the seawater temporarily (thus in its steady state) the density is a function of salinity, temperature and depth, explaining the varying measurements as shown in Figure 187.

Cooper [6]

This manuscript concerns itself with the engineering principles that support the design of explosives. The author's (of this dissertation) interest lies with the qualitative description of a shock wave (Cooper [6: p167]), which describes the shock wave in modern, easy-to-read language. He states that, in the elastic region of the explosion medium (Cooper [6: p169]), the sound velocity is constant.

$$c^2 = \frac{dP}{d\rho} \quad \text{----------------} \quad \mathbf{63}$$

Where
c = sound velocity
P = pressure in the medium
ρ = density of the medium

If the medium is pressurised to beyond the elastic region, the wave velocity increases with pressure or density and P / ρ is not linearly proportional.

Cooper [2: p170] describes the shock wave as a wave with a vertical front (an infinitely high slope rate of the leading edge), and the wave velocity in this region was equal to the sum of the sound and particle velocities, and the wave speed increases with increasing pressure (Cooper [6: p172]). He also makes the following remarks relative to this dissertation:

Cooper [6: p174]:

a. Shock waves occur when a material is stressed far beyond its elastic limit by a pressure disturbance.

b. Because the rarefaction wave moving into the shocked region travels faster than the shock front, the shock is attenuated from behind.

The comment b. above suggests that the form of the shock wave does not change with distance. It will be assumed by this study that this phenomenon occurs in the region (near field) where the elastic limit is exceeded, because in the far field Cole [5] and Kira *et al* [10] give equations that the time constant θ of the rarefaction wave increases with range.